

Silicon Electrolyte Interface Stabilization (SEISta)

Final Progress Report FY18

Anthony Burrell

National Renewable Energy Laboratory
15013 Denver West Parkway
Golden, CO 80401
Phone: (303) 384-6666
E-mail: anthony.burrell@nrel.gov

Brian Cunningham, DOE-EERE-VTO Program Manager

Hybrid Electric Systems, Battery R&D
Phone: (202) 586-8055
E-mail: brian.cunningham@ee.doe.gov

Table of Contents

	Page
Overview	1
SEISta Milestones FY18	4
SEISta Section 1: Intrinsic Chemical Reactivity of Silicon Electrodes— Very Initial Stages of SEI Growth	5
SEISta Section 2: The Influence of the Oxide Layer on the Formation and Stability of the SEI on Silicon	42
SEISta Section 3: Nature and Evolution of the Silicon SEI	92

Project Introduction

This report documents the Silicon Electrolyte Interface Stabilization team's approach in 1) characterizing the early-stage silicon-electrolyte interphase (SEI) including progress on identifying the specific reaction pathways present in the formation of the SEI layer, and 2) establishing a procedure for measuring SEI growth rate at fixed potentials and different cycling regimes.

Silicon is a viable alternative to graphitic carbon as an electrode in lithium-ion cells and can theoretically store >3,500 mAh/g. However, lifetime problems have been observed that severely limit its use in practical systems. The major issues appear to involve the stability of the electrolyte and the uncertainty associated with the formation of a stable SEI at the electrode. Recently, calendar-life studies have indicated that the SEI may not be stable even under conditions where the cell is supposedly static. Clearly, a more foundational understanding of the nature of the silicon/electrolyte interface is required if we are to solve these complex stability issues. A new multi-lab consortium has been formed to address a critical barrier in implementing a new class of materials used in lithium-ion batteries that will allow for smaller, cheaper, and better performing batteries for electric-drive vehicles. This consortium, named the Silicon Electrolyte Interface Stabilization (SEISta) project, was formed to focus on overcoming the barrier to using such anode materials. Five national laboratories are involved: the National Renewable Energy Laboratory (NREL), Argonne National Laboratory (ANL),

Lawrence Berkeley National Laboratory (LBNL), Oak Ridge National Laboratory (ORNL), and Sandia National Laboratories (SNL).

The SEISta project was specifically developed to tackle the foundational understanding of the formation and evolution of the solid-electrolyte interphase on silicon. This project will have as its primary goal an understanding of the reactivity of the silicon and lithiated silicon interface with the electrolyte in lithium-ion systems. It consists of researchers from multiple national laboratories (NREL, ANL, LBNL, ORNL, and SNL) working toward clear unified goals. The Silicon Deep-Dive team, which focuses on the science and technology barriers in functional electrodes, is a critical partner in this work. Many of the researchers are shared between both teams, and we hold joint meetings to ensure effective communication between the teams.

The current goals of SEISta are:

Quarter 1 Milestone:

- Have completed selection and characterization (X-ray photoelectron spectroscopy [XPS], secondary-ion mass spectrometry [SIMS], infrared [IR] and Raman spectroscopy), including determination of the surface-termination chemistry and impurity levels of the SEISta model research samples to be used by all members of the team in FY18. (100% complete)

Quarter 2 Milestone:

- Have characterized (XPS, SIMS, IR, and Raman) the surface chemistry and composition of the SEISta model research samples after contact with the electrolyte, before cycling, including the nature of the electrolyte decomposition products. (100% complete)

Quarter 3 Milestone:

- Completed characterization (electrochemistry, IR, and Raman) of the early-stage silicon-electrolyte interphase formation on the SEISta model research samples, specifically by establishing and demonstrating a procedure for quantitatively measuring the solubility of SEI on silicon surfaces. (100% complete)

Quarter 4 Milestones:

- Established and demonstrated a procedure for measuring the growth rate of silicon SEI components at fixed potentials and during cycling. (100% complete)
- Determined how the physical properties of the silicon/electrolyte interface are influenced by the nature of the silicon surface on the SEISta model samples. (100% complete)

Approach

The SEISta team works to ensure that protocols for sample preparation, experimental design, and implementation as well as data reporting are consistent across the whole team. Each laboratory is working toward the same set of quarterly milestones using its own specific talents and capabilities in a concerted effort with the other team members. This joint focus results in multiple researchers interacting to produce and analyze data to ensure that individual experimental variations will not lead to erroneous results. Critical to the success of this effort is the use of standard samples that can be shared by all parties. In the first FY, a round-robin sample test was established to ensure that data could be duplicated at the different laboratories by different researchers. In addition to weekly whole-team video presentations, we have held on-site face-to-face meetings each quarter for all team members and other interested parties to brainstorm and sort out issues with existing experiments and jointly develop new experimental plans.

The outcomes from FY17 indicated that the nature of the silicon starting materials has major implications for the formation and evolution of the SEI. This is most clearly seen in the inherent chemical reactivity of the silicon materials with electrolytes before electrochemistry. Much of our focus for FY18 will be in looking at

the initial chemistry of the silicon on contact with electrolytes. This will then lead to an understanding of how the electrode/electrolyte interface changes upon applied voltage and how the SEI forms and evolves.

Objectives

The critical issues that SEISta is attempting to determine are:

- What are the properties of the lithiated silicon/electrolyte interface?
- What is the silicon SEI actually made of and what reactions are contributing to it?
- How fast does the silicon SEI grow?
- Does it stop growing?
- Is it soluble?
- Can it be stabilized?

For FY18, the team focused on three broad tasks:

Materials Standardization – This task is critical to the development and deployment of standardized samples and experimental procedures across the team. We will continue to provide full characterization to any new sample that is to be used for SEI studies to ensure reproducibility and full understanding of the material. This quarter's work focused on developing new oxide coatings and methods to control the thickness and density of oxide samples. In addition, work on the silicon nanoparticles has made progress with the enhancement of the materials collection and handling system in the plasma reactor. *Although this work dominated the early part of the project and is still critical to its success, it is now only a minor part of the work and this is reflected in the relative balance of this quarterly report.*

Model Materials Development and Characterization – The nature of the electrode-electrolyte interaction in silicon electrodes is at the heart of the formation and stability of the SEI. The inherent chemical reactivity of silicon with common electrolytes has been a focus for this team and will be a primary focus moving to quarter 2. The synthesis of well-defined silicon nanoparticles and the different chemical markups of lithiated silicon surfaces is being probed by preparing model compounds and thin films that may/can exist in silicon anodes. Lithium silicides, silicates, and other inorganic material (LiF, Li₂O) are being prepared, and their reactivity with electrolytes is being determined. These materials also act as standard spectroscopy samples for the researchers who are looking at the formation of the SEI on different silicon materials.

SEI Characterization – The overall objective for SEISta is to understand the nature and evolution of the SEI on silicon anodes. The materials standardization and model compounds will enable the researchers to systematically investigate the formation of the solid-electrode interphase using a wide variety of the spectroscopy techniques—from different optical, microscopy, and electrochemistry—to determine how the SEI forms based on the nature of the silicon surface, and how it evolves over time. This section of work will continue to grow in scope as we move beyond the sample-characterization phase of the project and toward understanding the nature and evolution of the SEI. *This part of the project now represents the bulk of the work and, as such, this quarterly report is largely reporting on work leading to this outcome.*

SEISta Milestones FY18: Silicon Electrolyte Interface Stabilization (SEISta)

SEISta Team

Background

The overall objective of the SEISta project is to better understand the formation and evolution of the solid-electrolyte interphase (SEI) on silicon anodes. Silicon is a viable alternative to graphitic carbon as an electrode in lithium-ion cells and can theoretically store >3,500 mAh/g. However, lifetime problems have been observed that severely limit its use in practical systems. The major issues appear to involve the stability of the electrolyte and the uncertainty associated with the formation of a stable SEI at the electrode. Recently, calendar-life studies have indicated that the SEI may not be stable even under conditions where the cell is supposedly static. Clearly, a more foundational understanding of the nature of the silicon/electrolyte interface is required if we are to solve these complex stability issues. A multi-lab consortium has been formed to address a critical barrier in implementing a new class of materials used in lithium-ion batteries that will allow for smaller, cheaper, and better performing batteries for electric-drive vehicles. This consortium—the Silicon Electrolyte Interface Stabilization (SEISta) project—was formed to focus on overcoming the barrier to using such anode materials. Five national laboratories, led by the National Renewable Energy Laboratory (NREL), are involved: NREL, as well as Argonne (ANL), Lawrence Berkeley (LBNL), Oak Ridge (ORNL), and Sandia National Laboratories (SNL). The third-quarter milestone for SEISta in FY18 was:

Quarter 1 Milestone:

- Have completed the selection and characterization (XPS, SIMS, IR, and Raman), including determination of the surface termination chemistry and impurity levels, of the SEISta model research samples to be used by all members of the team in FY18.

Quarter 2 Milestone:

- Have characterized (XPS, SIMS, IR, and Raman) the surface chemistry and composition of the SEISta model research samples after contact with the electrolyte, before cycling, including the nature of the electrolyte decomposition products.

Quarter 3 Milestone:

- Completed characterization (electrochemistry, IR, and Raman) of the early-stage silicon-electrolyte interphase formation on the SEISta model research samples, specifically by establishing and demonstrating a procedure for quantitatively measuring the solubility of SEI on silicon surfaces.

Quarter 4 Milestones:

- Established and demonstrated a procedure for measuring the growth rate of silicon SEI components at fixed potentials and during cycling.
- Determined how the physical properties of the silicon/electrolyte interface are influenced by the nature of the silicon surface on the SEISta model samples.

Results

For FY18, all milestones are 100% complete.

SEISta Section 1: Intrinsic Chemical Reactivity of Silicon Electrodes—Very Initial Stages of SEI Growth

SEISta Team

Background

Although the bottle may say silicon on the label, it is becoming increasingly clear that not all “silicon” materials are the same. The variation in silicon chemistry—influenced by manufacturing process, history, and processing—results in dramatic variations in performance, stability, and processability of silicon electrodes. In addition, we suspect that the surface chemistry of the silicon contributes to calendar life, binder interactions, and the general variability in the silicon literature.

Due to the increasingly apparent correlation of silicon source and performance, we have undertaken a series of studies to understand the intrinsic reactivity of various well-defined silicon-based materials. The goal is to answer the following questions:

1. How does reactivity change depending on surface termination?
2. How does the initial surface chemistry direct the SEI formation?
3. What surface terminations are most stable?
4. Can we develop approaches to stabilize the surface and direct SEI formation?

To address these questions, we are working with a series of silicon materials including: hydrogen- and hydrocarbon-terminated silicon, silicon dioxide made by flame pyrolysis and solution precipitation, stoichiometric lithium silicates, Li-Si line compounds, and thin-film and wafer silicon. We hypothesize that the surface chemistry helps to direct the very initial stages of SEI growth *and* stability of the cell during formation cycling. These studies will provide a foundation to predict and explore stable surface chemistries as well as establish a basis to begin to understand the variation of results reported in the literature and technical reports.

Materials

Well-defined or commercially available silicon-based materials in large quantities were used in this work. Table 1 lists the representative silicon-containing materials used in these studies. Where possible, commercial materials were purchased. In other cases, they were manufactured using synthesis methods described below. For the aging studies, materials were exposed to standard SEISta electrolytes (1.2M LiPF₆ in 3:7 ethylene carbonate:ethyl methyl carbonate (EC/EMC), and 1.0M LiTFSI in 3:7 EC/EMC). For some experiments, LiClO₄ salt was added to a 3:7 EC/EMC solvent mixture to explore the role of fluorine in the observed chemical reactions.

Table 1. Summary of silicon-based materials used in this work

Material	Description/Synthesis	Ref
Si-H	Synthesized by plasma-enhanced chemical vapor deposition (PECVD). Particles 10 nm in diameter and materials mostly free of oxygen termination	1
Si powder	Milled silicon produced by nanoamor	
SiO ₂ – Stöbber	Synthesized through the controlled hydrolysis of tetraethyl orthosilicate (S5505 – Sigma Aldrich)	2
SiO ₂ – Fumed	Commercial SiO ₂ prepared by flame pyrolysis of SiCl ₄	
Li ₂ SiO ₃	Prepared by solid-state synthesis between SiO ₂ and Li ₂ CO ₃	
Li ₄ SiO ₄	Prepared by solid-state synthesis between SiO ₂ and Li ₂ CO ₃	
Li-Si alloy	Prepared by high-temperature reaction between Li metal and Si	
Si wafer	Commercial (100) wafer	
Li-Si-O films	Sputter-deposited lithium silicates	
Li-Si films	Evaporation of Li onto silicon film	

Results – Chemical Reactions with Electrolyte

It has been observed in the past that extensive gassing occurs upon sealing of a pouch cell, presumably based on chemical reactions that occur before electrochemical cycling. We believe that this is the very initial stages of SEI growth and that by exploring these reactions, one can predict surfaces that would be stable and direct the formation of a suitable SEI layer.

To evaluate the extent of gassing, sealed Surlyn pouches (same material used for pouch cells) were assembled. The pouches consisted of two wells—one chevroned and holding the powdered sample, and the other holding the liquid electrolyte—to be sealed with a pathway for the liquid to flow through as the pouch was turned on its side (Figure 1). This was to keep the reactants separate because the reaction occurred immediately upon mixing. Samples were prepared in the glovebox by placing the silicon material (~0.2 g) in the pouch, followed by 400 μ L of electrolyte. The pouches were sealed in the box and removed to atmosphere, where they were sealed again as a precaution. **NOTE – hydrofluoric acid was measured in some cells, so suitable precautions should be taken when using these cells.** The volume of gas produced was determined using the Archimedes buoyancy method. A photo of the experimental apparatus is shown in Figure 2.

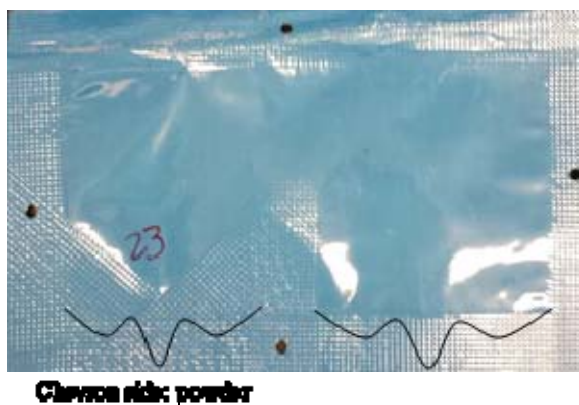


Figure 1. Pouch cells designed for gassing studies. The pouch has two wells—one for electrolyte and the other for material—to control initial mixing.



Figure 2. Buoyancy apparatus with a water bucket, indium wire to hang the pouch from the balance, and a bob (20 g dry).

To follow the gassing reaction rates and mechanisms, infrared (IR) experiments were run on an Agilent Technologies Cary 680 Fourier transform infrared (FTIR) spectroscope. These studies could track CO, CO₂, SiF₄, PF₃, HF, and electrolyte, but not H₂ or O₂ gas. In a glovebox, a known amount of silicon-based material (~0.2 g) is weighed and transferred onto a boat (40 mm × 13 mm × 2 mm). The boat is inserted into the IR gas cell (Figure 3). The cell had KBr windows as well as a septum (SupleCo GR-2 septum, 6 mm) for the injection port. A small syringe is filled with electrolyte (400 μL) and brought out of the glovebox along with the gas cell. The cell is placed on the holder in the IR spectrometer, and a background scan is taken. The electrolyte is injected through the injection port, first making sure that the boat is situated under the port inside the cell. Once the electrolyte is injected, the kinetic experiment is started. The data were taken as follows: a scan every 10 s for 30 min, then every 60 s for 60 min, then 120 s for 60 min, then 300 s for 600 min, and finally, 600 s for 80 min. The range of scans was from 4,000 to 350 cm⁻¹, and the resolution was 4 cm⁻¹. After the scans were taken, the peaks of interest were integrated to track their intensity over time.



Figure 3. IR gas cell used for kinetic measurements from two different angles. The path length through the cell is 11 cm, and the KBr windows are 25 mm in diameter by 2 mm thick from Sigma Aldrich. The injection port (circled in red) is sealed with a septum, and the outgas port (yellow) can be opened for purging, if necessary.

The CO₂ calibration curve was constructed by purging the gas cell with Ar gas, with a needle and hose leading through the injection port, and the outgas port open. The outgas port was closed, and the needle removed to take the background, and then a known concentration of CO₂ gas was flowed into the gas cell. Scans were taken with the outgas port closed and the injection needle removed so that there was no interference from the incoming gas or escaping gas in the resulting spectrum.

PECVD and Milled Silicon

The volume of gas produced between the plasma-enhanced chemical-vapor-deposited (PECVD) Si and the electrolyte, as measured from the buoyancy method, as a function of time is shown in Figure 4. All reactions were duplicated to confirm reproducibility. The data show that PECVD Si produced gas immediately upon contact with the electrolyte, which indicates the extreme reactivity of the native silicon surface. The addition of 10% fluorinated ethylene carbonate (FEC), a known additive that leads to a more stable SEI, has no influence on the extent of gassing. However, removing the LiPF₆ salt from the electrolyte eliminates the gassing, thus indicating that the PF₆⁻ anion plays a major role in the observed gas formation. To confirm these results, LiTFSI-based electrolytes were explored. The TFSI electrolyte showed slight gassing with the rate being 115 times slower than LiPF₆. The TFSI electrolyte evolved only 0.02 mL gas, so we conclude that the identity of the anion does matter in producing gas.

In comparison to the PECVD silicon, the oxide-terminated nanoamor took much longer (days to weeks) to begin gassing (see Figure 4, right). However, once the reaction with milled silicon began, it produced a much larger volume of gas (4 mL vs 0.4 mL). This was an order-of-magnitude more gas produced than with PECVD, although it was much slower, suggesting that the oxide layer influences the kinetics and mechanism.

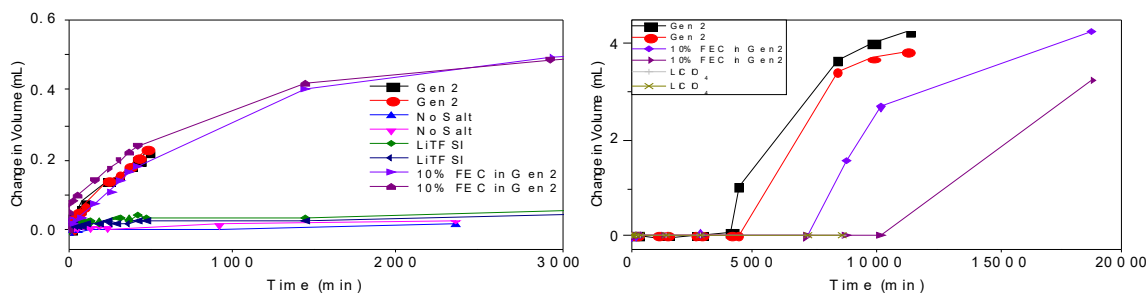


Figure 4. Plot of change in volume (calculated through buoyancy) of the nanostructured silicon compounds reacting with various electrolytes in pouches. The left plot is of the PECVD Si and the right is nanoamor silicon.

Here, we saw that the FEC doubled the time delay for gas production, but the same amount of gas was produced. Replacing the PF₆⁻ anion with ClO₄⁻ prevented the reaction from occurring, again indicating that the LiPF₆ salt is an integral part of the reaction. Note that the analysis of reactions between TFSI salt with nanoamor revealed a large amount of HF gas formation.

To explore the reactions with silicon, further mass spectrometry and IR spectroscopy measurements were employed. *In-situ* IR spectra of the gas evolution was recorded in real time. Representative transient spectra are shown in Figure 5A because many more spectra were taken to accurately follow the evolution over time. Within the data, most peaks are attributed to solvent vapor. Because the solvent is volatile, the referenced background was taken. Peaks that appeared at later times and grew throughout the reaction were attributed to products of the reaction, such as carbon dioxide (2,350 cm⁻¹), carbon monoxide (2,200 cm⁻¹), silicon tetrafluoride (725 cm⁻¹), and phosphorous trifluoride (475 cm⁻¹). The insets on the IR plot give a representative view of the products over time. Figure 5B shows the integrated signal intensity as a function of time for CO, CO₂, SiF₄, and PF₃. For the first 500 minutes, the only product changing is carbon monoxide. Around 500 minutes, CO starts to increase, as CO₂ decreases. From 900 minutes, all curves begin to increase, with CO,

SiF₄, and PF₃ peaks flattening slightly at 1,150 minutes. From this, it can be determined that the evolution of the gases is highly correlated. Further proof of their correlation can be found in the derivative plot, which is an inset of Figure 5B. All four curves line up from 650 to 950 minutes, and then begin to rise at varying slopes from there. There is a spike in CO, SiF₄, and PF₃ at 1,190 minutes, corresponding to the bump in the integrated signal vs time plot. The CO₂ peak went negative before growing, indicating that initial concentrations of the gas were used in the reaction, or simply dissolved into the solution, because CO₂ is known to be highly soluble in carbonates. Mass spectroscopy was conducted on the gases in the pouch cells. Figure 5C shows the mass spectrum of the PECVD Si pouch after 480 minutes. The gases evolved in the pouch were found to be O₂ (32 amu) and CO/ethylene (28 amu), known decomposition products of a similar electrolyte. The quick evolution of CO gas in the IR spectrum agrees with the rapid expansion of pouch cell and the high CO count in the MS.

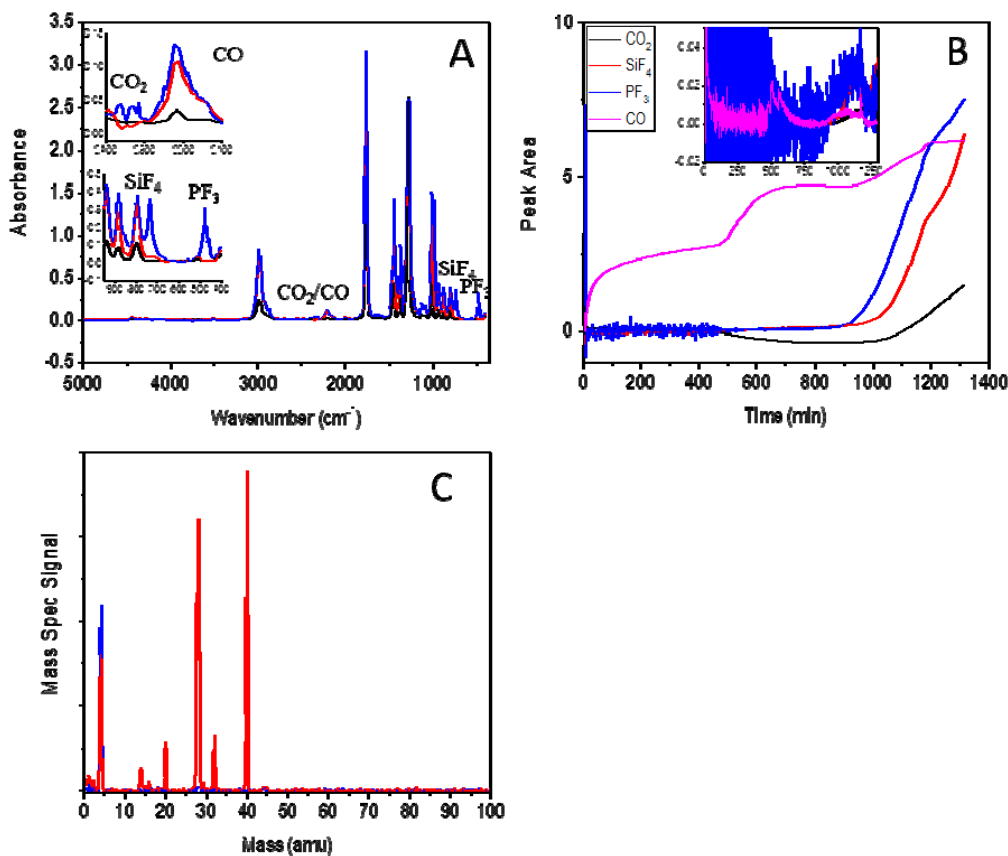


Figure 5. Characterization data for the gases produced in the reaction between the PECVD silicon LiPF₆ electrolyte. A. Kinetic IR (black = 14 min, red = 752 min, blue = 1,278 min), insets CO₂ and CO, and SiF₄ and PF₃. B. Peak area vs time plot to illustrate any correlation between the evolution of the different gases. Inset is derivative of plot with respect to time. (In both, black = CO₂, purple = CO, red = SiF₄, and blue = PF₃). C. Mass spectrum was taken after 480 minutes (sample is red, helium is blue). Boxes around peaks correspond to various compounds (blue = CO, purple = O₂), SiF₄ (104 amu, 85 amu, 86 amu, 87 amu), PF₃ (69 amu), CO₂ (44 amu), F (19 amu), and H₂ (2 amu).

In contrast to the PECVD, the milled silicon showed dramatically different products. Figure 6A shows representative FTIR spectra collected as a function of time. From these data, we did not observe the formation of CO, which directly contrasts with the PECVD data. Furthermore, the data show the immediate decomposition of salt to produce PF₃ and of silicon to produce SiF₄. The PF₃ evolves the fastest, but begins to slow down around 100 minutes when the CO₂ and SiF₄ rate increases. Just after 200 minutes, the CO₂ reaction

increases in rate again, and the SiF_4 decreases until equilibrium is presumably reached. The PF_3 gas begins to disappear around 500 min, suggesting its consumption for another reaction. The small amount of PF_3 in the MS may be from the continued consumption of PF_3 gas for the next two weeks before reaching the point that the mass spectrum was taken. Clearly, the mechanism of electrolyte degradation is different between the two Si particles. The major difference between the particles is the surface state. For nanoamor, the surface is covered by a native oxide layer having $-\text{OH}$, $-\text{O}$ termination, whereas that of the PECVD Si is terminated with surface $-\text{H}$. These results highlight opportunities to direct the surface reactivity.

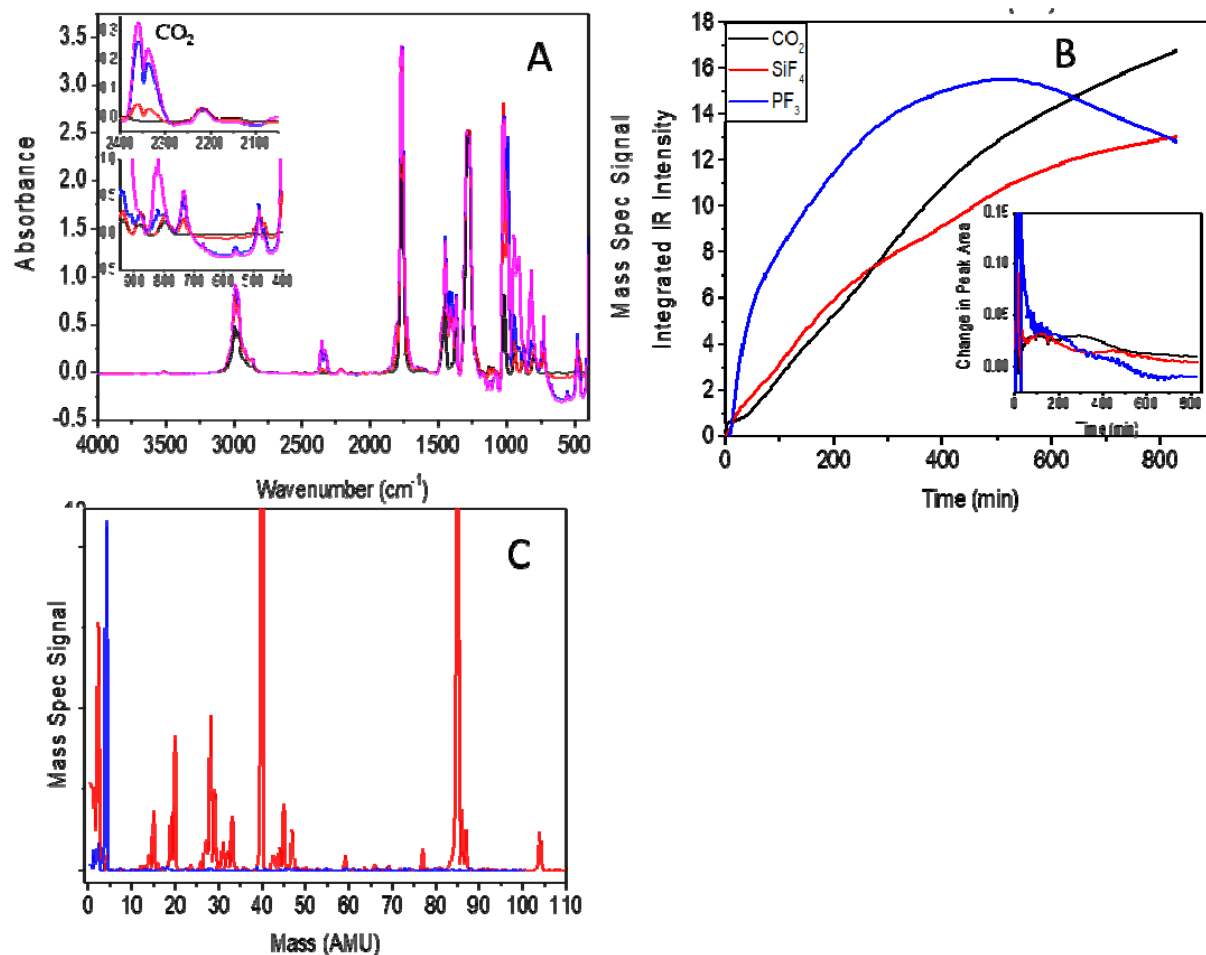


Figure 6. Characterization data for the gases produced in the reaction between the nanoamor silicon and the electrolyte. A. Kinetic IR (black = 0.936 min, red = 126 min, blue = 559 min, purple = 818 min), insets CO_2 , and SiF_4 and PF_3 . B. Mass spectrum was taken after 14 days (sample is red, helium is blue). Boxes around peaks correspond to various compounds (yellow = H_2 , black = F, blue = CO, purple = O_2 , orange = CO_2 , red = PF_3 , green = SiF_4). SiF_4 (104 amu, 85 amu, 86 amu, 87 amu), PF_3 (69 amu), CO_2 (44 amu), F (19 amu), and H_2 (2 amu). C. Peak area vs time plot to illustrate any correlation between the evolution of the different gases. Inset is derivative of plot with respect to time. (In both, black = CO_2 , red = SiF_4 , and blue = PF_3).

Intrinsic Reactivity of SiO_2

To test the theory of the importance of the native oxide layer for producing CO_2 , multiple silica compounds were tested in the same fashion. Fumed silica (S5505, Sigma Aldrich) was dried in a glovebox antechamber

before use. From the selected plots from the kinetic IR in Figure 7A, the reaction clearly produces CO_2 , SiF_4 , PF_3 , and CO , as seen in the previous reactions. Therefore, the solvent is still reacting to decompose, and the salt has access to the silicon to react with it, forming SiF_4 . The plot of the integrated intensity vs time is shown in Figure 7B. The CO_2 curve closely resembles that of the silane-sourced silicon. First, the curve is flat, indicating that any CO_2 produced is remaining in the solvent or in equilibrium with surrounding CO_2 gas dissolving in and out of the solvent. At 750 minutes, the CO_2 begins to disappear, again corresponding to the onset of SiF_4 production. As the CO_2 begins to increase again at 850 minutes, the SiF_4 peak has a plateau that jumps again as the CO_2 flattens off at 1,150 minutes. The PF_3 curve follows the same plateau and increase pattern as the SiF_4 , indicating that the evolution of all three gases is connected. Figure 7C shows the mass spectrum of the gas evolved in the pouch reaction between the S5505 and the Gen 2 electrolyte after 40 days. The products were found to be CO , CO_2 , H_2 , PF_3 , and SiF_4 : SiF_4 (104 amu, 85 amu, 86 amu, 87 amu), PF_3 (69 amu), CO_2 (44 amu), O_2 (32 amu), CO (28 amu), F (19 amu), and H_2 (2 amu). These results indicate that both the decomposition reaction of the solvent and the salt reaction with the silicon substrate are occurring.

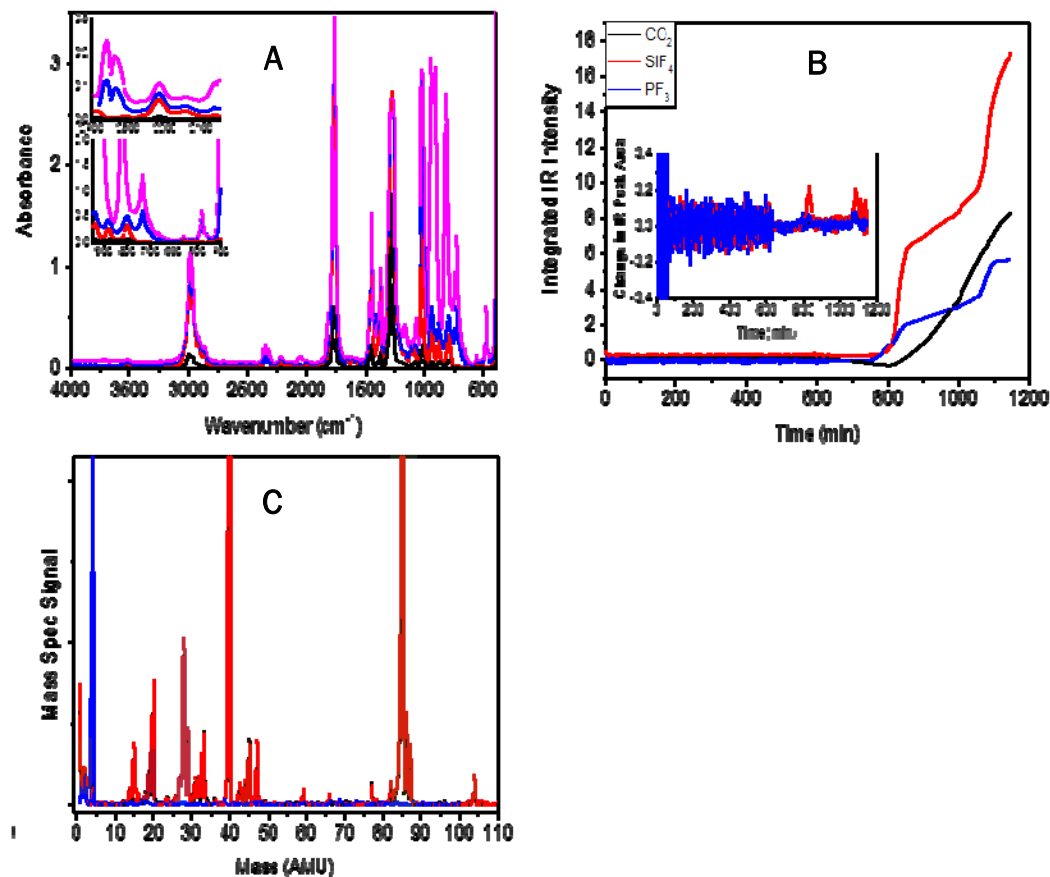


Figure 7. Characterization data for the gases produced in the reaction between the fumed silica and the electrolyte. A. Kinetic IR (black = 0.3 min, red = 184 min, blue = 1,019 min, purple = 1,147 min), insets CO_2 , and SiF_4 and PF_3 . B. Peak area vs time plot to illustrate correlation between the evolution of the different gases and trends. Inset: Derivative of plot with respect to time of peak area vs time plot. (In both, black = CO_2 , red = SiF_4 , and blue = PF_3). C. Mass spectrum was taken after 40 days (sample is red, helium is blue). Boxes around peaks correspond to various compounds (yellow = H_2 , black = F , blue = CO , purple = O_2 , orange = CO_2 , red = PF_3 , green = SiF_4). SiF_4 (104 amu, 85 amu, 86 amu, 87 amu), PF_3 (69 amu), CO_2 (44 amu), F (19 amu), and H_2 (2 amu).

Silica prepared by the Stöber method was used as a comparison to determine if morphology influenced the gassing. Figure 8A shows the IR spectra collected at several times. From the inset plots in Figure 8A, the CO_2 is decreasing in intensity, indicating that the initial amount present in the background spectrum is either dissolving into the solvent, or reacting to form another product. The CO peak is much stronger next to the decreasing CO_2 , and the SiF_4 and PF_3 peaks do not appear to be changing. Figure 8B, which is the IR integrated signal vs time plot, does not indicate any correlation between the gassing of each product relative to the others, which is supported by the derivative plot. After an extensive period of time, the mass spectrometry data (Figure 8C) of gases evolved were determined to be CO , O_2 , CO_2 , SiF_4 , F , and H_2 . The CO , O_2 , CO_2 , and H_2 can all be attributed to solvent decomposition or the reaction of the termination layer on the silica. The excess of CO and O_2 compared to the CO_2 may indicate the decomposition of the CO_2 , or simply that the solvent molecule decomposing, either the EC or the EMC, prefers to form CO than CO_2 . Again, the SiF_4 results from the reaction between the LiPF_6 salt and the silicon in the electrode. Interestingly, there is no presence of PF_3 , a natural product of the reaction generating the SiF_4 . It is possible that the PF_3 formed is used in a further reaction related to passivation of the silica. Another interesting detail from this reaction was that an orange liquid formed in both the pouch and the IR cell. Although the exact identification of this liquid is unclear, some phosphorous compounds such as P_2H_4 are orange.¹⁵ In the pouches, an orange gas is also present, which is corrosive and has a negative effect on the mass spectrometer. This would indicate the presence of a fluorinated compound, but it is unclear from the data gathered at this time what is the exact composition.

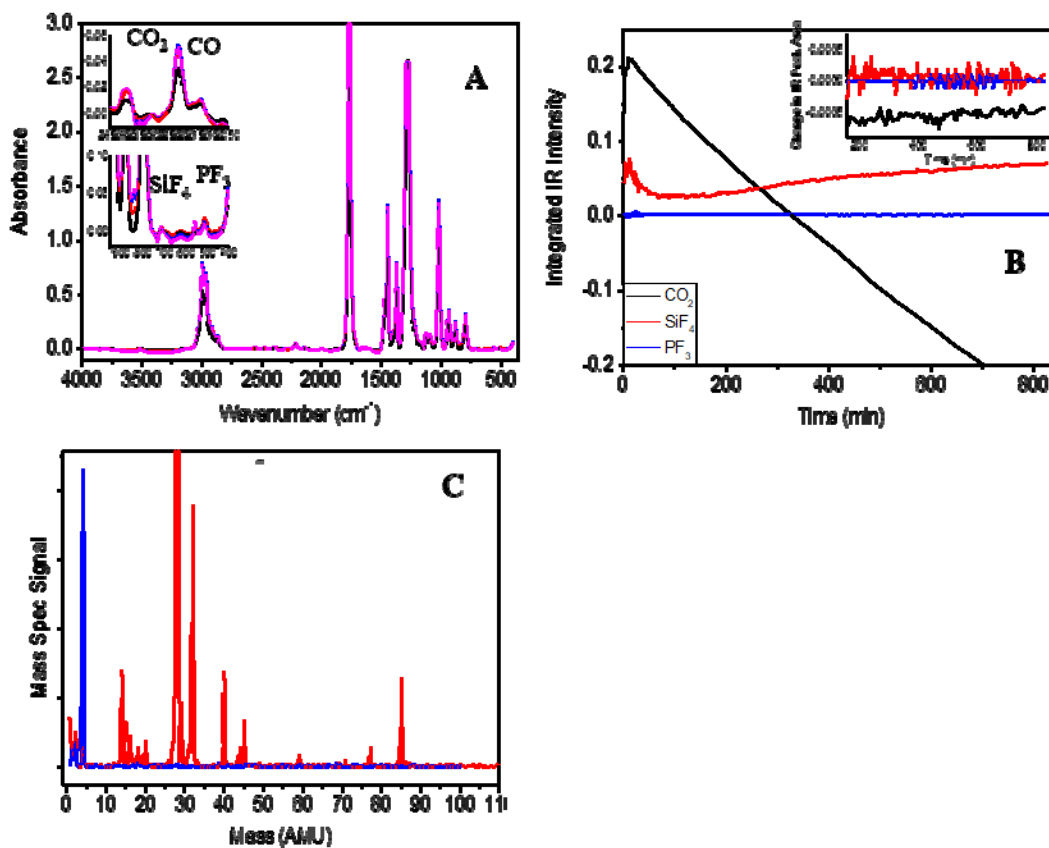


Figure 8. Characterization data for the gases produced in the reaction between the Stöber silica and the electrolyte. A. IR data as a function of time (black = 0.936 min, red = 126 min, blue = 559 min, purple = 818 min), the CO_2 , SiF_4 , and PF_3 peaks were nonexistent, as identified in the insets. B. Peak area vs time plot, the three gases produced (black = CO_2 , red = SiF_4 , and blue = PF_3). C. The mass spectrum was taken after 48 days, and the reaction gases were present in this

spectrum, indicating that the reaction took longer than the run time of the IR experiment (sample is red and black, helium is blue). SiF₄ (104 amu, 85 amu, 86 amu, 87 amu), PF₃ (69 amu), CO₂ (44 amu), F (19 amu), and H₂ (2 amu). Boxes around peaks correspond to various compounds (yellow = H₂, black = F, blue = CO, purple = O₂, orange = CO₂, red = PF₃, green = SiF₄).

Lithium Silicates

One potential silicon termination involves the formation of lithium silicates. Several known phases exist (Li₂SiO₃, Li₂Si₂O₅, Li₄SiO₄). Two end members of this series were investigated. Figure 9A shows IR data collected at various times, along with the corresponding insets. The data indicate that the only gas produced was CO₂, with resonance peaks appearing beyond the normal peak at 2,350 cm⁻¹. The peak that appears around 650 cm⁻¹ in the inset plot, usually attributed to SiF₄ and PF₃ peaks, can be attributed to CO₂ harmonics. Very little SiF₄ and PF₃ evolved in the reaction, as indicated by the small IR signal, which could also be seen in the integrated IR signal vs time plot (Figures 9C and D). The double-y axes allow for the trends between the materials to be compared, even as the change in the CO₂ is much greater than that of the other two. The carbon dioxide curve shows an increase in CO₂ over time, but the derivative plot shows the rate of evolution to be decreasing throughout the reaction. After 28 days, the mass spectroscopy data (Figure 9B) indicated the formation of CO, CO₂, H₂, and O₂ from solvent decomposition. However, the mass spectrum does not indicate the presence of SiF₄ or PF₃, even after the 28 days of reacting in the pouch. As with the Stöber silica, the CO evolution is rapid initially, but remains level at about 2.5 area units for the duration of the reaction.

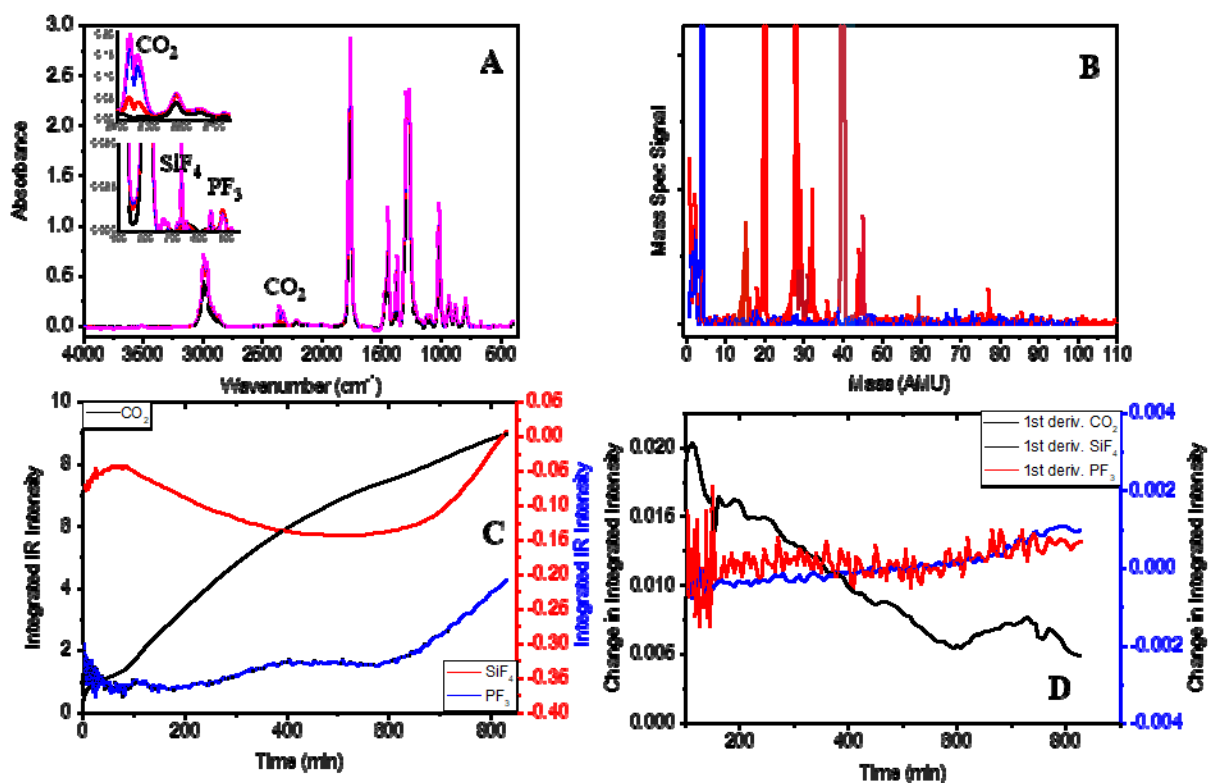


Figure 9. Characterization data for the gases produced in the reaction between the Li₂SiO₃ and the electrolyte. A. IR data as a function of time (black = 0.936 min, red = 126 min, blue = 559 min, purple = 818 min), insets CO₂, and SiF₄ and PF₃. B. Peak area vs time plot. C. Derivative of plot with respect to time of peak area vs time plot. (In both, black = CO₂, red = SiF₄, and blue = PF₃). b) Mass spectrum was taken after 27 days (sample is red, helium is blue). Boxes around peaks correspond to various compounds (yellow = H₂, black = F, blue = CO, purple = O₂, orange = CO₂, red = PF₃, green = SiF₄). SiF₄ (104 amu, 85 amu, 86 amu, 87 amu), PF₃ (69 amu), CO₂ (44 amu), F (19 amu), and H₂ (2 amu).

Similar stability is observed for the lithium orthosilicate (Li_4SiO_4) as for the metasilicate. Figure 10A shows the spectra from the kinetic IR experiment, where once again the only gases evolving are CO and CO_2 , not SiF_4 or PF_3 . This trend is further visible in Figure 10B, the plot of integrated intensity vs time, where the SiF_4 and PF_3 curves are flat lines, and the CO_2 peak increases to 0.8 area units, and stays relatively constant for the remainder of the reaction. This is also the case with the CO curve. Figure 10C shows the mass spectrometry data, collected after 19 days. The evolution of CO, CO_2 , and O_2 from the reaction with the electrolyte in the pouch is confirmed. There is no evidence of SiF_4 or PF_3 in the mass spectrum, indicating again that only the electrolyte solvent is decomposing. The fluorine peak seen in the mass spectrum is an artifact from the column, as the HF from other pouches started appearing in all spectra. The pouch data shows almost no growth over time, and the IR plots show very consistent behavior for each product throughout the reaction time, indicating that there was almost no reaction.

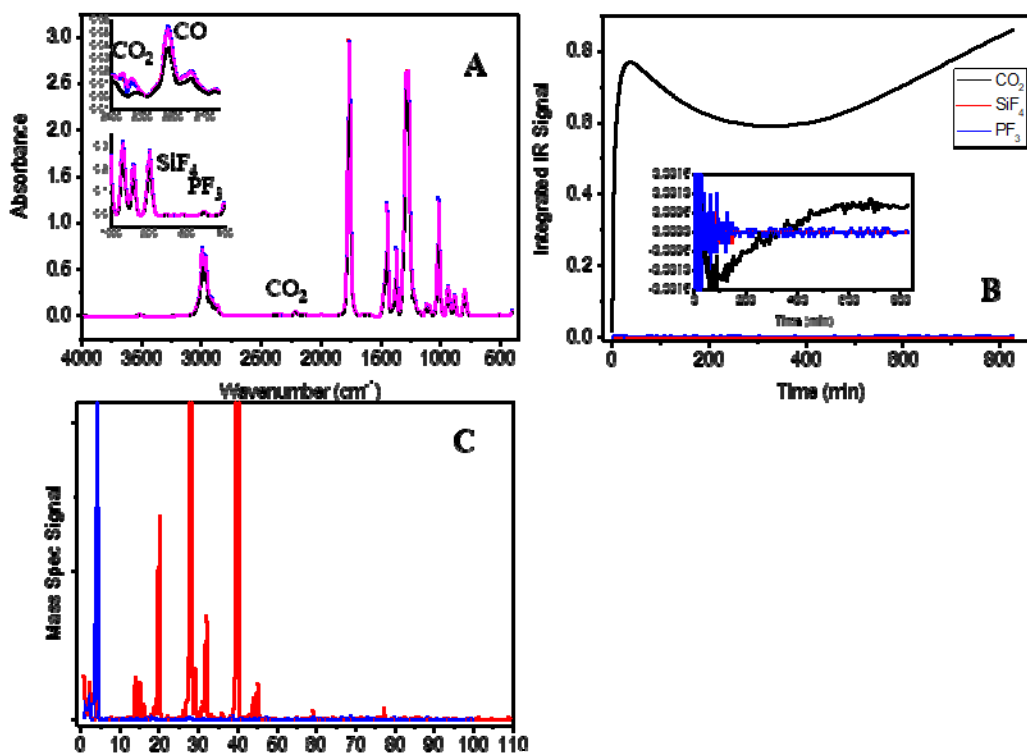


Figure 10. Characterization data for the gases produced in the reaction between the Li_4SiO_4 and the electrolyte. A. Kinetic IR data as a function of time (black = 0.936 min, red = 126 min, blue = 559 min, purple = 818 min), insets CO_2 , and SiF_4 and PF_3 . B. Peak area vs time plot. Inset is derivative of plot with respect to time. (In both, black = CO_2 , red = SiF_4 , and blue = PF_3). C. Mass spectrum was taken after 19 days (sample is red, helium is blue). Boxes around peaks correspond to various compounds (yellow = H_2 , black = F, blue = CO, purple = O_2 , orange = CO_2 , red = PF_3 , green = SiF_4). SiF_4 (104 amu, 85 amu, 86 amu, 87 amu), PF_3 (69 amu), CO_2 (44 amu), F (19 amu), and H_2 (2 amu).

From the results described above, one can clearly see radical differences in reaction rates and reaction mechanisms. Furthermore, the reactions are strongly correlated in that the onset of a new gas evolution product corresponds with the loss of another product. The question is why and how we can use this to our advantage. From the low level of gas evolved in the pouch, and the lack of SiF_4 and PF_3 peaks in the mass and IR spectra, it can be determined that the addition of lithium to the silicate compound helps prevent the reaction of the silicon with the LiPF_6 salt. This provides a possible pathway to neutralize gas evolution. Furthermore, characterization of the starting materials indicates widely different proton terminations (see Figure 11). Subsequent studies were performed to explore this issue.

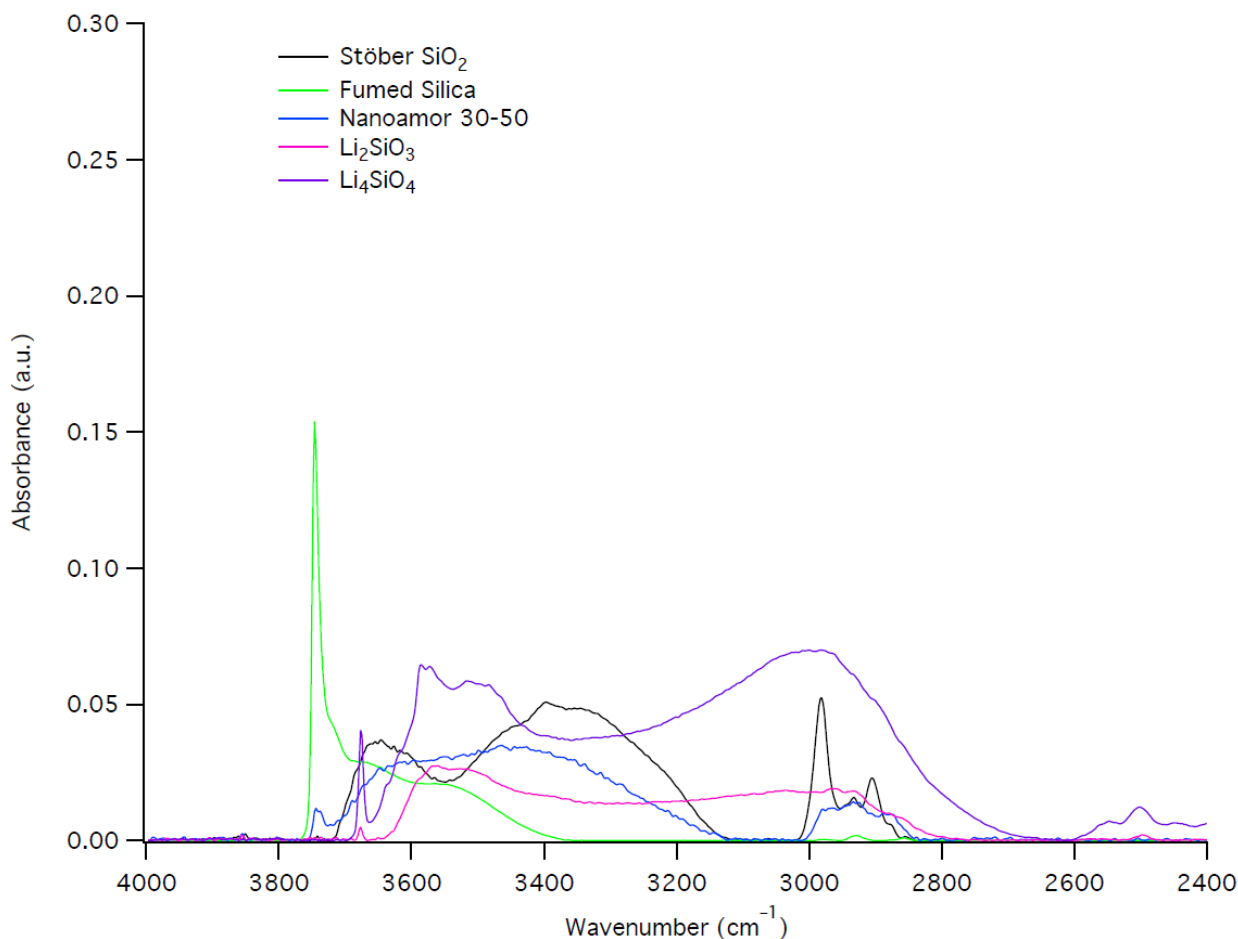


Figure 11. FTIR data showing the proton-termination region of several representative materials.

Surface Species after Chemical Reactions

The evolution of gas is an inherently surface-derived process. After the reaction, residual species are likely to be formed or trapped on the electrode surface. We suspect that the remaining species will be stable with respect to future reactions and could lead to insights into stable silicon surfaces that would prevent oxidation or decomposition reactions and may provide guidance into the choice of surface terminations that might lead to directed SEI formation reactions. To probe this hypothesis, the same materials discussed previously (PECVD

Si-H, nanoamor 30-50, fumed SiO₂, Stöber SiO₂, Li₂SiO₃, and Li₄SiO₄) were investigated using surface-sensitive IR spectroscopy after electrolyte exposure. All materials were exposed to either 1.2 M LiPF₆ in EC or standard electrolyte for 1–3 days to closely mimic that gas-evolution studies. Samples were well-washed with dimethyl carbonate, and subsequently subjected to surface characterization by diffuse reflectance Fourier transform infrared spectroscopy (DRIFTS) to evaluate the resulting surface chemistry.

Reactivity of Si Nanoparticles

DRIFTS spectra of as-prepared *SiH_x-Si nanocrystals (NCs) exhibit a broad peak corresponding to the Si-H stretching region (2,000–2,200 cm⁻¹), with peaks at 2,138 cm⁻¹ and 2,110 cm⁻¹ characteristic of the *SiH₃ and *SiH₂ surface terminations,³ as well as Si-H scissor (910, 863 cm⁻¹) and wag (669 cm⁻¹) modes (Figure 12). As-prepared Si NCs are highly oxophilic, with a broad peak at 1,110 cm⁻¹ assignable to the Si-O-Si stretching vibration due to surface oxidation resulting from reaction with trace impurities in the glovebox atmosphere apparent after two weeks.

Exposing as-prepared Si NCs in electrolyte at room temperature for 1–3 days followed by washing (to remove excess LiPF₆ and carbonate) showed that the particles react significantly with the electrolyte, which is evident by the large differences in IR spectra (red spectrum, Figure 12), consistent with the hypothesis of surface residue. Starting with the Si-H stretching region, the new shoulder at 2,244 cm⁻¹ is assigned to a *Si surface atom bound to oxygen, *Si(O)-H. The C=O stretching region shows low-energy peaks at 1,730 and 1,681 cm⁻¹ that do not correspond to features in the electrolyte. We assign the feature at 1,730 cm⁻¹ to a *Si-OC(O)R ester and that at 1,681 cm⁻¹—which is too low energy for an anhydride, ester, ketone, or aldehyde—to Li⁺ or *Si coordination. For example, the C=O stretch in 2-butanone is known to shift from 1,712 to 1,687 cm⁻¹ as well as give rise to an even lower-energy carbonyl feature at 1,610 cm⁻¹ upon coordination to a surface *Si atom via a hypervalent interaction (i.e., a 5-coordinate Si*) in Si NCs. Similarly, the C-H bending region exhibits two new intense peaks at 1,457 and 1,375 cm⁻¹ likely resulting from ring-opening of EC⁴ and/or reaction with EMC via radical-based processes to give either alkoxy- or carboxylate-functionalized Si NCs. Smaller but still evident C(O)-O resonances at 1,308, 1,294, 1,257, 1,239, and 1,147 cm⁻¹ at the high-energy side of the very broad Si-O-Si stretch centered at 1,110 cm⁻¹ speak to the complex nature of the reactivity of the electrolyte with *SiH_x-Si NCs. As-prepared *SiH_x-Si NCs were additionally soaked in 1.2 M LiPF₆ in EC, and new C=O modes (1,749 and 1,681 cm⁻¹), C-H bends (1,457 and 1,375 cm⁻¹), C(O)-O stretches (1,294, 1,263, and 1,147 cm⁻¹), and the Si-O-Si stretch (1,092 cm⁻¹) were observed (blue spectrum, Figure 12).

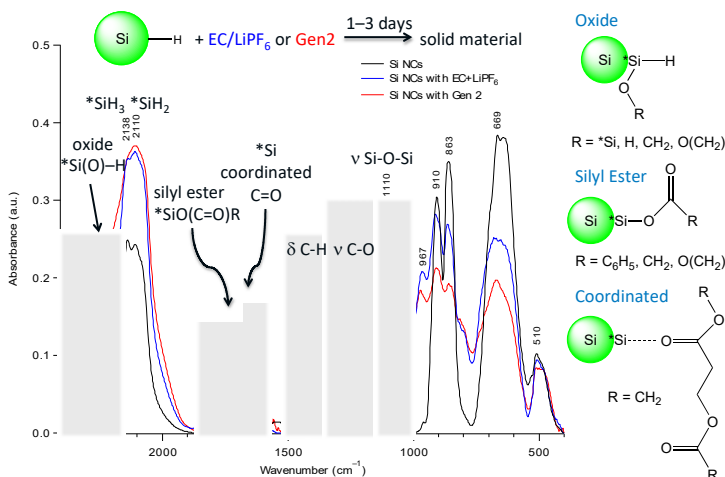


Figure 12. Left: Example FTIR data on chemical reactivity of plasma-grown Si nanoparticles (black) with 1.2 M LiPF₆ in EC (blue) or (red) electrolyte. Right: Cartoons showing various functional groups identified in the solid state.

Reactivity of SiO₂

Next, we probed the reaction of electrolyte with three different silica samples (in which we include nanomorph because the surface largely comprises SiO₂; see Figure 11). All samples exhibit a broad Si–O–Si stretch from ~1060–1210 cm⁻¹ prior to reaction with electrolyte. Surprisingly, fumed SiO₂—prepared by dry O₂ flame pyrolysis of SiCl₄—completely dissolved upon soaking in Gen 2 electrolyte. A colorless solid was precipitated and isolated using acetonitrile/toluene solvent/antisolvent and appears to be comprised largely of C–O stretches (1,265 and 1,167 cm⁻¹) with no Si–O–Si stretching mode (blue-shaded regions, Figure 13) and an intense, broad new feature at 724 cm⁻¹ (yellow-shaded region, Figure 13). However, the low-intensity peaks in the carbonyl (1,816, 1,788, and 1,755 cm⁻¹) and C–H bending (1,481–1,377 cm⁻¹) regions suggest that dissolution of fumed SiO₂ particles does not retain structural features from EC/EMC. The nanoamorph particles exhibit a less intense Si–O–Si stretch relative to other peaks following electrolyte reaction as well as distinct C–O stretches (1,206 and 1,167 cm⁻¹; blue-shaded region, Figure 13) and a broad, intense peak at 739 cm⁻¹ (yellow-shaded region, Figure 13) that is similar in shape and intensity to that at 724 cm⁻¹ in the reaction fumed SiO₂ with electrolyte. In addition, the nanoamorph particles clearly contain *SiH_x and *Si(O)–H stretches both before and after electrolyte exposure (grey-shaded region, Figure 13). The peak corresponding to unoxidized *SiH_x at 2,106 cm⁻¹ is more intense than the oxidized *Si(O)–H stretch at ~2,260 cm⁻¹ following reaction, all of which demonstrate that SiO₂ at the surface of nanoamorph particles dissolves in electrolyte. Additional work will be required to fully assess the molecular structure of this dissolved SiO₂ that is tentatively assigned to the C–H stretching modes from 2,855–2,957 cm⁻¹ and broad intense feature at ~730 cm⁻¹ observed for fumed SiO₂ and nanoamorph particles. In contrast, the DRIFTS data in Figure 13 show that Stöber SiO₂ particles display a low reactivity with carbonates (as evidenced by trace C=O and C–O stretching and hydrocarbon bending modes) and very similar Si–O–Si stretching region before and after electrolyte exposure. The very weak C–H stretching region and absence of the feature at ~730 cm⁻¹ following exposure to electrolyte provide further evidence that this form of SiO₂—prepared via a sol-gel process in which tetraethyl orthosilicate Si(OEt)₄ is hydrolyzed in alcohol (typically methanol or ethanol) using ammonia as catalyst—is robust against dissolution.

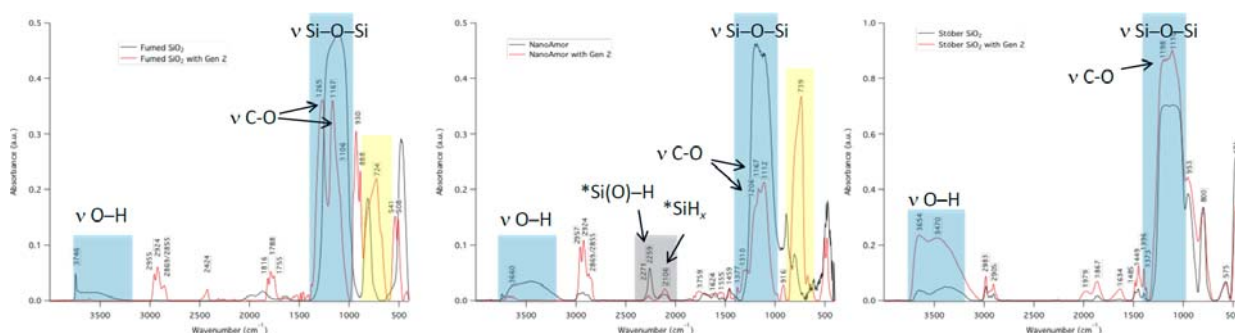


Figure 13. DRIFTS spectra showing fumed SiO₂ (top), nanoamorph 30–50 nm particles (middle), and Stöber SiO₂ (bottom) before (black) and after (red) exposure to electrolyte.

Reactivity of Lithium Silicates

Finally, we probed the reactivity of lithium silicate phases Li₂SiO₃ and Li₄SiO₄ with electrolyte. As can be seen in Figure 14, lithium silicate FTIR spectra have many unique features distinct from SiO₂. The Li₂SiO₃ sample appears to coordinate carbonates as evidenced by key new features at 1,814 and 1,781 cm⁻¹ (comparable to the uncoordinated/coordinated C=O stretches at 1,807/1,773 cm⁻¹ in electrolyte), C–H bending modes from 1,485–1,363 cm⁻¹ (comparable to C–H bending modes in EC and EMC), and C(O)–O stretching

modes at 1,300 and 1,210 cm^{-1} (comparable to EMC and ring EC coordination modes at 1,306 and 1,195 cm^{-1} , respectively). In contrast, very minimal differences between the Li_4SiO_4 samples before and after electrolyte exposure are observed. The results correlate very well with the gassing studies performed above and provide a general reactivity trend for the purported SEI components. More specifically, this work provides insight into the types of chemical species present in the SEI layer that either afford stability or lead to its dissolution. This work provides a foundation for FY19 planned work on tailoring the surface chemistry of Si nanoparticles and understanding electrochemical reactivity.

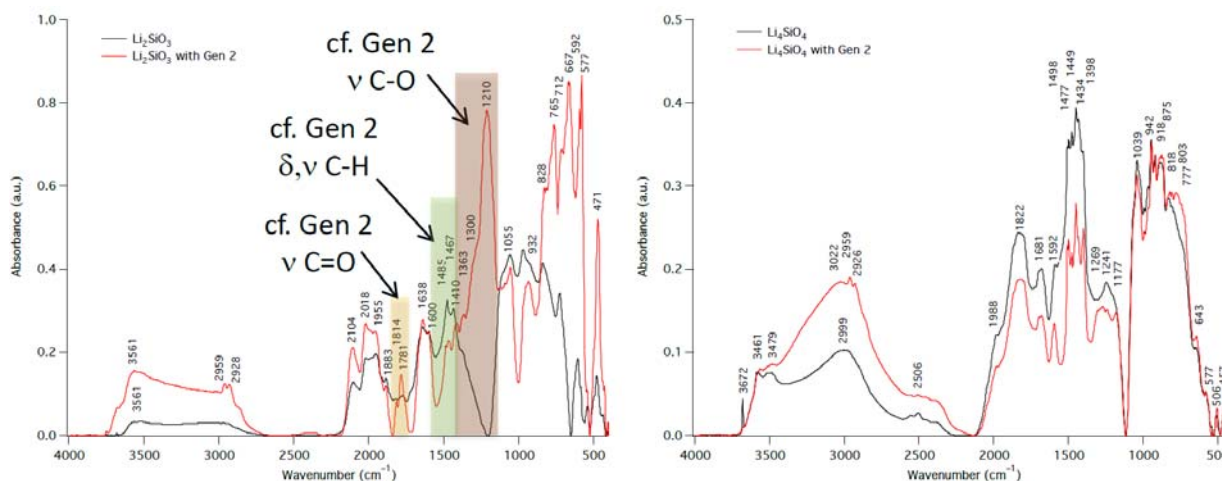


Figure 14. DRIFTS spectra showing Li_2SiO_3 and Li_4SiO_4 before (black) and after (red) exposure to electrolyte.

Chemical Reactivity of Li-Si-O

Given the apparent stability of the lithium silicates, greater focus was placed on understanding the reactivity of various Li-Si-O and SiO_2 materials. These studies used thin films of Li-Si-O compounds to improve surface-characterization studies and to facilitate modeling. Lithium silicate thin-film samples were deposited onto substrates by physical-vapor deposition using SiO_2 and Li_2O targets. Deposition times were controlled to achieve the desired thickness for each film. Inductively coupled plasma–mass spectroscopy (ICP-MS) was chosen to confirm composition. Samples were placed in 20-mL clear borosilicate glass bottles (VWR) and exposed to 3 mL of 1.2M LiPF_6 in 3:7wt% EC:EMC electrolyte for 0.5, 3, 24, 48, and 72 hours in an inert-atmosphere glovebox. The samples were removed with tweezers, rinsed with dimethyl carbonate (DMC) (Sigma Aldrich), and dried in the glovebox’s insertion chamber for 10 minutes. The soak times were chosen because they indicate the amount of time a typical cell may rest in a research setting.

The thin films had linearly increasing lithium content corresponding to an increased Li_2O to SiO_2 target power ratio to produce films with the following compositions: $\text{Li/Si} = 1.3, 1.8,$ and 2.8 . We refer to these films as $\text{Li}_2\text{Si}_2\text{O}_5$, Li_2SiO_3 and Li_3SiO_x , respectively. Deposition times were controlled to achieve a 40-nm thickness for each composition with deposition times ranging from 1.5 to 4 hours. Depositions with higher lithium-to-silicon ratio used lower target powers and thus required longer deposition times. Attenuated total reflectance (ATR) IR spectroscopy was used to observe changes in the bulk structure of the silicate films exposed to electrolyte over time. Figure 15 shows the IR spectrum for each film composition at 0, 3, 24, 48, and 72 hours of exposure time.

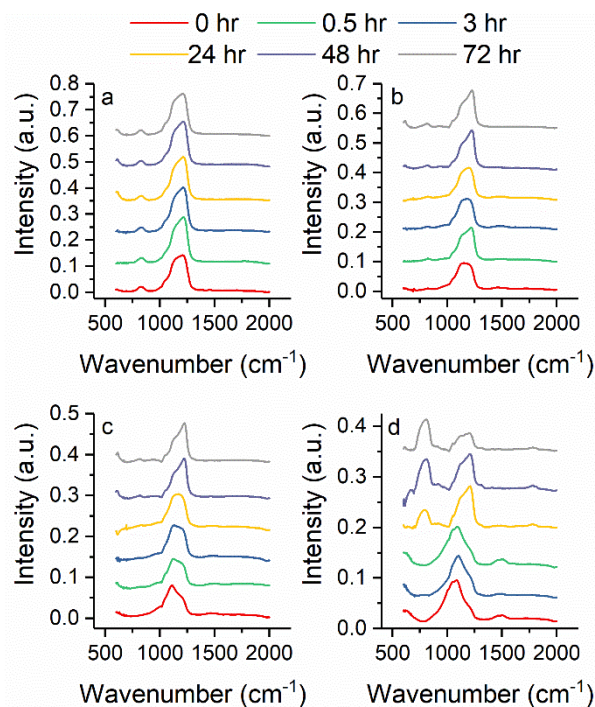


Figure 15. ATR IR spectra over exposure time for a) SiO_2 , b) $\text{Li}_2\text{Si}_2\text{O}_5$, c) Li_2SiO_3 , and d) Li_3SiO_x .

The absorption peaks detected in the range of $900\text{--}1,200\text{ cm}^{-1}$ by IR spectroscopy are characteristic of silicate vibrational modes.⁵⁻⁷ As reported in our previous work, the vibrational modes that are the most illustrative of the effect of lithium modifying the silicate network in the lithium silicates are the vibrational modes of non-bridging oxygens (NBO) and bridging oxygens (BO), or $\nu(\text{Si-O}^-)$ and $\nu_{\text{as}}(\text{Si-O-Si})$, at $\sim 1,000\text{ cm}^{-1}$ and $1,200\text{ cm}^{-1}$, respectively.⁸ As more lithium is incorporated into the silicate network, the wide amorphous peak in the silicate region shifts toward $\sim 1,000\text{ cm}^{-1}$ because lithium breaks apart the Si-O-Si network, creating more NBO. This can be observed in the silicate samples with initial 0-h exposure time. Li_3SiO_x starts with a silicate peak centered more closely to the NBO-indicative region, whereas the SiO_2 film has a relatively sharp peak at $\sim 1,200\text{ cm}^{-1}$ because it has the most intact silicate network. The lithium silicate films also feature small peaks of $\sim 1,450\text{ cm}^{-1}$, which are characteristic of Li_2CO_3 species.⁹ In Figure 15a, the silicate peaks for the SiO_2 thin film remain steady with increasing electrolyte exposure time all the way up to 72 hours. No peaks from typical SEI components, solvents, or salts appear, indicating that the bulk structure of the sputter-deposited SiO_2 film is relatively chemically stable against the electrolyte. The same is not true for the two films with lower lithium content, $\text{Li}_2\text{Si}_2\text{O}_5$ in Figure 15b and Li_2SiO_3 in Figure 15c. For both lithium silicate compositions, at about 24 hours of soaking time, the silicate vibrations that were initially shifted toward NBO begin to shift back toward BO, with both compositions having comparable silicate peaks after 72 hours. The shift of the silicate network peaks toward BO is even more evident for Li_3SiO_x in Figure 12d. At 24 hours, there is an abrupt shift of the silicate peaks for Li_3SiO_x from being centered at $\sim 1,083\text{ cm}^{-1}$ to being centered at $\sim 1,200\text{ cm}^{-1}$. At 24 hours, this silicate peak shift is accompanied by the appearance of a significant peak at $\sim 800\text{ cm}^{-1}$, a small peak at $\sim 1,780\text{ cm}^{-1}$, and the disappearance of the Li_2CO_3 peak at $1,450\text{ cm}^{-1}$. The small peak at $\sim 1,780\text{ cm}^{-1}$ is characteristic of C=O bonds that have previously been shown to be dominant peaks for EC.¹⁰ The large amorphous peak at $\sim 850\text{ cm}^{-1}$ is characteristic of several vibrations including alkyl phosphites, carbonate bending, Si-F bonds, or residual LiPF_6 .¹¹⁻¹⁵ This peak increases with continued exposure time, especially relative to the shifted silicate peak. The large amorphous silicate peak that initially shifts at 24 hours starts to degrade, or lose intensity, with continued exposure up to 72 hours. This degradation and shifting of the silicate network—combined with the appearance of peaks attributed to carbonates, phosphates, or fluorinated species and the disappearance of the Li_2CO_3 peak—indicates that after 24 hours, a significant breakdown occurs of the

silicate network in the bulk of the Li_3SiO_x film. This breakdown is possibly due to the introduction of fluorinate, phosphate, or carbonate species. The disappearance of the Li_2CO_3 characteristic peaks also shows that this surface species may participate or be consumed by the reactions occurring at the surface of the thin film.

The nature of the composition of the reaction species observed by ATR IR, as well as their spacing with depth in the films, was confirmed by XPS depth profiling. Before this depth analysis could be completed accurately, focus ion beam (FIB) cross sections of SiO_2 , $\text{Li}_2\text{Si}_2\text{O}_5$, Li_2SiO_3 , and Li_3SiO_x films for all six soaking times were examined. Cross sections taken of the Li_3SiO_x films at 0, 3, 24, and 72 hours are shown in Figures 16a–d. The initial thickness and the change in thickness over time were determined for each composition and visualized by the column heights in Figures 17a–d. As opposed to the 36% loss of thickness that the Li_3SiO_x film underwent over 3 days, the SiO_2 thin film remained relatively close to its initial pre-soaking thickness measurements of around 45 nm. The overall change in thickness after 3 days of soaking increases from almost no change in SiO_2 to ~25% loss for $\text{Li}_2\text{Si}_2\text{O}_5$ and ~33% for Li_2SiO_3 . The change in thickness over soaking time trends increasingly with increased initial lithium content in the silicate films. This is evidence that the reaction dominating the degradation of the silicate thickness depends on the lithium content of the silicate.

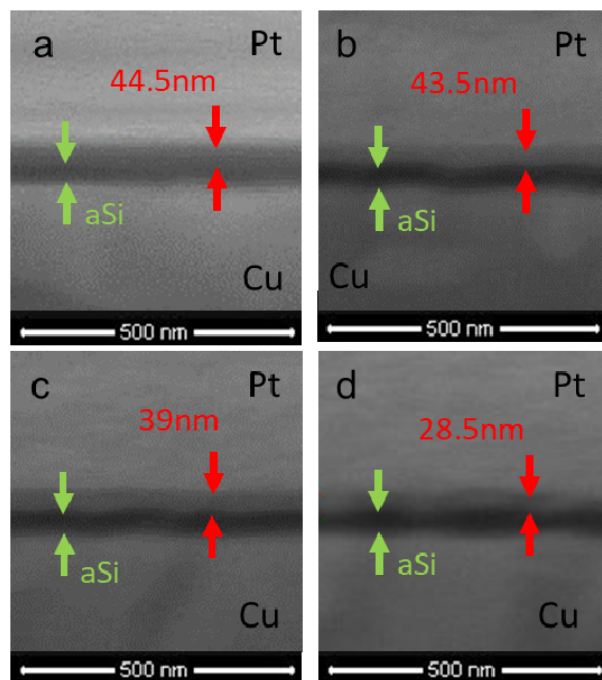


Figure 16. FIB cross sections of Li_3SiO_x samples soaked for (a) 0 hour, (b) 3 hours, (c) 24 hours, and (d) 72 hours.

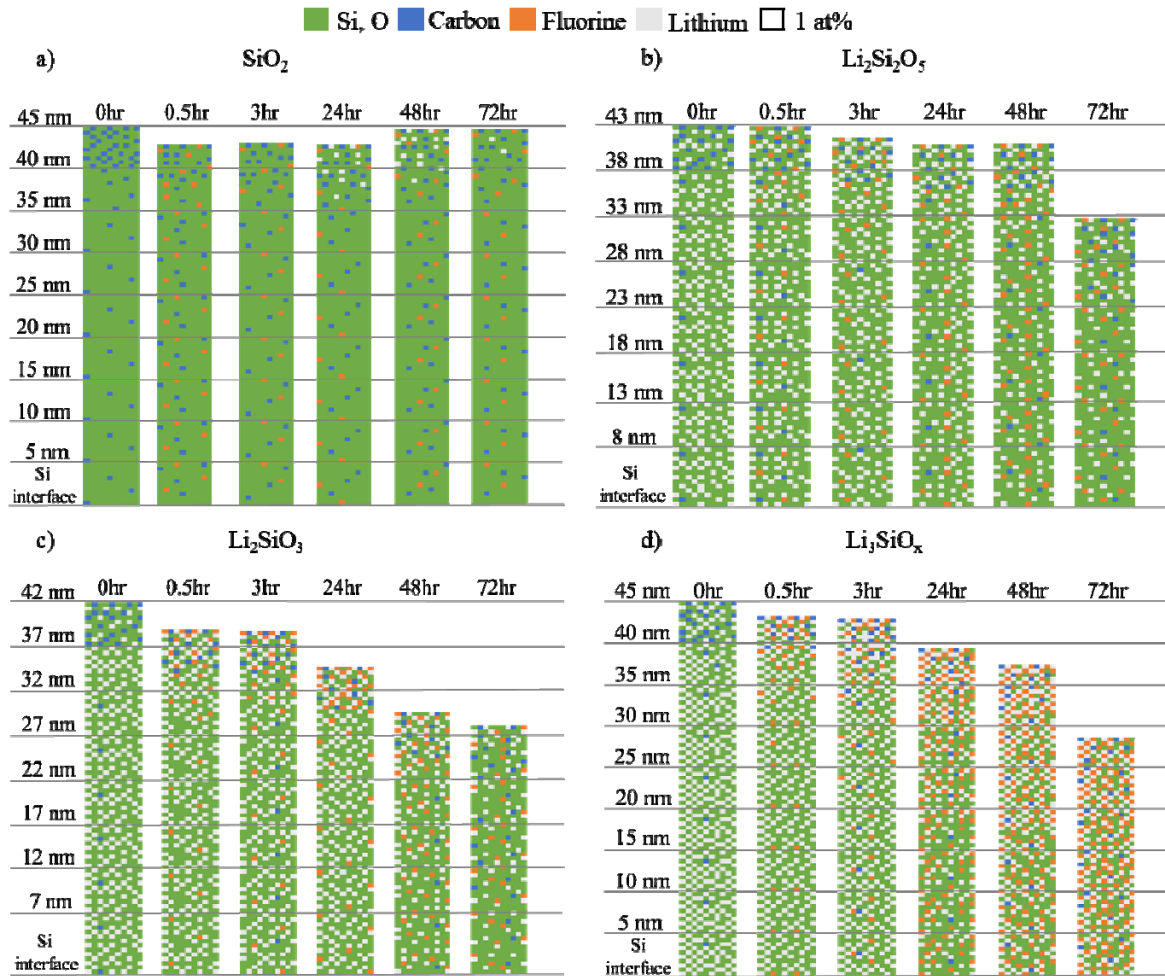


Figure 17. Illustration of thickness and compositional changes of (a) SiO_2 , (b) $\text{Li}_2\text{Si}_2\text{O}_5$, (c) Li_2SiO_3 , and (d) Li_3SiO_x films soaked in electrolyte over time.

XPS depth profiling provides more specific surface characterization with depth to clarify the bulk structure changes observed with ATR IR. XPS with argon depth profiling was performed on samples soaked for 0, 0.5, 3, 24, 48, and 72 hours for each thin-film composition. Figure 18 is the depth profile of the C 1s, F 1s, Li 1s, O 1s, and Si 2p binding regions with depth of the initial unsoaked Li_3SiO_x film.

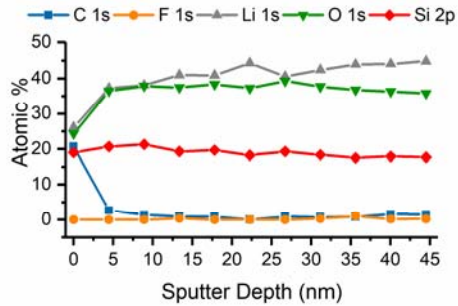


Figure 18. XPS depth profile of Li₃SiO_x thin film.

All the silicate films started with a similar lack of fluorine in the bulk of the film. The atomic percent of Li, F, C, Si, and O was calculated for ~5-nm sections throughout the thickness of each composition at each soaking time and represented by separately colored squares that approximate ~1 atomic percent in each section in the illustration in Figure 14. From this representation of the combined FIB cross-section thickness measurements and XPS depth profile composition measurements, the overall reactivity response for each composition of silicate thin films with depth is more clearly represented. The silicate degradation and fluorination observed in ATR IR is shown in the figure to be a process that occurs throughout the depth of the films, not just at the surface. From Figure 17, it appears that the lithium content in the bulk of the film decreases with soaking time whereas the fluorine content in the film increases.

To more closely examine this trend, the atomic percent of fluorine and lithium with depth for each soaking time for all four compositions is plotted in Figure 19. As seen in Figure 19, there is no fluorine present at the surface or in the bulk of any of the silicate thin films prior to exposure.

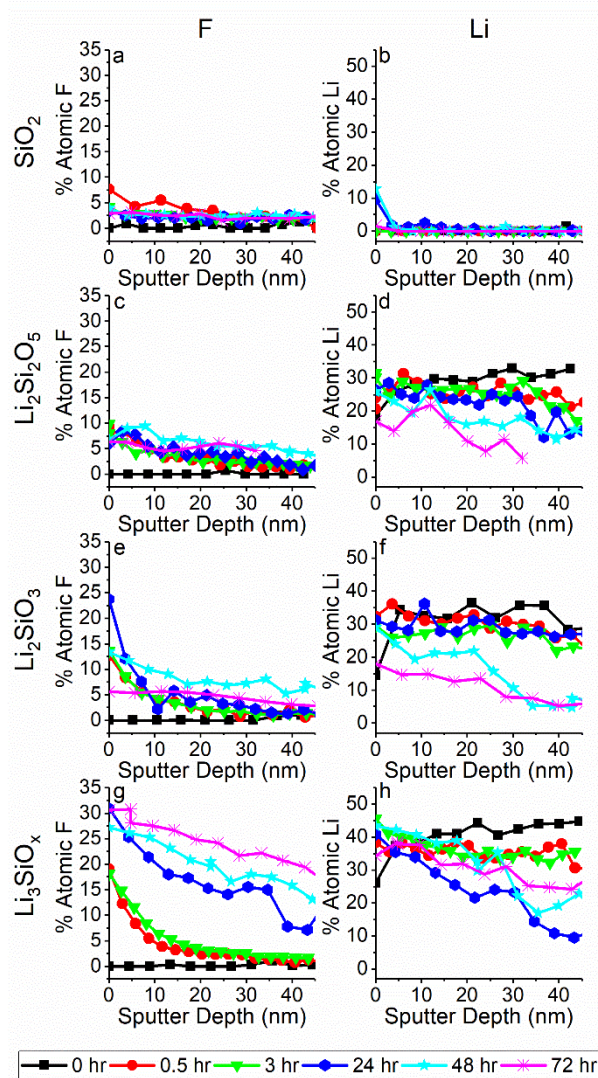


Figure 19. XPS sputter depth profiles for SiO_2 (a) F 1s and (b) Li 1s; $\text{Li}_2\text{Si}_2\text{O}_5$ (c) F 1s and (d) Li 1s; Li_2SiO_3 (e) F 1s and (f) Li 1s; and Li_3SiO_x (g) F 1s and (h) Li 1s.

The lithium and fluorine content in the SiO_2 film remains relatively low compared to the other silicates. However, there is still about 8 atomic percent fluorine species in the SiO_2 starting at only 30 minutes of electrolyte exposure. Lithium insertion into SiO_2 happens at a similarly low atomic percent of about 10–12 atomic percent, but does not appear in XPS depth measurements until about 24 hours of exposure time. This lithium insertion into the SiO_2 film is concentrated at the surface and it drops down to less than 1 atomic percent deeper than 5 nm into the SiO_2 film. Conversely, the fluorine species are observed at about 3 atomic percent through the bulk of the film. As the initial lithiation of the silicates increases, the lithium content and fluorination of the thin films have more intense changes over soaking time. For each of the lithium silicates, just as for the SiO_2 , fluorine species are observed at 30 minutes of exposure to electrolyte. The amount of fluorine present at the surface at 30 minutes increases from 9% on $\text{Li}_2\text{Si}_2\text{O}_5$ to 13% on Li_2SiO_3 to 19% on Li_3SiO_x then tapers off into the bulk of each film. This trend indicates that the more lithium that is initially incorporated in the film, the faster the rate of incorporation of fluorine species into the film. It also becomes more apparent with increasing lithium content that there is a large jump in the rate of fluorination over time from 3 hours to 24 hours. This jump in fluorine content is shown in the Li_3SiO_x film in Figure 20g, when the atomic percent of fluorine at the surface jumps from 18 atomic percent at 3 hours to 30 atomic percent at 24

hours. This increase at the surface is matched by an increase from around 2–3 atomic percent in the bulk of the film at 3 hours to around 15 atomic percent in the bulk at 24 hours. As this fluorination occurs, there is a corresponding loss of lithium in the bulk of each silicate. In the initial lithium silicate films, there is a lower lithium atomic percent at the surface than in the bulk, likely due to adventitious surface carbonates. With continued exposure to electrolyte, this lower atomic percent of lithium at the surface transitions to excess lithium at the surface compared to the bulk of the film. It appears that the same mechanism that allows for fluorination of the silicates starting at the surface and extending into the bulk of the film also facilitates lithium leaving the bulk of the film, gathering at the surface, and possibly being leached into the electrolyte.

XPS binding energy spectra with depth for Si 2p, O 1s, F 1s, and C 1s for SiO₂ and Li₃SiO_x are plotted in Figures 20 and 21 to investigate the molecular composition of the species observed during depth profiling. The peak assignments for XPS binding energies made in this work are summarized in Table 2.

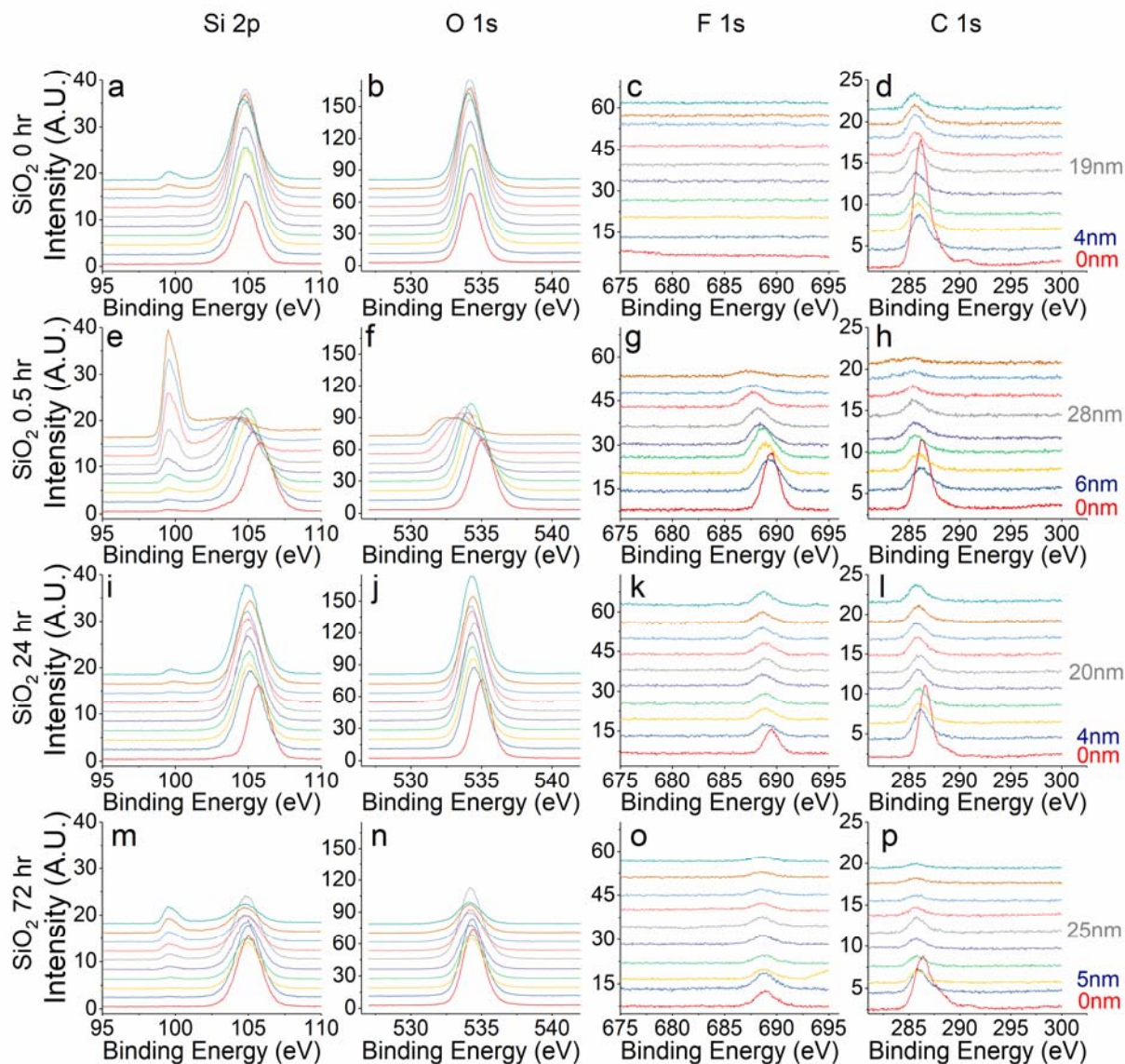


Figure 20. XPS Si 2p, O 1s, F 1s, and C 1s binding energies with depth for SiO₂ soaked for 0 hours (a–d), 30 minutes (e–h), 24 hours (i–l), and 72 hours (m–p).

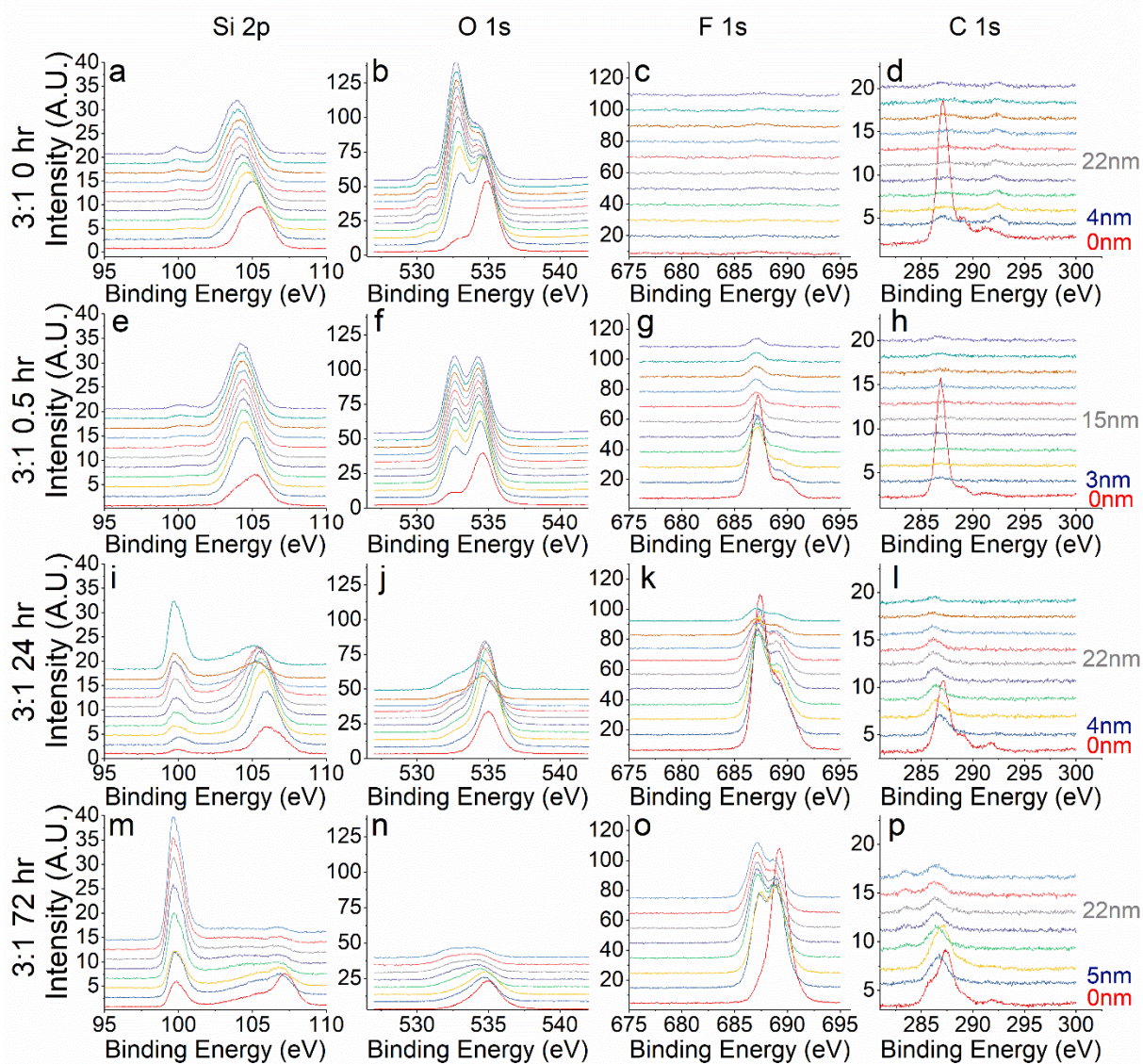


Figure 21. XPS Si 2p, O 1s, F 1s, and C 1s binding energies with depth for Li_3SiO_x soaked for 0 hours (a-d), 30 minutes (e-h), 24 hours (i-l), and 72 hours (m-p).

Table 2. Peak assignments for XPS analysis on soaked SiO₂ and Li₃SiO_x thin films

Assignments	Si 2p (eV)	O 1s (eV)	F 1s (eV)	C 1s (eV)	References
SiO _x	104	533-534			16-17
C-O		534-535		286	18-20
Li ₂ CO ₃		532-534		290-291.5	21-22
Si-F	107		687		23
Si-Si	99				18, 23
Li-O		534-535			18
Li _x PF _y			688		21-22
Li _x PF _y O _z		535			24
Si-C	100			283	25
C=O		533		287	19-20

SiO₂ Binding Energy Analysis

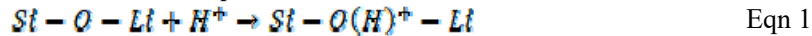
Figure 20 shows the binding energies for the SiO₂ thin films for samples soaked for 0, 0.5, 24, and 72 hours. For the initial SiO₂ samples before any electrolyte exposure, the Si 2p and O 1s binding-energy regions in Figures 20a–b have peaks at 104.8 eV and 534 eV, which correspond to Si-O bonds in the well-connected silicate network expected in the SiO₂ film. The sample starts with no fluorine peaks, a small CO₃ peak and a large C-O bond at the surface. The carbonate peaks appear at 290 eV and 286.4 eV, respectively, and are expected to form from surface adsorption during storage and/or exposure to low pressures during sample transfer.⁸ The Si-O peaks remain steady in the bulk of the film (>5 nm from surface) with extended soaking time. At the surface of the SiO₂ film, which is marked 0 nm on the right side of Figure 20, there is a slight shift to higher binding energies starting at 30 minutes of soaking time. This is likely associated with the F 1s peaks at 688 eV that also appear on the SiO₂ surface at 30 minutes. This peak at 688 eV is assigned to LiPF₆ or Li_xPF_y species and it also continues with less intensity into the bulk of the film. This fluorinate peak remains about the same for the duration of the rest of the soaking time for the SiO₂ samples. The C 1s binding-energy region for the SiO₂ samples does not show any significant change from the initial surface adsorption peaks until about 72 hours of soaking. The peaks at the surface for the C 1s binding-energy region broaden and decrease in intensity, indicating that the carbonate surface species are being consumed or changed by surface reactions with the electrolyte. The C 1s peak at around 286 eV in the bulk of the SiO₂ thin film is likely from process-chamber contamination and does not change with exposure time. Carbonate species do not seem to penetrate past the surface area of the SiO₂ thin films, unlike the fluorinate species, which maintain a < 5 atomic percent presence throughout the bulk of the film starting at 30 minutes of soaking and continue through the rest of the 72 hours of soaking.

Li₃SiO_x Binding-Energy Analysis

The addition of lithium as a silicate network modifier in the Li₃SiO_x significantly effects the stability of the silicate against electrolyte as demonstrated in Figure 21. The Li₃SiO_x starts with a wide Si 2p peak in the Si-O binding-energy region as well as peaks at 535 eV and 533 eV in the O 1s binding-energy region that correlate to Si-O and Li-O bonds, respectively. This film also starts with no fluorine peak prior to being exposed to the electrolyte along with typical carbonate soaking peaks. There is a stronger signal around 290 eV in the C 1s binding-energy region for lithiated silicates because Li₂CO₃ forms more facilely on lithium silicate surfaces due to their sensitivity to CO₂.²⁶⁻²⁸ The surface of the pre-soaked Li₃SiO_x has a smaller Si-O peak in the O1s binding-energy region compared to the bulk of the film due to these surface carbonates. The Si-O peak also has a higher intensity than the Li-O peak for the unsoaked Li₃SiO_x through the bulk of the film. This ratio of Si-O to Li-O peaks is reversed starting at just 30 minutes of soaking time. The peaks in the O 1s binding-energy region all decrease over soaking time, but the Si-O peak decreases in intensity compared to the Li-O much more quickly. By 24 hours of soaking time, the Si-O peak is just a shoulder compared to the Li-O peak. For the

72-hour samples, there is only a single small wide peak centered around the Li-O binding-energy region. The decrease in oxygen bonding is accompanied by peak shifts in the Si 2p binding energy away from Si-O bonds and by an increase of fluorine species peaks. At 24 hours, the Si 2p binding peak shifts from ~105 eV toward 106 eV, and there is also a corresponding appearance of a small peak at ~100 eV, which is characteristic of Si-Si or Si-C bonds. By 72 hours, the Si-O peak has almost entirely shifted or been replaced by a peak at ~107 eV, which is characteristic of Si-F bonds and by Si-Si or Si-C bonds at 100 eV at the surface and throughout the bulk of the film. This degradation of the silicate bonds appears with the advent of significant peaks in the F 1s binding-energy region starting at 30 minutes of exposure time. At 30 minutes of exposure time, the fluorine species are concentrated at the surface as shown in Figure 20g. These species appear as a sharp peak at 687 eV with a smaller shoulder peak at ~689 eV. These peaks are characteristic of F-Si and Li_xPF_y species, respectively. As the soaking time is increased to 24 hours and the silicate network appears to begin to break down, both F 1s binding-energy region peaks increase in intensity, particularly the shoulder at ~689 eV, and extend further into the bulk of the film. At 72 hours of soaking time, both peaks are about equal in intensity and are significantly present throughout the bulk of the Li_3SiO_x film. At the surface of the 72-hour sample, the Si-C or Li_xPF_y peak dominates the F 1s binding-energy region, with the F-Si peak only appearing as a shoulder. This is accompanied by a shift of the peaks in the C 1s binding-energy region that had been stable up to 72 hours. These C 1s peaks shift toward ~291 eV, or Li_2CO_3 species, as well as the appearance of a small peak at ~283 eV, which is assigned to Si-C peaks. Because C-O carbonate species at ~286 eV only appear as a small peak in the bulk of the Li_3SiO_x film at 24 hours and do not increase in intensity as rapidly as the fluorine species, it can be assumed that most of the peak at ~100 eV that is shared by Si-C and Si-Si species can be attributed to the latter. There is a single peak at the surface of the Li_3SiO_x samples after 72 hours at 689 eV without a shoulder at 687 eV, which indicates a lack of silicon at the surface and of a higher concentration of Li_xPF_y at the surface than in the bulk. These trends observed in the binding-energy regions shown in Figures 20 and 21 are clear evidence that, unlike the SiO_2 film, this lithiated silicate appears to undergo a process in which the Si-O bonds are etched away and replaced with Si-F, Li_xPF_y , and Si-C species.

A mechanism for etching vitreous SiO_2 in an aqueous HF solution, which is analogous to the type of etching observed in this study, was proposed by Knotter et al.²⁹ This mechanism is applicable to the experimental setup in this study because lithium-ion battery electrolytes such as the one used in this work are known to contain HF due to reaction of the LiPF_6 salt with water. Although efforts are made to make these electrolyte solvents non-aqueous, water can infiltrate the electrolyte over long-term storage even when it is stored in an inert-atmosphere glovebox.³⁰ The process for silicon dioxide etching proposed by the Knotter et al. study involved a nucleophilic substitution reaction, or a two-step reaction involving an elimination reaction followed by the addition of a nucleophile. This mechanism can be applied to the SiO_2 thin film and lithium silicate thin films because it assumed that the silicon dioxide surface includes some impurities leading to oxygens that are only linked to one silicon, or non-bridging oxygens. As discussed in our previous work, the structure of lithium silicates consists of a silicate network broken apart into non-bridging oxygens that are loosely bonded to lithium.³¹ The etching reaction for these lithium silicates in an electrolyte that likely contains HF, based on the mechanism proposed by Knotter et al., begins with the protonation of a surface oxygen atom bound to one silicon atom and one lithium atom as seen in Equation 1:



The following reaction is possible under the assumption that there is enough H_2O contamination in the electrolyte to make it an aqueous solution that would allow HF to dissociate into H^+ , F^- , and HF_2^- species.³² After the protonation of the surface oxygen, there is a nucleophilic attack by HF_2^- on the electrophilic silicon described in Equation 2:



This produces a stable leaving group of LiOH , which could be incorporated into the electrolyte solution and would account for the loss of lithium, with continued soaking/etching time for the lithium silicates shown in Figures 14 and 16. The reaction rate for the first two steps of this proposed etching mechanism is a function of reactant concentration, or $[\text{SiO}(\text{H})^+\text{Li}]$ and $[\text{HF}_2^-]$, and of the concentration of active surface sites according to Knotter et al. Because the films for this study were all deposited by the same method, it is safe to assume that

the reactant concentration, not the concentration of active surface sites, is the dominating factor for etching rates. For the unlithiated SiO₂ film, this etching mechanism would rely on surface impurities such as C or H instead of lithium in the previous equations. It follows that with increased network modifiers, or lithium, the etching rate increases. This is confirmed by the FIB cross-section thickness measurements that provide evidence that with increasing lithium content in these silicate films, more material is etched away from the film over the same amount of time. XPS analysis from Figures 20 and 21 also confirms that Si-O bonds decrease in quantity whereas Si-F bonds increase in quantity over time just as this etching mechanism predicts.

The etching of the silicate network in these films occurs simultaneously with other side reactions with the electrolyte that account for the significant Li_xPF_y or relatively smaller C-Si peaks in the XPS spectrum. Because each sample is rinsed in DMC for an equal amount of time and LiPF₆ is soluble in DMC, it is most likely that these Li_xPF_y-type species are bound into the reaction layer, not just residual LiPF₆ salt from rinsing. These Li_xPF_y species have been observed in previous aging studies using LiPF₆ salt and can be attributed to hydrolysis products from salt decomposition or as products of the decomposition reaction of LiPF₆ with Li₂CO₃.^{22, 33} The genesis of the small C-Si peaks is less clear, but it could be from the exposure of dangling bonds in the etched silicate being exposed to the carbonate solvents, or from dissolved CO₂ in the electrolyte, which provides an analogous pathway to attack of the NBO and subsequent substitution of the C into the Si network. More study to elucidate this is necessary.

In summary, in this study we synthesized four different thin-film silicates with increasing levels of lithium content from Li/Si = 0 to Li/Si = 3. These silicates were used to model the surface chemical reactivity of the potentially lithiated native oxide of a silicon anode against a typical carbonate electrolyte. The reaction products that occur from exposure to electrolyte for these silicate thin films are not isolated to just the surface of the film. XPS depth-profiling analysis confirms that reaction species penetrate the bulk of the films as early as at 30 minutes of exposure time. This indicates that the films are either quite porous or that there is a significant breakdown in the film integrity or density as soon as it is introduced to the electrolyte solution. The initial C-O or Li₂CO₃ contamination species at the surface of these silicate films are relatively stable against the electrolyte until about 72 hours of exposure, at which point they appear to be consumed by surface reactions to form more complex carbonates or Li_xPF_y species. The most significant effect on the model silicates came from HF etching of the Si-O bonds in the bulk and at the surface of the film that resulted in Si-O bonds being replaced by Si-F, loss of lithium potentially through the formation of LiOH that leaches into the electrolyte, and dramatic decreases in thickness of the films. A trend was observed that correlated increased reaction rate with lithium content in the film. It is theorized that this increased reaction rate is a function of the amount of non-bridging oxygens terminated by lithium metal ions in the silicate film. The reaction rate of the films also seems to undergo a waterfall effect that culminates in a considerable jump in content of reaction species in the films after 24 hours of electrolyte exposure time.

Together, these data show that Li-Si-O surfaces may react with the electrolyte, but trap the F species, thus preventing the loss/generation of SiF₄ and PF₃ gases.

Surface Species after Chemical Reactions

Continuing the investigation of oxide surface termination, the effect of oxide type on a silicon wafer was explored. In this study, we explored silicon wafers. The first wafer had a native (~2-nm) oxide. The second wafer had a thermally grown oxide (50-nm) Si wafer. Both materials were exposed to electrolyte (LiPF₆-based) and were analyzed with atomic force microscopy (AFM) to investigate electrolyte decomposition. After soaking in electrolyte, island-like accumulations of possible electrolyte decomposition products and residual salts were found on both surfaces as shown in Figure 22. However, on the 50-nm SiO₂ surface, the particles showed greater density and more uniform size than on the native-oxide surface, which is likely a result of a rougher pristine surface with more initial adhesion and nucleation sites. Studies are being performed to analyze this surface chemistry. An experiment to investigate stability of the thermally grown oxide immersed in electrolyte for 2 days and 7 days showed that in the absence of electrochemical reactions, the oxide film is

completely stable in electrolyte, and thus, the disappearance of the oxide film in the cycled samples results from the electrochemical reaction. A scanning spreading resistance microscopy (SSRM) depth profile of a 15-nm SiO₂ on crystalline-Si (c-Si) sample after soaking in electrolyte for 7 days can be seen in Figure 23, demonstrating the electronic contrast visible between the intact SiO₂ layer and the underlying c-Si after mechanically milling down to the interface. The results illustrate that the mechanical and electronic properties were not significantly altered by immersion in electrolyte. Future studies are planned using vapor-grown films and contrasting the results with thermally grown oxides. We hypothesize that the differences in surface chemistry due to growth mechanisms may direct electrolyte decomposition.

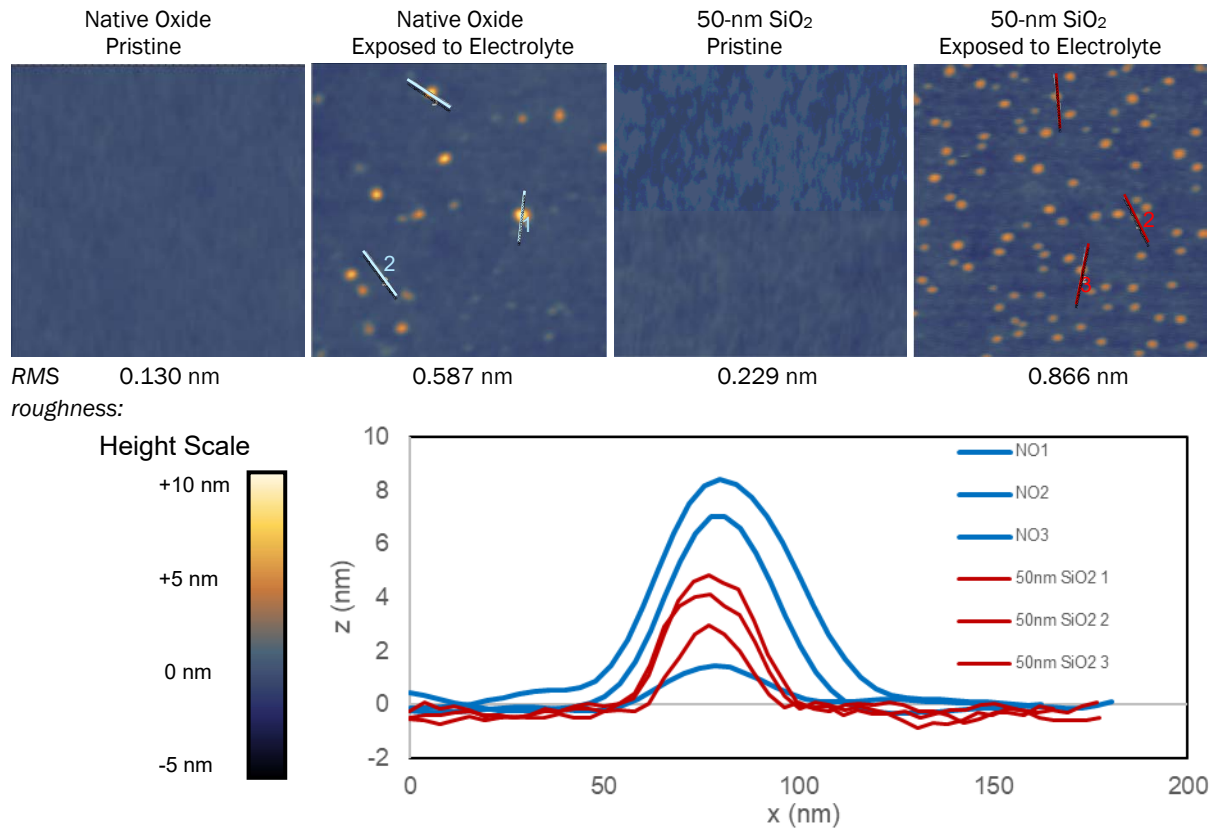


Figure 22. 1×1 μm AFM images from left to right: Native oxide pristine surface, after soaking in electrolyte, thermally grown 50-nm SiO_x wafer pristine surface, after soaking in electrolyte. A plot is shown displaying comparisons between linescans over surface islands on each sample.

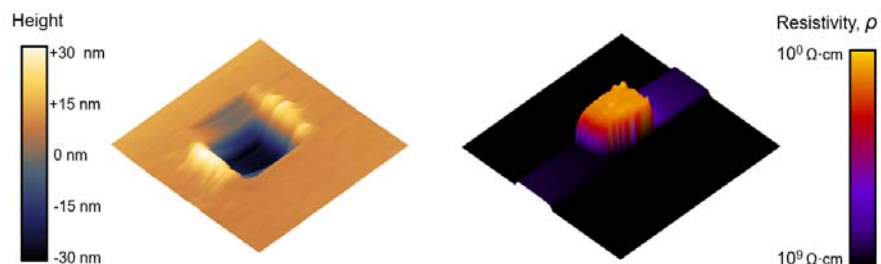


Figure 23. SSRM depth profiling on 15-nm SiO₂ on c-Si sample after soaking in electrolyte for 7 days. Height image is shown at left, and resistivity image is shown at right. Electronic contrast between SiO₂ and c-Si is manifest at a depth of 15 nm, showing that the integrity of the SiO₂ film is retained after soaking in electrolyte.

Simulation of Surface Interactions

As part of this study, density functional theory (DFT) was applied to explore the possible mechanisms of reactivity over the pure silicon (PECVD Si). The modeling was designed to capture the electrolyte-electrode interactions whereas infrared spectroscopy was used to support the simulation/validate some of the results. Fluoroethylene carbonate (FEC) was recently proposed as an effective electrolyte additive that significantly enhances the stability and flexibility of the solid-electrolyte interphase layer for Si anodes. However, uncertainties remain on the exact mechanism through which FEC alters the electrolyte decomposition and SEI formation mechanism. Herein, the influence of FEC on LiPF₆/EC electrolytes for Si anodes is investigated through classical molecular dynamics (MD) simulations, FTIR measurements, and quantum chemical calculations.

A sequential simulation for 1.0/1.2 M LiPF₆ in EC with 0/5/10 % FEC was conducted to investigate the influence of FEC to the solvation structures of LiPF₆/EC electrolyte. The radial distribution function $g(r)$ and the corresponding integrals $N(r)$ of Li-X (X = O(EC), F(PF₆⁻), Li, P(PF₆⁻) for EC and X = O(EC), F(PF₆⁻), O(FEC), P(PF₆⁻), F(FEC) for EC with FEC) pairs are summarized in Figure 24. The dominant peak of the Li-F pair at ~8 Å shown in Figure 24a suggests that for 1.0 M LiPF₆ in EC, most of the LiPF₆ salt forms solvent-separated ion pairs (SSIP), whereas the contact ion pairs (CIP) present as minority species (Figure 25b). In addition, a trace amount (less than 1%) of aggregate solvates (AGG) were also observed during the simulation. By integrating the $g(r)$ to 3.0 Å, the total coordination number (CN) for Li ion is obtained as shown in Figure 25a. Interestingly, although most of the first solvation shell is occupied by EC solvent molecules (5.84 out of 5.90) with a most-probable distance of 2.08 Å to Li⁺, the Li⁺ solvation sheaths also present an average of 0.06 PF₆⁻ anions, most of which form monodentate structures coordinated through a fluorine. The simulation produced a longer distance of 2.11 Å for the Li-F pair, illustrating that EC molecules take closer positions in solute complexes. The AGG species are rare, indicating an almost negligible number of Li ions that coordinate with more than one PF₆⁻ anion. Hence, the corresponding CIP ratio is estimated as 6%, with a SSIP ratio of 94%, in agreement with common assumptions that LiPF₆ is a weakly coordinating salt compared to LiBF₄ and well dissociated in EC solutions.

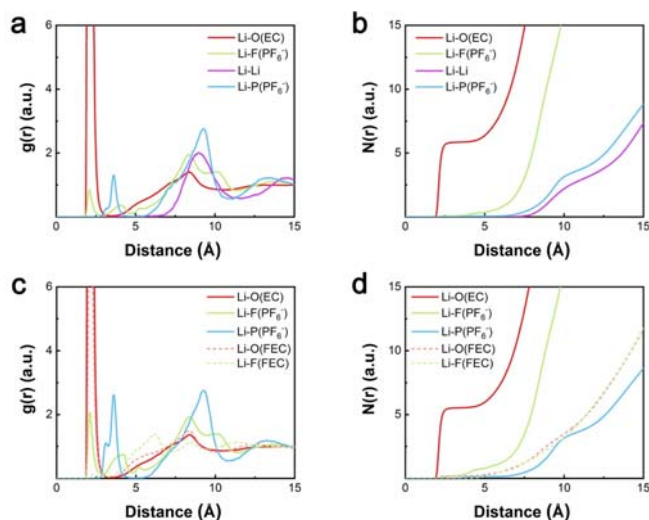


Figure 24. Calculated radial distribution functions $g(r)$ and the corresponding integrals $N(r)$ of Li-O(EC), Li-F(PF₆⁻), Li-Li, Li-P(PF₆⁻) pairs of (a) (b) 1.0 M LiPF₆ in EC, and Li-O(EC), Li-F(PF₆⁻), Li-P(PF₆⁻), Li-O(FEC), Li-F(FEC) pairs of (c) (d) 1.0 M LiPF₆ in EC with 10%mol FEC additive.

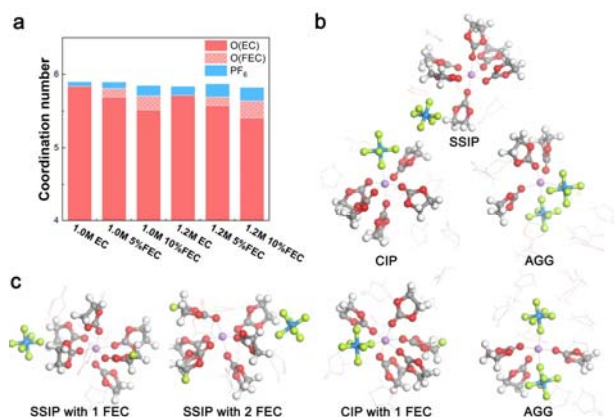


Figure 25. (a) The calculated total coordination number for Li⁺ in 1.0 M LiPF₆ in EC with 0/5/10% FEC and 1.2 M LiPF₆ in EC with 0/5/10% FEC with specifications of the contributions from EC, FEC and PF₆⁻. The representative solvation structures taken from MD simulation snapshots of (b) 1.0 M LiPF₆ in EC and (c) 1.0 M LiPF₆ in EC with 10% FEC.

Upon addition of 10% FEC into the LiPF₆/EC electrolyte, the solvation structure is evidently altered in several ways, primarily due to the weakened donor ability of FEC. Besides the similar solvation structures as shown in Figure 25b, other solute complex structures with FEC included were also observed in the snapshots of the MD simulation (Figure 25c). Intriguingly, it is the carbonyl O in FEC that binds with the Li ion rather than F binding, which means that the composition difference of the solvent molecule does not radically alter the binding behavior as compared with the parent EC molecule. However, the average CN for Li-O(EC) pair decreases from 5.84 to 5.51, allowing for an average Li-O(FEC) pair contribution of 0.19 to the first solvation shell. A maximum in $g(r)$ of 2.12 Å was observed for the Li-O(FEC) pair, suggesting a weaker interaction between Li-FEC as compared to Li-EC. Notably, the CIP ratio doubles from 6% to 14%, which significantly changes the population statistics of the SEI formation reaction precursors, indicating a prominent role of FEC,

even as a minority species. Similar to the EC electrolyte, the simulation with FEC additive results in a same Li-EC distance. Yet, the Li-FEC distance is slightly farther away (2.12 Å) as compared to the Li-EC counterparts, which results in a “looser” structuring of the first solvation shell. EC electrolytes are known to promote salt dissociation due to its high dielectric constant ($\epsilon = 90$), as well as donor number. In contrast, FEC exhibits a lower dielectric constant ($\epsilon = 78.4$), which results in less dissociation of LiPF_6 and weakened donor ability (i.e., smaller CN of Li^+ -solvent). If we compare all six simulated compositions listed in Figure 25a, it is obvious that a higher LiPF_6 concentration gives a higher CIP ratio. Somewhat less obviously, we surmise that when 5% of FEC is added to the system, the CIP ratio is elevated, and a non-negligible percentage of the solute complexes are modified with fluorine-containing FEC that occupy the first solvation shell.

The inclusion of 10% of FEC further reduces the solvating strength of the composite electrolyte and allows for more CIPs, i.e., for PF_6^- to directly contact/interact with Li^+ . The coordination number for the Li-FEC pair increases to ~ 0.2 , which means that 20% of the solvate structures on average now contains at least one FEC. We argue that this content change of the solute complex significantly changes the reduction potentials of the electrolyte constituents.

Based on the mean square displacement (MSD) of each component during the simulation, the self-diffusion coefficients and transference numbers were calculated and plotted along with the reference experimental results by collaborator Nanda’s group in Figure 26. Both 1.0 M and 1.2 M simulation results indicate that the diffusion coefficients of all components within the EC electrolyte and EC/FEC mixture exhibit similar values (Figure 26a). The trends for the three components EC, PF_6^- , and Li^+ are in good agreement with the simulation results obtained by the generalized AMBER force field (GAFF) as well as the trend from nuclear magnetic resonance (NMR) results in that solvent diffusivities are $2\sim 5\times$ larger than ion diffusivities. Although the simulations predict overall slower dynamics than the experimental results, the difference is within one order of magnitude ($10^{-10}\sim 10^{-11} \text{ m}^2 \text{ s}^{-1}$), illustrating that the classical MD simulation is adequately accurate to reproduce or predict the dynamical property trends of this system.

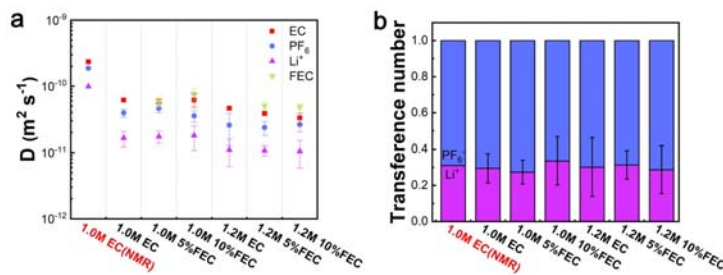


Figure 26. (a) Self-diffusion coefficients computed from MD simulations as compared with NMR experiments (1.0 M LiPF_6 in EC) (b) Transference numbers for Li^+ and PF_6^- from MD simulations and NMR experiments. The error bars represent the standard deviation of the data collected every 1 ns during the 5-ns production runs.

It is noteworthy that when FEC is added into the system, there is no significant variation of diffusion properties. EC and FEC exhibit almost the same diffusion coefficients within the calculation uncertainties, and we surmise that the intermolecular interaction behaviors of EC and FEC are similar due to the common cyclic carbonyl structures with only one different substituent. Hence, adding FEC does not directly affect the transport property of the electrolyte. On the other hand, FEC inclusion implicitly promotes the formation of CIPs; however, CIP species still remains a minority species in the electrolyte. According to the Nernst–Einstein relation, an 8% CIP ratio increase from EC electrolyte to EC with 10% FEC will lead to approximately the same percentage (8%) decrease in Li^+ ionic conductivity, and no conspicuous change in transference number was observed. In contrast, the salt concentration clearly affects the ionic diffusivity,

decreasing by an average of 10% from 1.0 to 1.2 M. As for the transference number, all the six electrolyte systems give similar results and coincide well with the NMR experimental value of 0.31. Hence, both the self-diffusion coefficient and the transference number results demonstrate the weak dependence of transport properties on the FEC additive up to 10%, elucidating that FEC modifies the solvation structure without greatly affecting the ion transport ability.

To verify the theoretical simulation results, the Nanda group performed FTIR measurements for a range of EC and EC/FEC electrolytes. The peaks from the FTIR spectrum are deliberately deconvoluted to quantitatively estimate the population proportion of each electrolyte species. In parallel, we performed quantum chemical calculations to obtain the theoretical IR vibrational information for each solvation structure observed in the MD simulations. The calculated spectral profiles are further linearly combined using the population ratios obtained from MD simulation that result in predicted theoretical IR spectra. In general, there are two major characteristic peaks that are shifted after the inclusion of FEC: 1) the C=O breathing band at 710–730 cm^{-1} , and 2) the P-F bond stretching band at 840–880 cm^{-1} . The C=O breathing vibrational band at 710–730 cm^{-1} can be used to distinguish the responses from different C=O binding states. Peaks from experimental results (Figures 27a and 27b) were designated as coordinated ones and uncoordinated ones based on our calculations and reference, which provide detailed information of the solvation structure.

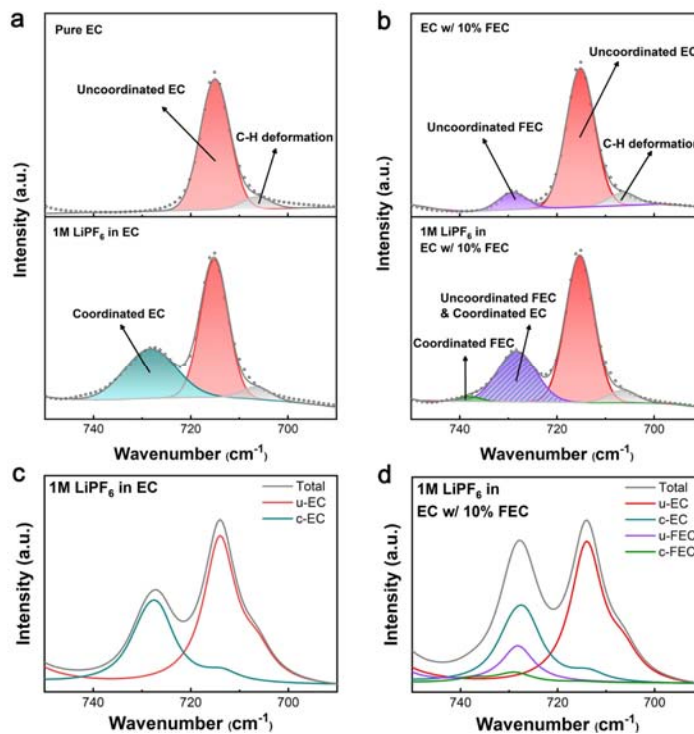


Figure 27. Measured FTIR spectra of the C=O breathing band of (a) pure EC and 1.0 M LiPF₆ in EC, and (b) EC with 10% FEC and 1.0 M LiPF₆ in EC with 10% FEC. (c–d) The corresponding calculated IR spectra as a comparison of the experimental results. Red, cyan, purple, green, grey, and dark grey lines correspond to uncoordinated EC, EC coordinated with Li⁺, uncoordinated FEC, FEC coordinated with Li⁺, C-H deformation, and total spectrum, respectively. Scatter points denote the original FTIR data points.

First, we note that the experimental results are in good agreement with the calculated spectra (Figures 27c, 27d), and identical peaks are found in the spectra from both methods, despite small deviations in the absolute frequency values. For the EC electrolyte (Figure 27a), two peaks at 728 cm^{-1} and 715 cm^{-1} were identified as

coordinated EC and uncoordinated EC, which were accompanied by a small C-H deformation peak at 706 cm^{-1} . By analyzing the measured peak area integrals, it was found that 38.1% of EC molecules are coordinated with Li^+ , which corresponds to a CN of 5.13 for Li-EC. Although the calculated CN (5.84) from MD simulations is slightly higher than the experimental result, it is notable that both approaches indicate a CN over 5 for the EC electrolyte system. When 10% of FEC is included, an additional peak arises at 738 cm^{-1} , corresponding to the coordinated FEC. Meanwhile, a free FEC breathing band at 729 cm^{-1} overlaps with the coordinated EC vibration band (Figure 27b), which makes it difficult to deconvolute the peaks and obtain the exact percentage of the coordinated EC and uncoordinated FEC. Nonetheless, by comparing the peak of the uncoordinated EC, we estimate an increase in uncoordinated EC area by 6.6% as compared to the 1M LiPF_6 in EC system, which further supports the decrease in CN of Li^+ -EC with respect to the EC electrolyte. Additionally, the CN of FEC to Li^+ is directly calculated as 0.21 from the green area, which corresponds well with our previous calculation results (0.19) from the MD simulations.

In addition to the CN of solvents, contact ion pairing was probed by analyzing the P-F bond stretching band. As shown in Figure 28, the peak at $838\text{--}840\text{ cm}^{-1}$ is identified as the response from uncoordinated PF_6^- , whereas two peaks at 878 cm^{-1} and 834 cm^{-1} arise through coordinated PF_6^- . For the EC electrolyte (Figure 28a), coordinated PF_6^- contributes 6.4%, showing an excellent agreement with our simulated 6% CIP ratio. With the inclusion of FEC in the EC electrolyte (Figure 28b), an FEC ring-deformation vibration band appears at 862 cm^{-1} , which complicates the integral area calculation. By carefully deconvoluting the peaks, we estimate that 7.2% of the total PF_6^- ions are in the form of coordinated structure with Li^+ .

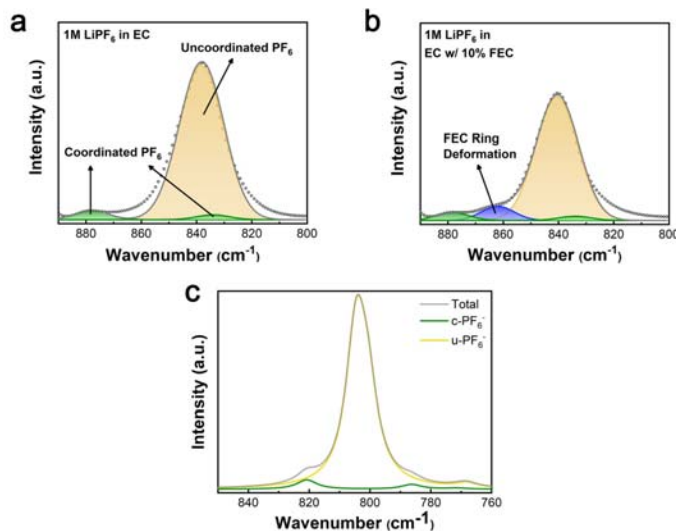


Figure 28. Measured FTIR spectra of the P-F bond stretching band of (a) 1.0 M LiPF_6 in EC, and (b) 1.0 M LiPF_6 in EC with 10% FEC. (c) The corresponding calculated IR spectra for 1.0 M LiPF_6 in EC as a comparison of the experimental results. Yellow, green, blue, and dark grey lines correspond to uncoordinated PF_6^- , coordinated PF_6^- , FEC ring deformation, and total spectrum, respectively. Scatter points denote the original FTIR data points.

Interfacial properties of 1.0 M LiPF_6/EC at the Si anode at the initial charging step are studied with classical MD. We first investigated the solvation structure close to the neutral (uncharged) interface. An OPLS force field is employed for the electrolyte constituents, and the anode interface is represented by neat c-Si covered with a thin, native silicon oxide layer. We found that the solvation structure of Li^+ changes quite significantly from the bulk to the interface, such that the overall Li^+ coordination changes from about 6 to about 4 (Figures 29a and 29b). This effect is due to two components: 1) a significant interaction between the SiO_2 oxygen and Li ion reduces the EC coordination number (CN) from 5.5 to 2.5, and 2) the Li-F CN increases from 0.4 in bulk to 1.2 at the interface. Because the PF_6^- anion can donate more than one F to each Li, the CIP ratio

increases from ~ 0.3 to ~ 0.65 from the bulk to the interface. We also find that the CIP ratio in bulk increases from 0.07 to 0.3 with temperature increasing from 300 K to 400 K, which we attribute to a decrease in the dielectric constant of the solvent.

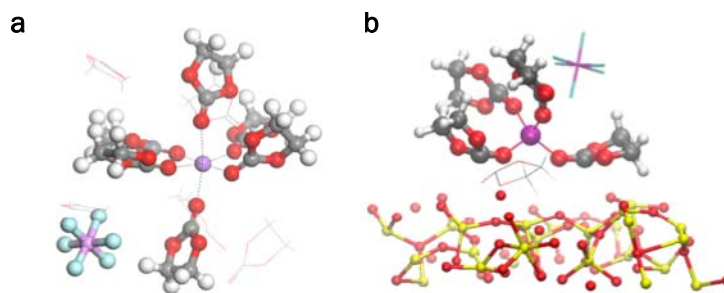


Figure 29. Structures of EC molecules around a Li ion (a) in bulk and (b) at interface.

We then analyzed the solvation structure of electrolyte molecules for an interface with a constant charge. As previously, the chemical characteristics of the Si anode interface is modeled with an amorphous SiO_2 layer on top of the c-Si bulk electrode. The equilibrium MD simulation is performed for 1 M LiPF_6 in EC at 400 K (Figure 30a). The applied voltage is modeled by assigning a uniform charge, $\pm 6.25e^{-4} e$, to each silicon atom at the negative/positive electrodes so that the voltage applied at the negative silicon electrode is ~ -0.47 V (Figure 30b). Interestingly, the constant charged interface causes a reduction in the CIP ratio between the bulk and the interface as compared to the neutral case. Both a negatively as well as positively charged SiO_2 interface result in a CIP ratio of 0.4 and 0.45 at the negative- and the positive-charged electrode interface, respectively (Figure 31), which should be compared to the neutral case of 1.2. Nevertheless, it should be stressed that the CIP ratio still is increased as compared to the bulk for both charged (marginally) and neutral (substantially) SiO_2 interfaces. Furthermore, similar to the neutral electrode, the CIP ratio increases from bulk to interface with increasing temperature, spanning 313, 350, and 400 K (see Figure 30c). In summary, the neutral silicon SiO_2 interface exhibits the largest CIP ratio, and it becomes smaller at the charged interface. Specific interaction between ions and SiO_2 enhances the CIP forming at the interface, which provides a hint toward preferential reaction pathways of the early SEI formation.

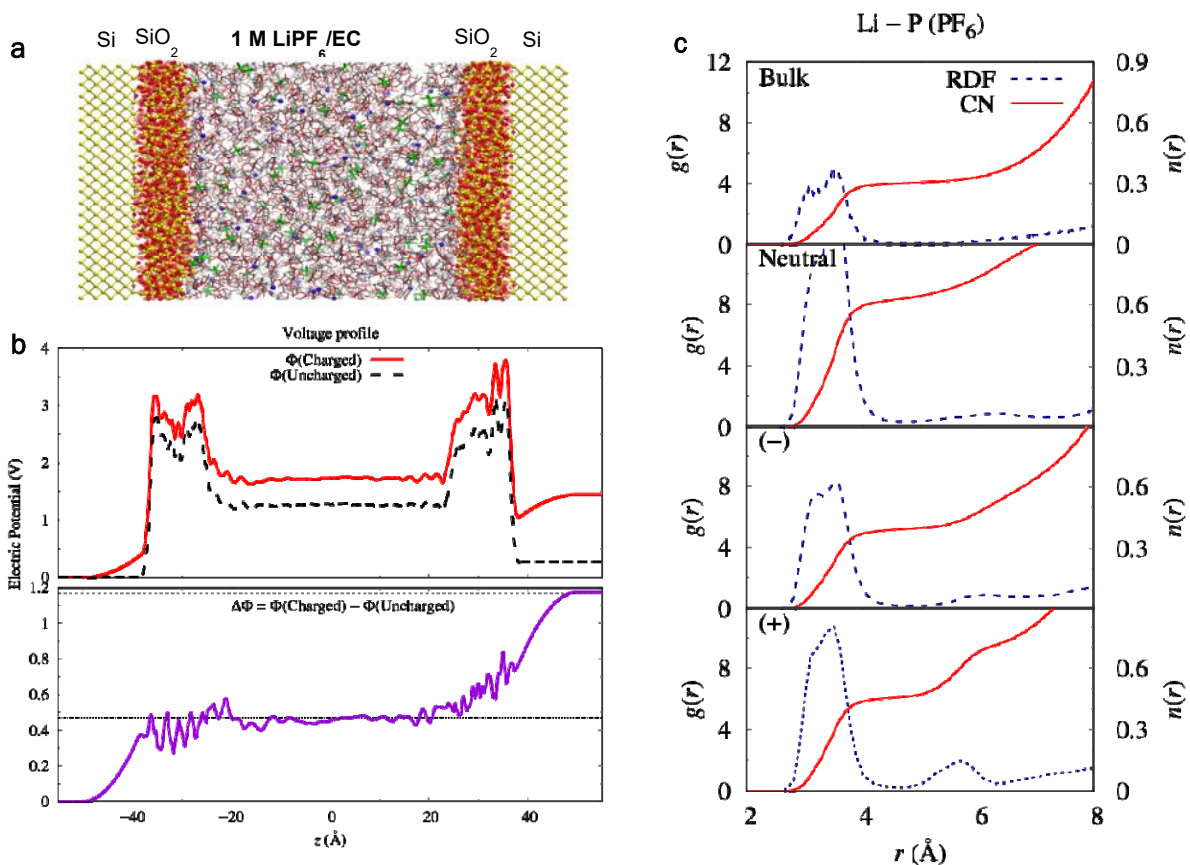


Figure 30. (a) The model Si anode interface, and (b) the voltage profile in the electrolyte region between the electrodes. The electric potentials are -0.47 V and +0.7 V at the negative and the positive electrodes, respectively. (c) Radial distribution functions and the coordination numbers (CN) of PF₆ ions around a Li ion in bulk and at the neutral, negative and positive electrodes, from top to bottom, and the CN values are 0.3, 0.65, 0.4, and 0.45, respectively.

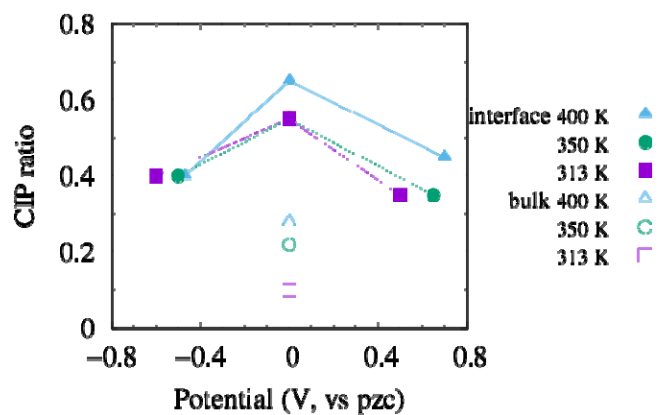


Figure 31. Contact ion pair (CIP) ratio in the bulk electrolyte and at SiO₂ interface at temperatures of 400 K, 350 K, and 313 K. The CIP ratio increases from the bulk to interface. The neutral silicon interface shows the largest CIP ratio, and it becomes smaller at the charged interface.

We find the total solvation number of Li in EC to be close to 6 in the bulk electrolyte, and it reduces to 4 at the interface. Explicit interaction between the SiO₂ interface and electrolyte results in a higher CIP ratio at the interface. The CIP ratio increases from the bulk to the SiO₂ interface. The neutral silicon interface shows the largest CIP ratio, which decreases for a charged interface; however, it is still larger than the bulk value. Enhanced CIP at the SiO₂ interface hints at reaction pathways of SEI formation.

In summary, collaborative FTIR experiments and the MD simulations provide consistent solvation structure information. Both approaches demonstrate that the LiPF₆/EC electrolyte with or without FEC results in a Li⁺ CN of 5–6. Furthermore, our results conclusively suggest that adding FEC increases the CIP ratio without significantly impacting the transport properties of either Li⁺ and PF₆⁻ ions. This minority FEC coordination with Li⁺ is important because the Li⁺ solvate complex serves as a key precursor for electrode-surface reduction reactions. The inclusion of FEC in the first solvation shell, even as a minority species, increases the reduction potential of FEC due to its close proximity of Li⁺, as compared to a freely solvated FEC.

Reactivity of Lithium Silicides

One possible approach to stabilizing silicon anodes against lithium losses is through prelithiation. However, this once again introduces new problems due to SEI formation and stability with electrolyte and electrode components. To explore this issue, we have focused on the synthesis of Li-Si materials and evaluated their reactivity with various solvents and binders. It is possible to form a range of lithium-silicon alloys as a series of Zintl phases as noted in the phase diagram, Figure 32. Previous work by Key et al. has shown that although average lithium content reflects the state of charge, the underlying structure of the electrode is a mixture of various Zintl anions that reflect the components of the various anions in the salts from the phase diagram. To assess the reactivity of these charge electrode components, we synthesized several of the compounds as bulk phases. Li₇Si₃ is the highest-melting binary in the phase diagram and reflects the predominant species around 300 mV vs Li.

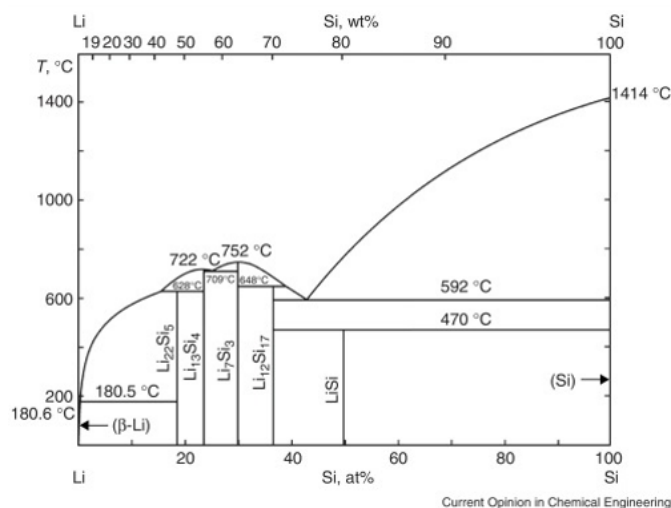


Figure 32. Li-Si phase diagram.

Li₇Si₃ was synthesized by a direct stoichiometric reaction of lithium metal (FMC lithium) and micron-sized silicon powder (Sigma-Aldrich). Best synthetic conditions were identified as the following:

- Vertical Ta tubes with a BN cap
- Heating to 760°C, slow cooling to 700°C
- Radiative cool to room temperature.

For other compounds evaluated ($\text{Li}_{22}\text{Si}_5$, $\text{Li}_{13}\text{Si}_4$) were synthesized in a similar manner with temperatures determined by phase-diagram data. Purity was determined by powder X-ray diffraction and general stability was determined by storing the powder in a low- O_2 glovebox and examining the material on an irregular basis by powder diffraction. To systematically study the reactivity of different battery components (including binders and electrolyte solvents) in direct contact with lithiated Si electrodes, Li_7Si_3 composition (voltage of about 350 mV vs. Li) was mixed with various solvents and polymers. ^7Li and ^{29}Si MAS NMR data were collected.

Figure 33 shows the *in-situ* ^7Li and ^{29}Si MAS NMR results of the bulk LS model compound and its mixture with different electrolyte solvents, including EC, EMC, FEC, and triglyme. The bulk Li content of lithium silicides has previously been shown to be directly correlated with ^7Li NMR shifts, where a positive increase in shift indicates Li loss from the bulk.³⁴⁻³⁵ The results showed the highest Li loss and bulk reaction for EC and the lowest for FEC/triglyme after mixing with Li_7Si_3 . Furthermore, no LiF at ~ 0 ppm in ^7Li NMR (and ^{19}F NMR, data not shown) was detected in the Li_7Si_3 + FEC experiment, contrary to the common notion that a FEC defluorination reaction would be prevalent in the presence of lithiated Si species. The FEC results suggest that Li_7Si_3 of $\sim 300\text{--}400$ mV potential vs. Li is either not reducing enough and/or a flow of electrons is also required for FEC passivation reaction. The results confirm the hypothesis that EC may not be the best solvent choice for Li-Si chemistry in the absence of SEI passivation and leads to major coulombic inefficiencies and Li loss. The results suggest that more inert electrolytes could lead to better coulombic efficiencies and to improved electrolyte formulations specifically designed for silicon anodes.

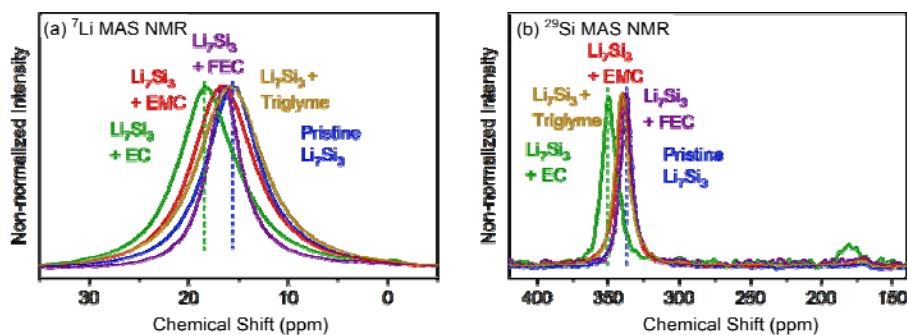


Figure 33. (a) ^7Li and (b) ^{29}Si solid-state *in-situ* MAS NMR for Li_7Si_3 and its physical with different electrolyte solvents.

To test the above hypothesis, a new lithium silicide compound with higher Li contents (i.e., representing lower charging potential, $\text{Li}_{13}\text{Si}_4$) were synthesized, and then mixed with FEC and other solvents. Because of the excess Li in the reaction container to mitigate Li loss, the newly synthesized lithium silicide was instead identified as $\text{Li}_{22}\text{Si}_5$ according to its ^7Li MAS NMR spectrum shown in Figure 34, which corresponds to about 0.05–0.1 V vs. Li. The ^7Li and ^{29}Si MAS NMR results of the mixture of $\text{Li}_{22}\text{Si}_5$ and different electrolyte solvents, including EC, FEC and triglyme, are shown in Figure 34. After mixing with FEC or EC, the main ^7Li peak of $\text{Li}_{22}\text{Si}_5$ at ~ 75 ppm shifted by ~ 4 ppm, indicating the lithium loss caused by the reaction between $\text{Li}_{22}\text{Si}_5$ and FEC/EC. Meanwhile, unlike the minor ^7Li and ^{29}Si NMR shifts previously observed after mixing Li_7Si_3 with triglyme, this time we observed clear positive peak shifts and notable broadening after mixing $\text{Li}_{22}\text{Si}_5$ with triglyme. Such obvious peak evolution indicated that although triglyme might be relatively stable when in contact with the slightly charged Si anode, it could react with the Si anode charged to lower voltages.

It must be noted that $\text{Li}_{22}\text{Si}_5$ NMR shifts are non-diamagnetic and the shift mechanism is due to conduction-band electrons at the Fermi level, i.e., a Knight shift; therefore, a simple interpretation of shift changes to higher or lower frequencies cannot be easily made as in the case of Li_7Si_3 . Still, the results indicate a bulk reaction and can partially explain our earlier observation that in half-cell tests using 1M LiTFSI in triglyme as the electrolyte, the capacity of Si anodes dropped faster over cycles compared with the LiPF_6 electrolyte + 10% FEC electrolyte. In addition, in the ^7Li MAS NMR spectra shown in Figure 34, a clear diamagnetic ^7Li peak around 0 ppm (could be ascribed to LiF, ^{19}F NMR pending) appeared after mixing $\text{Li}_{21}\text{Si}_5$ with FEC. This means that our earlier observation that the mixing of FEC and Li_7Si_3 causes no LiF formation results from the Li_7Si_3 not being sufficiently reducing enough to break a C-F bond. The above results suggest that triglyme alone may not be stable/passivating enough for high-Li-content Li_xSi .

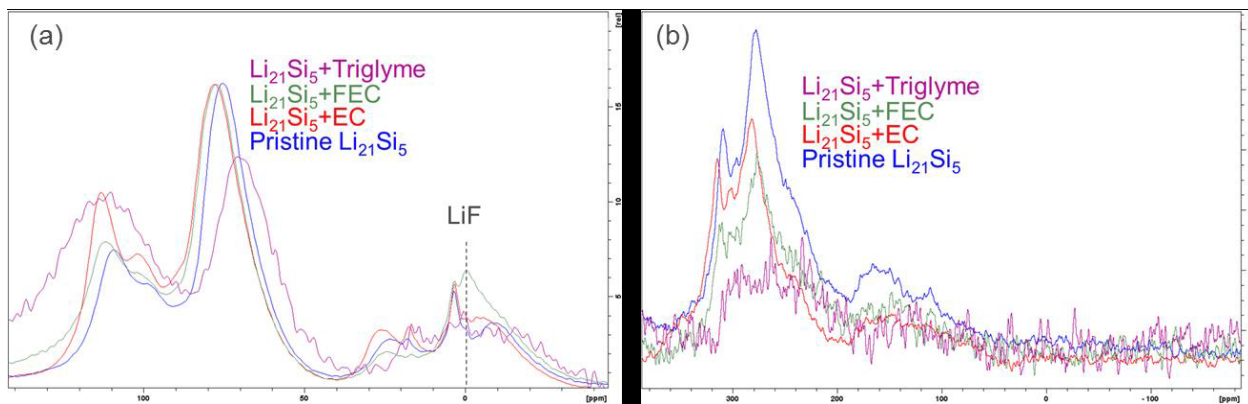


Figure 34. (a) ^7Li and (b) ^{29}Si *in-situ* solid-state MAS NMR for $\text{Li}_{22}\text{Si}_5$ and different electrolyte solvents. ANL, unpublished results.

In parallel, thin films of Li-Si were prepared by evaporating lithium onto 50-nm Si films supported on a copper substrate. Specific capacity was calculated by the total mass of lithium and silicon. Electrolytes were dropped on the surface of the lithium silicide thin film, which was deposited on a Pt-coated silicon wafer. Attenuated total reflection-Fourier transform infrared spectroscopy (ATR-FTIR) was performed with a Bruker Alpha spectrometer under argon atmosphere in a glovebox. Figure 35 shows the ATR-FTIR spectra of FEC and LiPF_6 EC/EMC electrolyte on lithium silicide. Peak assignment was referred to a previous ATR-FTIR study³ of lithium metal immersed in electrolytes. FEC helps form the uniform surface and suppresses the decomposition of PF_6^- . Similar findings are observed in this study. More organic phases formed with FEC and more inorganic phases formed in LiPF_6 electrolyte. In addition, LiPF_6 electrolyte generated more F-containing phases than FEC. XPS also shows similar composition with ATR-FTIR. This study shows that FEC, EC, and DEC can be chemically reduced by lithium silicide. This result and the NMR studies indicate that the Li content in the silicide needs to be controlled to optimize the reduction potential.

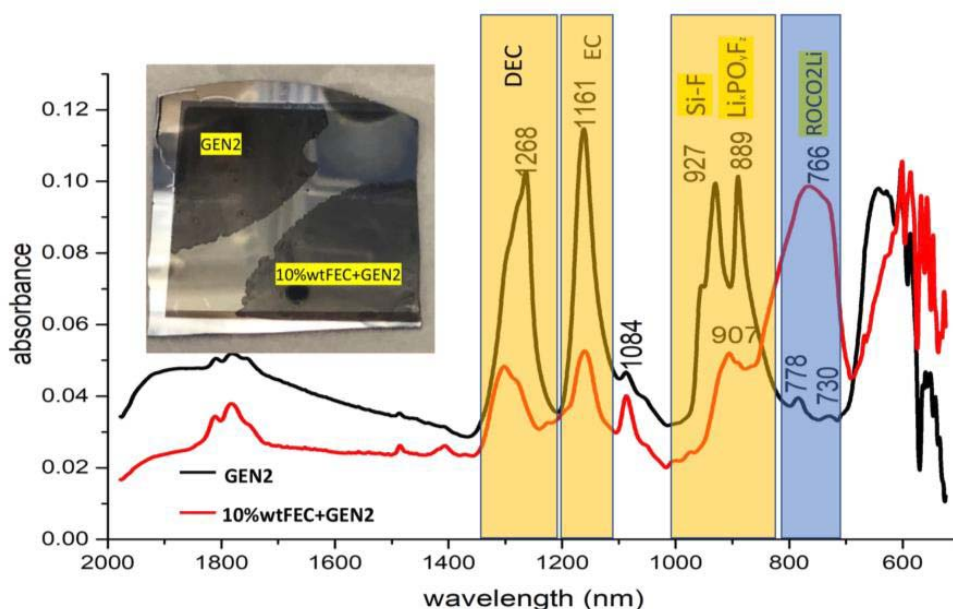


Figure 35. Inset photo: Electrolyte drop on lithium silicide thin film on silicon wafer. Main plot: ATR-FTIR spectra of the FEC and Gen2-treated lithium silicide surface.

References

- Wheeler, L.M., N.C. Anderson, P.K.B. Palomaki, J.L. Blackburn, J.C. Johnson, and N.R. Neale, Silyl Radical Abstraction in the Functionalization of Plasma-Synthesized Silicon Nanocrystals. *Chem. Mat.* 27 (2015): 6869–6878.
- Veith, G.M., B.L. Armstrong, H. Wang, S. Kalnaus, W.E. Tenhaeff, and M.L. Patterson, Shear Thickening Electrolytes for High Impact Resistant Batteries. *ACS Energy Letters* (2017): 2084–2088.
- Wheeler, L.M., N.C. Anderson, P.K.B. Palomaki, J.L. Blackburn, J.C. Johnson, and N.R. Neale, Silyl Radical Abstraction in the Functionalization of Plasma-Synthesized Silicon Nanocrystals. *Chem. Mater.* 27 (2015): 6869–6878.
- Jarry, A., S. Gottis, Y.-S. Yu, J. Roque-Rosell, C. Kim, J. Cabana, J. Kerr, and R. Kostecki, The Formation Mechanism of Fluorescent Metal Complexes at the $\text{Li}_x\text{Ni}_{0.5}\text{Mn}_{1.5}\text{O}_{4-\delta}$ /Carbonate Ester Electrolyte Interface. *J. Am. Chem. Soc.* 137 (2015): 3533–3539.
- Wang, S.N., D.K. Wang, S. Smart, and J.C.D. da Costa, Ternary Phase-Separation Investigation of Sol-Gel Derived Silica from Ethyl Silicate 40. *Sci Rep-Uk* 5 (2015).
- Koroleva, O.N., M.V. Shtenberg, and P.V. Khvorov, Vibrational Spectroscopic and X-Ray Diffraction Study of Crystalline Phases in the $\text{Li}_2\text{O-SiO}_2$ System. *Russ J Inorg Chem+* 59 (2014): 255–258.
- Li, X.Y., H.M. Yang, Morphology-Controllable Li_2SiO_3 Nanostructures. *Crystengcomm* 16 (2014): 4501–4507.
- Coyle, J., C. Apblett, M. Brumbach, J. Ohlhausen, and C. Stoldt, Structural and Compositional Characterization of RF Magnetron Cosputtered Lithium Silicate Films: From $\text{Li}_2\text{Si}_2\text{O}_5$ to Lithium-Rich Li_8SiO_6 . *Journal of Vacuum Science & Technology A* 35 (2017).
- Brooker, M.H. and J.B. Bates, Raman and Infrared Spectral Studies of Anhydrous Li_2CO_3 and Na_2CO_3 . *J Chem Phys* 54 (1971): 4788–.
- Shi, F.F., P.N. Ross, H. Zhao, G. Liu, G.A. Somorjai, and K. Komvopoulos, A Catalytic Path for Electrolyte Reduction in Lithium-Ion Cells Revealed by In Situ Attenuated Total Reflection-Fourier Transform Infrared Spectroscopy. *J Am Chem Soc* 137 (2015): 3181–3184.

- ¹¹ Xiao, A., L. Yang, B.L. Lucht, S.H. Kang, and D.P. Abraham, Examining the Solid Electrolyte Interphase on Binder-Free Graphite Electrodes. *J Electrochem Soc* 156 (2009): A318–A327.
- ¹² Nie, M.Y., D. Chalasani, D.P. Abraham, Y.J. Chen, A. Bose, and B.L. Lucht, Lithium Ion Battery Graphite Solid Electrolyte Interphase Revealed by Microscopy and Spectroscopy. *J Phys Chem C* 117 (2013): 1257–1267.
- ¹³ Yang, J.F., N. Solomatin, A. Kraysberg, and Y. Ein-Eli, In-Situ Spectro-Electrochemical Insight Revealing Distinctive Silicon Anode Solid Electrolyte Interphase Formation in a Lithium-Ion Battery. *Chemistryselect* 1 (2016): 572–576.
- ¹⁴ Profatilova, I.A., C. Stock, A. Schmitz, S. Passerini, and M. Winter, Enhanced Thermal Stability of a Lithiated Nano-Silicon Electrode by Fluoroethylene Carbonate and Vinylene Carbonate. *J Power Sources* 222 (2013): 140–149.
- ¹⁵ Reiche, M., M. Wiegand, and U. Gosele, Infrared Spectroscopic Analysis of Plasma-Treated Si(100)-Surfaces. *Mikrochim Acta* 133 (2013): 35–43.
- ¹⁶ Radvanyi, E., E. De Vito, W. Porcher, and S.J.S. Larbi, An XPS/AES Comparative Study of the Surface Behaviour of Nano-Silicon Anodes for Li-Ion Batteries. *J Anal Atom Spectrom* 29 (2014): 1120–1131.
- ¹⁷ Park, J.K., E.T. Lee, B.K. Kim, S.W. Jeong, and Y. Roh, Characteristics of Hf-Silicate Interfacial Layers Formed by Wet Etching. *J Korean Phys Soc* 55 (2009): 1022–1025.
- ¹⁸ Pfeiffer, H., P. Bosch, J.A. Odriozola, A. Lopez, J.A. Ascencio, and S. Bulbulian, Sol-Gel Synthesis of Li-ZrSiO₄. *J Mater Res* 15 (2000): 1490–1495.
- ¹⁹ Nie, M.Y., J. Demeaux, B.T. Young, D.R. Heskett, Y.J. Chen, A. Bose, J.C. Woicik, and B.L. Lucht, Effect of Vinylene Carbonate and Fluoroethylene Carbonate on SEI Formation on Graphitic Anodes in Li-Ion Batteries. *J Electrochem Soc* 162 (2015): A7008–A7014.
- ²⁰ Stankovich, S., D.A. Dikin, R.D. Piner, K.A. Kohlhaas, A. Kleinhammes, Y. Jia, Y. Wu, S.T. Nguyen, and R.S. Ruoff, Synthesis of Graphene-Based Nanosheets via Chemical Reduction of Exfoliated Graphite Oxide. *Carbon* 45 (2007): 1558–1565.
- ²¹ Bryngelsson, H., M. Stjern Dahl, T. Gustafsson, and K. Edstrom, How Dynamic is the SEI? *J Power Sources* 174 (2007): 970–975.
- ²² Andersson, A.M. and K. Edstrom, Chemical Composition and Morphology of the Elevated Temperature SEI on Graphite. *J Electrochem Soc* 148 (2001): A1100–A1109.
- ²³ Pereira, J., L.E. Pichon, R. Dussart, C. Cardinaud, C.Y. Duluard, E.H. Oubensaid, P. Lefauchaux, M. Boufnichel, and P. Ranson, In Situ X-Ray Photoelectron Spectroscopy Analysis of SiO_xF_y Passivation Layer Obtained in a SF₆/O₂ Cryoetching Process. *Appl Phys Lett* 94 (2009).
- ²⁴ Andersson, A.M., M. Herstedt, A.G. Bishop, and K. Edstrom, The Influence of Lithium Salt on the Interfacial Reactions Controlling the Thermal Stability of Graphite Anodes. *Electrochim Acta* 47 (2002): 1885–1898.
- ²⁵ Wang, Y.Y., K. Kusumoto, and C.J. Li, XPS Analysis of SiC Films Prepared by Radio Frequency Plasma Sputtering. *Physcs Proc* 32 (2012): 95–102.
- ²⁶ Rodriguez-Mosqueda, R., and H. Pfeiffer, Thermokinetic Analysis of the CO₂ Chemisorption on Li₄SiO₄ by Using Different Gas Flow Rates and Particle Sizes. *J Phys Chem A* 114 (2010): 4535–4541.
- ²⁷ Essaki, K., K. Nakagawa, M. Kato, and H. Uemoto, CO₂ absorption by Lithium Silicate at Room Temperature. *J Chem Eng Jpn* 37 (2004): 772–777.
- ²⁸ Alcantar-Vazquez, B., P.R.D. Herrera, A.B. Gonzalez, Y.H. Duan, and H. Pfeiffer, Analysis of the CO₂-H₂O Chemisorption in Lithium Silicates at Low Temperatures (30-80 Degrees C). *Ind Eng Chem Res* 54 (2015): 6884–6892.
- ²⁹ Knotter, D.M., Etching Mechanism of Vitreous Silicon Dioxide in HF-Based Solutions. *J Am Chem Soc* 122 (2000): 4345–4351.
- ³⁰ Xu, K., Electrolytes and Interphases in Li-Ion Batteries and Beyond. *Chem Rev* 114 (2014): 11503–11618.
- ³¹ Coyle, J., C. Apblett, M. Brumbach, T. Ohlhausen, and C. Stoldt, Structural and Compositional Characterization of RF Magnetron Cosputtered Lithium Silicate Films: From Li₂Si₂O₅ to Lithium-Rich Li₈SiO₆. *JVST A* 35 (2017).

- ³² Warren, L.J., Measurement of Ph in Acid Fluoride Solutions and Evidence for Existence of (Hf)₂. *Anal Chim Acta* 53 (1971): 199–.
- ³³ Duncan, H., D. Duguay, Y. Abu-Lebdeh, and I.J. Davidson, Study of the LiMn_{1.5}Ni_{0.5}O₄/Electrolyte Interface at Room Temperature and 60 Degrees C. *J Electrochem Soc* 158 (2011): A537–A545.
- ³⁴ Key, B., R. Bhattacharyya, M. Morcrette, V. Seznéc, J.-M. Tarascon, and C.P. Grey, Real-Time NMR Investigations of Structural Changes in Silicon Electrodes for Lithium-Ion Batteries. *J. Am. Chem. Soc.* 131 (2009): 9239–9249.
- ³⁵ Key, B., M. Morcrette, J.-M. Tarascon, and C.P. Grey, Pair Distribution Function Analysis and Solid State NMR Studies of Silicon Electrodes for Lithium Ion Batteries: Understanding the (De)lithiation Mechanisms. *J. Am. Chem. Soc.* 133 (2011): 503–512.

SEISta Section 2: The Influence of the Oxide Layer on the Formation and Stability of the SEI on Silicon

SEISta Team

Theoretical Predictions for Li-Si-O

Understanding the underlying atomistic mechanisms for the Si anode performance is crucial for improving current materials and incorporating higher-capacity anodes into future, improved lithium-ion technology. Current research focuses on the formation of the silicon/electrolyte interface (SEI) and its constituents, but fewer publications exist on modifications to the bulk Si. Dopants and alloys can be an effective way of modifying electrochemical properties. For that, we utilize theoretical and computational approaches including the density functional theory (DFT) calculation and molecular dynamics simulation methods. Our efforts will focus on identifying systems with lower volumetric expansion.

Computation of the bulk moduli shows that lithium silicates are stiffer than the silicides (Figure 1). The higher modulus of the silicates suggests that the native SiO₂ oxide is less accommodating to expansion. As Li penetrates into the Si and forms Li_xSi, the volumetric expansion will build internal pressure, ultimately resulting in the fracture of the silicate layer. This is consistent with two observations. First, that the particles that make up a Si electrode crack during the first few lithiation cycles and expose more surface area, which is observed especially in Si films. Second, the SiO₂ layer can be used to restrict expansion of the silicide phases, as demonstrated by Wu et al. when encasing a Si nanotube in SiO₂ to prevent outward expansion of the Si interior during lithiation.¹

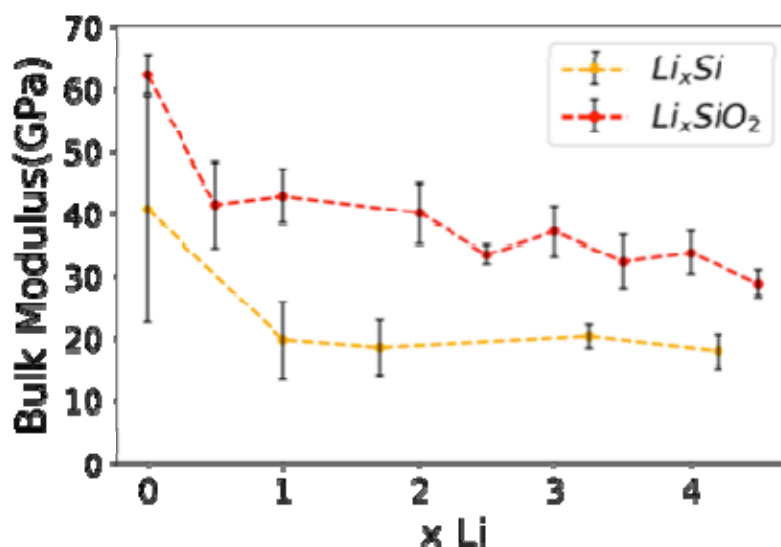


Figure 1. Bulk modulus of lithium silicates and lithium silicides.

Synthetic Methods for Producing Li-Si-O (Coyle, Teeter)

The method used to synthesize the model lithium silicate thin films was chosen to control composition and thickness of the films. The deposition method also needed to provide uniform, defect-free thin films with minimal exposure to ambient atmosphere. Sputter deposition was identified as the optimal available method.

A radiofrequency (RF) magnetron co-sputtering technique was used to provide more freedom in the range of composition used and to prevent preferential sputtering seen in other studies attempting to sputter lithium silicates.² Magnetron sputtering uses magnets installed behind the negatively charged electrode to trap more free electrons in a magnetic field above the target surface, which facilitates the ionization of neutral gas atoms and increases the rate at which material can be removed from the target and deposited onto a substrate. An RF power source was chosen due to the insulating nature of the target materials.

The deposition used for this thesis was a Kurt J. Lesker PVD 75 system with two RF sputter targets capable of sputtering at the same time. The sputter targets were oriented to sputter upward, as demonstrated in Figure 2.

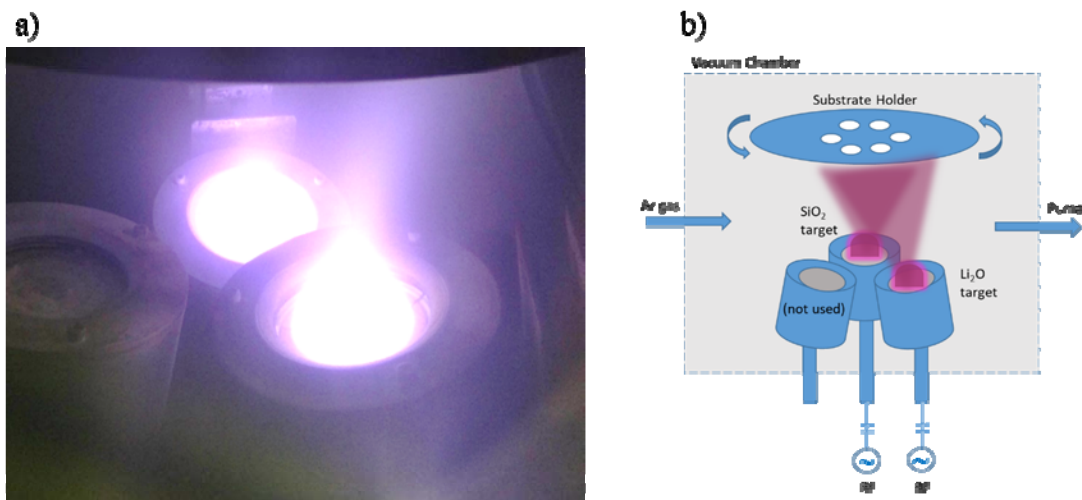


Figure 2. a) Photo of sputter targets, and b) diagram of sputter conditions in the process chamber of Lesker PVD75 system.

Films were sputtered from a SiO₂ (99.995%, Kurt J. Lesker) target and a fabricated Li₂O target in a pure argon (99.999%, Airgas) atmosphere. The Li₂O target was made from pressed disks of lithium dioxide powder (97% 9060 mesh, Aldrich). These disks were calcined at 900°C for 10 hours separated by mica sheets to prevent disks from fusing together. The SiO₂ target was sputtered under a range of powers from 9–28 W whereas the Li₂O target was sputtered under a constant power of 20 W for all compositions to achieve different Li/Si ratios. Both targets were sputtered for at least 40 minutes with a shutter in place before actual deposition to avoid cross-contamination. During deposition, the substrate holder was rotated to achieve homogeneous films. Two substrate holders were designed to fit diverse deposition needs. These substrate holders are pictured in Figure 3.

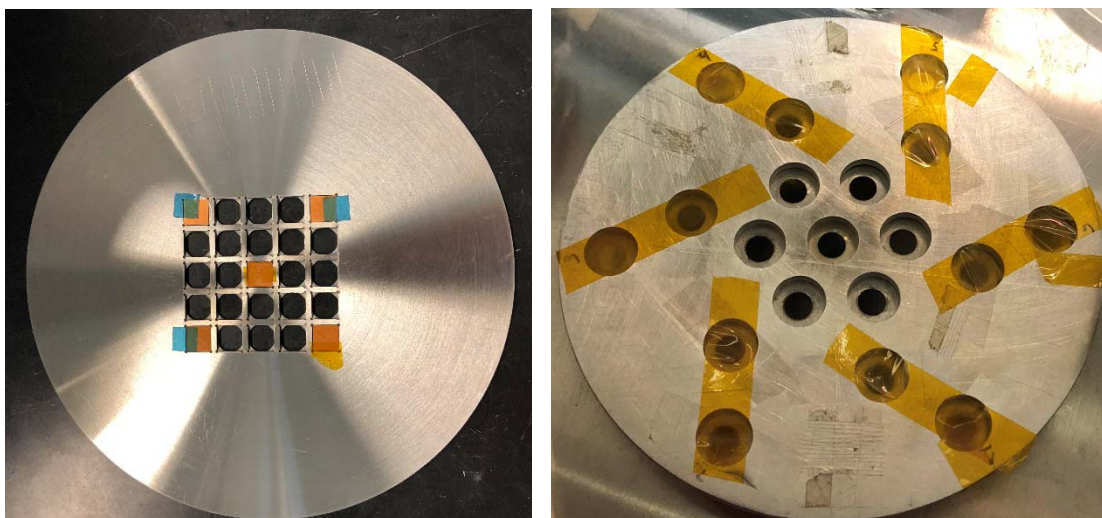


Figure 3. Substrate holders used for sputter deposition. Left: Holder for Si chips, Right: Holder for KCl chemical test samples.

Film deposition rates varied between 3 to 7.5 angstroms/minute. Deposition times were controlled to achieve the desired thickness for each film. Substrates were introduced to an inert atmosphere glovebox from atmosphere, loaded into the substrate holders, and placed in the secondary load-lock chamber that opens directly into the glovebox. The load-lock chamber was pumped down to suitably low vacuum ($\sim 10^{-6}$ torr) using a combination of roughing and turbo pumps. A gate valve was opened between the transitional load-lock chamber and the main process chamber, which was kept at a low vacuum ($\sim 10^{-8}$ torr), and the substrates were passed into the process chamber using an automated retractable arm. This process, along with the reverse process, allowed for thin-film samples to be removed from the deposition chamber directly into an inert atmosphere glovebox. Figure 4 depicts the sputter system and the glovebox used for this study with the sample transfer process labelled.

RF magnetron sputter conditions were controlled to determine the effect of deposition time and power ratios on the structure and composition with depth of the thin films produced. The results of this study allowed for evaluation of whether this synthesis technique gave adequate control over the material synthesis (and thus, material performance) for a model SEI on a silicon anode. Five different compositions of lithium silicates with distinct structures were produced, and the deposition time was controlled to create films with a desired thickness. Results from this thesis indicate that the co-sputtering technique still results in surface contamination and that target synthesis has a direct effect on the purity of these films; but otherwise, this technique provides uniform reproducible amorphous films ideal for this study.

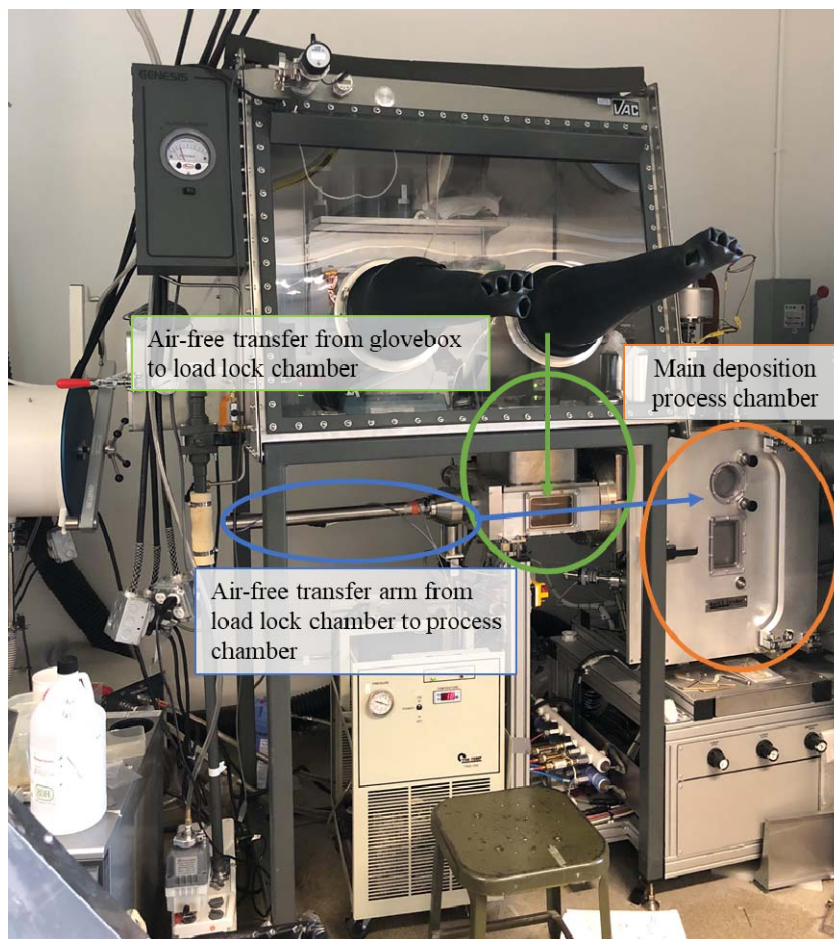


Figure 4. Sputter system and sample transfer process.

The first effort was to characterize the thin sputtered silicates for composition and quality. This was done in several ways by several different partner institutions in the program. Amorphous lithium silicate films about 550 nm thick were deposited for chemical analysis, and 50-nm-thick silicate films were deposited for all other analyses. Film thickness measurements were made with a Dektak 3030 profilometer. Each sample was replicated at least six times for reproducibility and error analysis. Inductively coupled plasma optical emission spectrometry (ICP-OES), Fourier transform infrared spectroscopy (FTIR), X-ray photoelectron spectroscopy (XPS) and time-of-flight secondary-ion mass spectrometry (TOF-SIMS) measurements were used to characterize the films.

The ICP-OES results for the thin films sputtered onto KCl substrates are shown in Figure 5. From elemental analysis, there is a linear relationship between the ratio of powers on the Li_2O and SiO_2 target and the lithium-to-silicon ratio in the thin films. There is only a small error associated with each power setting intended for the following compositions: $\text{Li/Si} = 1.4, 1.9, 2.9, 4.8,$ and 7.7 . The error bars indicate compositional variation across multiple depositions. The data in Figure 6 represent seven different deposition runs for each composition. Film deposition rates varied between 3 to 7.5 angstroms/minute based on the power ratio on the targets. Deposition times were controlled to achieve the desired thickness for each film (~550 nm). The time for each deposition ranged from 14 to 26 hours, with runs using higher $\text{Li}_2\text{O/SiO}_2$ target ratios requiring longer deposition times to achieve the desired thickness.

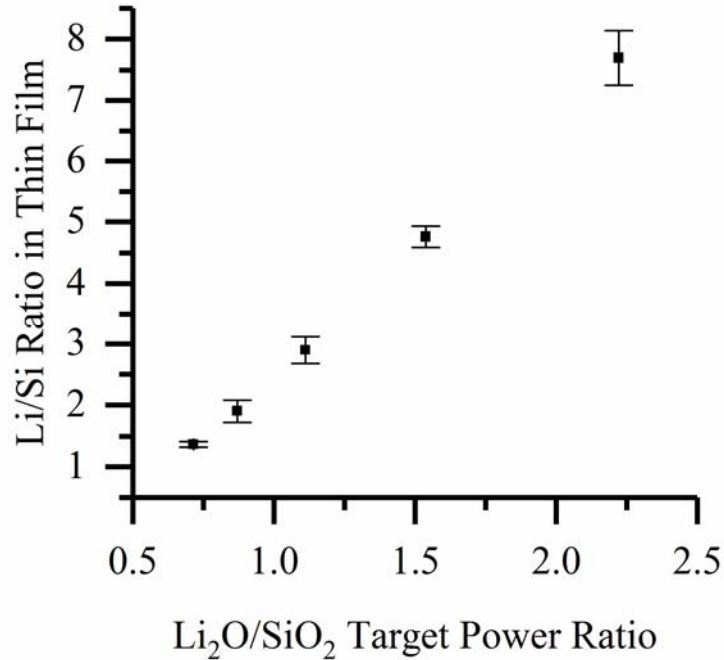


Figure 5. ICP-OES results for Li/Si ratio in each thin film at each power setting.

Structure/Composition in the Bulk and with Depth

FTIR in transmission mode was used to examine the bulk structure of the sputtered lithium silicate samples. Figure 6 shows a representative FTIR spectrum for each of the five compositions of sputtered lithium silicates. The peaks at $\sim 1,450\text{ cm}^{-1}$ and $\sim 880\text{ cm}^{-1}$ are observed in all five film compositions and are characteristic of a Li_2CO_3 species.³ The small, but visible, peak at $\sim 3,700\text{ cm}^{-1}$ results from O-H stretching vibrations and is characteristic of LiOH species.⁴ Because these spectra are obtained using bulk transmission-mode infrared (IR) spectroscopy, there is no information on whether the Li_2CO_3 and LiOH species are found in the bulk of the film or result from surface contamination during transfer to the FTIR spectrometer. This issue will be further addressed in conjunction with the results of the surface analysis in this chapter.

The absorption peaks detected in the range of $400\text{--}1,200\text{ cm}^{-1}$ by FTIR are characteristic of silicate vibrational modes as well as Li-O type bonds, and their measured ratio is used to evaluate the structural changes to the silicate network as the Li content is increased. The vibrational modes associated with each absorption peak in this region are previously reported and summarized in Table 1.^{5,6,7,8}

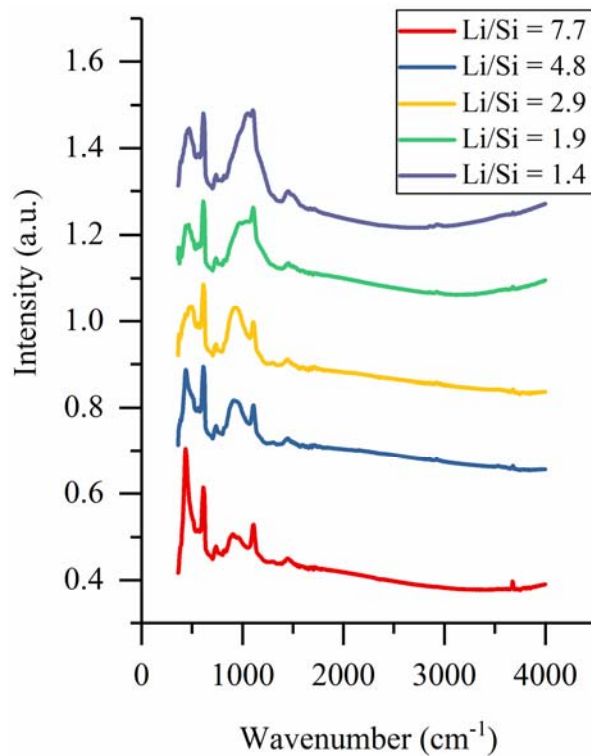


Figure 6. FTIR spectra of all five sputtered lithium silicate compositions.

Table 1. Vibration-Mode Assignments for FTIR Peaks

Wavenumber (cm ⁻¹)	Vibration Mode Assignment
~440	$\delta(\text{Si-O-(Li+)})$ $\nu(\text{Li-O})$
~500, ~560	$\delta(\text{O-Si-O})$ $\delta(\text{S-O-Si})$
~600	$\nu_s(\text{Si-O-Si})$
~740	$\nu_{as}(\text{Si-O-Si})$
~900	$\nu(\text{Si-O-})$
~1,000	$\nu_s(\text{O-Si-O})$
~1,100	$\nu'_{as}(\text{Si-O-Si})$
~1,160	$\nu_{as}(\text{Si-O-Si})$

The symmetric or asymmetric stretching modes (ν_s or ν_{as}) near 1160, 1100, 1000, 900, and 740 cm⁻¹ are attributed to $\nu_{as}(\text{Si-O-Si})$, $\nu'_{as}(\text{Si-O-Si})$, $\nu_s(\text{O-Si-O})$, $\nu(\text{Si-O-})$, and $\nu_{as}(\text{Si-O-Si})$, respectively. The lower wavenumber band near 600 cm⁻¹ corresponds to the $\nu_s(\text{Si-O-Si})$ mode, and the spectral features in the range of 500 to 560 cm⁻¹ correspond to deformation vibrations associated with $\delta(\text{O-Si-O})$ or $\delta(\text{S-O-Si})$ modes. The vibrational bands centered around 440 cm⁻¹ result from deformation of the non-bridging oxygen Si-O-(Li⁺) type bonds and the Li-O symmetric stretching mode. Due to the constraints of the FTIR instrument used, the asymmetric stretching modes of these Li-O bonds under 400 cm⁻¹ that are observed in higher-order lithium silicates^{9,10} could not be detected. The location of all vibrational modes shifts to slightly lower frequencies as

the lithium content in each thin-film composition increases. Because lower frequencies correspond to lower bond strengths and the number of weak Li bonds are increased in the structure, the entire bulk network weakens, resulting in a uniform redshift of the vibrational spectrum.

To evaluate the ratio of each type of bond in these amorphous thin-film materials, Gaussian-peak deconvolution is necessary to decompose and identify overlapping peaks. Once the peaks for each vibration mode are assigned and integrated, structural analysis of the lithium silicates can be completed. The Gaussian-peak deconvolution of this lithium silicate characteristic region for the thin film with a Li/Si = 7.7 composition ratio is shown in Figure 7 as an example for this method.

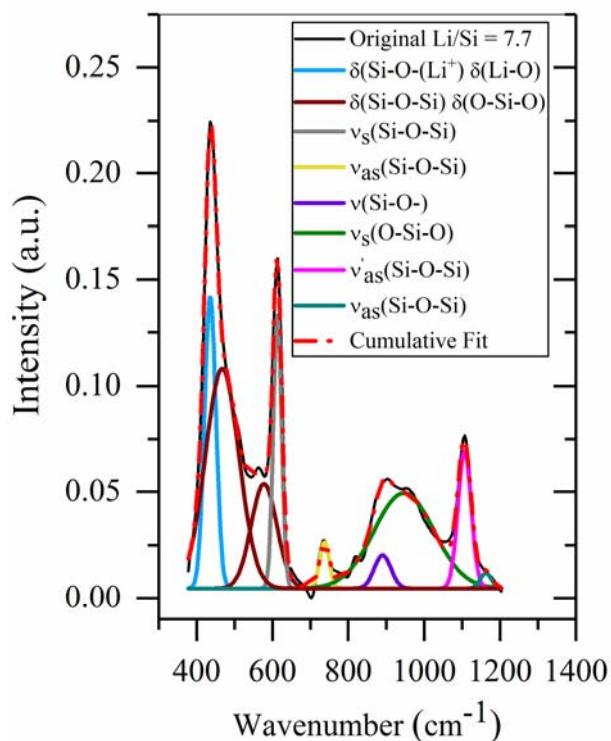


Figure 7. Gaussian-peak deconvolution of Li/Si =7.7 film.

The Gaussian peak fits were also completed for the other four compositions as well, with similar results. See Figure 8 for the Gaussian-peak deconvolution of the other four film compositions.

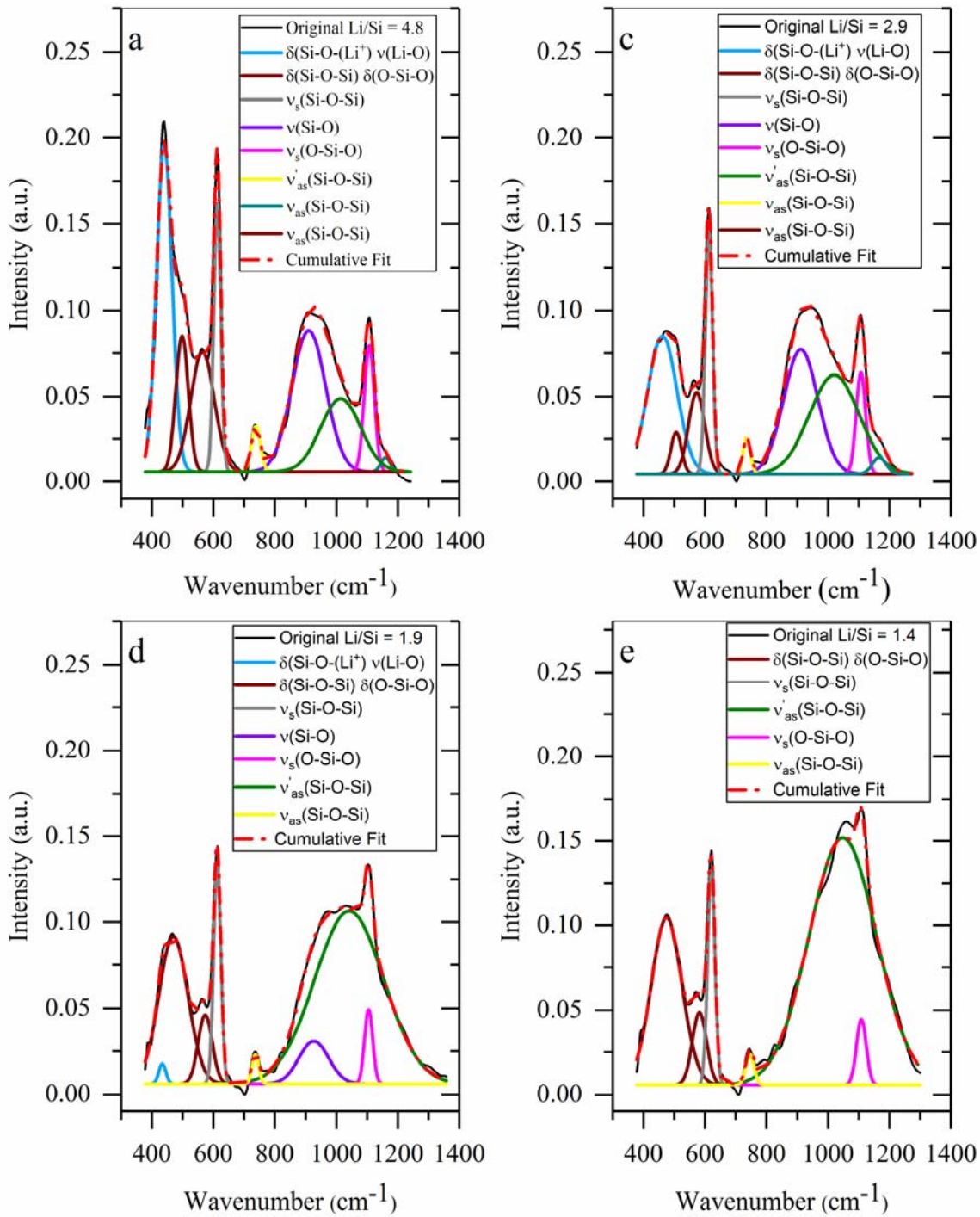


Figure 8. Gaussian-peak deconvolution of a) Li/Si = 4.8 film, b) Li/Si = 2.9 film, c) Li/Si = 1.9 film, and d) Li/Si = 1.4 film.

The peak positions remained the same as those described in Table 1 for all five compositions, but the intensity of the peaks shifted in a way that indicated increasing non-bridging oxygens (NBOs) as lithium content was increased in the thin films. A quantitative look at how these peaks shifted is shown in Figure 9 by comparing

the peak integration for the most-relevant vibration modes to the thin-film structure as the lithium content increases.

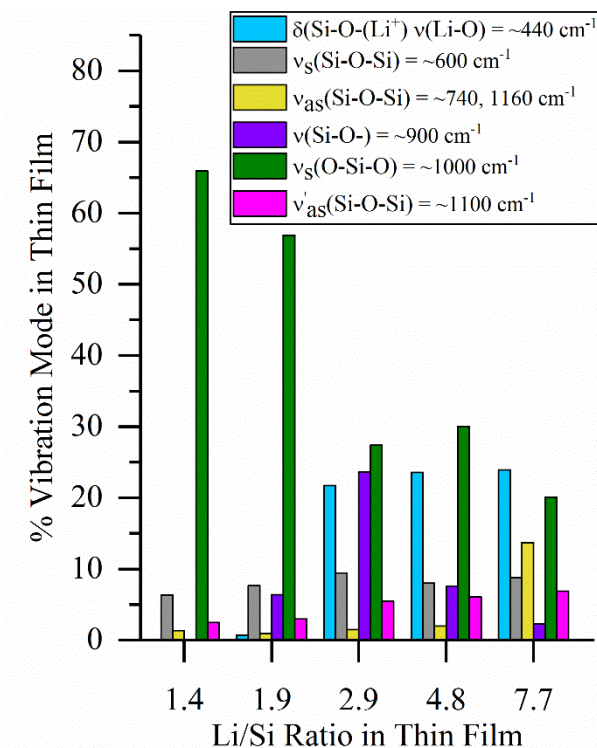


Figure 9. Percent of vibration modes relevant to lithium silicate film with for each composition.

The peaks that show minimal variation across the film compositions (~ 600 , 740 , and 1100 cm^{-1}) are also too sharp to be associated with an amorphous material. Because sharp peaks in FTIR indicate a more-ordered structure, these bands are assigned to the crystalline-silicon substrate that is detected in transmission mode.

The vibrational modes that are most indicative of the structure of the lithium silicate films are $\nu(\text{Si-O-})$ at $\sim 900 \text{ cm}^{-1}$, and $\delta(\text{Si-O-(Li}^+))$ and $\nu(\text{Li-O})$ at $\sim 440 \text{ cm}^{-1}$ for the relative amount of NBOs in the material versus $\nu_s(\text{O-Si-O})$ at ~ 1000 for the relative amount of bridging oxygens (BOs) in the material. The fraction of $\nu_s(\text{O-Si-O})$ at $\sim 1000 \text{ cm}^{-1}$ in Figure 9 (green) indicates that the number of BOs in the thin film decreases steadily as lithium is added, thus breaking up the silicate network. Up to $\text{Li/Si} = 3$, as lithium is added to the silicate network and the silicate chains break apart, more NBO bonds are observed; increased Li-O vibrations are observed, as well.

As more lithium is added past $\text{Li/Si} = 3$, sufficient lithium is now introduced such that it is possible for O^{2-} species to begin to form, which could create a decrease in NBOs as they dissociate from Si^{4+} altogether. This process can be observed by analyzing the variation in the $\nu(\text{Si-O-})$ mode at 900 cm^{-1} (shown in purple) as it increases in intensity up to $\text{Li/Si} = 3$ and then decreases for films with higher lithium content. In conjunction with this trend, the $\delta(\text{Si-O-(Li}^+))$ and $\nu(\text{Li-O})$ at $\sim 440 \text{ cm}^{-1}$ (shown in blue) increases as the lithium content is increased, suggesting that more lithium is bonding with the silicate network. The $\delta(\text{Si-O-(Li}^+))$ and $\nu(\text{Li-O})$ vibrational modes) at $\sim 440 \text{ cm}^{-1}$ are not observed to increase as much as might be expected for films with $\text{Li/Si} > 3$. The ratio of Li-O-type bonds in these higher-lithium-content films may not be fully represented in these spectra because there are Li-O bonds at frequencies $< 400 \text{ cm}^{-1}$ that are not observed due to limitation in the wavenumber range of the FTIR spectrometer used in this study. These results provide significant insight into

how increasing lithium content acts to break apart the silica network, and they provide an important building block in understanding how lithium moves through the lithium silicate thin films.

XPS and TOF-SIMS was also used to further characterize the co-sputtered thin films and to assess the nature of the carbonate vibrational modes seen in FTIR, i.e., whether they are a surface or bulk impurity. XPS was performed on Li/Si = 1.4, 2.9, 4.8, and 7.7 compositions with depth profiling using an argon ion beam. Lithium silicates are electronically insulating, so a low-energy electron flood source was used to compensate for the positive charge that accumulated during depth profiling. For each sample, the uppermost carbonate and oxide contamination layer was removed (~120-second sputter time) to examine the chemistry of the underlying thin film. Figure 10 shows the O 1s, Si 2p, and C 1s spectra of the Li/Si = 1.4 lithium silicate. See Figure 11, Figure 12, and Figure 13 for the XPS spectra of the other three film compositions. Table 2 is a list of peak assignments for these spectra derived from literature.^{11,12,13} Each set of spectra shows two relatively discrete layers within the films composed of the surface contamination layer on top of the film and the bulk film. Binding energy shifts show the transition zone at around 120 s of sputtering (green line).

Table 2. Peak Assignments for O 1s, C 1s, and Si 2p Binding-Energy Regions

Binding-Energy Region	Peak (eV)	Assignment
O 1s	532.7	SiO ₂
	531	LiOH
	531.5	Li ₂ CO ₃
	530–530.5	Li _x SiO _y
	528–528.5	Li ₂ O
C 1s	290	Li ₂ CO ₃
	288.5	CO ₂
	286.5	C-O
	284.6	C-C
Si 2p	103.2	SiO ₂
	100.5–101.3	Li _x SiO _y

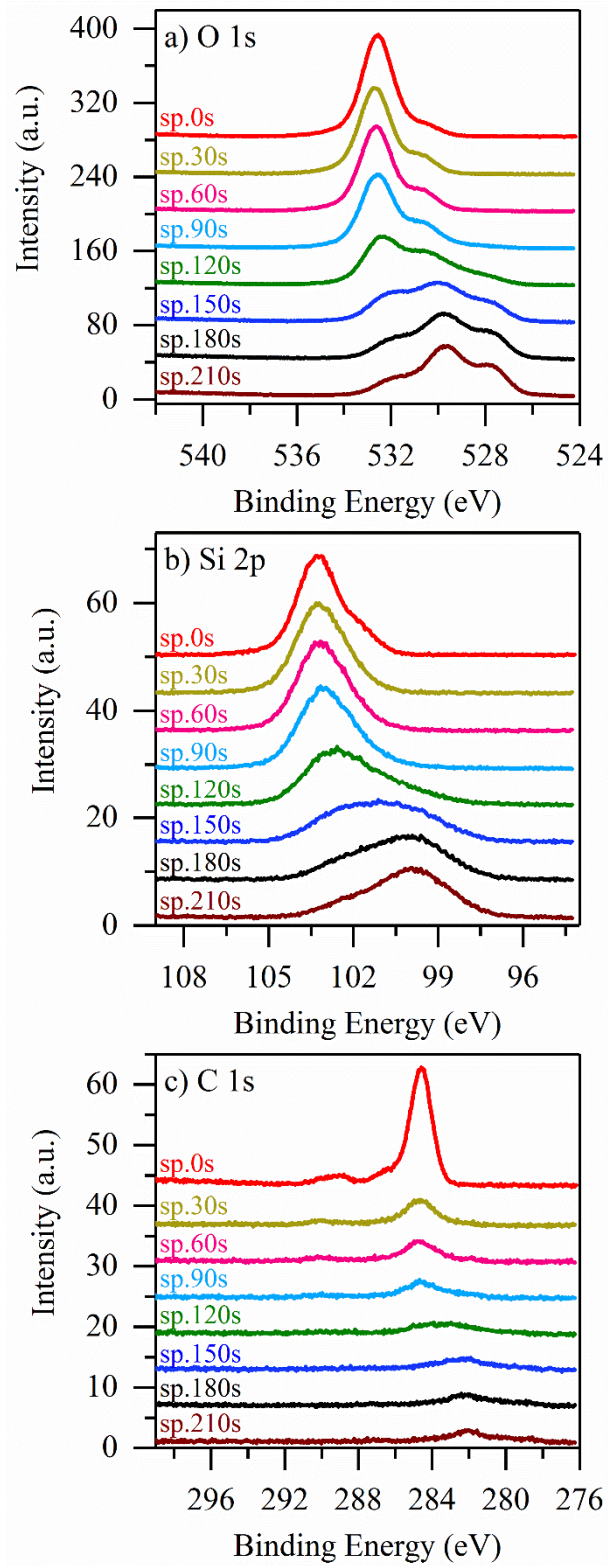


Figure 10. XPS a) O1s, b) Si 2p, and c) C 1s binding energy regions with depth profiling of Li/Si = 1.4 sample.

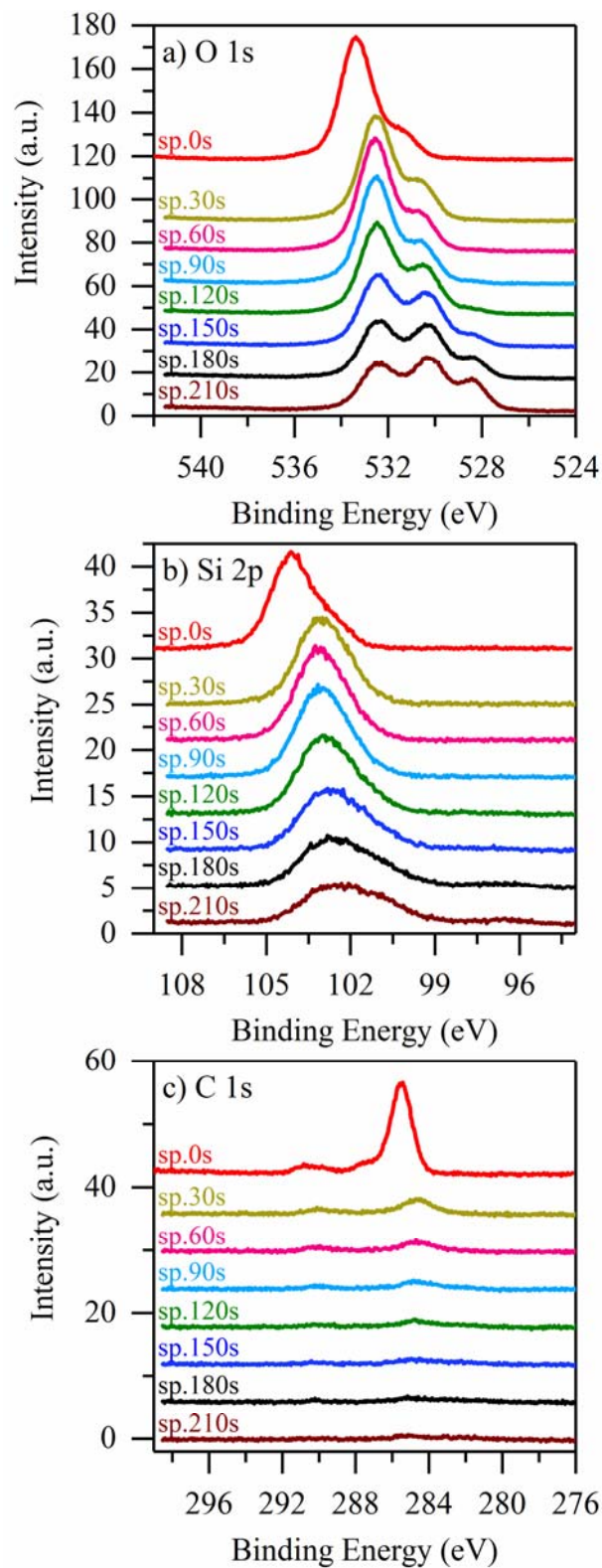


Figure 11. XPS a) O1s, b) Si 2p, and c) C 1s binding-energy regions with depth profiling of Li/Si = 2.9 sample.

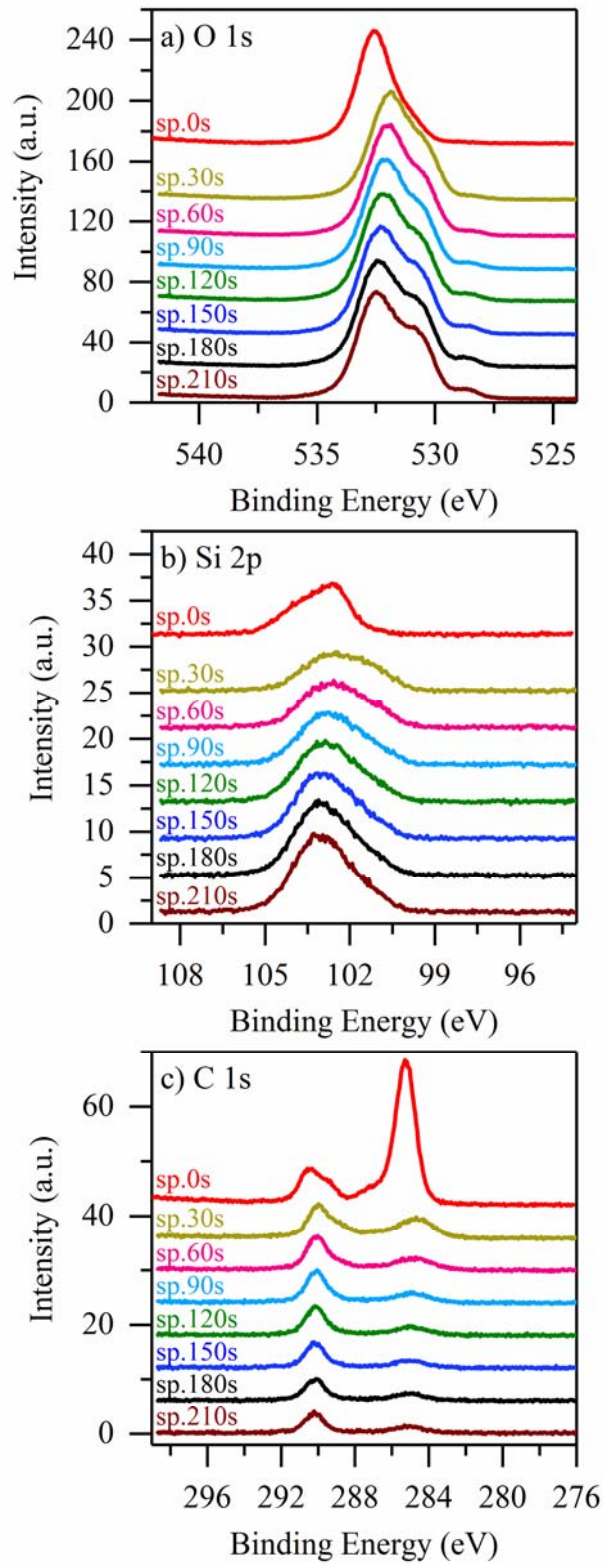


Figure 12. XPS a) O1s, b) Si 2p and c) C 1s binding-energy regions with depth profiling of Li/Si = 4.8 sample.

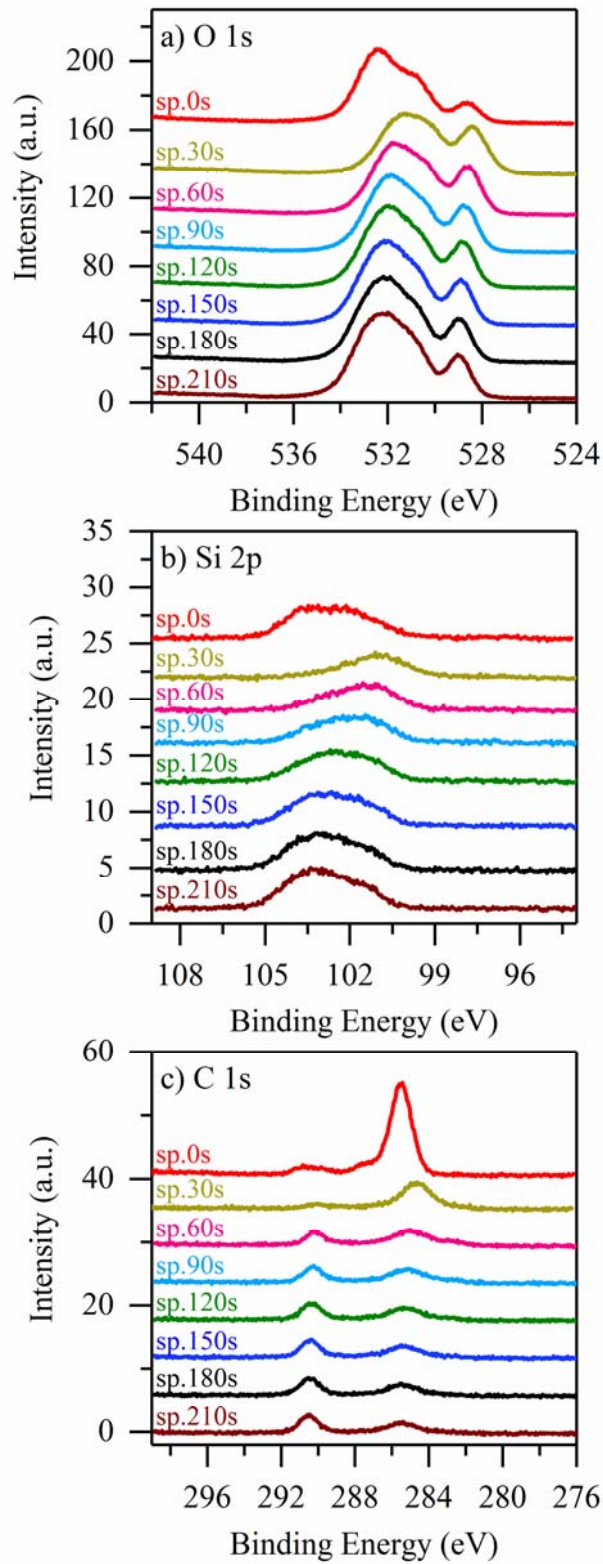


Figure 13. XPS a) O1s, b) Si 2p, and c) C 1s binding-energy regions with depth profiling of Li/Si = 7.7 sample.

The analysis for these XPS depth profiles begins with the spectra characteristic of the surface contamination layer (<120-s sputter). From the O 1s spectra shown in Figure 10a, peaks are resolved at 532.7, 531.5, and 531 eV, indicating that the surface layer of the lithium silicate films consists of SiO₂, Li₂CO₃, and LiOH, respectively. The peak at around 103.2 eV observed in the Si 2p spectra in Figure 10b and the peak at around 290 eV observed in the C 1s spectra in Figure 10c also support the presence of Li₂CO₃ and SiO₂ at the surface of the thin film. The C 1s spectra in Figure 10c (red line) shows some carbon surface contamination. Peaks are observed at 288.5, 286.5, and 284.6 eV assigned to CO₂, C-O-type bonds, and C-C bonds, respectively. The Li₂CO₃, CO₂, and C-O bonds are expected from surface adsorption during storage and/or exposure to low pressures during sample transfer. C-C bonds are observed into the bulk of the lithium silicate thin-film material, indicating a bulk contamination of higher-order carbon, such as graphite, in the thin film.

As the analysis transitioned into the bulk of the material (>120-s sputter time), some effect of charging became evident. This is most likely caused by differential charging that occurs in layered systems where the conductivity varies with each layer.^{14,15} The charging results in the peaks in the bulk of the thin film appearing at lower binding energies due to the charge neutralizer, and they are broadened. This makes it challenging to assign these peaks to specific bonding structures. For this analysis, assigned peaks were chosen based on a uniform shift to lower binding energies that correlate to the shift in binding energies from known materials on the surface that are also present in the bulk of the film. Li 1s spectra were collected for these samples, but were confounded by the broadening and shifting of peaks due to charging—to the point that they could not be considered in this analysis. There are three main peaks that occur between 528 and 532 eV in the bulk of the thin film for the O 1s spectra. Taking into account a slight shift to lower eV as mentioned, the peaks were assigned to SiO₂ (532.7 eV), Li_xSiO_y (530–530.5 eV), and Li₂O (528–528.5 eV). The presence of SiO₂ as well as Li_xSiO_y can be explained by the fact that the Li/Si = 1.4 thin film has the lowest amount of lithium in the silicate network of the compositions studied in this work. This indicates that there may be some nanoscale phase separation in these films. The Li₂O is most likely also a reduced product from adventitious oxygen on the surface or weakly bound oxygen in the thin film, charge neutralization, X-ray exposure, or argon bombardment.

The thin film's bulk Si 2p spectra show a decrease in the SiO₂ binding energy at 103.2 eV and a shift toward Li_xSiO_y at 100.5–101.3 eV. The components found by XPS in the surface contamination layer and bulk of the thin films agree with the silicate, Li₂CO₃, and LiOH vibration-mode peaks observed in FTIR spectroscopy. The depth profiling provided by XPS confirms that the carbonate peaks observed in FTIR come from both surface and bulk carbon contaminations.

The high-order carbon contamination observed in C 1s spectra in Figure 10c was verified with TOF-SIMS. Figure 14 shows that high-order carbon species even up to C₄ are present in the bulk of the lithium silicate film Li/Si = 1.4. These highly ordered carbon species were seen in all five compositions of the lithium silicates prepared in this work. See Figure 15 for the TOF-SIMS analysis of the other four film compositions.

It is very unlikely that such highly ordered carbon would come from air contamination or handling of samples. Instead, this contamination is proposed to result from the sintering step during the synthesis process used to prepare the Li₂O target itself. The Li₂O target disks were separated by graphite sheets in the furnace to prevent incidental contact and unwanted reactivity such as melting. The graphite sheets visibly transferred some carbon onto the surface of the targets. The targets were mechanically abraded to remove any visible graphite and then sputtered for 24 hours prior to thin-film deposition; but evidence of graphite contamination is verified by our TOF-SIMS analysis. However, although this carbon exists within the films, there is no reason to expect it to adversely impact the structural analysis reported herein.

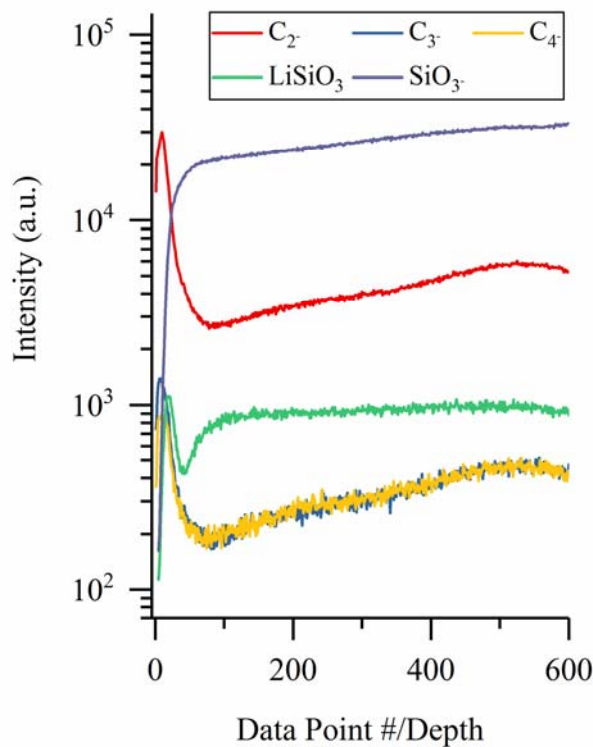


Figure 14. TOF-SIMS analysis of Li/Si = 1.4 thin film.

Similar studies were carried out at NREL using TOF-SIMS and XPS and similar results were observed. They also used additional characterization techniques on the films to better understand ion mobility in the silicates, and they compared them to other stoichiometric compositions. The chemical composition and homogeneity of prepared individual SiEI component thin films were analyzed first, which can influence their intrinsic properties. Figure 16 shows representative TOF-SIMS depth-profiling analysis of Li_2O , Li_3SiO_x , and Li_2SiO_3 thin films deposited on IPEs. In general, TOF-SIMS has ppm or better sensitivity, and negligible impurities were detected in the deposited films. In addition, similar chemical composition was confirmed for the deposited thin film in between and on top of Pt digits. XPS depth profiling was used to analyze the chemical composition of deposited thin films of individual SiEI components.

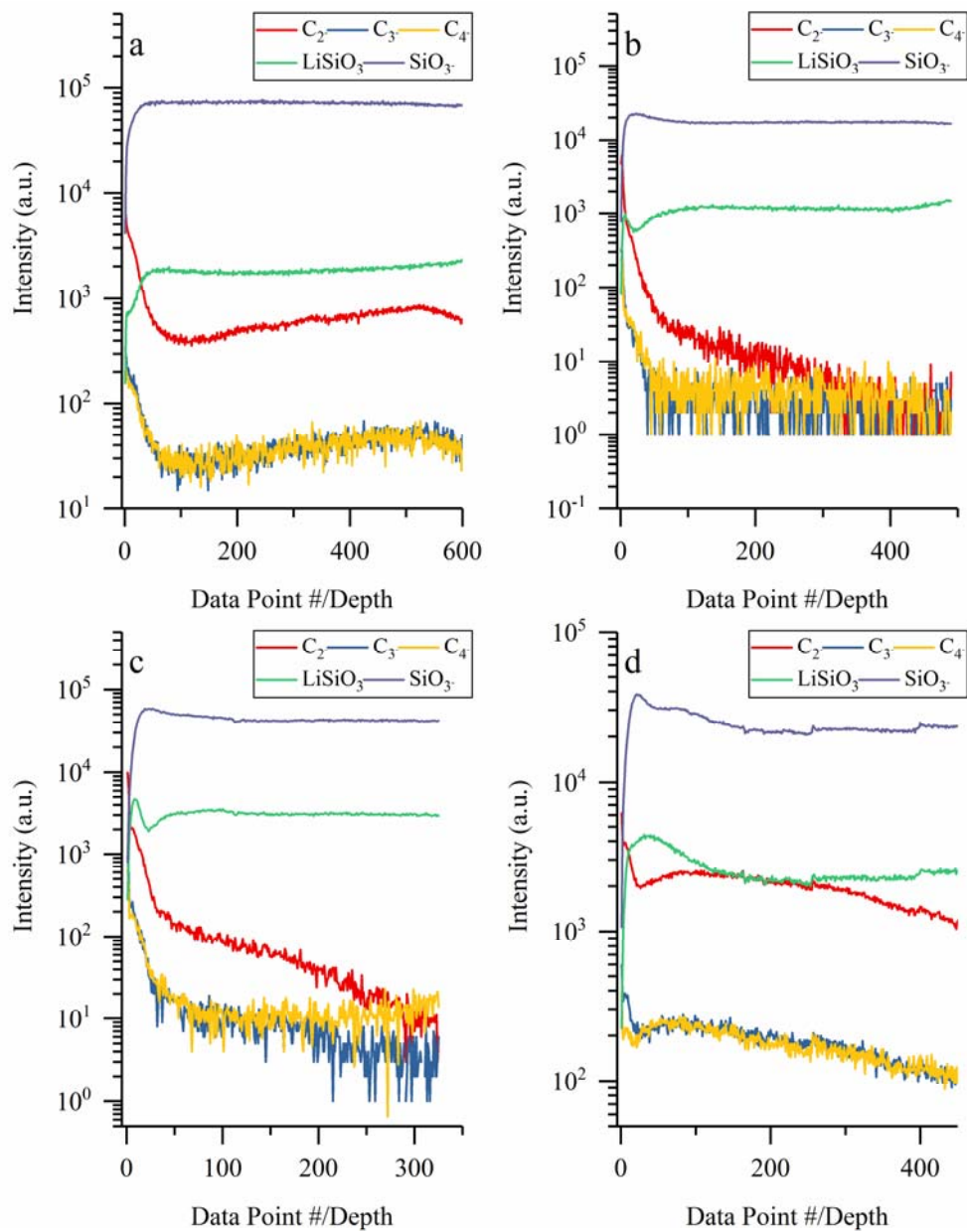


Figure 15. TOF-SIMS analysis of a) Li/Si = 1.9 thin film, b) Li/Si = 2.9 thin film, c) Li/Si = 4.8 thin film, and d) Li/Si = 7.7 thin film.

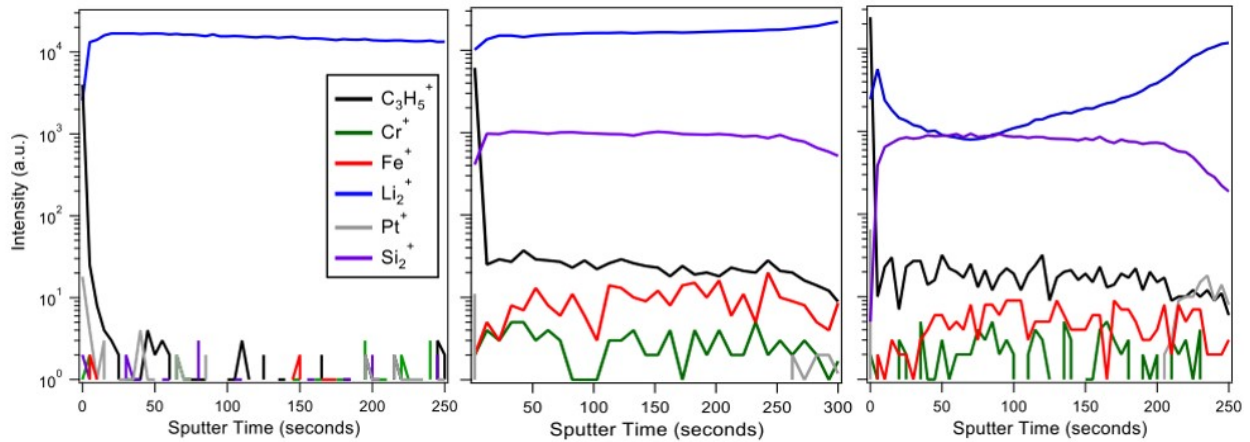


Figure 16. TOF-SIMS depth profiling of Li_2O (left), Li_3SiO_x (middle), and Li_2SiO_3 (right).

Figure 17 demonstrates that LiF was successfully grown on both a Li foil and Pt-coated Si wafer. Analysis of the change in binding energy (ΔBE) between the LiF peak in the F 1s and Li 1s was identical (629.41 eV) regardless of substrate, even though differences in surface charging occur because of the electrically insulating nature of LiF. Interesting, both of these films were deposited during the exact same run, but exhibited a difference in thickness of almost 6x. This is likely due to the reaction between the native Li surface and the evaporated LiF and/or the rough surface morphology of Li substrate.

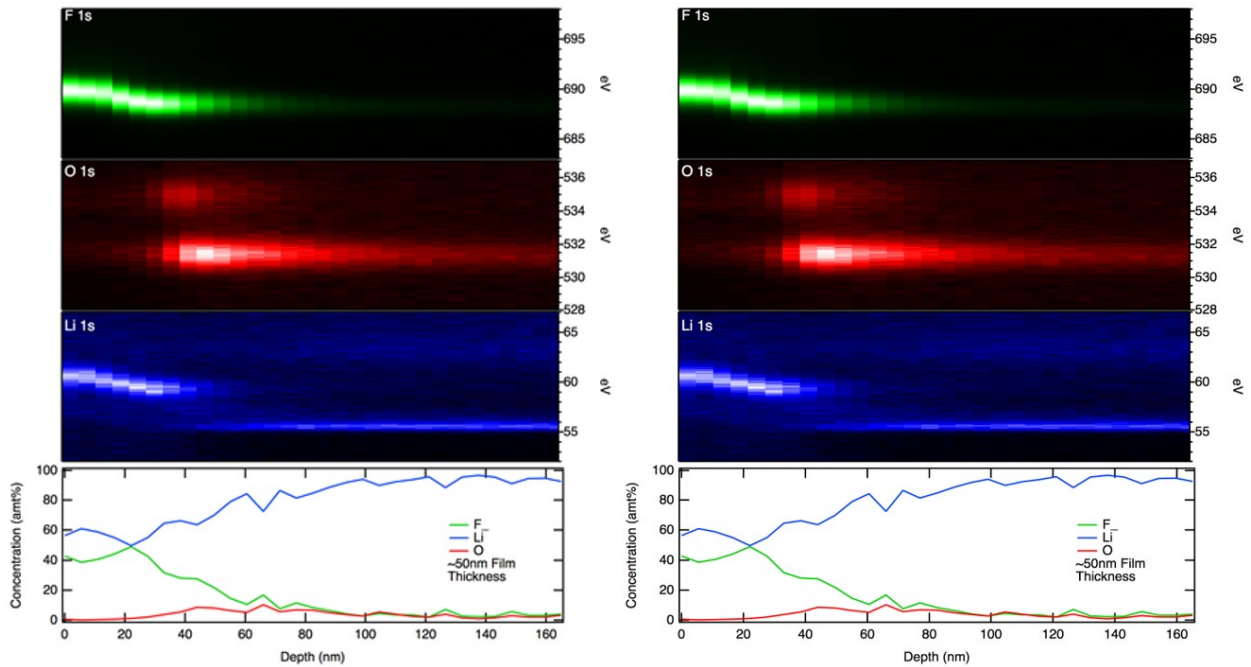


Figure 17. XPS depth profile analysis of LiF thin films on a Li foil (left) and a Pt-coated Si wafer (right).

A similar set of experiments was outlined for other SiEI components (e.g., SiO_2 , $\text{Li}_2\text{Si}_2\text{O}_5$, Li_2SiO_3 , Li_3SiO_x , and Li_2O), and analysis of these sputter-deposited films demonstrated that the intended phase was present when deposited on a Pt-coated Si wafer.

The morphology and root-mean-square (RMS) roughness of the well-prepared thin-film samples were analyzed using atomic force microscopy (AFM), and the thickness of several samples was determined using scanning spreading resistance microscopy (SSRM) resistivity mapping and depth profiling. Unlike the surface morphologies of SiO₂ and LiF, those of lithium silicates and Li₂O display different nanoscale features (Figure 18, 1×1 μm): Li₂Si₂O₅ shows small-scale features; Li₂SiO₃ shows large-scale features; Li₃SiO_x shows intermediate-scale features; and Li₂O shows the largest-scale features. The RMS roughness values of the Pt-coated Si wafer (as a blank sample for comparison), LiF, SiO₂, Li₂Si₂O₅, Li₂SiO₃, Li₃SiO_x, and Li₂O are 2.48, 2.77, 3.98, 13.4, 17.6, 26.6, and 69.1 nm, respectively. For lithium silicate surfaces, an increased Li:Si ratio has the trend of increased roughness, and Li₂O has the greatest roughness of all samples. One possible explanation for the largest-scale features and the greatest roughness of Li₂O thin film is that the sample was prepared with a relatively higher deposition rate, where the atoms do not have sufficient time to diffuse when they reach the substrate.

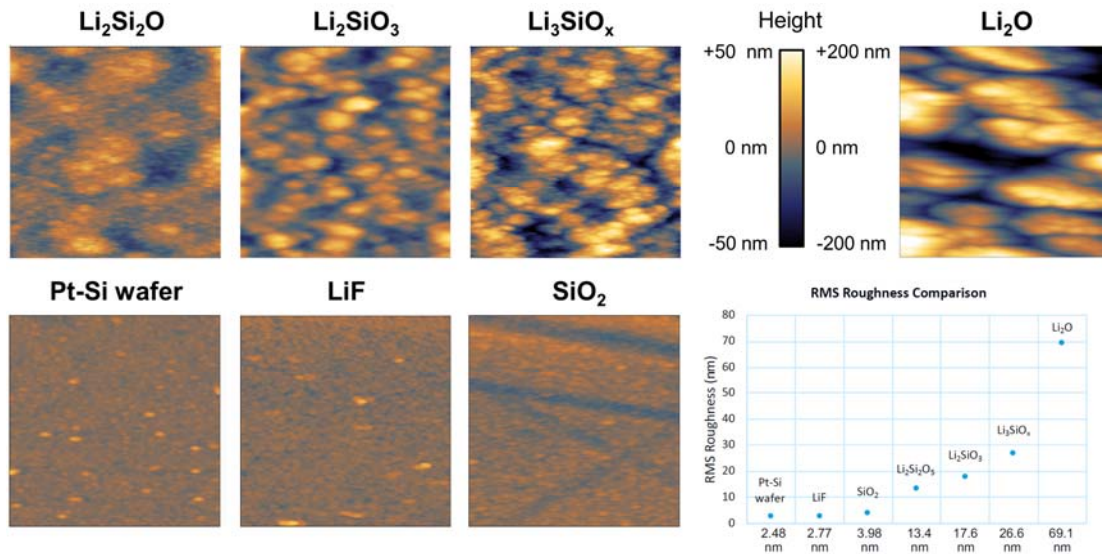


Figure 18. Morphologies and RMS roughness of individual SiEI components deposited on Pt-coated Si wafers.

SSRM depth profiles were carried out to investigate deposition uniformity and thickness. Depositions showed uniformity of electronic properties throughout the deposited layers, and deposited layer thickness was measured at 100 and 200 nm for LiF and Li₂O, respectively, which shows good agreement with estimated deposition thickness.

The physical and electrochemical properties (e.g., ionic conductivity and activation energy) of individual SiEI component thin films (deposited on IPEs) were characterized using an EIS. The ionic conductivities with varying temperature and the activation energies (from Arrhenius relationship) of each thin film are shown in Figure 19 and noted in Table 3, respectively. In the case of a LiF thin film, increasing conductivity rates (in terms of slope) are different in two temperature regions (468–498 K vs. 528–588 K), possibly due to phase transition (e.g., growth of large grains, based on previous studies^{16,17}) at around 508 K. To verify this, XRD analysis was performed for as-prepared LiF and annealed LiF (at 523 K). Annealing of the LiF film with thermally induced reordering slightly shifts the (111) reflection peak toward a higher angle, which corresponds to a smaller lattice spacing. The shift very likely originates from residual stresses present in the film, as shown in previous research.¹⁶

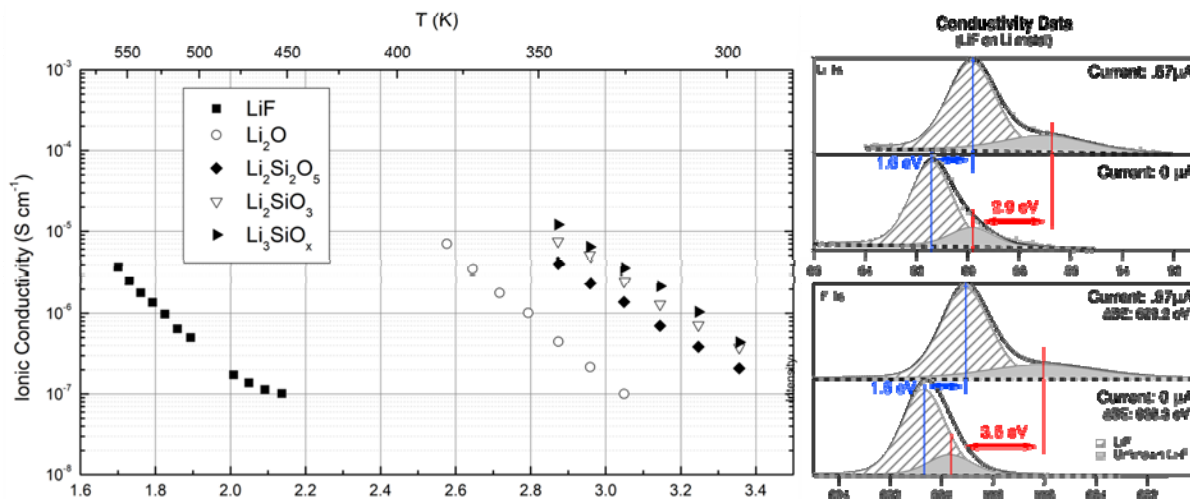


Figure 19. Ionic conductivity of individual SiEI components with varying temperature (left) and binding energy variation of a LiF thin film on a Li foil obtained from operando XPS (right).

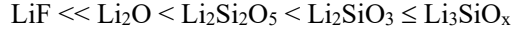
A complementary experiment using *operando* XPS has been designed to probe electronic/ionic conductivity. This novel technique uses sample biasing by creating a negative surface charge using an electron gun to measure shifts in binding energy, which can be related to either ionic or electronic conductivity (Figure 19).¹⁸

Table 3. Ionic Conductivities and Activation Energies of Individual SiEI Components.

Component	Conductivity (S cm ⁻¹)	Activation Energy (mV)
Li ₃ SiO _x	1.20×10 ⁻⁶ (at 298 K)	0.53 (298–348 K)
	2.20×10 ⁻⁵ (at 348 K)	
Li ₂ SiO ₃	9.49×10 ⁻⁷ (at 298 K)	0.56 (298–348 K)
	2.15×10 ⁻⁵ (at 348 K)	
Li ₂ Si ₂ O ₅	4.81×10 ⁻⁷ (at 298 K)	0.53 (298–368 K)
	9.52×10 ⁻⁶ (at 348 K)	
Li ₂ O	7.66×10 ⁻⁷ (at 348 K)	0.61 (348–408 K)
	1.42×10 ⁻⁵ (at 408 K)	
LiF	1.02×10 ⁻⁷ (at 468 K)	0.36 (468–498 K)
	~2.00×10 ⁻¹⁰ (at 298 K) ²	0.82 (528–588 K)

¹at infinite temperature; ²obtained from *operando* XPS measurements

Overall, the following order is observed for increasing ionic conductivities of individual SiEI components with varying temperature:



It is noted that the ionic conductivities increased from low-lithium-content $\text{Li}_2\text{Si}_2\text{O}_5$ (1:1 Li/Si) to high-lithium-content Li_3SiO_x (3:1 Li/Si). Compared with surface electronic resistivity values in Figure 20, the ionic conductivities of each sample (e.g., lithium silicates and LiF) are several orders of magnitude higher than the electronic conductivities of them, which is in accordance with our assumption for ionic conductivity measurements. Resistivity mapping at moderate forces at the surfaces of the deposited layers shows very low resistance for Pt-coated Si wafer, and very high resistivity (above the instrumental resolution limit, $10^{10} \Omega \cdot \text{cm}$) for SiO_2 and LiF (Figure 20).

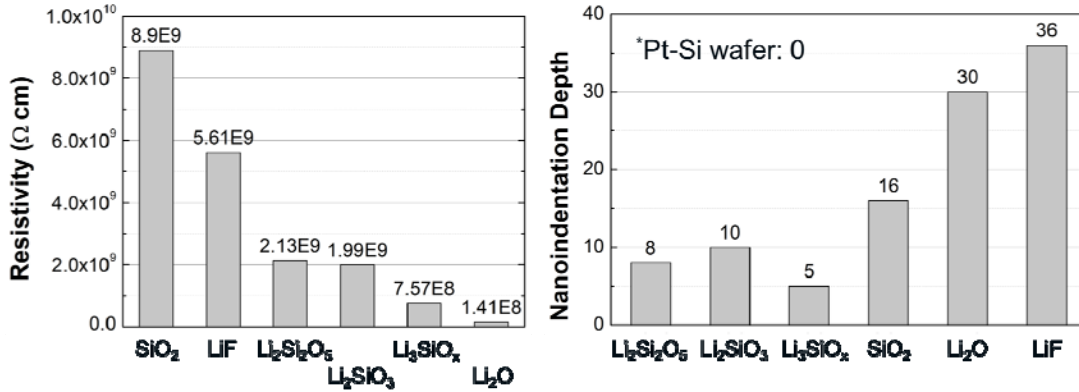


Figure 20. Average surface electronic resistivity (left) and nanoindentation depth (right) of individual SiEI

AFM-scanning probe microscopy (SPM)-based nanoindentation was carried out at a determined force, $30 \mu\text{N}$, exerted for 10 seconds (Figure 20). At this force, no indentation was measured on a Pt-coated Si wafer, indicating a high measure of hardness. Relatively minor indentation was measured on lithium silicates and SiO_2 for this force (5–16 nm). LiF showed the least hardness among six samples, with the force resulting in an indentation of 36 nm. It is critical to note that all physical, electrochemical, and mechanical property values in this study are relative ones, for comparison only, among six inorganic amorphous thin-film samples. So, the relativity may be changed if we consider other known SiEI components (in particular, organic ones) or other types of samples (prepared with different methods).

Nanoindentation was carried out on the as-deposited silicate films with a SPM nanoprobe by exerting a force of $30 \mu\text{N}$ for 10 seconds on the surface of the sample, then measuring the indentation depth of the probe. The results of these measurements are shown in Figure 21.

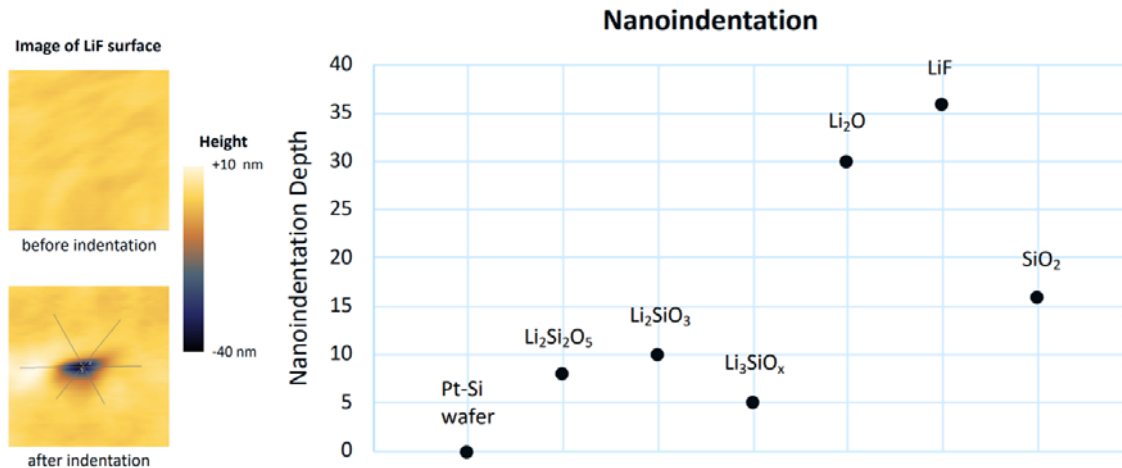


Figure 21. 500×500 -nm AFM images of the LiF surfaces before and after nanoindentation was performed, illustrating the AFM-based nanoindentation technique. Hardness results for each deposited film are plotted at

SSRM resistivity profiling on LiF and Li₂O deposited on Si wafers showed high resistivity (10⁹ Ω·cm and 10⁸ Ω·cm, respectively) with consistency throughout the film thickness, shown in Figure 22.

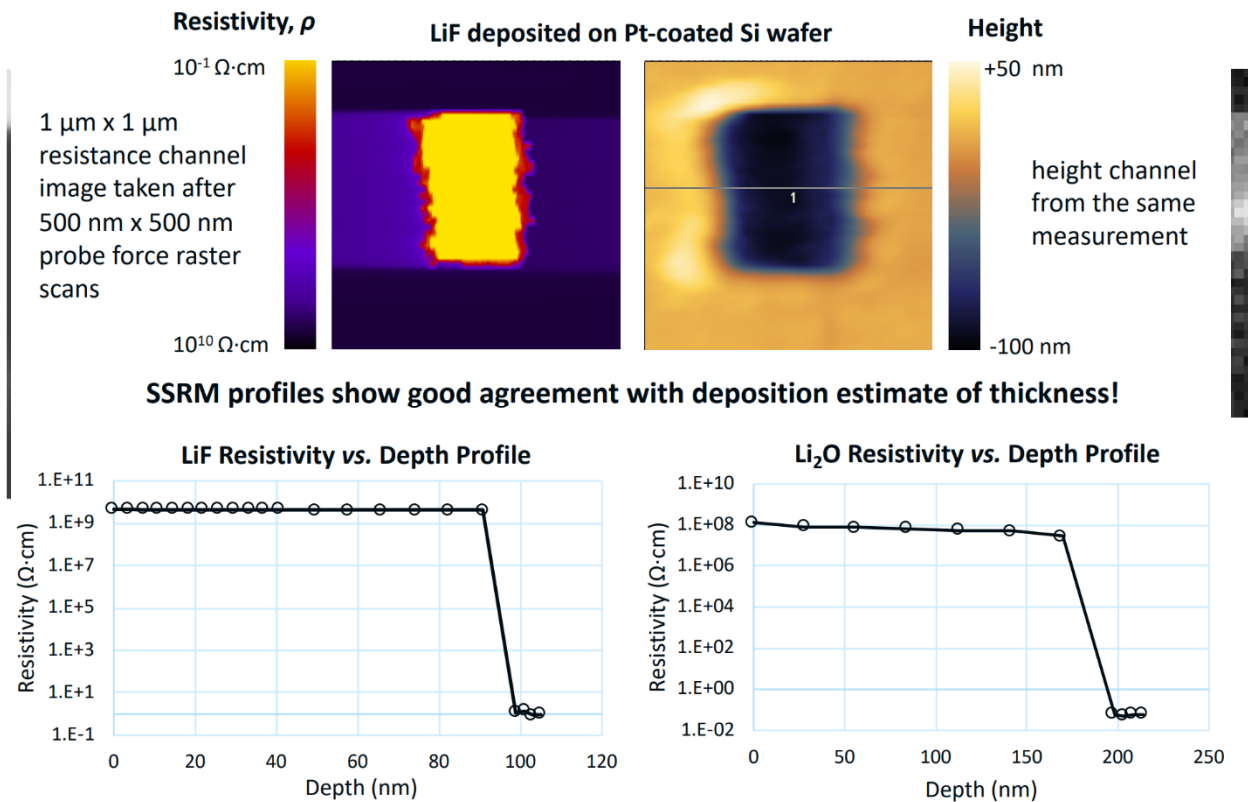


Figure 22. 1×1- μm SSRM images of the LiF surface showing resistance and height channels after SSRM resistivity vs. depth profiling was performed. Resistivity vs. depth profiles for LiF and Li₂O are plotted.

Several of the deposited films (Li₂O and Li₂SiO₃) were also examined in scanning transmission electron microscopy (STEM) electron energy loss spectroscopy (EELS). Results showed Li₂O to be nonuniformly deposited. EELS O K edge maps and Li K edge maps of the Li₂O sample showed oxygen to be located predominately in the Li₂O film, while significant amounts of Li had migrated into the e-beam Pt while exposed to the electron beam. See Figure 23.

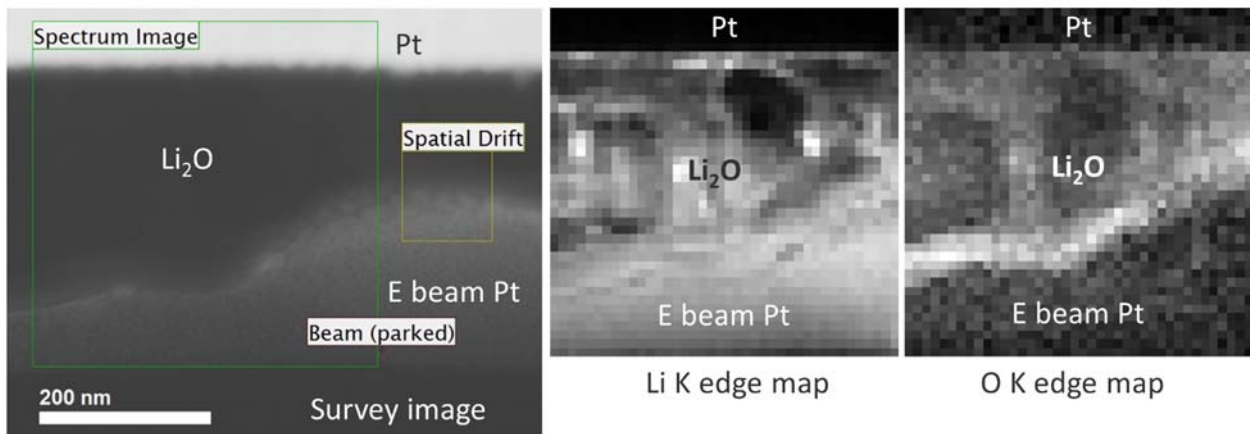


Figure 23. EELS spectrum images of Li₂O film deposited on Pt on c-Si showing the Li K edge and O K edge maps.

EELS O K edge maps, Si L maps, and C K maps of the Li_2SiO_3 sample showed high O and Si content in the Li_2SiO_3 film. However, the Li K edge was unable to be mapped, likely because the Li migrated into nearby Pt layers due to electron-beam exposure. Atomic percent ratio calculations for this sample, obtained via Gatan Digital Micrograph EELS Analysis Software, showed Li to range from 58–63 at.%, whereas Si ranged from 37–42 at.%. The deposited film thickness showed greater continuity in this sample. See Figure 24.

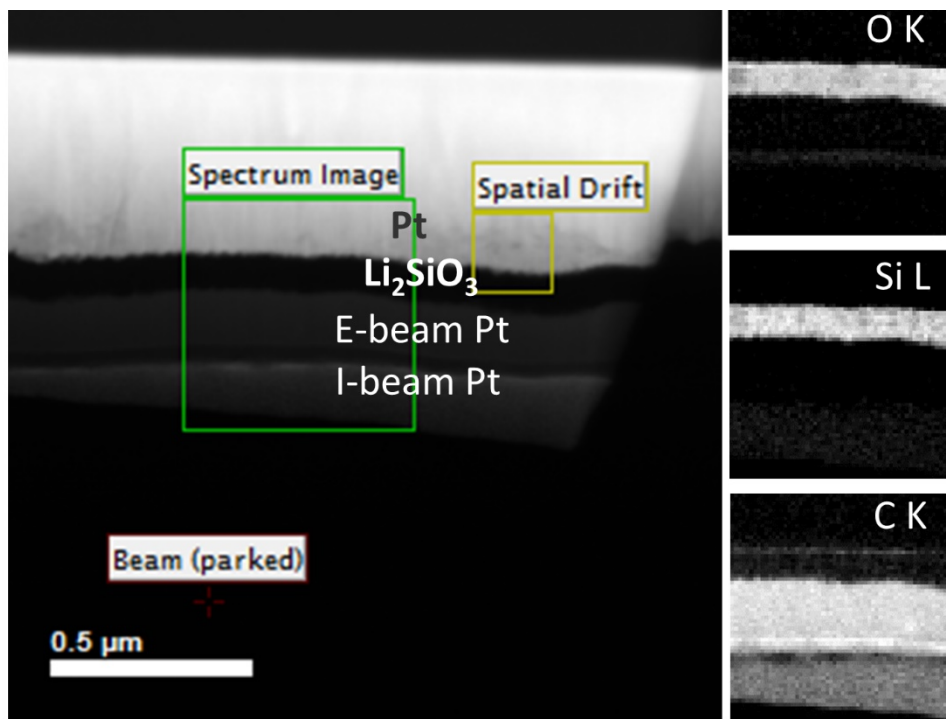


Figure 24. EELS spectrum images of Li_2SiO_3 film deposited on Pt on crystalline Si showing O K edge, Si L edge, and C K edge maps.

To measure nanoscale electronic resistivity of SEI, an experimental approach was developed using SSRM to characterize SEI formed on Si. Reference samples were designed and measured to validate the technique and better understand instrumental resolution. The approach was implemented on SEI and results were compared to STEM results. Electronic resistivity of SEI is highly dependent on formation conditions (electrolyte mixture, cycling parameters, and original Si surface). But, in general, it shows a layered structure with high electronic resistivity at the surface, decreasing toward the SEI/Si interface.

Reactivity of Si surfaces exposed to electrolyte was investigated with AFM and SSRM. AFM measurements showed island-like accumulations of possible decomposition products and salts on the surfaces of both native oxide on crystalline Si (c-Si) and thermally grown SiO_2 on c-Si. However, immersion of a 15-nm-thick, thermally grown SiO_2 film on c-Si for 2 days and 7 days showed no decomposition of the film when investigated with SSRM resistivity vs. depth profiling.

Early-stage SEI characterized with SPM showed distinct trends with respect to alterations to resting protocol, cutoff voltage limit, and total number of cycles. These trends showed that resting the cell after cycling decreased roughness, increased thickness, and formed a less-resistive SEI. Using a higher cutoff-voltage limit led to the formation of SEI with decreased roughness and thickness, and less electronic resistivity. Continued cycling served to decrease surface roughness, increase thickness, and increase SEI resistivity.

SEI formed on a thin film of SiO₂ on c-Si showed interesting electronic, structural, and chemical properties when compared to that formed on native oxide on c-Si. Electronic resistivity measured via SSRM resistivity vs. depth profiling showed that a thinner, more-resistive SEI formed on the SiO₂ model system. STEM characterization verified the thickness trend and also indicated a higher composition of C and O and lower levels of F in this SEI. High electronic resistivity may thus be a result of greater relative organic composition. Moreover, these results suggest that the initial SEI formation mechanism on SiO₂ depends on an intermediate Li_xSiO_y phase that forms during lithiation, because the SiO₂ film is no longer present after cycling. SEIs formed on these two model Si systems were also investigated with SSRM in their lithiated and delithiated states. Comparison showed lithiated SEI, after the first half cycle, is thinner and more resistive when compared to delithiated SEI after one full cycle.

Sputter-deposited films representative of proposed components of SEI on Si were characterized using AFM, SSRM, and STEM. Surface morphology, electronic resistivity, and mechanical hardness were measured for seven depositions using AFM and SSRM. Structure and chemical composition of several films were investigated with STEM to study the structure and elemental composition of the films.

STEM was used to characterize particulate materials for Si anodes. Elemental composition, particle size, and particle crystallinity were investigated. Additional samples were prepared to study the effects of exposure purely to glovebox environments, with no electrolyte or electrochemical cycling at all. In this case, the staff at Oak Ridge National Laboratory (ORNL) made thin-film Si (~200-nm) on Cu foil substrates and distributed samples from the same deposition run to each of the five partner national laboratories. Upon receipt by the different national laboratories, the thin-film samples were opened in gloveboxes and exposed for 5 days. After this 5-day period, the samples from each laboratory were sealed and shipped to NREL for surface analysis with XPS and TOF-SIMS. Each national laboratory partner also received the materials needed to make three Si-Li coin cell samples. These samples were electrochemically tested to establish correlations between the electrochemistry and surface chemistry.

After receiving samples from the various national laboratories, a control sample (sent directly to NREL from ORNL and not subjected to a 5-day glovebox exposure) was analyzed first, followed by each sample from the five partner laboratories. Normalized XPS surface spectra are shown in Figure 25 (note that intensities are normalized for clarity). From this dataset, it is clear that the only new chemical states present on the surface are associated with F, whereas the Si, O, and C chemical states change very little. However, significant differences are observed in the relative atomic concentrations of these species on the surface.

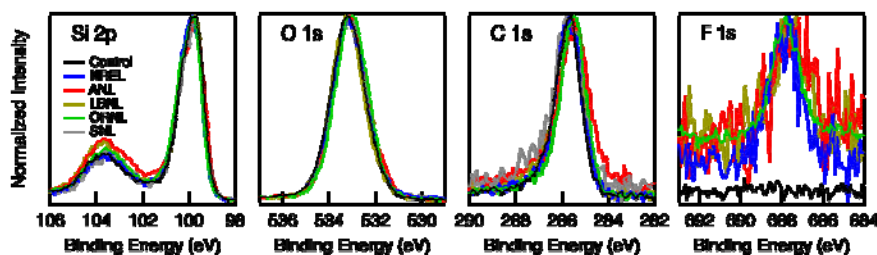


Figure 25. XPS data showing little to no variation in chemical states present on the surface of the Si thin-film samples.

The atomic concentrations for each aged Si thin film are shown in Table 4. These data show that storing a Si thin-film sample in any glovebox environment unsealed causes significant changes to the ratios of surface chemical states. Some boxes appear to introduce less surface contamination than others, whereas the relative amount of Si present at the surface always decreases with glovebox aging, while F, C, and O (O in every glovebox but one) increases. Consistent results were observed in the TOF-SIMS surface spectra. Perhaps even

more interestingly, storing a Si thin-film sample in air caused the surface C and F content to decrease dramatically.

Table 4. Elemental Surface Analysis after Aging Si Thin Films for Five Days in Different Gloveboxes across Different National Laboratories. Controlled Unaged and Air-Exposed Samples are Shown for Comparison.

	SNL	NREL	ORNL	ANL	LBNL	Control	Air Exposed
Si	54.0	53.4	51.3	50.9	45.2	56.5	51.7
C	19.2	20.9	20.5	13.5	22.6	17.2	12.6
O	26.5	24.6	26.1	34.9	31.4	25.9	35.7
F	0.1	1.2	2.2	0.7	0.8	0.0	0.0

TOF-SIMS and XPS analyses also reveal interesting changes in the aged materials' behavior with regard to apparent sputter rates. The sputter-depth scales for each technique were calibrated by correlating the sputter time to a sputter rate obtained from separate measurements on a smooth 100-nm-thick SiO₂ reference film on a Si wafer, because the films in this study were too rough for optical or stylus profilometry measurements. As seen in Figure 26a, all of the glovebox-aged Si thin-film samples sputtered more quickly than the control, giving the appearance that the films thinned with aging. This effect might be due to 1) a relative increase in sputter rate that results from changes in film chemistry induced by the different ambient glovebox environments that altered aggregate bond strength in the films; or 2) the expulsion of water vapor, causing these films to densify.¹ By comparison, data in Figure 26b show that it takes longer to sputter through the air-aged film than it does to sputter through the glovebox-aged samples or the unaged control. This interesting result might indicate that glovebox-aged films do in fact densify, because the partial pressure of water vapor will be much higher in air than in an Ar glovebox environment, thereby leading to a larger driving force for water expulsion during glovebox storage.

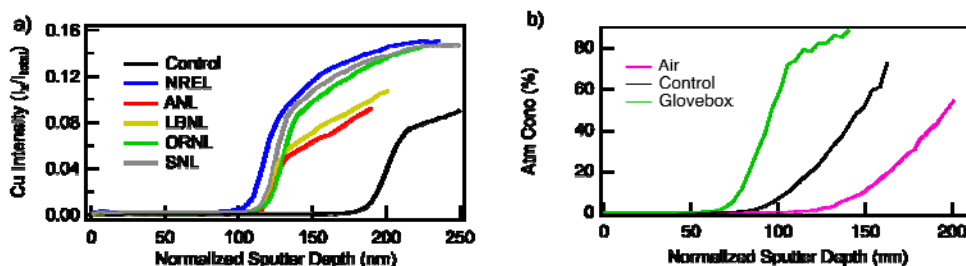


Figure 26. a) TOF-SIMS profile data showing the apparent change in sputter rate of Si thin-film samples that have been aged in different gloveboxes across the five national laboratories; b) XPS profile data showing the difference between glovebox, control, and air exposed.

XPS and TOF-SIMS measurements demonstrated that exposure of Si thin films to ambient glovebox environments can lead to significant changes in the surface chemistry and film properties. Unsurprisingly, results showed that different gloveboxes produced varying degrees of surface contamination, whereas the chemical states associated with observed contamination were nearly identical for each glovebox in the study. When comparing glovebox storage to samples stored in air, air-stored films had more O present at the surface, but significantly less C and F. Further analysis of these materials revealed that glovebox storage might lead to film densification, while air storage might cause the reverse effect. Preliminary analysis of electrochemical data shows a trend suggesting that different surface chemistries indeed affect electrochemical performance. There appears to be a link between the amount of C present on the surface of the sample and the amount of observed capacity obtained in the first half-cycle; higher C content tends to increase capacity.

Electrolyte Exposure Results (Harvey, Coyle, Han, Veith, Stetson, Zavadil)

Once the samples had been analyzed for composition and stability, the next step was exposure to electrolyte. Most of the laboratories involved in the study did some level of direct electrolyte exposure without electrochemical cycling, just to determine the chemical effects of exposure to unstable electrolyte on the silicates. The first set of these, a collaboration between ORNL and NREL, slightly modified the sample preparation from above to address where oxygen was coming from in the growth and modification of the SEI. In this particular case, the oxide was grown with isotopically pure ^{18}O , rather than standard oxygen. The oxygen contained in the electrolyte was not isotopically enhanced, so differences in the positions of ^{18}O vs. ^{16}O could give some indication as to where oxygen was coming from during the growth and modification of the film. Virtually all silicon electrode materials are terminated with an oxide coating. The thickness and composition of the oxide ($x = ?$ in SiO_x) in most materials is not known. Furthermore, identifying the true oxide is difficult due to the challenges in elucidating the silicon oxidation state and proton termination of the oxides. One of the unanswered questions regarding the interfacial chemistry of silicon is what is the role of this SiO_x surface termination layer on the SEI formation reaction, lifetime, and cyclability on the starting film. Modeling data from Perrson (see above) indicates that with lithiation, one should proceed through the formation of Li-Si-O phases before lithiating the metallic silicon. Thus far, there have been multiple sets of conflicting information regarding the influence of the SiO_2 and whether this SiO_2 reacts to form a lithium silicate on the Si surface. There is IR and NMR spectroscopy data that show the growth of Li-Si-O species. In contrast, X-ray absorption data shows the absence of Li-Si-O with cycling.

The goal of this work is to identify the presence or absence of Li-Si-O as well as its location within the electrode and its role in SEI formation. The reactions are predicted to occur at open-circuit voltage from the chemical reaction with Li-salt or during lithiation. To answer these questions, we are performed experiments using ^{18}O -terminated silicon electrodes. The benefit of this isotope labeling is that it will enable us to identify where the potential Li-Si-O is forming, and also, where the oxygen used to form the Li-Si-O materials comes from—specifically, oxygen from the termination of the silicon electrode or oxygen from the carbonate solvent used in the electrolyte.

Samples were fabricated using physical vapor deposition. Pre-sectioned silicon wafers were fabricated at Sandia National Laboratories and battery-grade copper foil was used to grow the electrodes for this study. Figure 27 shows a photo of the silicon-wafer-supported electrodes fabricated for this study and a cross-section schematic of the electrodes. The amorphous silicon was 50 nm thick whereas the oxide thickness varied depending on deposition time. These materials were distributed to Silicon Electrolyte Interface Stabilization (SEISta) team members for cycling and chemical characterization.

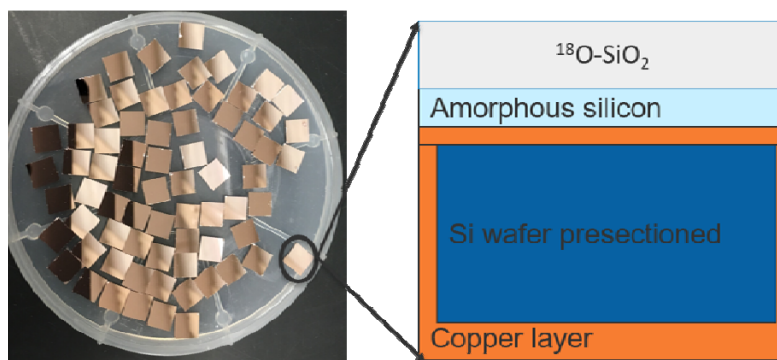


Figure 27. (left) Photo of the silicon-supported electrodes; (right) Schematic of the electrode cross section.

Figure 28 shows TOF-SIMS data collected for the as-prepared sample grown on a silicon wafer. The data show a 50-nm-thick silicon layer supported on a copper film. The surface oxide shows a large signal originating from the ^{18}O layer (black line). The apparent signal enhancement at the Cu/Si interface is likely due to matrix effects from the conductive copper underlayer.

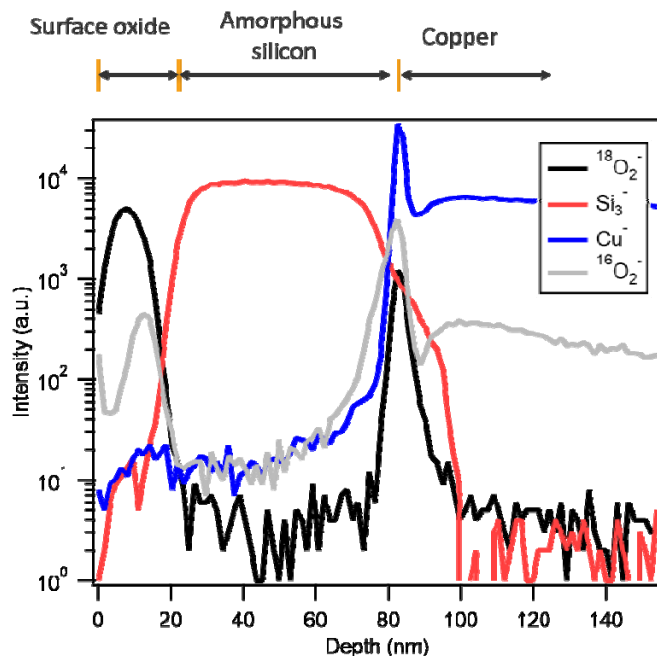


Figure 28. TOF-SIMS data collected on the as-prepared electrode.

The samples were exposed to the GEN2 electrolyte used in the SEISa program (1.2M LiPF_6 3:7 wt% ethylene carbonate/ethylmethyl carbonate) for 1, 3, and 19 hours. To match electrode reaction conditions, we used a “dry” electrolyte (3 ppm H_2O) and a “wet” electrolyte (500 ppm H_2O). Figure 29 shows TOF-SIMS data collected on samples aged for 3 hours in the wet and dry electrolytes. These data are shown in two plots for clarity. We observe several trends from these data. First, the electrode exposed to wet electrolyte slowly dissolves with time. This is observed by the smaller ^{18}O trace for the wet sample versus the dry sample, indicating the shrinking of the oxide coating.

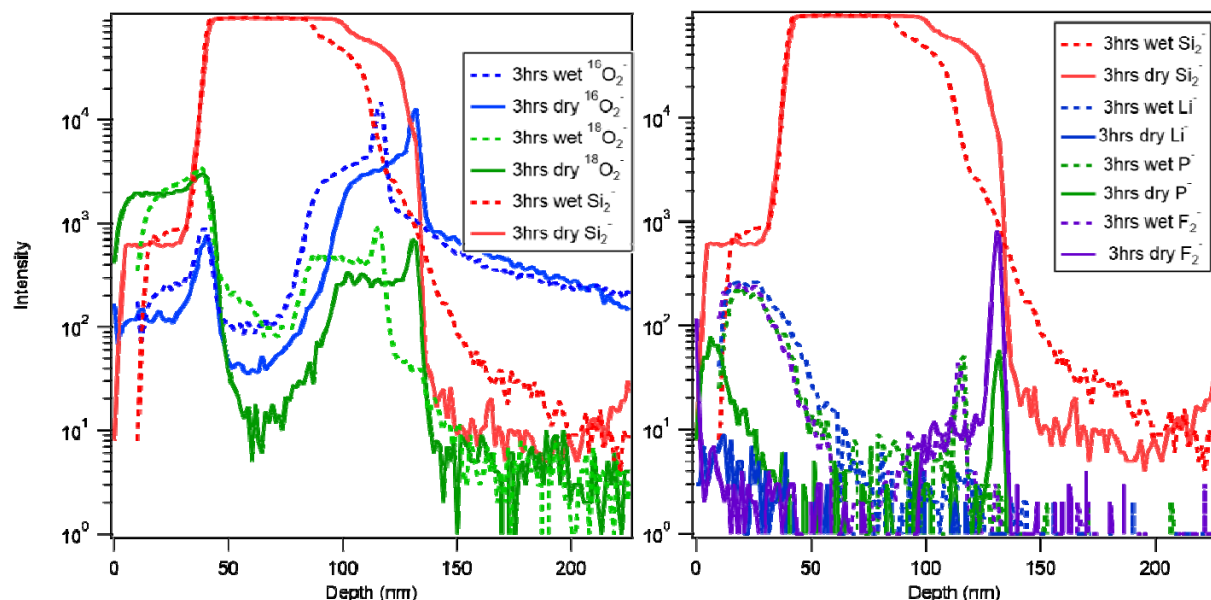


Figure 29. TOF-SIMS data collected for ^{18}O labeled electrodes aged for three hours in wet and dry electrolyte.

The second trend we observe is the clear evidence for Li incorporation within the Si^{18}O_2 layer. This incorporation of lithium matches the same incorporation with P and F from the electrolyte and C and ^{16}O from the carbonate solvent. Interestingly, under the dry conditions, we do not see Li incorporation within the Si^{18}O_2 layer. Furthermore, we observe an apparent concentration of P and F for the dry samples at the silicon/copper interface. Together, these data indicate that the water is promoting the salt decomposition and reaction at the interface. This does not indicate the formation of Li-Si-O's at open-circuit voltage, so this is not a major component of the initial SEI formation reaction.

Stability of Lithium Silicate – $\text{Li}_2\text{Si}_2\text{O}_5$

Films of $\text{Li}_2\text{Si}_2\text{O}_5$ were specifically synthesized on amorphous silicon by sputtering. In this study, the samples were subjected to an aging study using dry electrolyte and investigated using neutron reflectometry (NR). In neutron reflectometry, the specular reflection of neutrons from an interface is measured as a function of the wave vector transfer, $Q = 4\pi\sin(\theta)/\lambda$, perpendicular to the sample surface. The angle of incidence θ is between the incoming neutron beam and the sample surface, and λ is the wavelength of the neutron. Analyzing the neutron reflectivity gives us information about the thickness and composition of the film layers.

Figure 30 shows NR data collected for the as-prepared sample and sample soaked in electrolyte for 3 hours and 71 hours. The peaks in the NR data are called Kessing fringes and are due to constructive and destructive interference of the scattering pattern as a function of angle. The position is related to layer thickness whereas the amplitude is due to nuclear cross-section. In Figure A, the most-intense peak is highlighted. As one can see, the data are changing with time. Indeed, the position is shifting to lower Q values and the intensities are changing. This shift to lower Q values indicates a thickening of the oxide or a mixing of the surface and the underlying silicon layer. The structure is complex and difficult to fit due to the diffusion of Li within the structure or some other chemical changes to the layer chemistry.

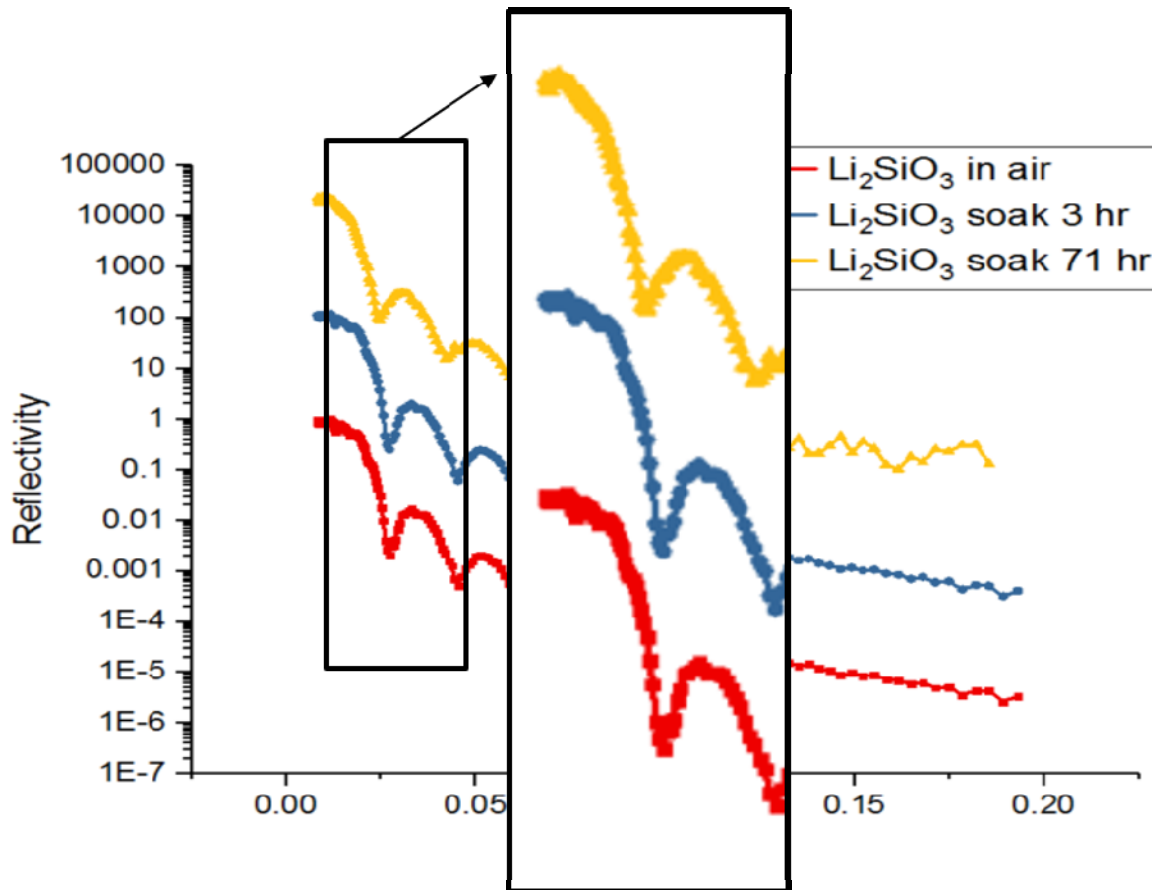


Figure 30. NR data collected for Li₂Si₂O₅/Si films as a function of time aging in electrolyte.

Amorphous silicate films ranging from 40 to 72 nm in thickness sputtered onto Si wafers were used as electrodes for this study. Imaging of the lithiation and alloying process was monitored using an electrochemical AFM (Bruker Dimension) to track morphology change. A cantilever sensitive to measuring surface deformation for materials with an elastic module of 1 to 100 MPa was used to both image and capture the mechanical response of the silicate film. A typical cyclic voltammogram (scan rate = 100 μ V/s) generated for the first several cycles into the onset of Li-Si substrate alloy formation is shown in Figure 31. Minimal reductive current is generated until the silicate film is polarized to \sim 100 mV, at which point the current increases in magnitude, which signals the onset of alloy formation. The return potential sweep exhibits anodic current due to de-alloying. Subsequent potential cycles demonstrate a lower potential onset for alloy formation, indicating that the initial barrier to Li⁺ transport and alloy nucleation imposed by the silicate is significantly reduced. Details of the extent to which this process occurs can be learned by conducting *operando* imaging while conducting electrochemistry coupled with subsequent *ex-situ* analysis of the morphology, structure, and composition of the cycled silicate film.

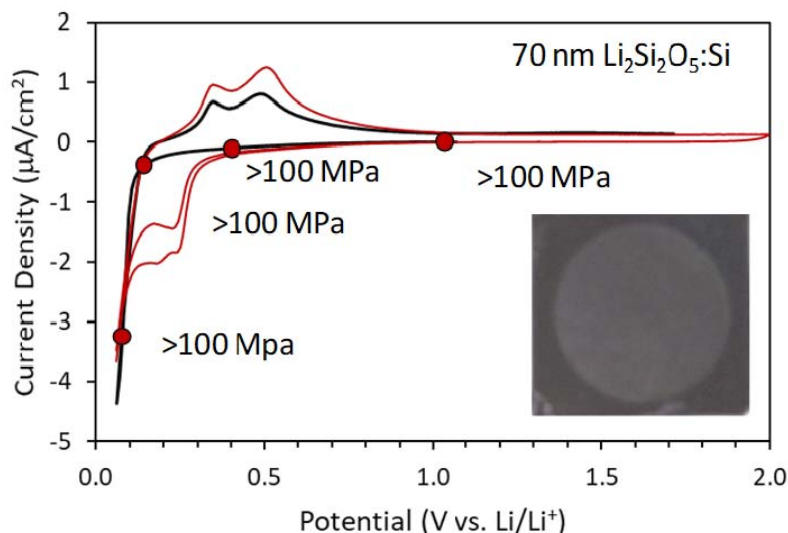


Figure 31. Cyclic voltammetric response of 70-nm-thick amorphous $\text{Li}_2\text{Si}_2\text{O}_5$ films on a Si wafer in 1 M LiPF_6 1:1 EC:DMC at scan rate of 0.1 mV/s. Markers indicate the potential-dependent elastic modulus measured with an electrochemical AFM. The inset shows the change in optical properties with Li-Si substrate alloying.

Operando AFM imaging was used to track morphological and mechanical property changes with silicate lithiation and Si substrate alloying. AFM images were acquired for the $\text{Li}_2\text{Si}_2\text{O}_5$ film by sweeping to and holding the potential at select values based on the typical voltammetric response (labeled markers in Figure 31). Minimal change in morphology is observed for this film up to the alloying threshold, and the elastic modulus of the silicate remains greater than 100 MPa, above the upper sensitivity limit of the AFM cantilever. With sufficient alloying at 90 mV (increased time of potential hold), the nodular morphology of the $\text{Li}_2\text{Si}_2\text{O}_5$ is preserved, but the elastic modulus of the silicate:LiSi bilayer decreases to 20 MPa, signaling “softening” or an increased mechanical compliance. Similar softening transitions are observed for the higher-Li-content amorphous silicates, including Li_2SiO_3 and Li_3SiO_x . AFM imaging shows that the basic morphology of the film is largely unchanged, shown in Figure 32.

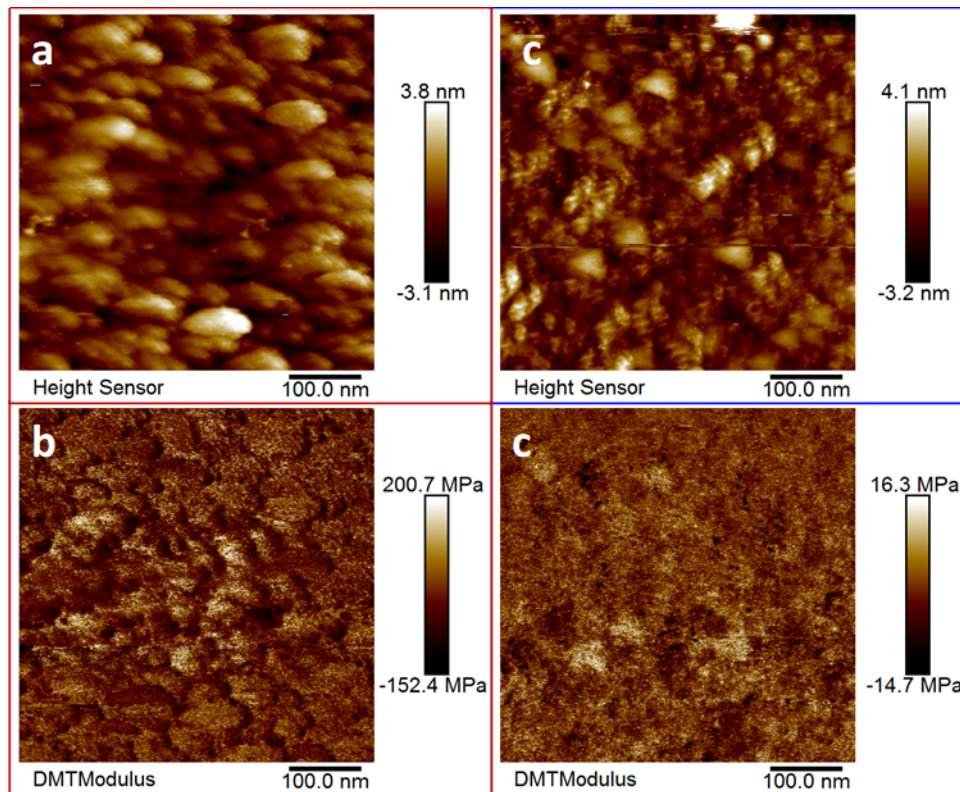


Figure 32. *Operando* AFM images on 70-nm-thick $\text{Li}_2\text{Si}_2\text{O}_5\text{:Si}$ electrodes undergoing lithiation and substrate alloying. Topography and effective elastic modulus a,b) prior to the Li-Si alloy threshold and c,d) after alloying at 50 mC/cm², 90 mV (vs. Li^{0/+}).

The extracted, rinsed, and dried electrode was transferred under argon to a scanning electron microscope (SEM) to confirm that the silicate film remained intact on the wafer surface. Figure 33 shows the original area imaged during the AFM experiment. This location was readily identified by a unique pattern of film disruption to either side of the AFM cantilever but projected outward at a distance of 15 μm . In the *operando* imaging, we demonstrated that displacement of the tip and scanning reproducibly recreated this pattern numerous times. SEM imaging showed that the silicate film morphology is unchanged with respect to the original (as-deposited) silicate, arguing that the silicate film does indeed remain intact during early-stage alloying of the underlying substrate. We interpret the decrease in modulus to detection of the more-compliant Li-Si alloy forming below the silicate. As depicted in Figure 33, we hypothesize that the relatively rigid silicate film vibrates on top of the compliant alloy, yielding an effective decrease in elastic modulus of the silicate:LiSi bilayer. The observed mechanical disruption displaced from the tip likely corresponds to a node at which stress is concentrated, resulting in local fracture of the silicate. Such fracture could be correlated with the thickness of the silicate film because we have not observed this phenomenon on thinner 40-nm-thick films. We also argue that the flat nature of these films contributes to their stability. Silicate films on particles, a more representative geometry for a practical Si anode, will experience curvature and stress concentration, likely yielding film fracture.

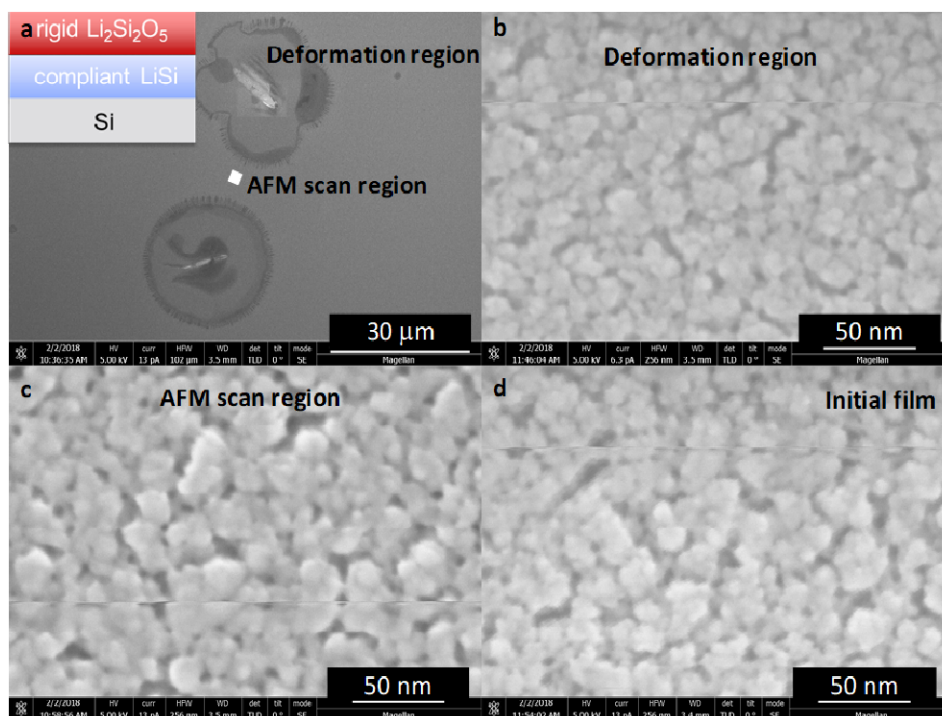


Figure 33. Scanning electron micrographs of a $\text{Li}_2\text{Si}_2\text{O}_5:\text{Si}$ electrode alloyed to $50 \text{ mC}/\text{cm}^2$ at 90 mV (vs. $\text{Li}^0/+$). a) Silicate film disruption (localized cracking and delamination) is induced by low-force AFM scanning but at a considerable distance from the imaging area. b–d) The morphology of the silicate is unchanged with electrochemical lithiation, early-stage alloying of the underlying Si, and low-force (nN) imaging.

The fate of the silicate film under lithiation and substrate alloying conditions can also be tracked through compositional profiling of the electrode after removal from the electrochemical environment. TOF-SIMS depth profiles are shown in Figure 34 that highlight the silicate film indicated by SiO^+ (shown) and $\text{LiSiO}^+/\text{LiO}^+$ (not shown for simplicity) ion yield, the silicate/Si interface where ion milling produces Li accumulation as indicated by LiSi^+ yield, and the bulk Si wafer with Si^+ yield apparent at the greatest depths. SIMS provides a clear signature for alloying of the substrate as the Si interface systematically shifts to greater relative depth with increased extent of alloying: from 5 nm at $6 \text{ mC}/\text{cm}^2$ (Figure 34c) to 20 nm at $50 \text{ mC}/\text{cm}^2$ (Figure 34a). Electrodes left in the alloyed state exhibit enhanced, depth-distributed LiSi^+ ion yield (Figure 34a) as the direct measure of the alloy, whereas de-alloyed electrodes (Figure 34c) yield a modest enhancement in LiSi^+ yield. We find minor variation in ion yield for the LiSiO^+ and LiO^+ families of ions with depth, arguing minimum modification of the basic composition and structure of the silicate film and emphasizing the stability of these films when used in this flat form factor. The silicate film appears resilient to repeated cycling (14 cycles) into the early stage of alloying over time (70 h), exhibiting minor compositional change (Figure 34b,c).

Measurable but small amounts of fluoride incorporation in the silicate are observed beyond the near surface and silicate/Si interface residual levels observed for the as-deposited silicate, signaling a degree of chemical reaction between silicate and electrolyte. The extent of interaction appears to increase with extent of alloying as opposed to contact time with electrolyte. Minimal compositional change is also observed for the higher-Li-content Li_2SiO_3 and Li_3SiO_x silicates with early-stage alloying, consistent with the observed short-term structural stability of these films.

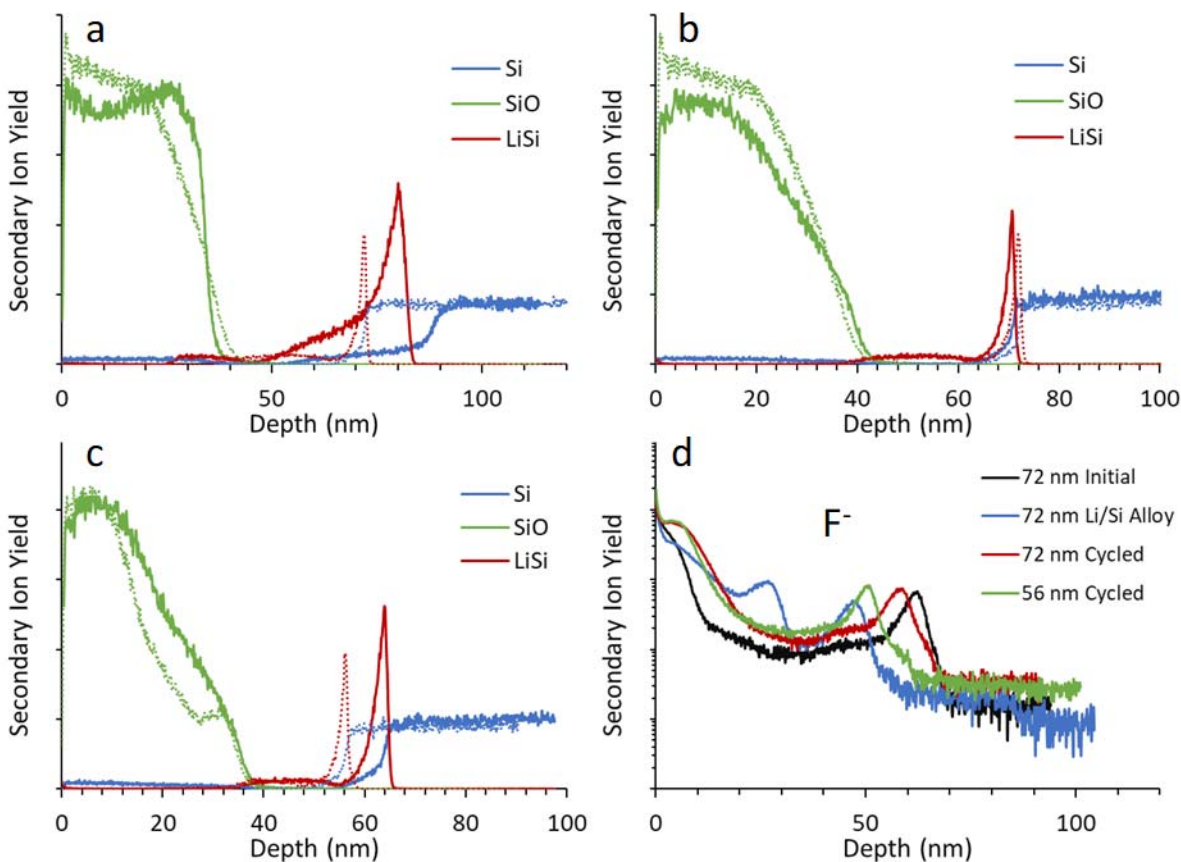


Figure 34. TOF-SIMS depth profiles (25-keV Bi⁺ for analysis, 1-keV Xe⁺ for milling) of Li₂Si₂O₅:Si electrodes at various stages of LiSi alloying. a) 72-nm-thick silicate alloyed to 50 mC/cm² at 90 mV (vs. Li^{0/+}) left in the alloyed state. b) 72-nm-thick silicate alloyed to 8 mC/cm², de-alloyed, repeatedly potentiodynamically cycled to 7 mC/cm² at 0.1 mV/s, and left in the de-alloyed state. c) 72-nm-thick silicate alloyed to 8 mC/cm², de-alloyed, repeatedly potentiodynamically cycled to 12 mC/cm² at 0.1 mV/s, and left in the de-alloyed state. d) Comparison of F⁻ ion yield for each of the electrodes. Dashed traces correspond to as-deposited silicate controls.

Cycling Results (Coyle, Han, Stetson, Teeter, Veith, Zavadil, Xu)

No previous studies have conducted electrochemical analysis on the impact of lithium silicates at the surface of the silicon anode. To magnify the electrochemical effects of lithiated silicates at the silicon anode surface, this study uses model lithium silicate thin films deposited onto thin-film silicon anodes. Much of this analysis focuses on the discharge of the half cells, or lithiation of the silicon anode, particularly the first lithiation. This is because this work is an attempt to understand how the lithiation of the native oxide, which theoretically occurs during the first lithiation, affects the silicon anode performance. Analysis of more-extended cycling based on the native oxide lithiation is touched on here, but in-depth analysis of the stability of lithium silicates with cycling or their effect on the overall stability of the silicon anode was beyond the scope of this work. The synthesis and composition verification of the 40-nm-thick SiO₂, Li₂Si₂O₅, Li₂SiO₃, and Li₃SiO_x thin films for this study will be published in the near future. As a reminder, these films were deposited on degenerately doped silicon (p⁺, boron, 0.004 to 0.04 Ωcm) substrates with 500-nm gold sputtered on their backside, as well as 20-nm Ti deposited on the front side as an adhesion layer for 500-nm copper coated with 40-nm evaporated amorphous silicon. Silicate-coated silicon thin films were assembled in coin cells in half-cell configuration

using a Celgard 2325 separator and 1.2M LiPF₆ EC:EMC 3:7 wt% electrolyte in an argon-filled glovebox. Galvanostatic cycling was completed with a constant current of 0.5 μA to provide a C/100 cycle rate. A voltage window of 0.26 V to 1.5 vs Li/Li⁺ was chosen to prevent additional reactions from volume expansion of silicon and to avoid undesirable side reactions with the c-Si substrate. Half cells with each composition of model thin film were in triplicate to provide assurance against any outliers in the results. For cyclic voltammetry, coin cells in half-cell configuration were swept from 1.5 V to 0.08 V vs Li⁺/Li at a 0.01 mV/s scan rate, or at an approximately C/50 cycle rate.

The high cut-off voltage of 0.26 V for the galvanostatically cycled cells was applied to ease the degradation from volume expansion and contraction, but it also served another purpose. Half cells that we attempted to lithiate below 0.26 V at a constant current at a C/100 rate experienced a voltage hold phenomenon, as seen in Figure 35.

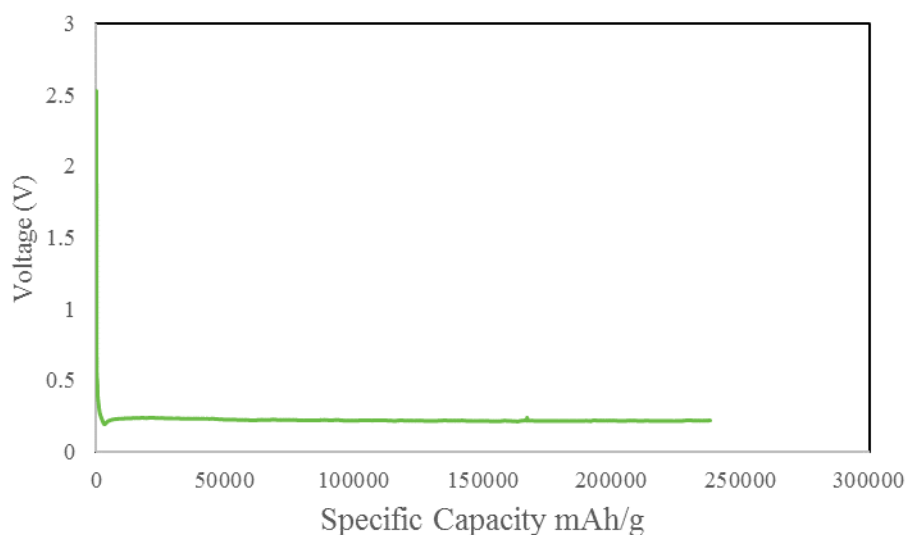


Figure 35. Uncoated amorphous silicon galvanostatically cycled with 0.05 V cutoff voltage at C/100 rate.

Once the cells with or without any of the four silicate coatings reached ~0.21 V, a side reaction occurred resulting in the potential holding at ~0.21V for up to weeks at a time. This reaction could be due to unintentional lithiation of the underlying c-Si substrate, unintentional lithiation of the Au layer on the backside of the substrates, or an unknown SEI formation reaction. This reaction is not observed in CV, possibly due to the nature of the cycling (controlling current in cycling vs controlling voltage in CV) or due to the cycle rate. Given the observed behavior, the issue of continuous discharging was mitigated by limiting the voltage window before the voltage hold begins. Further study outside the scope of this work is necessary to verify the cause of this voltage hold for these substrates.

Cyclic voltammetry plots for the first cycle of thin-film silicon anodes with SiO₂, Li₂Si₂O₅, Li₂SiO₃, and Li₃SiO_x thin-film coatings are presented in Figure 36.

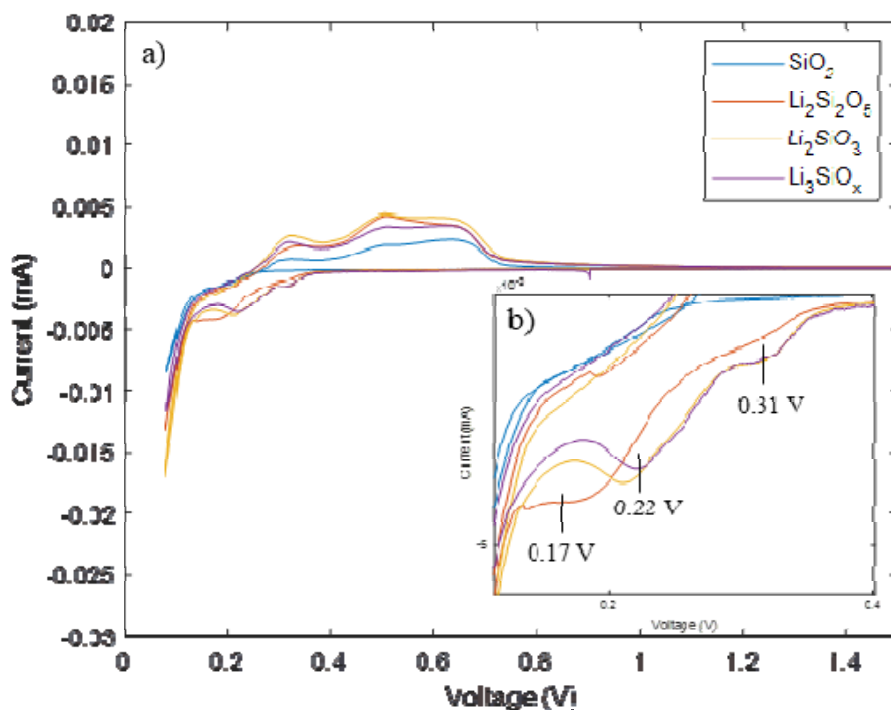


Figure 36. a) First-cycle CV for silicon anodes with silicate coatings and b) discharge profiles.

Figure 36b is a closer look at the discharge, or reduction, peaks for the first lithiation for each composition. The silicon anode with SiO₂ thin film does not show significant reduction current until about 0.23 V, whereas the lithiated silicate-coated silicon anodes show the onset of reduction current occurring around 0.4 V, with peaks associated with lithiation occurring at voltages as high as 0.31 V. This is evidence that the lithiated silicates provide a lower barrier to lithium-ion insertion than the unlithiated SiO₂, which makes sense considering their ionic conductivities. There is a sharp difference in the lithiation/delithiation mechanism of SiO₂ in comparison to the lithiated silicates. However, there is a less significant difference in the electrochemical performance as the lithium increases in the lithium silicate coatings. All anodes with the three different lithium silicate coatings exhibited step-wise lithium insertion into amorphous silicon, with reduction peaks or shoulders at around 0.31, 0.22, and 0.1 V, forming amorphous Li_xSi.¹⁹ The silicon anode with an SiO₂ coating has only a small shoulder starting at ~0.23V with a sharp lithiation peak at ~0.1 V. This may be due to the higher impedance of the SiO₂ film at the surface compared to the Li_xSiO_y requiring lower potentials to overcome this transport barrier.

A closer look at the step-wise insertion peaks for lithium-silicate-coated anodes in Figure 36b shows some subtle trends with increasing lithium content. The lowest-lithium-content film, Li₂Si₂O₅, has only a small shoulder at ~0.31V and a wave-type peak centered at ~0.17 V. Wave-like peaks show that a reaction that is causing the current to form a wave-like peak is not diffusion-controlled; additional overpotential does not increase the current because it is limited by the kinetics at the surface and current is not lost because there is no shortage of reactants. This shows that whereas Li₂Si₂O₅ provides a lower barrier to lithiation than SiO₂, it is not as low a barrier as the two higher-lithium-content silicates. These higher-lithium-content coatings, Li₂SiO₃ and Li₃SiO_x, show more complete lithiation reactions at 0.31 V and 0.22 V because they have a more-distinct shoulder and sharper peak at each respective potential. The difference between Li₂SiO₃ and Li₃SiO_x-coated silicon anodes is minimal. The silicon anode with a Li₂SiO₃ coating has a slightly larger peak at 0.22V than the

Li_3SiO_x -coated silicon anode. This may indicate that the impedance presented by a Li_2SiO_3 coating is very similar to the impedance presented by a Li_3SiO_x coating. The delithiation, or oxidation, part of the first cycle from each silicate coating shows similar peaks for all compositions. Each silicate coating has broad delithiation peaks at 0.33 V, 0.5 V, and 0.68 V, which indicate lithium extraction from amorphous Li_xSi .²⁰ The differences in heights of these peaks correlate to the extent of lithiation of the silicon anodes during the discharge part of the cycle. That is why the SiO_2 coating has the lowest-intensity oxidation peaks. However, the delithiation peaks for the lithiated silicates increase in order from Li_3SiO_x to $\text{Li}_2\text{Si}_2\text{O}_5$ to Li_2SiO_3 , which is not the same order as the depth of the lithiation peaks, as expected. This shows that the delithiation of the silicon anode following the first round of SEI formation is less dependent on the initial lithium content of the film than the first lithiation.

CV samples are controlled to spend a specific amount of time scanning across voltages and are reported with respect to current generated at each voltage. Because of this, CV plots only observe electrochemical reactions that produce current through the silicon anode. Chemical or thermodynamic reactions, such as electrolyte degradation or SEI formation—which consume electrons or lithium ions but do not produce measurable current—are not documented by the CV technique. Constant-current (CC) samples have a controlled current applied to them and are free to hold at any voltage in the cut-off voltage window for the time that is required to complete the reactions that occur at said voltage. The raw data for CC samples is reported with regard to time (hours), then converted to capacity (mAh/g) using the mass of the anode and current applied. CC plots depend on the capacity, or time, consumed by any reaction (electrochemical, thermal or chemical) at a certain voltage instead of just the current produced by electrochemical reactions. So, they present a more comprehensive picture of what is occurring at the silicon anode during charge or discharge. When comparing CV and CC plots, it is important to remember that the CV curves represent only electrochemical reactions (typically just lithium-silicon alloying) whereas the CC curves describe both silicon-lithium alloying and chemical SEI formation reactions.

In Figure 37, the first lithiation of a set of SiO_2 , $\text{Li}_2\text{Si}_2\text{O}_5$, Li_2SiO_3 , and Li_3SiO_x coatings on silicon cycled at a constant current at a $C/100$ cycle rate are plotted. This graph shows a similar pattern as Figure 36 regarding the effect of the lithiation resistance of each silicate with a key additional piece of information.

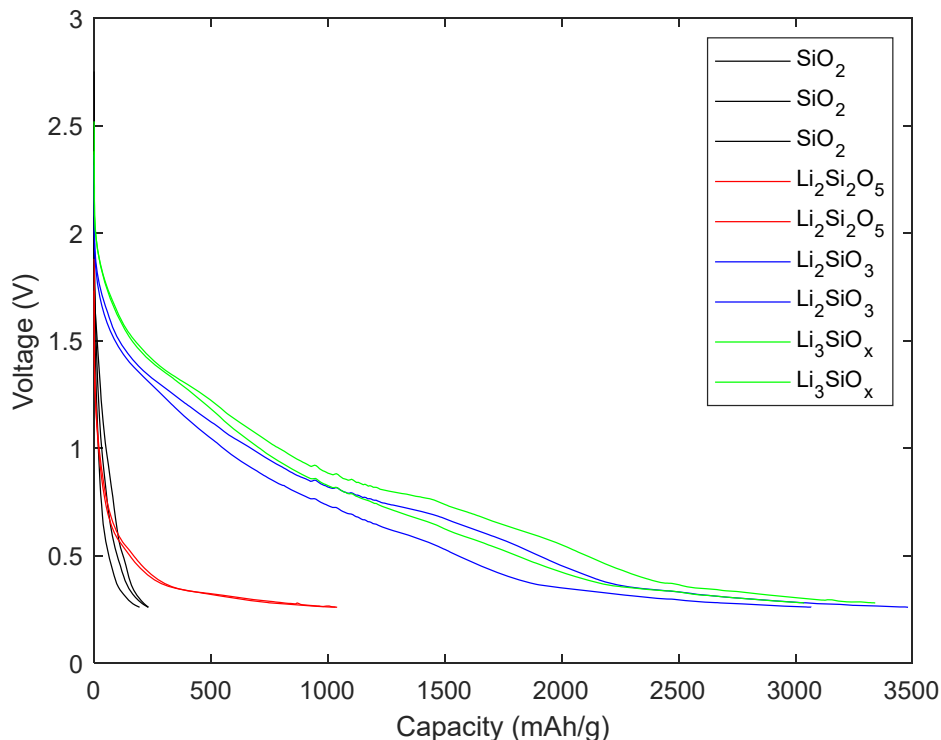


Figure 37. First lithiation of silicate-coated silicon anodes at C/100 with replicates for each coating composition.

As in the CV lithiation reduction peaks, the plateaus that indicate lithiation in this graph occur at a lower potential for SiO_2 (in black) than for the lithiated silicates. Similarly, the $\text{Li}_2\text{Si}_2\text{O}_5$ curves (in red) have a slightly lower plateau than the higher-lithium silicates (high capacity blue and green curves). The three SiO_2 curves on the left side of Figure 37 do not actually show a significant lithiation plateau because the voltage cutoff of 0.26 V is above 0.23 V, where silicon coated with SiO_2 starts to lithiate according to the CV plots in Figure 36. The key additional piece of information gained from the cycling data even with the low cutoff voltage is the evidence of a large amount of capacity loss for the higher-lithium-content lithium silicates. According to the area under the CV curve in Figure 36, which indicates the electrochemical capacity of the first discharge, the capacity from lithium-silicon alloying for a Li_3SiO_x -coated silicon anode during the first lithiation is only ~ 500 mAh/g. When examining the capacity from both current-producing lithium-silicon alloying and SEI formation as in Figure 37, the overall capacity for the first lithiation cycle for Li_3SiO_x -coated silicon anode is $\sim 3,000$ mAh/g. This shows that a great deal of the capacity shown for the Li_3SiO_x -coated silicon anodes in Figure 37 comes from electrolyte degradation and formation of the SEI. This large capacity loss from SEI formation is evident for both Li_3SiO_x and Li_2SiO_3 -coated silicon anodes. The higher-order silicate coatings result in a more-reactive surface that consumes more electrolyte to create more SEI than the lower-order silicates.

Continued Cycling Analysis

Further cycling for CV samples is summarized in Figure 38—with Figure 38a showing the second cycle, Figure 38b showing the seventh cycle, and Figure 38c showing the fourteenth cycle for each composition of silicate coating.

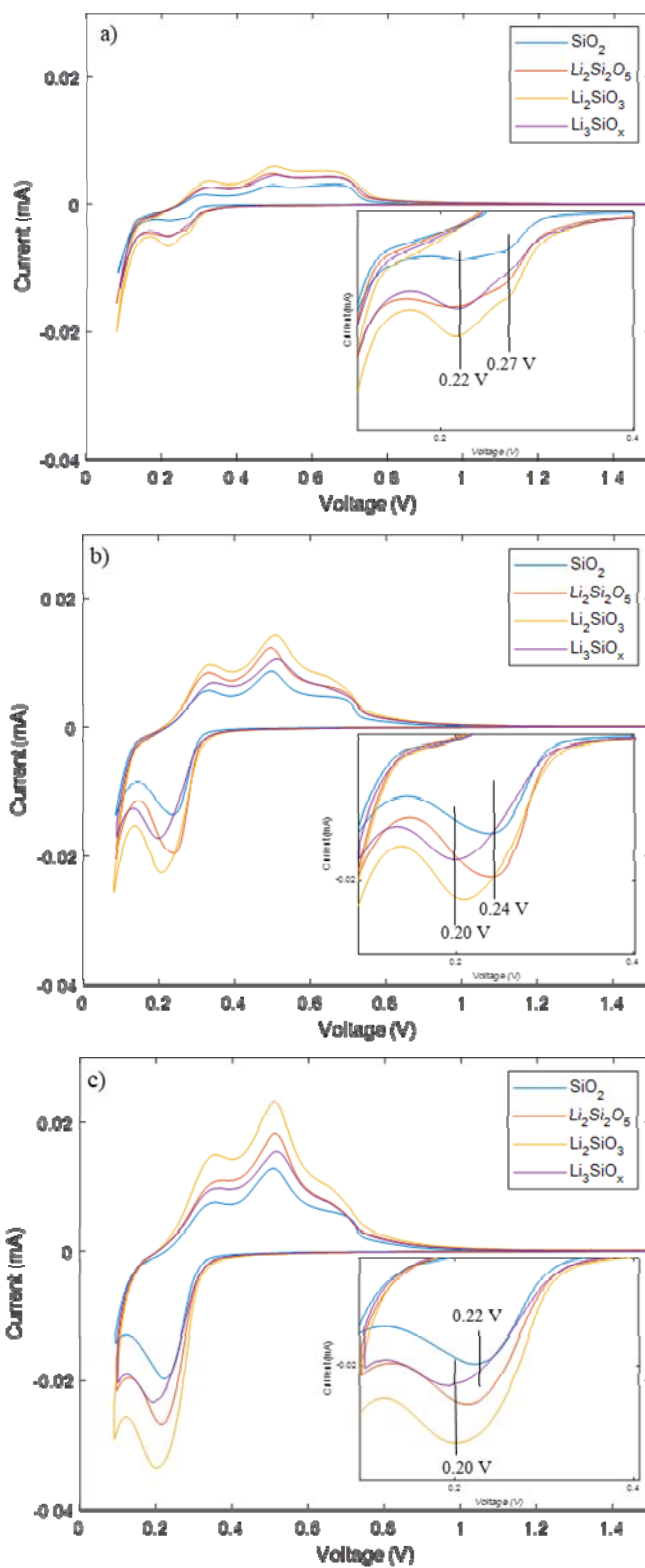


Figure 38. CV plots for the a) second, b) seventh, and c) fourteenth cycle for each silicate coating cycling at a C/50 cycle rate.

The scale of the y-axis, or current, for each set of CVs is kept constant to illustrate that the area under the CV curve is increasing for each composition with continued cycling from Figure 38a to Figure 38c. This increase indicates increased silicon alloying with more cycling. From the insets of each graph in Figure 38, it is also clear that the peaks for amorphous-silicon lithiation shift to lower potentials with continued cycling. The peaks shift from between 0.31 V and 0.22 V in the first cycle, to between 0.27 V and 0.22 V in the second cycle, to between 0.24 V and 0.20 V for the seventh cycle, and finally, between 0.22 V and 0.20 V for the fourteenth cycle. This shift to lower lithiation potentials is a sign of silicon anode and electrolyte degradation. Volume expansion from the silicon anode leads to electrical disconnection of sections of the silicon, and the SEI that forms may have a higher barrier to lithium-ion diffusion than the initial silicates, resulting in a higher overpotential upon subsequent cycling. Both of these processes lead to less active silicon material, which means that the remaining active silicon material must lithiate to higher lithium-to-silicon ratios to retain the same storage capacity. These lithium-rich alloys are formed at lower potentials, as seen in the potential shifts in Figure 38.²¹

Figure 39 is the capacity per cycle calculated from the area under the CV curves in Figure 38c and Figure 39 for a full CV scan, or with a 0.08 V cutoff voltage. Figure 40 is the capacity per cycle calculated from the area under the CV curves with a 0.26 V cutoff voltage for comparison with cycled cells cut off at the same voltage.

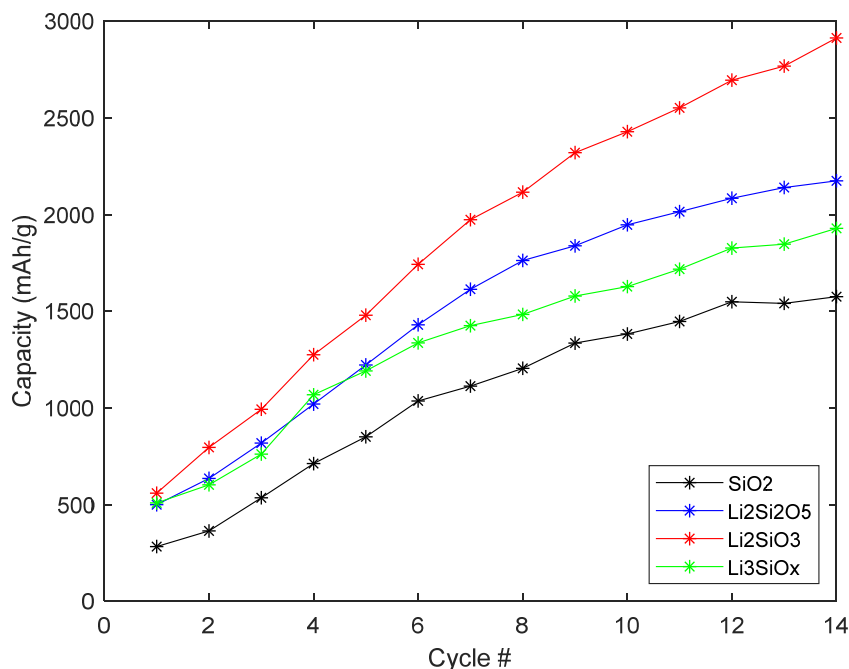


Figure 39. Discharge capacity per cycle calculated using area under CV curve with 0.08 V cutoff voltage.

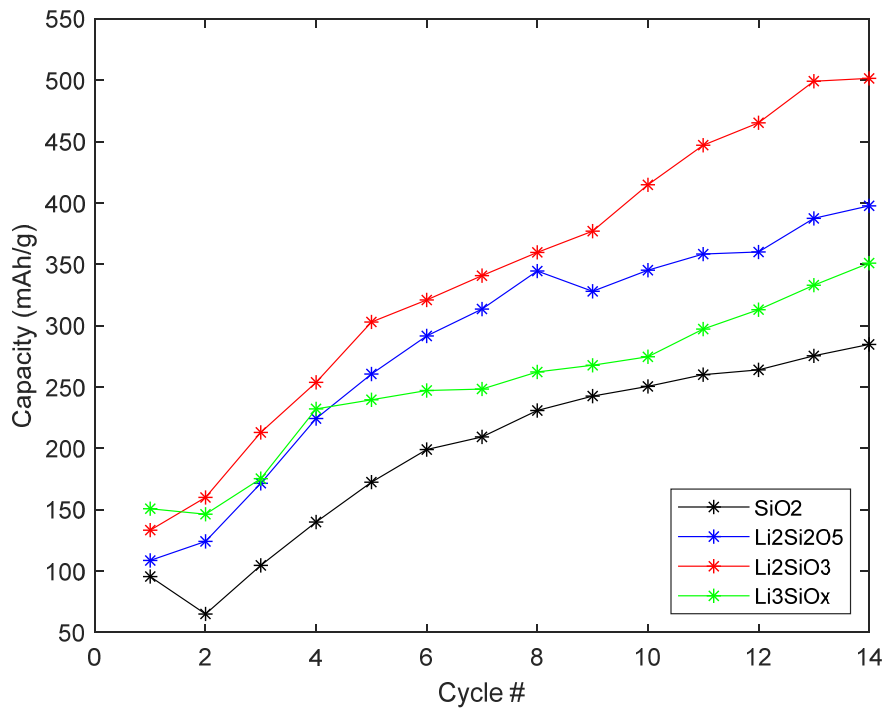


Figure 40. Discharge capacity per cycle calculated using area under CV curve with 0.26 V cutoff voltage.

Figure 39 and Figure 40 both show an increase in capacity with cycling for all compositions of silicate coatings. Figure 40 illustrates that capacities per cycle with the higher cutoff voltage of 0.26 V have lower values than the capacities with a full CV scan to 0.08 V. This is because the high cutoff voltage at 0.26 V cuts off some of the main lithiation peaks observed in CV scans for all four compositions of silicate coatings.

Figure 41 is the discharge capacity per cycle for constant-current cycling data with a 0.26 V cutoff voltage. Figure 40 and Figure 41 can be used to examine the differences in capacity from lithium-silicon alloying to capacity loss from SEI formation.

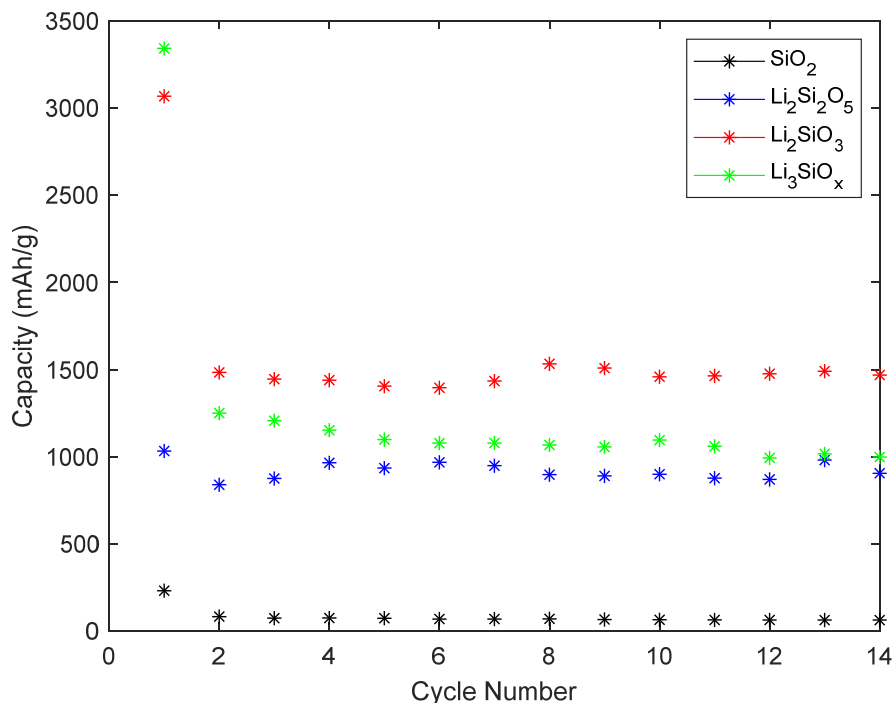


Figure 41. Discharge capacity per cycle for cycling data with a 0.26V cutoff voltage

There is a very clear difference in the capacity trends for CC and CV cycling. The CV capacity for each silicate coating, representing current from lithium-silicon alloying, increases with cycling. The capacity from CC cycling for each silicate coating, which includes SEI formation, is higher on the first cycle, drops 20%–60% from the first to second cycle (depending on the composition), and then remains relatively stable up to fourteen cycles compared to the initial capacity loss.

Figure 42 describes the change in capacity with cycling from the first to second and second to fourteenth cycle for each silicate coating composition for the C/100 CC cells as well as the C/50 CV cells.

From Figure 40, Figure 41, and Figure 42, it appears that although the capacity from lithium-silicon alloying increases with cycling, the overall capacity (including SEI formation) does not increase or decrease as dramatically. If the SEI continued to cause as great a capacity loss as in the first to second cycle, the capacities in Figure 41 would trend upward, along with the increasing capacity in Figure 40. This is evidence that with continued cycling, the SEI causes less capacity loss. There are also some trends for capacity loss per cycle that depend on the initial lithium content of the silicate coatings.

As demonstrated by the solid blue columns in Figure 42, the discharge capacity loss from the first to second cycle for cells with Li_xSiO_y coatings cycled at CC with a 0.26 V cutoff voltage increase with lithium content from 20% for an $\text{Li}_2\text{Si}_2\text{O}_5$ -coated silicon anode to 63% for an Li_3SiO_x -coated silicon anode. A SiO_2 -coated anode has a capacity loss of 63%, just like a Li_3SiO_x -coated silicon anode. These same trends are not observed in the capacity change from the first to second cycle for the CV cells, represented by the blue-hatched columns in Figure 42. This suggests that the trend of increasing capacity loss with increasing lithium content in the silicate coatings and the high capacity loss of SiO_2 are mostly due to their SEI formation mechanism during the first lithiation process.

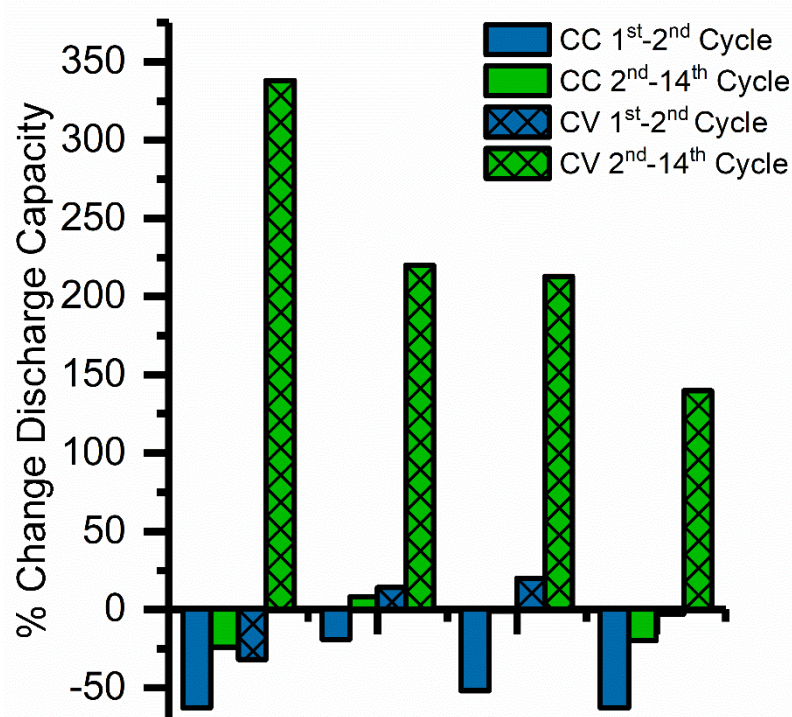


Figure 42. Discharge capacity change from the first to second and second to fourteenth cycle for cyclic voltammetry and constant current samples.

A more extensive study on identical samples was done by the NREL group, using both cycling and EIS. XPS was collected for two films with different Li/Si ratios. In Figure 43, depth profiles are shown for Li 1s, Si 2p and O 1s core-level spectra, for both lithium-rich and silicon-rich regions of the thin film. From the XPS depth profile, significant oxidation was observed at the surface, even though the samples were protected from ambient atmosphere during the transfer from the deposition to the characterization instrument. Compositions obtained via peak fitting these spectra are listed in Table 5. As can be seen from the XPS fitting results in Table 5, for both lithium-rich and silicon-rich side of the film, lithium silicate and lithium silicide are the main components in the film, with some contribution from SiO₂. The average compositions for lithium-rich area and silicon-rich area are Li_{4.88}Si_{2.85}O_{2.52} and Li_{1.58}Si_{1.31}O_{1.95}, respectively. Hence, the thin film is subsequently referred to as a Li_xSiO_y composite film. We note that the lithium-rich area has more lithium and more O compared to the silicon-rich area. Higher oxygen content in the lithium-rich area results from the higher affinity of lithium to oxygen.

Electrochemical Impedance and Cycling

Chemical reactivity of Li_xSiO_y was studied indirectly by EIS. A 50-nm-thick sample was assembled into a coin cell and investigated by impedance spectroscopy and by galvanostatic charge and discharge measurements (Figure 44). Capacity is not normalized in this work because all the films have the same thickness and area. As shown in Figure 44a, a low amount of lithium could be extracted from the film even up to 1.5 V during the first charge cycle. This high open-circuit voltage is due to the lower electrochemical potential of lithium in Li_xSiO_y, which has part of the lithium bonded with oxygen. To investigate the reaction of the Li_xSiO_y composite film with electrolyte, it was measured by AC impedance at the open-circuit voltage, as shown in Figure 44b. When the Li_xSiO_y composite film comes into contact with electrolyte, the charge transfer resistance increases with time. In contrast, for the silicon electrode, the impedance is not time dependent at open-circuit voltage.

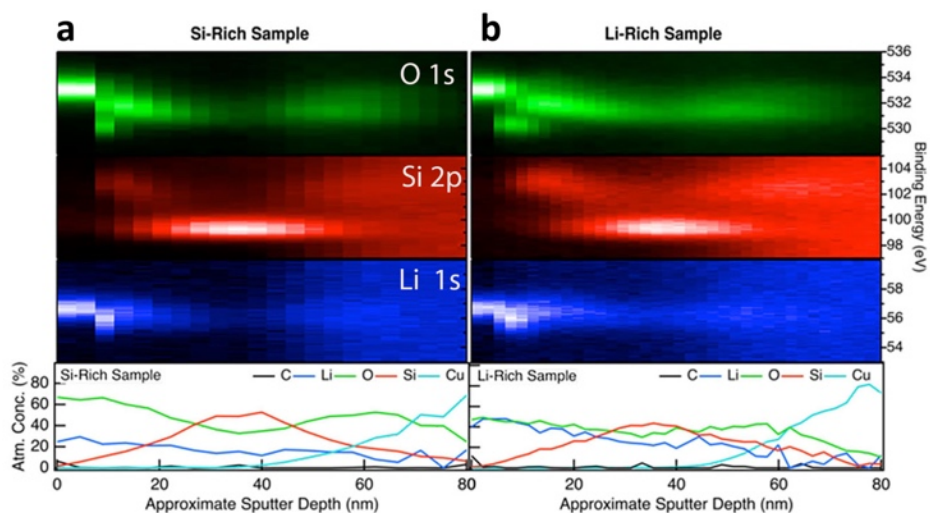


Figure 43. XPS depth profile analysis of Li_xSiO_y composite thin film on copper foil for a) Si-rich region and b) Li-rich region. The top panels show binding-energy depth profile of O 1s (green), Si 2p (red), and Li 1s (blue). The bottom panel shows atomic percentage as a function of sputter depth.

Table 5. Fitting Results Show the Components in the Film

Li-Rich		Si-Rich	
Li_2SiO_4	58.01%	Li_2SiO_3	63.68%
$\text{Li}_{12}\text{Si}_7$	31.56%	LiSi_2	32.72%
SiO_2	10.43%	SiO_2	3.6%
Film composition	$\text{Li}_{4.88}\text{Si}_{2.85}\text{O}_{2.52}$	Film composition	$\text{Li}_{1.58}\text{Si}_{1.31}\text{O}_{1.95}$

To correlate the measured Li_xSiO_y properties with the electrochemical cycling performance of an electrode with Li_xSiO_y at the surface, a double-layer sample was deposited with Li_xSiO_y on top of a silicon thin film and then compared to a Si film. The thickness of Li_xSiO_y was set to 10 nm to emulate the native-oxide thickness, and the thickness of the silicon thin film was set to 50 nm, as shown in the inset in Figure 45a. As shown in Figure 45a, during the first-cycle discharge profile, $\text{Li}_x\text{SiO}_y/\text{Si}$ exhibited a lower open-circuit voltage of only 1.5 V (compared to 2.5 V for Si) due to the existing lithium on the silicon surface. The difference of the CV profiles above 0.25 V (before Si starts lithiating) results from the surface reaction between Li_xSiO_y and electrolyte. Both low potential of Li_xSiO_y and its reaction products make the electrochemical reduction different than that in the silicon case. The lower potential range profiles for both films are very similar because the same thickness of silicon film was deposited. The cycling of $\text{Li}_x\text{SiO}_y/\text{Si}$ showed a lower coulombic efficiency and less stable performance as compared to the bare silicon (Figure 45b). We note that the coulombic efficiency of silicon is higher than that of the Li_xSiO_y -coated Si, indicating that the Li_xSiO_y film exhibits a greater reactivity with electrolyte (Figure 45). We hypothesize that the Li_xSiO_y composite film continuously reacts with the electrolyte, preventing the stabilization of the SEI on the silicon electrode. These results suggest that SiO_2 does not help stabilize the surface of the Si electrode, because the lithiation products are not stable upon cycling. Previously, there has been study² of the effect of SiO_2 with various thickness—

from 2 nm, to 7 nm, to 10 nm. Only the 7-nm SiO₂-coated Si showed improved performance compared to Si. This is a complementary result due to both mechanical property and reactivity. More studies of the reactant product between Li_xSiO_y and electrolyte are in progress to clarify the role of Li_xSiO_y in the functionality and SEI stabilization of the Si anode.

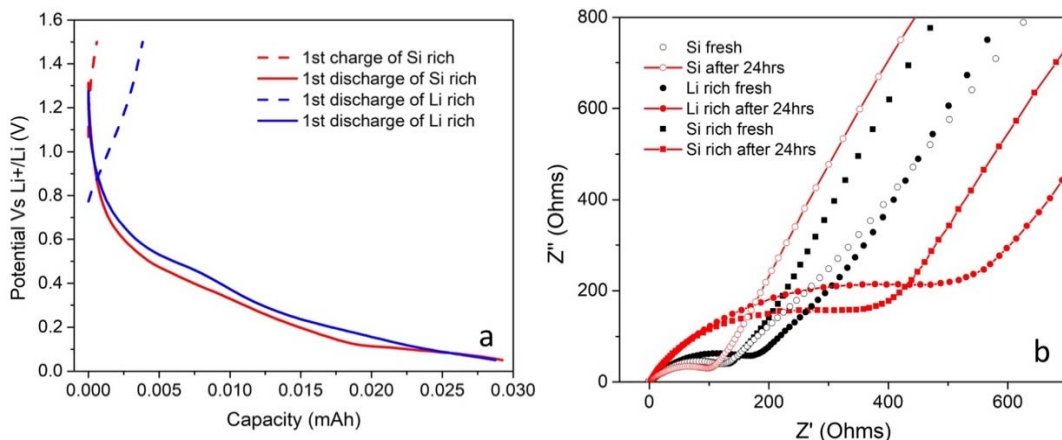


Figure 44. a) Voltage profile of lithium-rich Li_xSiO_y composite film and silicon-rich Li_xSiO_y composite film; b) Impedance evolution of lithium-rich Li_xSiO_y composite and silicon-rich Li_xSiO_y composite as well as Si film.

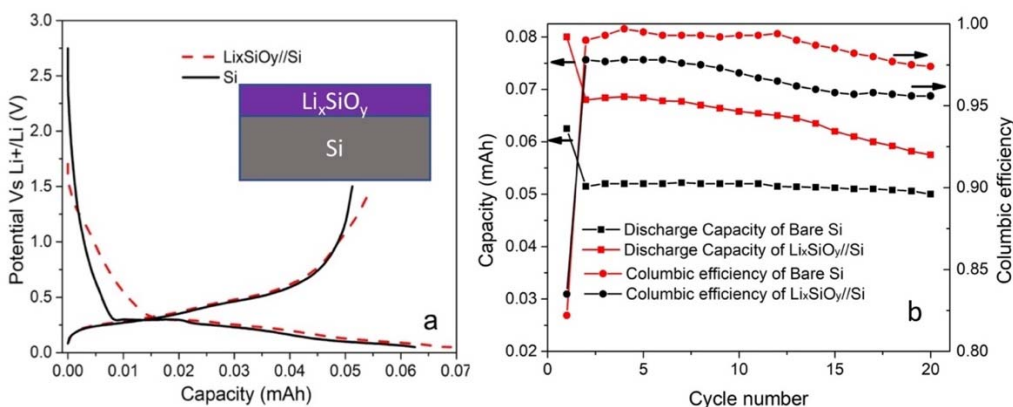


Figure 45. a) Charge and discharge profile of Si and Li_xSiO_y/Si, with inset showing the schematic of double-layer thin film; b) Cycle performance and coulombic efficiency of double-layer thin film and pure silicon.

Finally, an interesting “cycling” of native oxides to produce silicates was performed by using a charged Li⁺ beam as the anode in a cycle and injecting ionized lithium into various surface layers with low (10-eV) incident energy—essentially performing an atomic beam lithiation of the film. To investigate the lithiation of SiO₂/Si(001), in a “SEISta round-robin,” a 50-nm SiO₂/Si(001) sample was subjected to a flux of 10-eV Li⁺ ions while performing XPS measurements. Current through the sample was ~20 nA, and the Li⁺ spot size was on the order of 2 mm in diameter. The XPS results during lithiation are shown in Figure 46a. From these data, a clear charging effect can be observed during the initial lithiation: all peaks shift to higher binding energy by ~7.5 eV, corresponding to a positive increase in the surface electrochemical potential of 7.5 V. This overpotential drops to near zero after about 200 minutes of lithiation, which likely indicates that the SiO₂ layer has been fully converted to one or more Li_xSi_yO_z phases. In the O 1s spectral profile (Figure 46a; green), evolution in the chemical states can be observed between 300–500 min. In that region, the peak initially centered at ~533 eV splits into two peaks around 534.5 and 531.5 eV. This might be due to the formation of a more Li-rich Li_xSi_yO_z phase. On the other hand, the data also indicate that Li₂O may be forming during this

time. After the XPS *in-situ* lithiation measurement, the sample was depth profiled using Auger electron spectroscopy (AES), as shown in Figure 46b. These data clearly show three compositionally distinct regions within the sample, including a $\text{Li}_x\text{Si}_y\text{O}$ phase at the surface, a buried Li_xSi layer, and the bulk Si wafer.

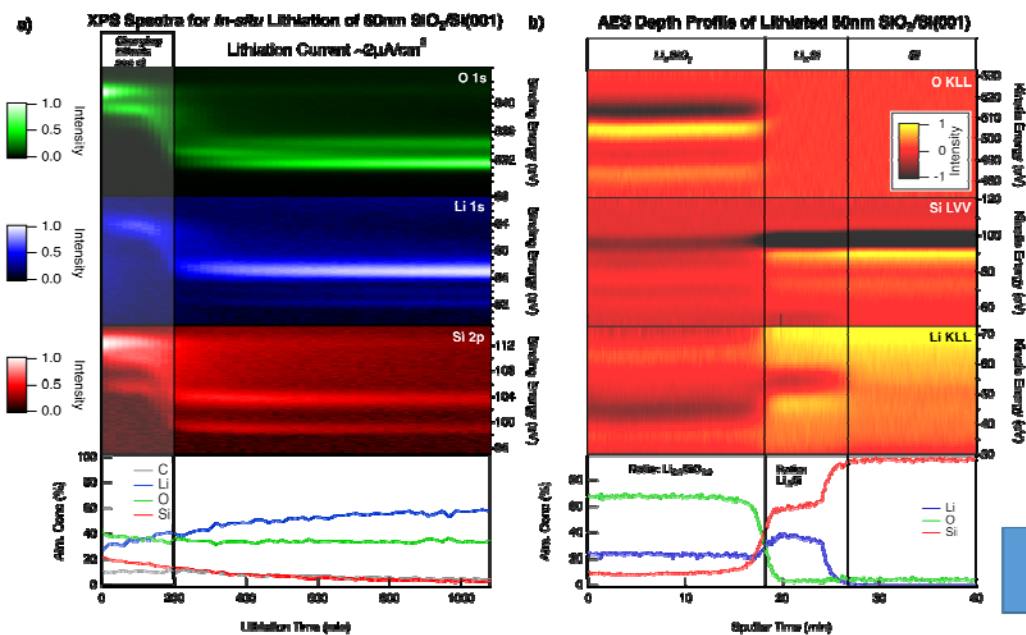


Figure 46. a) Evolution of XPS core-level spectra during *in-situ* lithiation of 50-nm $\text{SiO}_2/\text{Si}(001)$ wafer. b) AES depth profile of the lithiated sample reveals that the entire SiO_2 layer has been converted to a $\text{Li}_x\text{Si}_y\text{O}$ phase and that an underlying Li_xSi phase has also formed.

In addition to the measurements summarized above for 50-nm $\text{SiO}_2/\text{Si}(001)$, preliminary *in-situ* lithiation experiments have also been completed on native oxide/ $\text{Si}(001)$ and on sputter-cleaned $\text{Si}(001)$. The XPS data sets comparing evolution of these different surfaces during *in-situ* lithiation are shown in Figure 47. From these data, it is clear that differences in the XPS spectra—corresponding to differences in evolution of various Li-Si-O phases—can be observed that depend on the initial condition of the Si wafer. Perhaps the most striking difference is a low binding-energy peak in the Li 1s core level. This peak, possibly associated with Li-rich Li-Si phases, is significantly more intense when less surface oxide is present. To our knowledge, these Li 1s peaks have not yet been described in the literature; additional studies will be needed to conclusively assign them to particular phases.

Comparing spectra acquired with and without Li^+ ion gun current bias enables determination of overpotentials associated with lithiation for the various Si wafer samples that were studied. As can be seen in Figure 48, the overpotential associated with lithiation of the 50-nm $\text{SiO}_2/\text{Si}(001)$ is ~ 7.5 V. Compared to the native oxide/ $\text{Si}(001)$ sample, this overpotential is over 100x larger in magnitude, even though the SiO_2 layer (estimated ~ 2 nm for native oxide) is only ~ 25 x thicker. This observation supports the conclusion that excessively thick SiO_2 layers will significantly increase cell overpotentials during the first cycle of a Si-based anode.

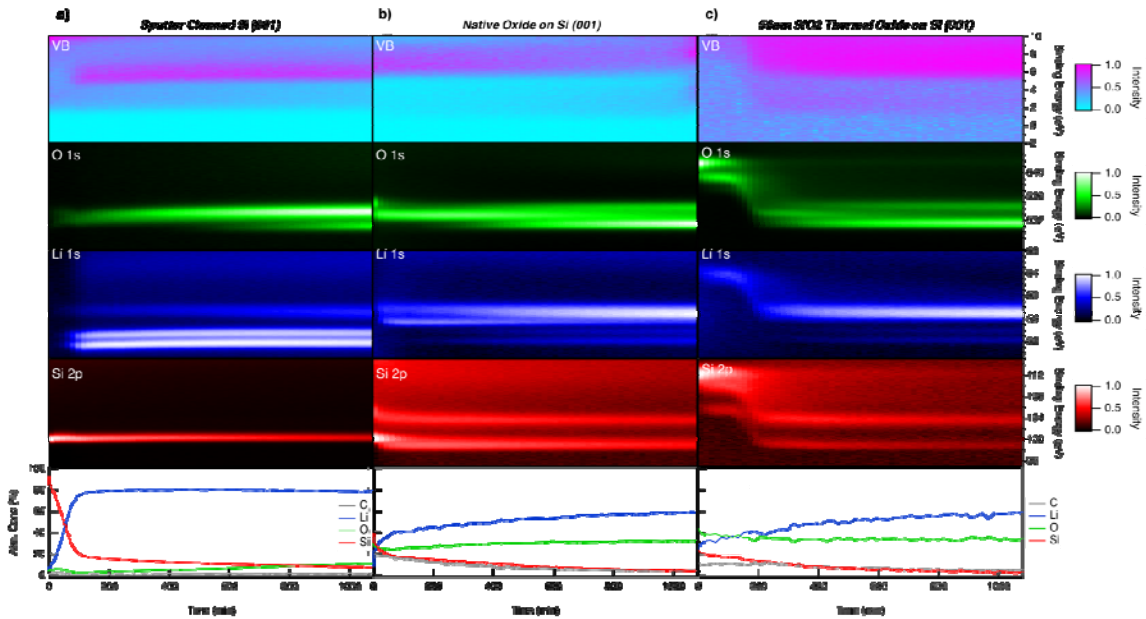


Figure 47. Evolution of XPS core-level spectra during *in-situ* lithiation of an: a) sputter-cleaned Si(001) wafer, b) wafer with a native oxide, and c) Si (001) wafer with a 50-nm-thick thermally grown SiO₂ layer.

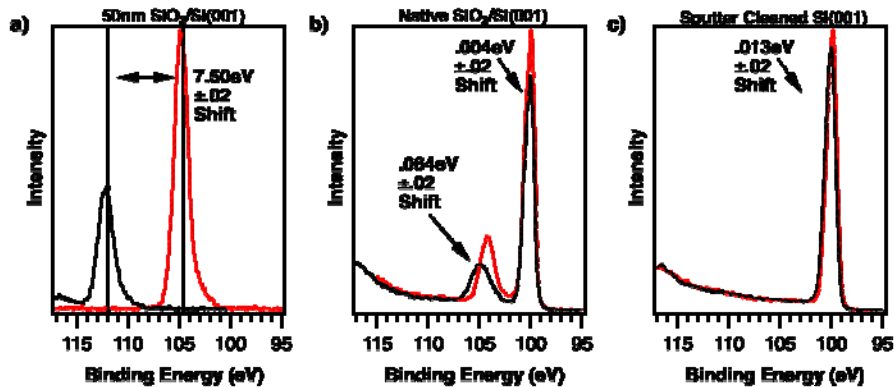


Figure 48. Overpotential variations for the three different Si wafers tested: a) 50-nm SiO₂/Si (001) b) native oxide on Si (001) and c) sputter-cleaned Si (001). The black curve was acquired with the Li⁺ ion gun current bias on and the red curve without. Binding-energy shifts can be used to estimate overpotentials of lithiation, and ultimately, Li diffusivity as a function of Li-Si-O phase.

In Q4, to further investigate the role of SiO_x in SEI formation during early-stage lithiation, three types of samples were studied: bare Si(001) substrates, native-oxide SiO_x/Si samples, and thermal-oxide (5–100-nm) SiO₂/Si(001) samples.

Evolution of the Si 2p, O 1s, Li 1s, and C 1s core levels as a function of lithiation time reveals that the three samples shown in Figure 49 behave quite differently. All of the samples show evidence for the formation of

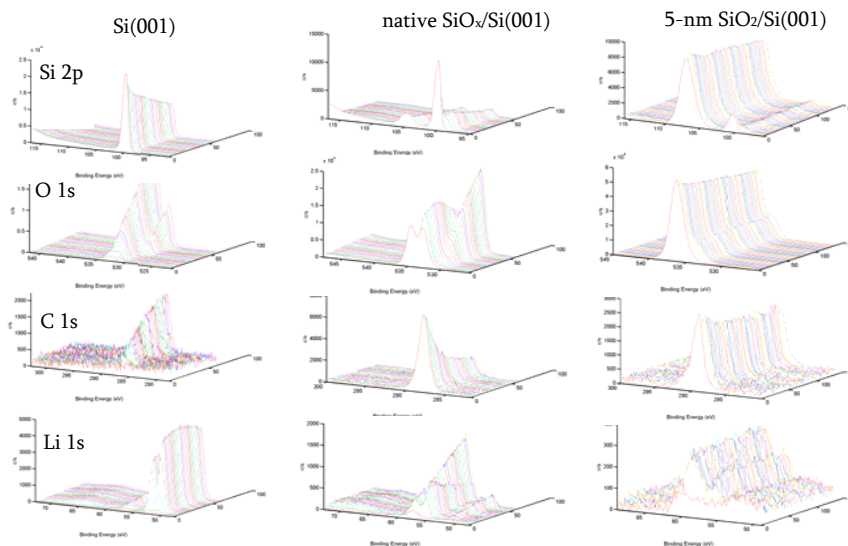


Figure 49. XPS core-level spectral evolution monitored as a function of lithiation time for three samples: bare Si(001), native oxide SiO_x/Si(001), and 5-nm thermal-oxide SiO₂/Si(001). The evolution of the core levels in the first two cases—and, in particular, the evidence for uptake of residual gas species by the exposed surfaces—shows that these surfaces are more reactive in comparison to the 5-nm SiO₂/Si(001) sample.

Li_xSi phases, although it appears that different Li_xSi phases form depending on the initial oxide composition and thickness. Specifically, both the bare Si(001) and native-oxide SiO_x/Si(001) samples show evidence for a Li_xSi phase characterized by a peak doublet in the range of 50–55 eV. On the other hand, a higher-binding-energy Li 1s peak (~55 eV) is observed in both the native-oxide SiO_x/Si(001) and 5-nm SiO₂/Si(001) samples. The cause of this variability is not yet understood, but nevertheless, it reveals that the nature of the SEI can influence the formation and evolution of particular Li_xSi phases. The surface of the bare Si(001) wafer appears to be the most reactive, as evidenced by the appearance and growth of peaks in the O 1s and C 1s core-level spectra, due to reactions with trace residual gases (primarily H₂O, CO, and CO₂) in the XPS chamber. The native-oxide SiO_x/Si(001) sample appears to be less reactive. For example, the C peak associated with surface contamination that is initially present attenuates as lithiation progresses, indicating that the C contamination is being progressively covered by other phases, and that new C-containing phases are not forming due to reaction with residual gases. On the other hand, peaks in the Li 1s and O 1s core-level spectra are consistent with the growth of Li₂O, indicating that O-containing residual-gas species such as H₂O are likely reacting with the surface. The surface of the 5-nm SiO₂/Si(001) is the least reactive, and, in fact, there is no evidence for any uptake of residual gases by this surface. This seems to indicate that the surface remains chemically passivated indefinitely, although Li⁺ migration through the lithiated SiO₂ is apparent.

As illustrated in Figure 50, shifts in O 1s and Si 2p core levels measured before and after the Li⁺ ion gun is turned on reveal peak shifts associated with the overpotential required to drive Li⁺ ion through the SiO₂ layer. In the case of 5-nm SiO₂, with an estimated Li⁺-ion current density of 500 nA/cm², the measured overpotential is ~2.2 eV. Accounting for the SiO₂ thickness and dielectric properties, we estimate that the resulting electric field within the SiO₂ layer is ~10⁶ V/cm, which is approaching the dielectric breakdown threshold. Figure 50 also reveals interesting changes in the Si⁰ peak in the Si 2p core level that accompanies Li⁺ ion gun current bias. The Si 2p peak broadens and shifts to higher binding energy, which likely results from downward band bending in the Si(001) substrate in response to the surface charge associated with Li⁺ current bias. Following the *in-situ* lithiation measurements, samples were analyzed with angle-resolved XPS (ARXPS) measurements. This non-destructive technique leverages the surface sensitivity of XPS measurements to reveal the depth distribution of detected phases. Nine distinct chemical states were observed in the XPS spectra, and curve fitting enabled preliminary identification of specific phases (e.g., SiO_x, Li_ySiO_x, and Li_xSi), each with distinctive angular intensity profiles as shown in Figure 51. For the lithiated 5-nm SiO₂/Si(001) sample, preliminary results reveal a layered structure composed of a layer of surface C contamination, a Li_ySiO_x layer, a SiO_x layer (possibly Li-doped), and a Li_xSi layer.

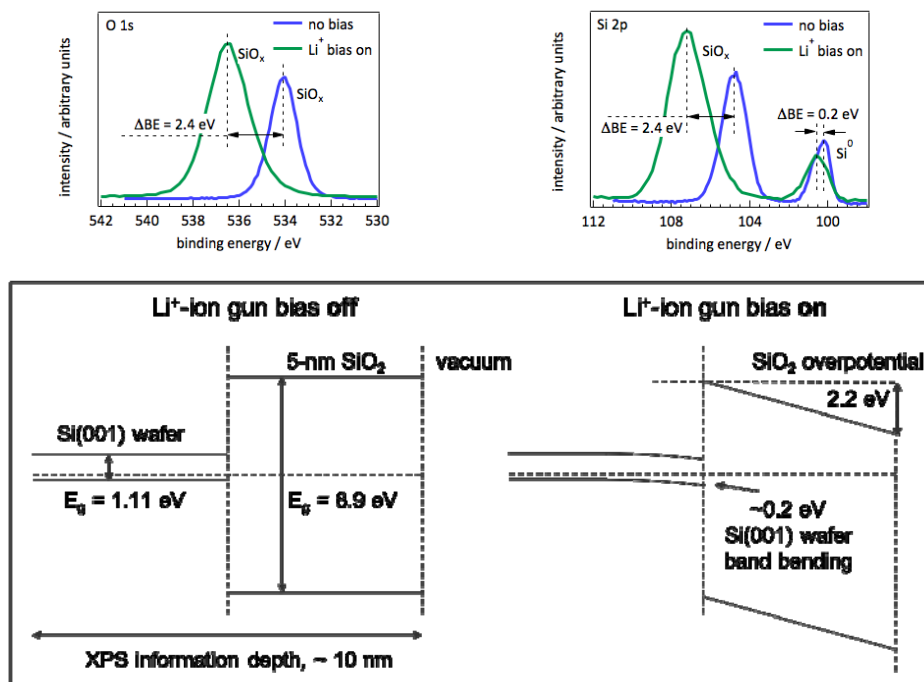


Figure 50. XPS O 1s (upper left) and Si 2p (upper right) core levels recorded on the 5-nm SiO₂/Si(001) sample before the Li ion gun was turned on and immediately after. The shifts in SiO₂ core levels reveal the overpotential associated with the 5-nm-thick SiO₂ layer. Changes in the Si⁰ peak likely result from downward band bending in the p-type Si(001) wafer substrate, as illustrated in the schematic energy-band diagrams in the lower panel.

The finding that the SiO_x layer remains largely intact during the initial phase of lithiation is somewhat surprising, but we emphasize that this is a preliminary result. To validate and refine the ARXPS modeling results, in FY19 we will apply a more rigorous data-analysis algorithm such as the Maximum-Entropy Method or use suitable software such as Simulation of Electron Spectra for Surface Analysis (SESSA, developed by NIST).

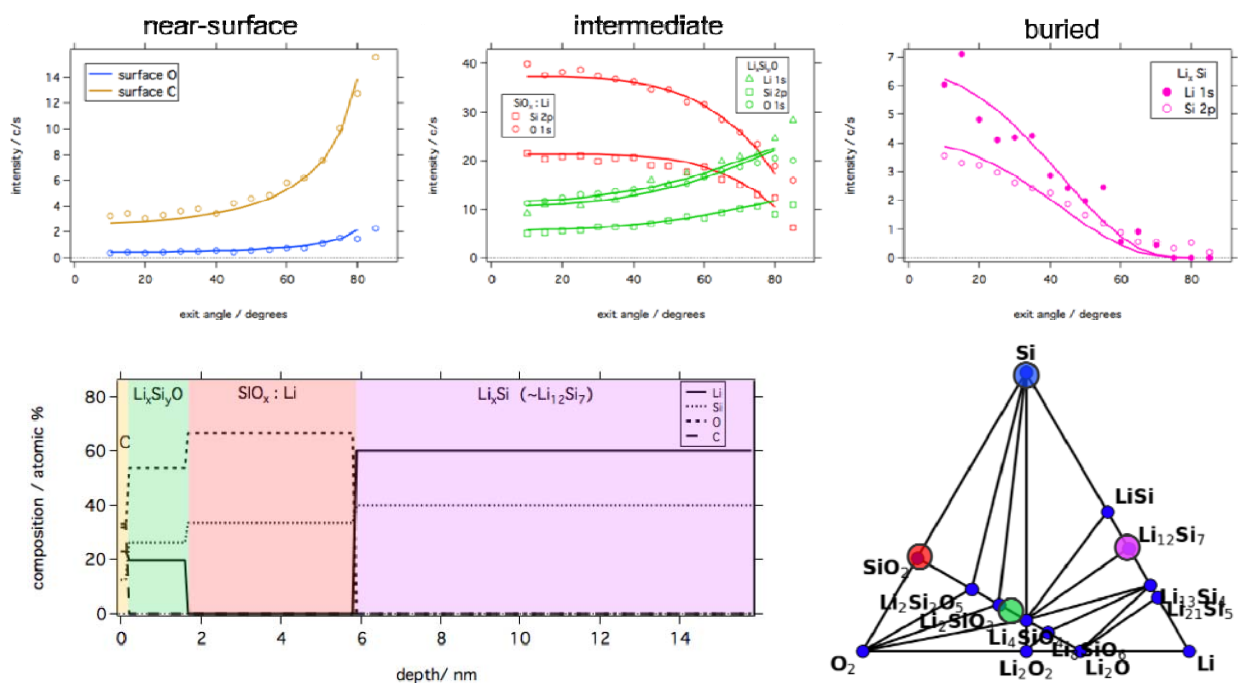


Figure 51. Measured (symbols) and calculated (solid lines) ARXPS angular profiles of detected chemical states highlighting near-surface, intermediate, and buried phases (upper panels). The preliminary model structure shown in the lower left panel agrees well with the measured data and indicates that very little Li is incorporated into the SiO_x layer at early stages of lithiation. The colored circles in the ternary phase diagram (lower right) represent approximate compositions of detected phases based on XPS intensities.

We observed evidence that Li-containing Si-based electrodes drive electrolyte decomposition reactions at the electrode surface. By comparison, in some cases, SiO_2 layers on Li-free Si electrodes appear to be etched by the electrolyte solution, leaving behind Si and a surface layer consisting of adsorbed organics. Furthermore, this behavior in the Si-only electrodes is observed for both the GEN2 electrolyte and the electrolyte containing an FEC additive. Conversely, the FEC additive appears to make a difference in the decomposition product on the surface of Li-containing Si electrodes by reducing the amount of LiF and increasing the amount of organic functionalities.

A novel method for studying the fundamental lithiation processes of Si-based anode materials was demonstrated. Preliminary results show that *in-situ* lithiation via a Li^+ ion gun combined with XPS measurements effectively probes the lithiation of Si-based electrode materials. These data will help with phase identification, validation of theoretical Li-Si-O ternary phase-diagram predictions, and the quantification of fundamental lithiation properties (e.g., chemically resolved overpotentials, impedances, and Li^+ diffusivities).

The virtual-electrode approach has been further developed as a means for studying fundamental lithiation mechanisms in Si-based anode materials by monitoring the lithiation process *in-situ* with XPS, while delivering Li^+ ion to the surface using a low-energy Li^+ ion gun. With this method, it is possible to directly observe the formation of Li_xSi phases and to assess overpotentials necessary to drive lithiation. Initial results presented here show that SiO_x layer thickness influences surface reactivity: for the bare Si(001) and native-oxide $\text{SiO}_x/\text{Si}(001)$ samples, all core levels evolve continuously throughout the course of the lithiation process due to reactions with trace residual gases present in the XPS chamber during the experiment. In contrast, the 5-nm-thick SiO_2 layer appears to chemically passivate the surface, at least with respect to residual gases.

Preliminary analysis of ARXPS data from the lithiated 5-nm SiO₂/Si(001) sample suggests a layered structured comprising Li_ySiO_x, SiO_x (possibly Li-doped), and Li_xSi. Additional ARXPS data modeling to validate and refine these initial results is in progress.

References

- ¹ Wu, H., G. Chan, J.W. Choi, I. Ryu, Y. Yao, M.T. McDowell, S.W. Lee, A. Jackson, Y. Yang, L. Hu, and Y. Cui. Stable Cycling of Double-Walled Silicon Nanotube Battery Anodes through Solid–Electrolyte Interphase Control. *Nat. Nanotechnol.* 7 (5), (2012): 310–315.
- ² Dudney, N.J., J.B. Bates, and J.D. Robertson. Radiofrequency Magnetron Sputtering of Pure and Mixed Targets of Li₄SiO₄, Li₃PO₄, and Li₂O. *Journal of Vacuum Science & Technology A-Vacuum Surfaces and Films* 11(2), (1993): 377–389.
- ³ Brooker, M.H. and J.B. Bates, Raman and Infrared Spectral Studies of Anhydrous Li₂CO₃ and Na₂CO₃. *Journal of Chemical Physics* 54(11), (1971): 4788.
- ⁴ Parker, S.F., et al. Assignment of the Vibrational Spectra of Lithium Hydroxide Monohydrate, LiOH Center Dot H₂O. *Journal of Chemical Physics* 134(8), (2011): 084503
- ⁵ Mahmoud, M.M., et al., Crystallization of Lithium Disilicate Glass Using Microwave Processing. *Journal of the American Ceramic Society* 95(2), (2012): 579–585.
- ⁶ Wang, S.N., et al., Ternary Phase-Separation Investigation of Sol-Gel Derived Silica from Ethyl Silicate 40. *Scientific Reports* 5 (2015): 14560.
- ⁷ Li, X.Y. and H.M. Yang, Morphology-Controllable Li₂SiO₃ Nanostructures. *Crystengcomm* 16(21), (2014): 4501–4507.
- ⁸ Koroleva, O.N., M.V. Shtenberg, and P.V. Khvorov, Vibrational Spectroscopic and X-Ray Diffraction Study of Crystalline Phases in the Li₂O–SiO₂ System. *Russian Journal of Inorganic Chemistry* 59(3), (2014): 255–258.
- ⁹ Carella, E. and M.T. Hernandez, High Lithium Content Silicates: A Comparative Study Between Four Routes of Synthesis. *Ceramics International* 40(7), (2014): 9499–9508.
- ¹⁰ Nocun, M. and M. Handke, Identification of Li–O Absorption Bands Based on Lithium Isotope Substitutions. *Journal of Molecular Structure* 596 (2001): 145–149.
- ¹¹ Young, B.T., et al., Hard X-ray Photoelectron Spectroscopy (HAXPES) Investigation of the Silicon Solid Electrolyte Interphase (SEI) in Lithium-Ion Batteries. *ACS Applied Materials & Interfaces* 7(36), (2015): 20004–20011.
- ¹² Philippe, B., et al., Role of the LiPF₆ Salt for the Long-Term Stability of Silicon Electrodes in Li-Ion Batteries – A Photoelectron Spectroscopy Study. *Chemistry of Materials* 25(3), (2013): 394–404.
- ¹³ Jaumann, T., et al., SEI-Component Formation on Sub 5 nm Sized Silicon Nanoparticles in Li-Ion Batteries: The Role of Electrode Preparation, FEC Addition and Binders. *Physical Chemistry Chemical Physics* 17(38), (2015): 24956–24967.
- ¹⁴ Kelly, M.A., Analyzing Insulators with XPS and AES, in *Surface Analysis by Auger and X-ray Photoelectron Spectroscopy*, J.T.G. D. Briggs, Editor. 2003, IM Publications: Chichester. p. 191–210.
- ¹⁵ Metson, J.B., et al., Suppression of Molecular-Ions in the Secondary Ion Mass-Spectra of Minerals. *Surface and Interface Analysis* 5(5), (1983): 181–185.
- ¹⁶ G. Baldacchini, M. Cremona, S. Martelli, R.M. Montekali, and L.C. Scavarda Do Carmo, *Phys. Stat. Sol.* 151 (1995): 319.
- ¹⁷ U. Kaiser, N. Kaiser, P. Weißbrodt, U. Mademann, E. Hacker, and H. Müller, *Thin Solid Films* 217 (1992): 7.
- ¹⁸ Wood, K.N., K.X. Steirer, S.E. Hafner, C. Ban, S. Santhanagopalan, S.-H. Lee, and G. Teeter, *Nat. Commun.* 9 (2018): 2490.
- ¹⁹ Nguyen, C.C. and B.L. Lucht, Comparative Study of Fluoroethylene Carbonate and Vinylene Carbonate for Silicon Anodes in Lithium Ion Batteries. *Journal of the Electrochemical Society* 161(12), (2014): A1933–A1938.

- ²⁰ Obrovac, M.N. and L.J. Krause, Reversible Cycling of Crystalline Silicon Powder. *Journal of the Electrochemical Society* 154(2), (2007): A103–A108.
- ²¹ Delpuech, N., et al., Critical Role of Silicon Nanoparticles Surface on Lithium Cell Electrochemical Performance Analyzed by FTIR, Raman, EELS, XPS, NMR, and BDS Spectroscopies. *Journal of Physical Chemistry C* 118(31), (2014): 17318–17331.

SEISta Section 3: Nature and Evolution of the Silicon SEI

SEISta Team

Background

The objective of this project is to develop a systematic understanding of solid-electrolyte interphases (SEIs) for silicon (Si) electrode materials and to provide practical strategies for stabilization of the SEI in Si-based electrodes. The SEI layer begins to form as soon as the Si electrode contacts the electrolyte. In fact, the reductive decomposition of the electrolyte in lithium-ion systems employing silicon anodes is inevitable, because the working potential of the electrode lies far below the electrochemical stability window of the electrolyte components. In principle, the insoluble decomposition products precipitate on the electrode surface, and if sufficiently insulating, result in the formation of a passivating surface film, which suppresses further electrolyte decomposition.^{1,2} The SEI comprises the products from many reduction reactions of salts, solvents, and electrolyte additives. These reduction reactions compete with each other; and their kinetics depend heavily on current density, overpotential, and the catalytic properties of the electrode surface, which finally determine the composition and structure of a SEI layer. Moreover, the phase transformation and mechanical deformation caused by the Si lithiation/delithiation process present additional challenges in investigating the SEI layer. The continuous reduction of electrolyte observed in Si-based composite electrodes may be attributed to the never-ending appearance of fresh surfaces during the volume changes, which continuously consumes electrolyte and leads to cell failure by loss of cyclable lithium.³ These reactions create a mix of soluble and insoluble organic and inorganic decomposition products that produce the SEI layer.

This chapter aims to summarize the results and progress made in investigating the chemistry, physical properties, and formation mechanism of SEI for the Si anodes. The discussion explores three main themes including: 1) solvation structure of the carbonate electrolytes by using molecular dynamic computation, 2) SEI chemistry, which covers the formation of early-stage SEI, SEI chemistry evolution, and reduction of fluoroethylene carbonate additive, and 3) SEI inhomogeneity by using tip-enhanced Raman spectroscopy. In addition, two new techniques—scanning spread-resistance microscopy (SSRM) and fluorescent probes for fluorescence microscopy—have been developed and are summarized in this report. In addition, a variety of characterization techniques have been employed and further developed to better understand the SEI, including X-ray photoelectron spectroscopy (XPS), X-ray absorption spectroscopy (XAS), Fourier-transform infrared spectroscopy (FTIR and ATR-FTIR), and apertureless IR near-field scanning optical microscopy (aNSOM), tip-enhanced Raman spectroscopy (TERS), scanning transmission electron microscopy (STEM), and electrochemical quartz-crystal microbalance (EQCM). All the techniques have been discussed and employed in our previous study; thus, they are not elaborated in this report. The Si samples used in this study are our SEISta model samples: Si(100)-doped wafers with a native oxide, which have been studied and selected in FY2017. The cleaning protocol established in FY2017 has been used in this study.

Discussion and Results

1. Solvation structure of the carbonate electrolytes

To elucidate the dominant early SEI formation reaction pathways, we examine the majority- as well as minority-specie solvation structures of the Li-ion electrolyte at the bulk electrolyte and at the interface. The

solvation structure of the electrolyte (1.0 M LiPF₆/EC) has been studied with the classical molecular dynamic (MD) method. We first investigated the solvation structure close to the neutral (uncharged) interface at the Si anode, during the initial charging step. An OPLS force field is employed for the electrolyte constituents, and the anode interface is represented by neat crystalline-Si (c-Si) covered with a thin, native silicon oxide layer. We found that the solvation structure of Li⁺ changes quite significantly from the bulk to the interface, such that the overall Li⁺ coordination changes from about 6 to about 4 (Figures 1a and 1b). This effect is due to two components: 1) a significant interaction between the SiO₂ oxygen and Li ion reduces the EC coordination number (CN) from 5.5 to 2.5, and 2) the Li-F CN increases from 0.4 in the bulk to 1.2 at the interface. Because the PF₆⁻ anion can donate more than one F to each Li, the contact ion-pair (CIP) ratio increases from ~0.3 to ~0.65 from the bulk to the interface. We also find that the CIP ratio in bulk increases from 0.07 to 0.3 with temperature increasing from 300 K to 400 K, which we attribute to a decrease in the dielectric constant of the solvent.

We then analyzed the solvation structure of electrolyte molecules for an interface with a constant charge. As previously, the chemical characteristics of the Si anode interface is modeled with an amorphous SiO₂ layer on top of the c-Si bulk electrode. The equilibrium MD simulation is performed for 1 M LiPF₆ in EC at 400 K (Figure 2a). The applied voltage is modeled by assigning a uniform charge, $\pm 6.25e^{-4} e$, to each silicon atom at the negative/positive electrodes so that the voltage applied at the negative silicon electrode is ~ -0.47 V (Figure 2b). Interestingly, the constant charged interface causes a reduction in the CIP ratio between the bulk and the interface, as compared to the neutral case. Both a negative as well as positively charged SiO₂ interface result in a CIP ratio of 0.4 and 0.45 at the negative- and the positive-charged electrode interface, respectively (Figure 3), which should be compared to the neutral case of 1.2. Nevertheless, it should be stressed that the CIP ratio still is increased as compared to the bulk for both charged (marginally) and neutral (substantially) SiO₂ interfaces. Furthermore, similar to the neutral electrode, the CIP ratio increases from bulk to interface with increasing temperature—spanning 313, 350, and 400 K (see Figure 2c). In summary, the neutral silicon SiO₂ interface exhibits the largest CIP ratio, and it becomes smaller at the charged interface. Specific interaction between ions and SiO₂ enhances the CIP forming at the interface, which provides a hint toward preferential reaction pathways of the early SEI formation.

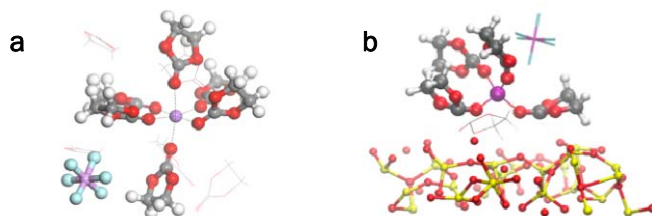


Figure 1. Structures of EC molecules around a Li ion (a) in the bulk and (b) at the interface.

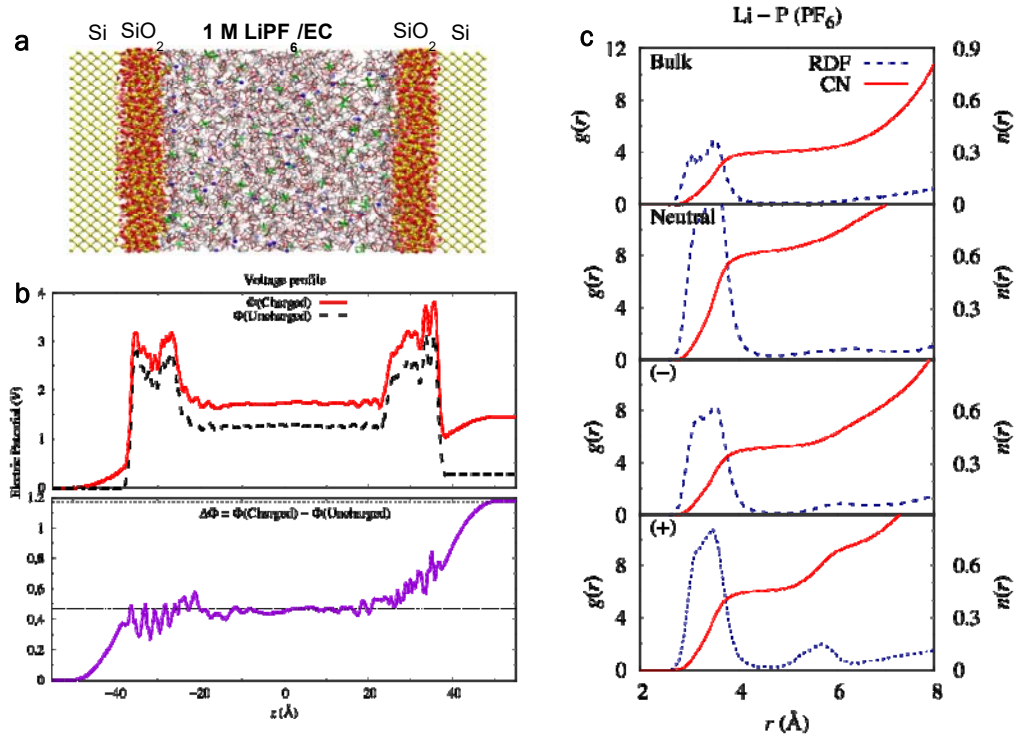


Figure 2. (a) The model Si anode interface, and (b) the voltage profile in the electrolyte region between the electrodes. The electric potentials are -0.47 V and +0.7 V at the negative and the positive electrodes, respectively. (c) Radial distribution functions and the coordination numbers (CN) of PF₆ ions around a Li ion in bulk and at the neutral, negative, and positive electrodes, from top to bottom; the CN values are 0.3, 0.65, 0.4, and 0.45, respectively.

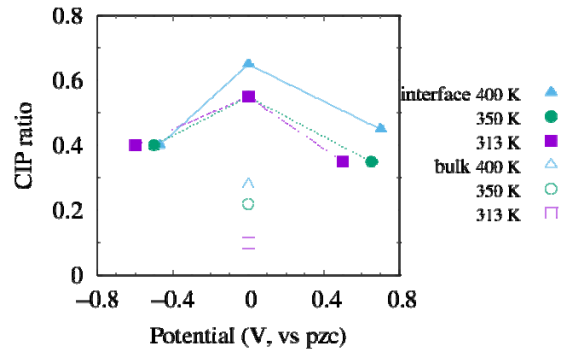


Figure 3. Contact ion-pair (CIP) ratio in the bulk electrolyte and at SiO₂ interface at temperatures of 400, 350, and 313 K. The CIP ratio increases from the bulk to interface. The neutral silicon interface shows the largest CIP ratio, and it becomes smaller at the charged interface.

2. Chemistry in the SEI layer

a. Early-stage SEI formation

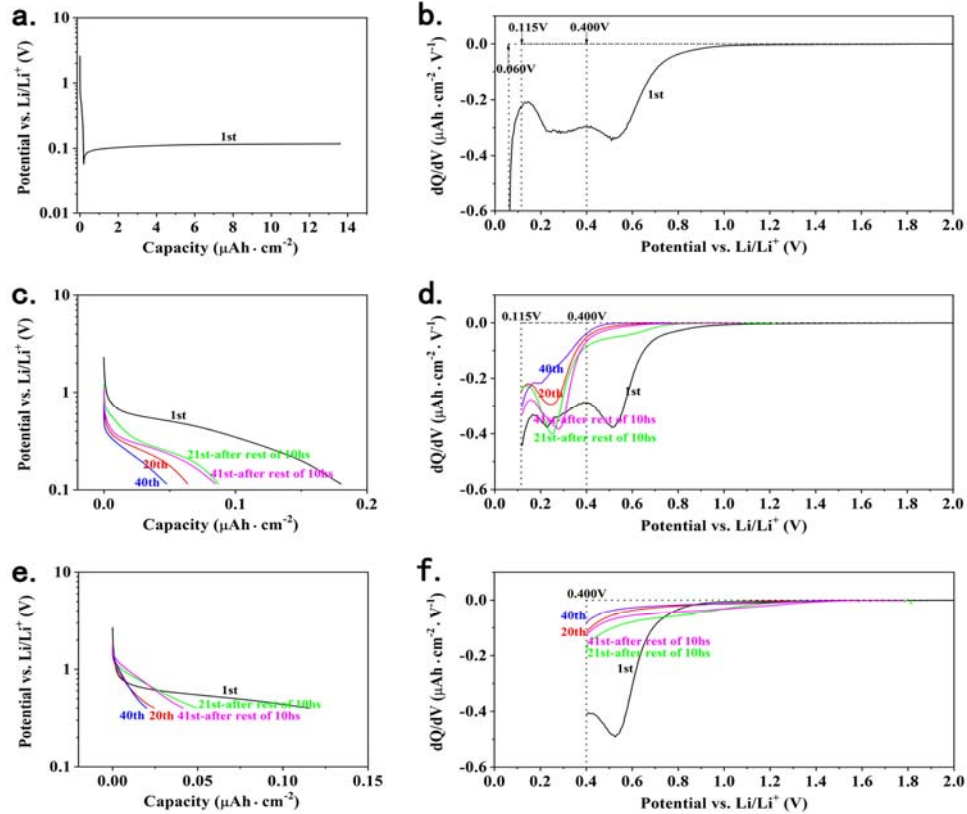
The electrolyte reduction and its interaction with electrode materials are involved in the early stage of SEI formation for Si anodes. To better understand the early-stage SEI chemistry, a new methodology has been developed here to decouple the lithiation-induced mechanical deformation from the SEI formation, to directly

investigate the interphase formation and evolution. Galvanostatic reduction was performed on the Si anode with a specific cut-off voltage before Si lithiation voltage, which allows the formation of an early-stage SEI (es-SEI) without the mechanical deformation.

A typical electrochemical procedure has been applied on the Si wafer anode: apply a galvanostatic reduction current of 6.82 mA cm^{-2} and keep it for the time up to 2 hours, then rest for 10 hours and repeat the above steps for 20 cycles. Figure 4a shows the voltage profile as the function of capacity under this regular condition including both the electrolyte reduction and Si lithiation. The slope section of this voltage profile is ascribed to the reduction of electrolyte, and the low-voltage plateau section of this voltage profile corresponds to the two-phase region when the lithiated amorphous Si is formed. Figure 1a well agrees with the initial lithiation behavior of c-Si reported in literature.¹² Figure 4b shows the differential capacity profile of this Si anode. There are two peaks at the potential of 250 mV and 550 mV shown in the profile, respectively. The deep dropping of this differential capacity profile at the potential of 60 mV is derived from the initiating Si lithiation.

To quantitatively study the reduction behavior of the electrolyte and Si anode, we divide this differential capacity profile into the following three regimes by the voltage range: 1) Regime 1 ranges from 400 mV to the open-circuit potential (OCP), which corresponds to the reduction behavior around the peak at 550 mV; 2) Regime 2 ranges from 115 mV to 400 mV, which corresponds to the reduction behavior around the peak at 250 mV; and 3) Regime 3 ranges from 60 V to 115 mV, which corresponds to the initiating Si lithiation. We focus on Regimes 1 and 2 in this work to understand the chemistry involved in the es-SEI formation. Therefore, we have designed a two-step electrochemical experiment: 1) Apply a galvanostatic reduction current of 6.82 mA cm^{-2} from OCP to the cut-off voltage of 115 mV (or 400 mV), then rest for 3 hours, and repeat the above steps for 20 cycles; and 2) Interval long rest for 10 hours.

Figures 4c and 4d show the voltage profile and the differential capacity profile when using a cut-off voltage of 115 mV, including Regime 1 and Regime 2. Figures 4e and 4f show the voltage profile and the differential capacity profile when using a cut-off voltage of 400 mV, including only Regime 1. Both Figure 4c and Figure 4e show the slope curves because of involving Regime 1 and Regime 2. In these well-designed experiments, the Si wafer samples only experience the reduction of electrolyte and the interaction with the electrolyte in an absence of the lithiation process—no plateau curve is observed in the voltage profile. The Si wafer samples were collected after the aforementioned electrochemical reduction process and were characterized using scanning electron microscopy (SEM). Figure 5 exhibits the three SEM images from the samples at (a) 400 mV, (b) 115 mV, as well as (c) 115 mV and a 20-hour rest. The sample collected at 400 mV has a very smooth surface as compared to the samples collected at 115 mV. Surprisingly, the surface of the sample collected at



115 becomes much smoother after the 20-hour rest. The surface morphology evolves during the rest, indicating instability of some SEI components in the carbonate electrolyte.

Figure 4. (a) The voltage profile and (b) differential capacity profile when lithiation to 60 mV. (c) The voltage profile and (d) differential capacity profile when using a cut-off voltage of 115 mV including both Regime 1 and Regime 2. (e) The voltage profile and (f) differential capacity profile when using a cut-off voltage of 400 mV including only Regime 1.

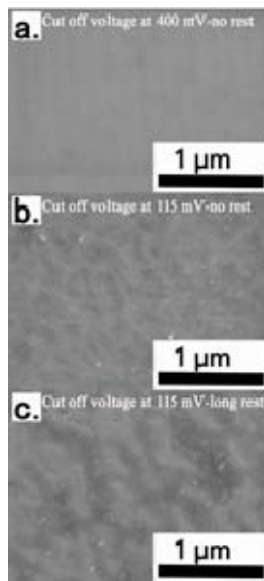


Figure 5. The SEM morphology of es-SEI on the Si surface after cathodic cycling with the cut-off potential of (a) 400 mV and no rest, (b) 115 mV and no rest, as well as (c) 115 mV and long rest.

For the Si sample collected at 400 mV, the XPS spectra reveal the formation of both organic and inorganic components in the es-SEI, as shown in Figure 6. Peak fitting has been carried out taking spin-orbit splitting into account for both the Si and P peaks and a constant binding-energy separation between elements belonging to the same chemical species. This allows corrections to eventual small charging effects or differential charging as described in Wood et al.¹

The outcome of the analysis of the C 1s core levels shows that carbonate groups (CO_3) with the peak at 292 eV, ester groups (O-C=O) with the peak at 290–291 eV, ether (C-O) with the peak at 288–289 eV, and aliphatic (C-C/C-H) with the peak at 286–287 eV are present as organic components. The O 1s spectra include the peaks at 535 eV and 533 eV, showing the existence of C=O and C-O , respectively, which is consistent with the carbonate/ester and ethers suggested by C 1s spectra. Regarding the carbonate groups, both organic carbonates such as LiEDC and inorganic carbonates such as Li_2CO_3 might be present. LiF is also the part of es-SEI, being accountable for the vast majority of the fluorine signal. LiPF_6 is present as well, but only in trace quantity. This might be due to residual salt that was not thoroughly washed out during the gentle rinsing procedure with DMC. The es-SEI appears to be a relative thin layer, as demonstrated by the fact that the signal of the underlayer SiO_x with the peak at 104–105 eV and the Si substrate with the peak at ~ 100 eV are still visible even on the most surface-sensitive measurements at 5° .

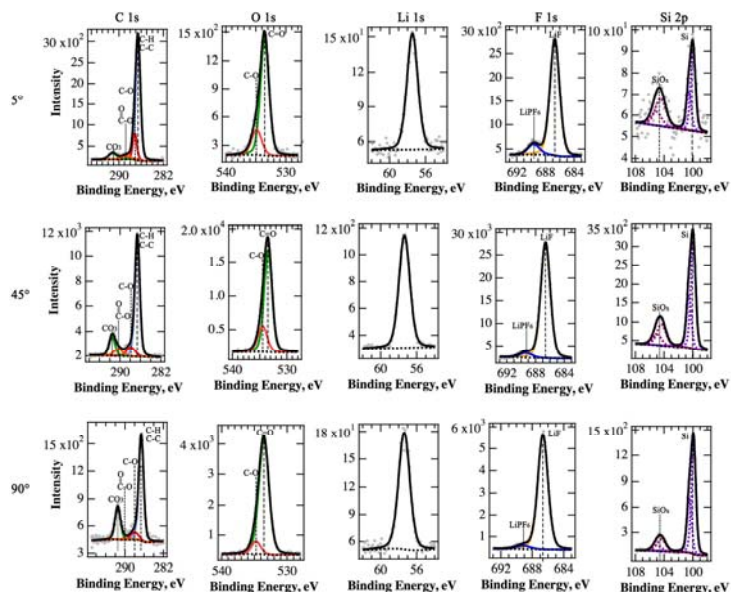


Figure 6. The XPS spectra obtained from the es-SEI with the cut-off potential of 400 mV. The spectra show that the LiEDC starts to form at the potential higher than 400 mV.

Figure 7 summarizes the XPS results from the Si sample collected at 115 mV. It shows that the es-SEI appears to be thicker, with the underlying SiO_x/Si not visible in the most surface-sensitive measurements (5°) and its signal being much more attenuated in the more depth-probing measurements. Qualitatively, the es-SEI composition is different, as well: the organic components appear to be more pronounced and the amount of carbonates and ester species is much higher for this sample in comparison to the 400-mV/no-rest sample. LiF and a trace amount of LiPF₆ are also present in the es-SEI.

Being similar to the 115-mV/no-rest sample, the 115-mV/long-rest sample also shows a thicker es-SEI in comparison to the es-SEI formed on the 400-mV/no-rest sample, as displayed in Figure 8. It demonstrates that the signal of the underlying Si layer is not detectable for the samples measured at grazing exit and attenuated for the other take-off angles. Comparison between the 115-mV/no-rest sample and the 115-mV/long-rest sample shows that the composition of the es-SEI with long rest and no rest is different. The sample with no rest shows a much higher concentration of carbonate/ester group species compared to the sample after long rest. LiF is the other major component in the es-SEI. There are trace amounts of LiPF₆ and trace amounts of another F-containing species that could not be identified at present.

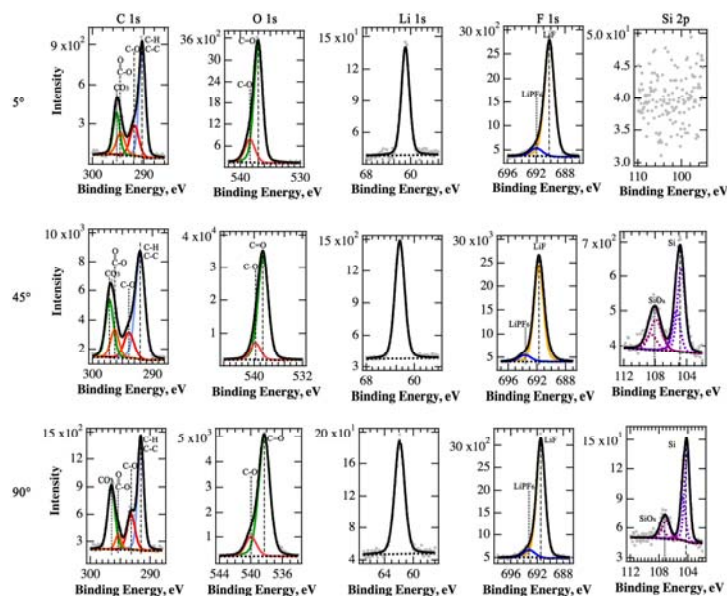
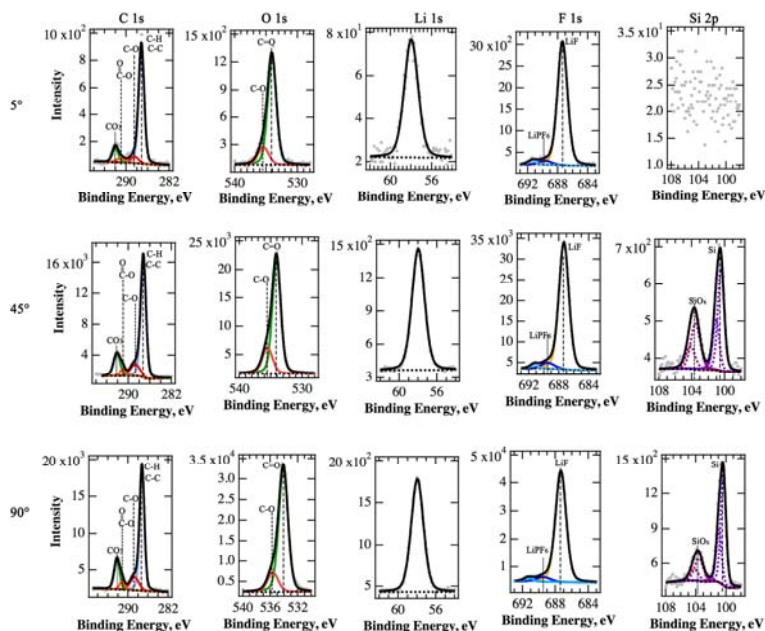


Figure 7. The XPS spectra obtained from the es-SEI after HVIST cycling with the cut-off potential of 1.15 mV and no rest.



The spectra show that the SiO_x was reduced to Li_xSiO_y during the potential between 115 mV and 400 mV.

Figure 8. The XPS spectra obtained from es-SEI after HVIST cycling with the cut-off potential of 1.15 mV and long rest. During the long rest, the spectra show that the LiEDC was decomposed because the LiEDC reduced. It also shows that there is no lithiation on the Si wafer because the lithium silicide was not found in Si.

b. Chemical evolution of the SEI layer

The electrochemical processes occurring upon (de-)lithiation and the SEI formation mechanism on the silicon electrodes have been investigated by cyclic voltammetry (CV) and galvanostatic cycling test.

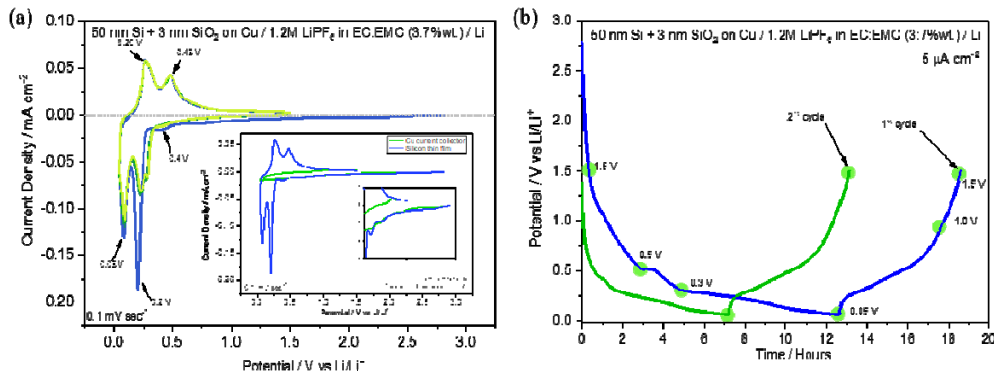


Figure 9. (a) Cyclic voltammetry of 50-nm Si thin film in Gen 2 electrolyte (1.2M LiPF₆ in EC:EMC 3:7 wt.%). Inset represents the comparison of the first-cycle voltage profile of the Si thin-film electrode and the bare-copper current collector. (b) First and second galvanostatic cycle of a 50-nm Si thin-film electrode cycled in 1.2M LiPF₆ in EC:EMC 3:7 wt.% electrolyte at 5 $\mu\text{A cm}^{-2}$ within the 0.05 V–1.5 V vs Li⁺/Li potential range.

Figure 9a displays the CV profile obtained by cycling the 50-nm Si thin film for 10 cycles at a scan rate of 0.1 mV s^{-1} within the 0.05 V–1.5 V potential range using 1.2 M LiPF₆ in EC:EMC 3:7 wt.% as electrolyte solution. At 0.4 V, a small feature is observed and is most likely related to an early stage of lithiation of silicon.² At low voltage values, i.e., 0.2 V and 0.08 V, the two main characteristic peaks of lithiation of amorphous silicon are observed. The two redox processes are also detected in the delithiation process at about 0.26 V and 0.48 V. The reductive decomposition of the electrolyte evolves through two main peaks at about 1.4 V and 0.8 V, attributable to the decomposition of EMC and EC, respectively. It is worth mentioning that for thin-film electrodes, a non-negligible contribution also arises from the interaction of the electrolyte with the copper current collector.³ Indeed, we also observe electrolyte reduction within the 2.0–0.5 V voltage range by cycling the bare-copper current collector in the same condition as the silicon thin-film electrode (see inset Figure 1a). The compared voltage signatures, reported in the inset of Figure 9a, show an overlapping behavior, with a small fraction of extra current attributable to the inherent reactivity of silicon toward carbonate-based electrolytes.

Upon further cycling, a stable electrochemical behavior is observed that is characterized by a decrease of the current involved in the electrolyte reduction region and a constant and reversible lithiation and delithiation process. The latter one is attributed to the properties of the thin-film electrode. Indeed, it is generally reported that the magnitude of the lithiation and delithiation peaks increase upon cycling due to the increased electrochemical reactivity of freshly exposed silicon generated by the cracking effect. However, in our study, this behavior is not observed due to the structural stability of the electrode conferred by the limited thickness of the thin films in which the cracking effect is well buffered.² This fundamental property of the 50-nm-thick thin film enables the study of the silicon reactivity toward the electrolyte, avoiding any possible effect related to the volume expansion experienced by the active material upon cycling.

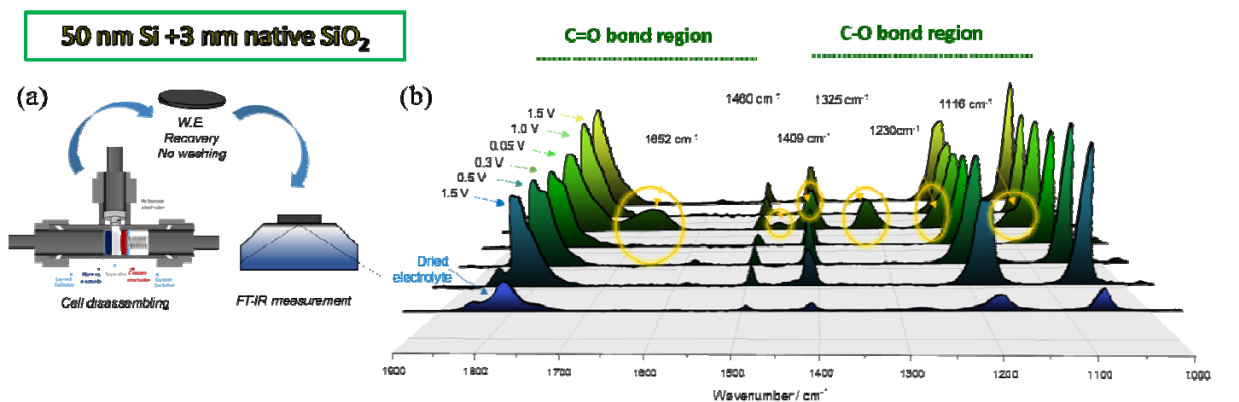
Figure 9b reports the voltage profile of the first and second (de)lithiation process obtained applying a constant current of 5 $\mu\text{A cm}^{-2}$ within the 0.05 V–1.5 V potential range. The cycling behavior is a good match with the CV analysis. Indeed, all the redox peaks observed during CV are also well defined in the constant-current-mode test. The green dots represent the different state of charge at which the electrode surface has been analyzed. The interfacial properties of the 50-nm Si thin-film model electrodes have been investigated by *ex-situ* ATR-FTIR analysis at different states of charge during the first (de)lithiation process.

Figure 10 reports the *ex-situ* ATR-FTIR spectra collected at 1.5, 0.5, 0.3, and 0.05 V during the reduction process and at 1.0 and 1.5 V in the following oxidation. The electrodes have been analyzed as recovered from the cell without any washing treatment to remove electrolyte residuals (see schematic in Figure 10a). The spectra have been recorded after a drying step, enabling the evaporation of the most volatile solvent of the

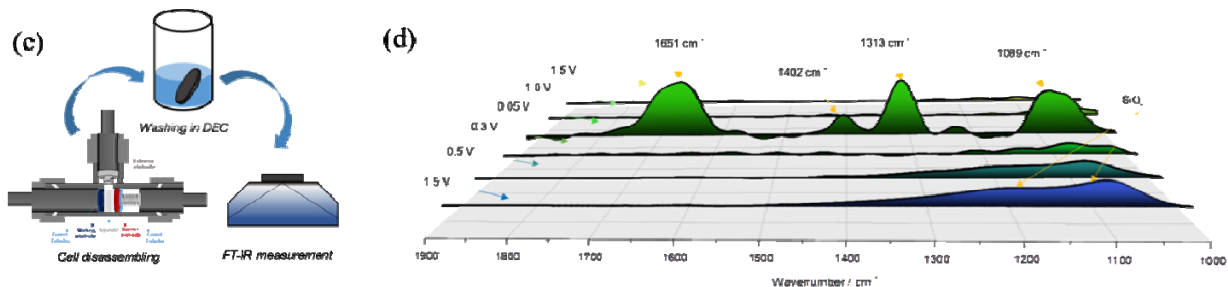
electrolyte, represented by EMC. For comparative purpose, the reference spectra of the so-called “dried” electrolyte is also reported; it is considered to be a more representative reference spectra for the *ex-situ* ATR-FTIR analysis performed on the recovered dried electrodes. The absorption peaks characterizing the spectra obtained at 1.5, 0.5, and 0.3 V mostly belong to electrolyte residuals as compared with the peaks of the dried electrolyte spectra. However, the analysis reported in Figure 10b offers the ability to detect some major changes in the 1,000–1,900 cm^{-1} spectral region in the fully lithiated state, i.e., 0.05 V. Three new main features appear at about 1,652 cm^{-1} (ν C=O), 1,460 cm^{-1} (δ C-H), and 1,325 cm^{-1} (ν C=O), whereas broadening of the electrolyte peaks is observed at 1,409 cm^{-1} (ν O-C-O and δ C-H), 1,230 cm^{-1} (ν C-O or ν P=O, P-O-C), and 1,116 cm^{-1} (ν C-O-C). The new contributions observed in the fully lithiated state are attributed to the presence of lithium ethylene dicarbonate ((CH₂OCO₂Li)₂-LiEDC) on the electrode’s surface. LiEDC was firstly proposed by Aurbach et al.^{2,3} as the primary decomposition product of EC-containing electrolytes. Indeed, it has been reported that LiEDC is the result of a single-electron reduction process of EC (see schematic in Figure 10e), which has been detected on noble metals and the surface of lithium electrodes.^{6,7} Later, the presence of LiEDC on lithium electrodes was further confirmed and implemented, with its detection also on nickel surfaces^[8] and more recently on carbonaceous⁷ and silicon-based electrodes,⁸ suggesting LiEDC as a main component of the passivating film formed on the surface of working electrodes when using EC-containing electrolytes.

Although the detection of LiEDC does not itself represent a new finding, Figure 10b offers a fundamental observation related to the instability of the passivating film formed on silicon electrodes. Indeed, the new features assigned to LiEDC in the spectra obtained at 0.05 V disappear upon delithiation both at 1.0 V and 1.5 V. This new fundamental observation leads to the correlation between the presence of LiEDC on the surface film and its passivating properties, making it one of the components most likely responsible for the poor passivating properties of silicon electrodes. Interestingly, in the 1,900–1,000 cm^{-1} spectral region, no other relevant features are observed in all the spectra collected at different states of charge. This can be explained considering the high solubility of the electrolyte decomposition products, which then diffuse into the electrolyte. The latter ones may indeed either solubilize in the solvents or detach from the electrode’s surface, thus inhibiting the formation of a stable passivating film.

SEI on un-washed Silicon thin film electrodes: Visualization of the SEI evolution



SEI on washed Silicon thin film electrodes: Detection of the insoluble SEI components



Identifying LiEDC as main electrolyte decomposition product of 1.2 M LiPF₆ EC:EMC 3:7 wt.%

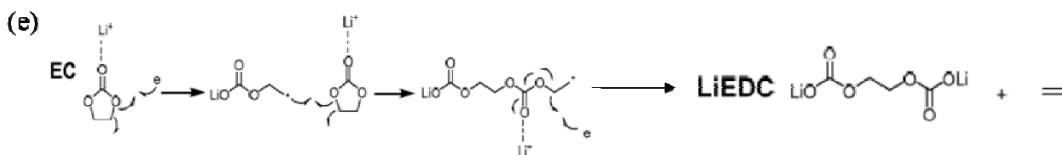


Figure 10. Schematic representation of the electrode recovery and ATR-FTIR testing of unwashed (a) and washed (c) Si thin-film model electrodes. Cells have been cycled at $5 \mu\text{A cm}^{-2}$ employing 1.2 M LiPF₆ in EC:EMC (3:7 wt.%) as electrolyte. *Ex-situ* ATR-FTIR analysis of cycled Si thin films at different states of charge during the first (d)lithiation process in the 1,900–1,000 cm^{-1} spectral region of unwashed (b) and washed (d) electrodes. (e) Schematic representation of LiEDC formation as a decomposition product of EC.^[8]

In an effort to detect further hidden components of the surface layer and investigate the solubility of the formed products, two different approaches have been undertaken. The first one is a physical approach consisting in a rinsing step of 10 seconds in DEC followed by a drying process in a glovebox under inert atmosphere (see FigureFigure 10c). The FTIR analysis on the rinsed electrode is reported in FigureFigure 10d. The washing process adopted leads to the disappearance of all the electrolyte features on the silicon surface, disclosing the appearance of the native SiO₂ layer features at 1.5 V and 0.5 V and 0.3V. Indeed, it is believed that the surface-layer thickness at these states of charge is fairly limited and most likely constituted by soluble products, which totally disappear upon rinsing. Interestingly, it is seen that in the fully lithiated state, at 0.05 V, the features attributed to LiEDC are still present.

Indeed, as previously reported,⁸ the lithiated silicon represents a suitable surface for the deposition of LiEDC, which results in an insoluble product of the SEI because its main absorption features at about 1,651 cm^{-1} , 1,402 cm^{-1} , 1,313 cm^{-1} , and 1,089 cm^{-1} can still be detected even after the washing process.

It is worth mentioning that generally, one of the main challenges while performing *ex-situ* analysis is represented by the rinsing step. The use of a carbonate-based solvent to eliminate electrolyte residuals is seen as a necessary step to avoid the massive contribution of electrolyte species, which may hinder the detection of hidden compounds associated with the film formation. On the other hand, the rinsing process may deeply affect and modify the film composition, especially at a high degree of lithiation of the electrodes, when the electrode is more likely to further react and may also further solubilize other film components. To enable the detection of hidden compounds, while avoiding the side effects possibly induced by the rinsing step, we adopted an additional approach, consisting in a mathematical subtraction of the electrolyte peaks from the spectra obtained at different states of charge, thus avoiding any possible side reaction with the solvent during the washing step. The subtraction analysis (data not reported here) shows that for all the spectra—except the one for the fully lithiated silicon electrode—there is no evidence of other components on the surface layer. The only detectable features appear for the fully lithiated sample at 0.05 V at about 1,654 cm^{-1} , 1,326 cm^{-1} , 1,110 cm^{-1} , and 1,062 cm^{-1} , which can still be attributed to LiEDC.

The surface of the fully lithiated silicon thin-film electrode has been investigated with an apertureless near-field scanning optical microscopy (aNSOM), employing a metallized AFM tip in contact with the sample surface as an optical probe for high-resolution spectroscopy and imaging measurements. The technique offers the extraordinary ability to combine the unique capability of infrared near-field microscopy with FTIR spectroscopy to map the chemical distributions on the electrode's surface, while guaranteeing the detection of single components at high spatial resolution (see Figure 11a).^{9,10}

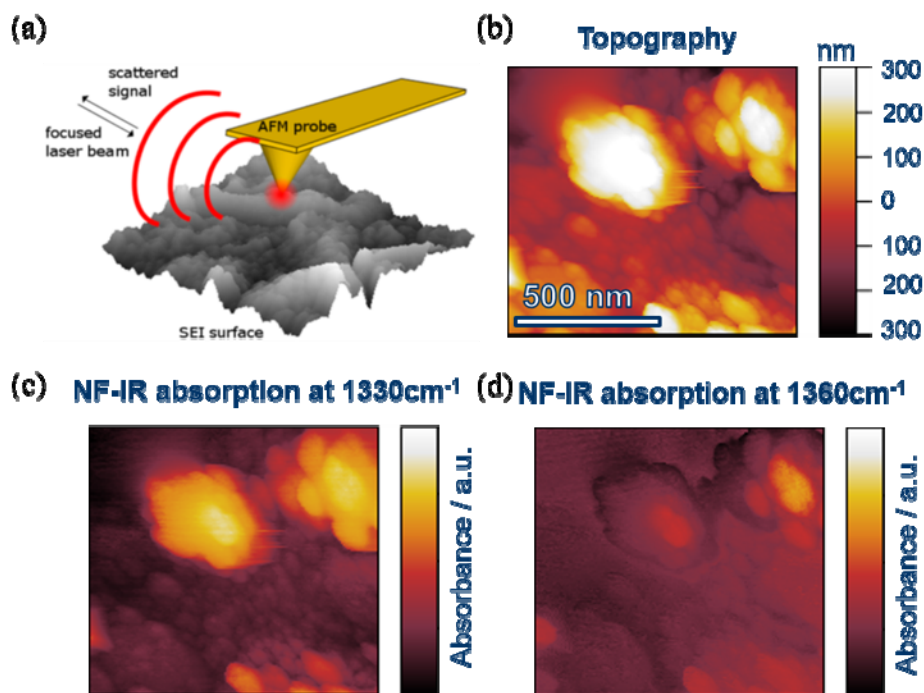


Figure 11. (a) 3-D schematic of aNSOM experimental setup and operational principle. aNSOM 1- $\mu\text{m} \times 1\text{-}\mu\text{m}$ image of 50-nm silicon thin-film electrode cycled up to 0.05 V after the first lithiation process. (b) Topography of a region of the surface film formed on the fully lithiated silicon thin-film electrode obtained by AFM. Near-field IR absorption maps over the same region at (c) 1,330 cm^{-1} and (d) 1,360 cm^{-1} wavenumbers.

Figure 11b reports the obtained AFM topography image of the SEI layer on the lithiated silicon thin film. The morphology of the detected surface layer is characterized by a nonuniform distribution and roughness.

Figures 11c and 11d report the variation in contrast as a function of IR wavelength, indicating changes in surface structure and composition. Indeed, by using a $1,330\text{ cm}^{-1}$ excitation wavelength, corresponding to an adsorption peak of LiEDC, i.e., $\nu\text{ C=O}$ (see Figure 10), a strong absorbance is detected; however, changing the wavelength to $1,360\text{ cm}^{-1}$ revealed no significant absorbance, as indeed observed in the ATR-FTIR analysis reported in Figure 10, which does not present any IR feature at $1,360\text{ cm}^{-1}$. Indeed, it can be observed that the contrast in the corresponding IR images in Figures 11c and 11d shows a direct correlation of specific features in the topography to chemical properties, which vary according to the IR absorption at different wavenumbers. The absorbing aggregates observed, which are most likely composed of round-shaped primary particles, are highlighted at $1,330\text{ cm}^{-1}$ in Figure 11c, whereas they undergo a contrast inversion in Figure 11d at $1,360\text{ cm}^{-1}$. This observation represents a direct observation of LiEDC aggregates on the electrode's surface, thus confirming our ATR-FTIR analysis and further implementing it with the gained spatial distribution on the electrode's surface.

In addition to the $1,900\text{--}1,000\text{ cm}^{-1}$ spectral region, the low-frequency region within the $1,000\text{--}700\text{ cm}^{-1}$ region has also been investigated by ATR-FTIR. This spectral region is generally characterized by P-F- and Si-O-bond-containing compounds. The analysis has been performed on both unwashed and washed electrodes and is reported in Figs. 12a and 12b, respectively.

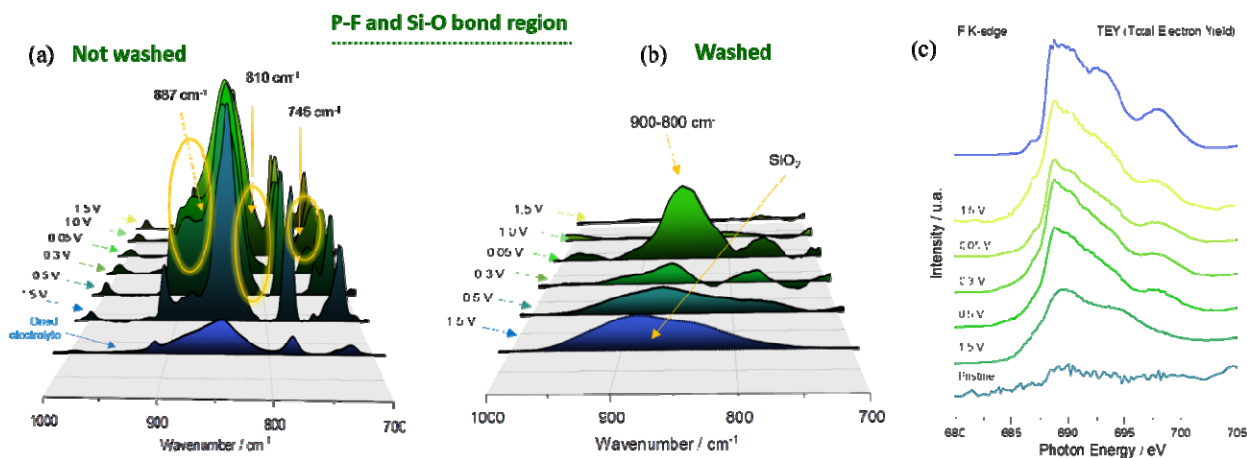


Figure 12. *Ex-situ* ATR-FTIR analysis of cycled Si thin films at different states of charge during the first (de)lithiation process in the $1,000\text{--}700\text{ cm}^{-1}$ spectral region of unwashed (a) and washed (b) electrodes. (c) *Ex-situ* XAS analysis at the F K-edge collected in TEY mode.

The spectra recorded at different states of charge clearly indicate an accumulation of species that are IR active within the $800\text{--}900\text{ cm}^{-1}$ spectral region, most likely related to P-F- and P-O-F-containing compounds. It is generally accepted that LiPF_6 precipitates in the form of Li_xPF_6 and LiF after reduction. Moreover, the eventual presence of water traces generally catalyzes the formation of PF_5 and POF_3 species.¹¹⁻¹³

The detection of P-F- and P-O-F-containing compounds have been previously observed;¹¹⁻¹³ however, our analysis offers more insights on a clear accumulation of P-F- and P-O-F-containing species upon cycling. Indeed, it is observed that upon lithiation, already starting at 1.5 V, the IR-band centered at about 850 cm^{-1} starts to broaden and becomes larger. The largest observed contribution is visible in the fully lithiated state (0.05 V). During the delithiation process, the band intensity decreases; however, the process is not totally reversible, leading to the deposition and accumulation of P-F- and P-O-F-containing species on the electrode's

surface and suggesting a dynamic growth and disappearance of the surface layer. In addition, in the analysis performed on washed samples, it is clearly observed that primarily all the features disappear to be replaced by the Si-O contributions of the native SiO₂ layer, suggesting a solubility of the P-F and P-O-F species in the solvent used to wash the electrodes. The prominent feature observed at about 850 cm⁻¹ in the fully lithiated state can be still attributed to the presence of LiEDC, as previously reported.⁶

In relation to fluorine-containing compounds, X-ray absorption spectroscopy (XAS) at the fluorine K-edge has been performed. The analysis suggests the formation of LiF (see reference spectra in blue in Figure 12c), starting at 1.5 V and accumulating upon cycling. XAS offers the ability to detect LiF as a stable SEI component, which is otherwise not detectable by FTIR because it is a non-active FTIR compound.

Our investigation leads to a fundamental observation related to the dynamic evolution of the SEI upon cycling, most likely related to the formation and disappearance of LiEDC and P-F- and P-O-F-containing compounds. To corroborate our hypothesis linking the passivation properties of the surface layer formed on silicon electrodes with the presence of LiEDC and the P-F/P-O-F-containing species, we also further investigated the behavior of the silicon thin-film model electrodes during the second cycle.

In the 1,900–100 cm⁻¹ spectral region, three main peaks and additional smaller features are observed to constantly appear and disappear upon (de)lithiation, during both the first and second cycle (see Figure 13a). All the features are related to the formation and disappearance of LiEDC on the electrode's surface. In addition, the dynamic growth and dissolution of P-F/P-O-F-containing species is observed in the 1,000–700 cm⁻¹ spectral region (see Figure 13b).

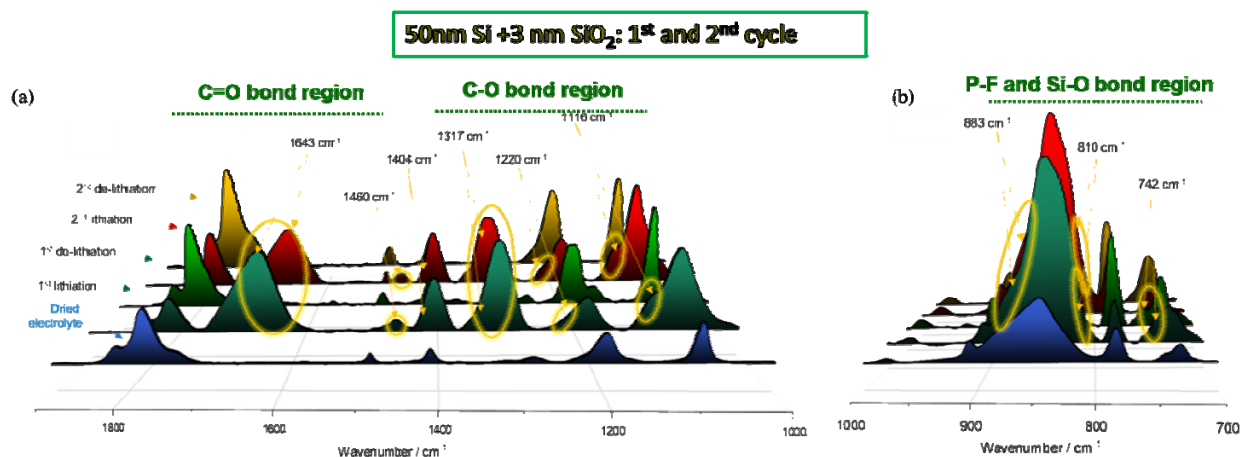


Figure 13. *Ex-situ* ATR-FTIR analysis of cycled Si thin films in the fully lithiated and delithiated state upon the 1st and 2nd cycle in the 1,900–1,000 cm⁻¹ (a) and 1,000–700 cm⁻¹ (b) spectral regions. Cells have been cycled at 5 $\mu\text{A cm}^{-2}$ employing 1.2M LiPF₆ in EC:EMC (3:7 wt.%) as electrolyte.

The results discussed here represents a step forward in understanding the stability of the SEI. The accumulation and following disappearance of different species on the electrode's surface clearly suggest a dynamic SEI formation and “dissolution.” The “breathing” mode of the passivating layer on top of the silicon thin films has also been detected by XAS.

The analysis of the silicon L-edge employing a total electron yield (TEY) detector—which is surface-sensitive (with a detection depth on the order of a few nanometers)—clearly reveals the formation and thickening of a

surface layer upon lithiation. Upon delithiation, it reduces considerably in thickness, further confirming the dynamic growth and disappearance of the surface layer (see Figure 14a).

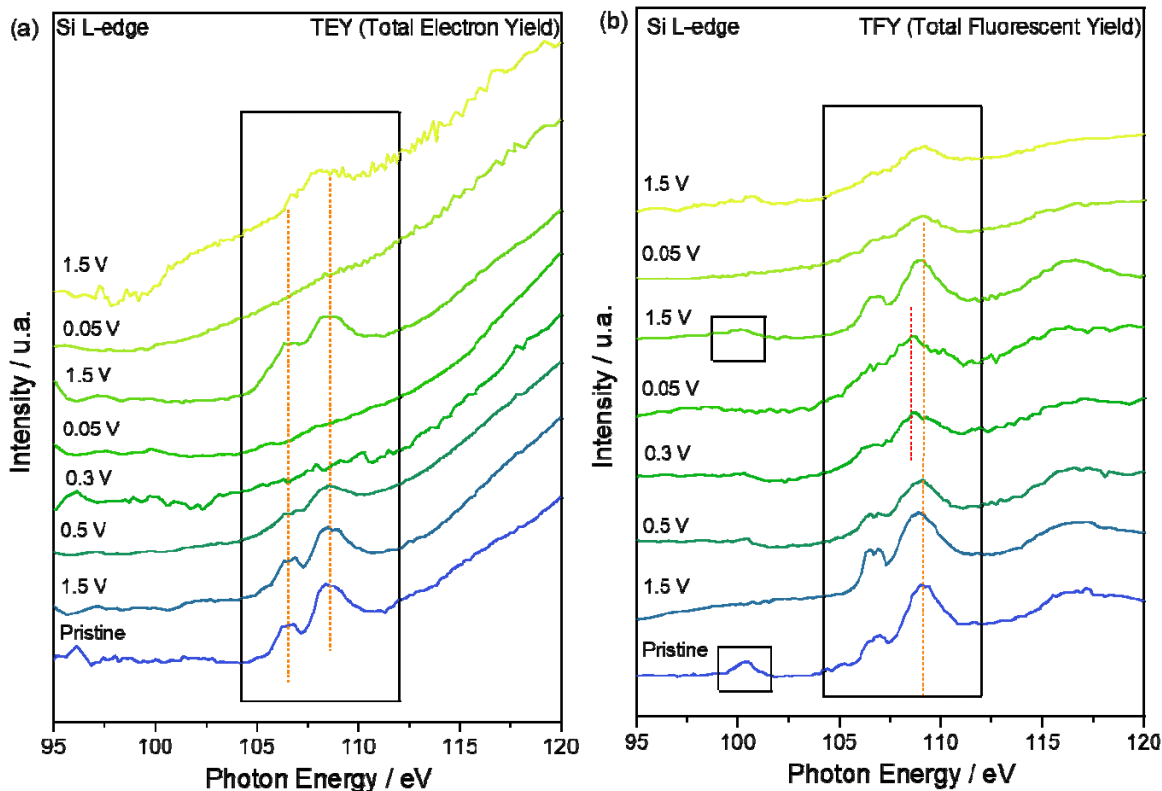


Figure 14. *Ex-situ* XAS analysis at the Si L-edge collected in TEY (a) and TFY (b) mode for the 50-nm Si thin film with native oxide.

Indeed, the typical double feature of SiO₂ gradually disappears upon lithiation and further reappears upon delithiation. A total fluorescence yield (TFY) detector (see Figure 14b) is more bulk-sensitive than the TEY, but still has a detection depth in the order of nanometers. Its use gives further insight on the behavior of both the SiO₂ (see peaks within 106–111 eV) and Si underneath the native oxide layer (see peak at about 100 eV). In Figure 14b, the breathing effect is visualized following the peak related to the silicon, which disappears upon lithiation, to then reappear in the delithiated state. In addition, the typical double feature of SiO₂ undergoes some minor changes both in terms of shape and peak position. The changes are reversible, and in the delithiated state, the pristine features are recovered.

A change in the XAS spectra in the Si L-edge may indicate a change in the electronic state of the native SiO₂ surface layer on top of the silicon thin-film model electrodes.¹⁴ It has been proposed that the SiO₂ may undergo a conversion reaction upon lithiation, leading to the formation of Li₂O and metallic silicon by forming intermediate stoichiometric or non-stoichiometric silicate species.¹⁵⁻¹⁷

To evaluate the hypothesis of the silicate formation, a new model electrode has been adopted. The electrode presents a thicker SiO₂ layer on top of the 50-nm Si thin film. ATR-FTIR analysis has been performed upon cycling and the related results are reported in Figure 15.

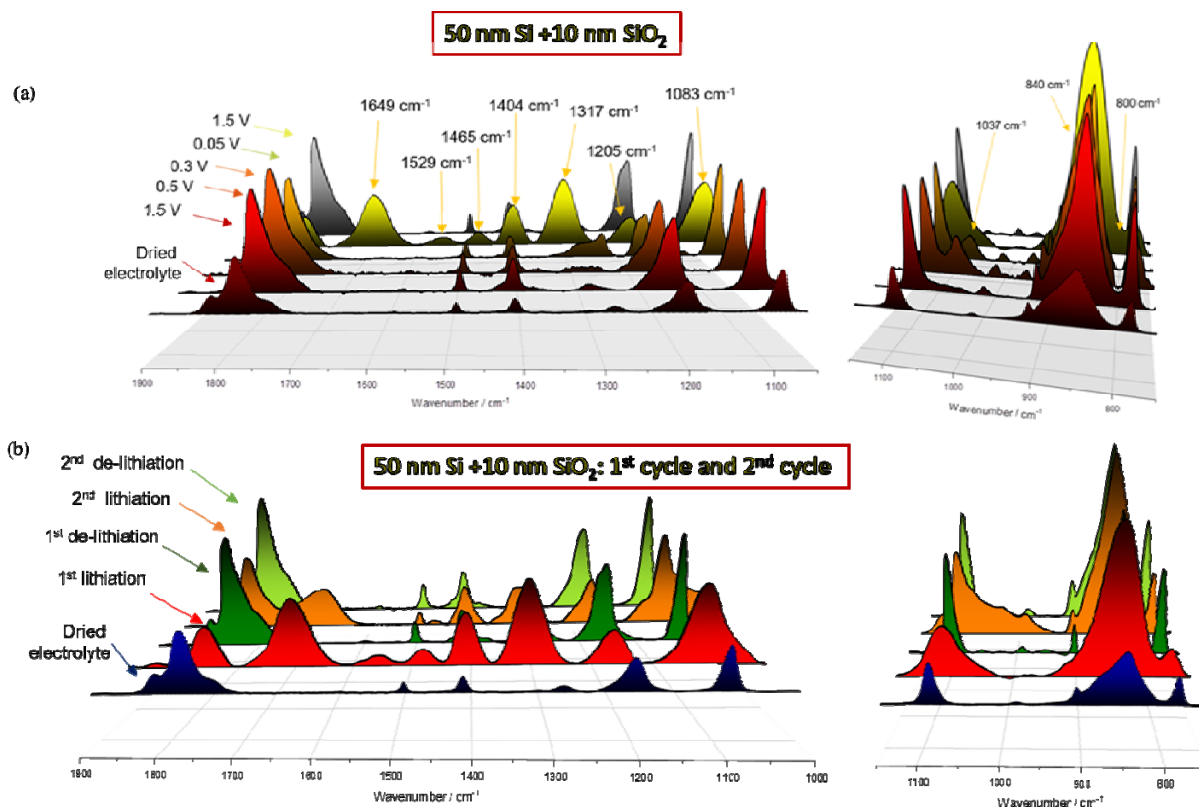


Figure 15. *Ex-situ* ATR-FTIR analysis of unwashed cycled 50-nm Si thin films with 10-nm SiO₂ at different states of charge during the first (de)lithiation process (a) and following 2nd cycle (b).

The 50-nm Si thin films with a 10-nm SiO₂ layer have been investigated at different states of charge during the first lithiation and delithiation (see Figure 15a) and also during the 2nd cycle (see Figure 15b).

Interestingly, it is observed that the 1,900–1,000 cm⁻¹ spectral region is fairly comparable with the model electrode presenting only the native oxide layer (see Figure 10), suggesting that the formation of LiEDC is not affected by the SiO₂ layer. In addition, a comparable presence of P-F/P-O-F-containing species is observed; however, new peaks at about 1,037 cm⁻¹ are also detected starting at 0.5 V until the fully lithiated state (see Figure 15a), to then disappear again during the delithiation process. In addition to the P-F/P-O-F-containing compounds, the new features may be related to the presence of other electrolyte decomposition products, such as DEDOHC,² or the eventual presence of non-stoichiometric silicates. Interestingly, upon further cycling, the accumulation of these species in the fully lithiated state is enhanced, and a clear broad signal is detected that was not observed with the previous model electrodes (see Figure 15b). It is worth mentioning that in this spectral region, features related to the presence of silicates have been proposed in the literature.¹⁸ However, work toward identifying and assigning these peaks is still in progress. In addition to the discussion related to the eventual formation of silicates, it is important to mention that our study is mainly focused on understanding the effect of the silicates on the silicon-passivating properties. The assignment of the observed features to silicates may lead to an important observation linked to the breathing behavior of silicon. Indeed, silicates, as well as LiEDC and P-F/P-O-F-containing compounds, may be linked to the breathing effect of the SEI and can be indicated as the SEI components responsible of the poor passivating properties of silicon electrodes and the poor stability of the SEI layer. Further studies in this regard are still in progress.

c. Reduction of fluoroethylene carbonate (FEC)

In this study, we are seeking to assess the role of adding FEC to the electrolyte and how it changes the physical properties of the SEI. Recent NMR and FTIR work on silicon cells cycled with FEC in the electrolyte have shown that whereas the initial reaction to activate the FEC is a defluorination reaction to create insoluble LiF and a vinoxyl radical, the majority of the FEC is then involved in a radical vinoxyl-driven polymerization of the FEC to form a cross-linked poly(fluoro-carbonate).^{18, 19, 20} In the absence of FEC, common carbonate battery solvents, such as ethylene carbonate (EC), appear to give co-polymers between a vinylene carbonate (VC)-derived species and PEO-like species.¹⁸ The latter reaction also resulted in a series of soluble PEO oligomers that dissolve into solution.²⁰ In our EQCM study on similar materials and with similar FEC concentrations, we are able to note (see Figure 16) that the silicon electrode responds, without FEC, as a stable mass increase on cycling (SEI formation) and an increase in dissipation that tracks the weight changes. The dissipation tracks film density. Consistent with previous observations, the Gen2 electrolyte forms a porous film on the silicon anode. In contrast, the addition of FEC has been noted to improve cycling whereas NMR data have noted that the film formed is more cross-linked (denser) and stable. The EQCM data are consistent with that interpretation because the initial gain of film weight stabilizes, whereas the dissipation data are consistent with the film formed being less porous and likely to have trapped solvent or electrolyte components. The percentage of FEC did not appear to have a significant impact on the data (up to 20% evaluated) although it should have an effect on electrolyte conductivity.

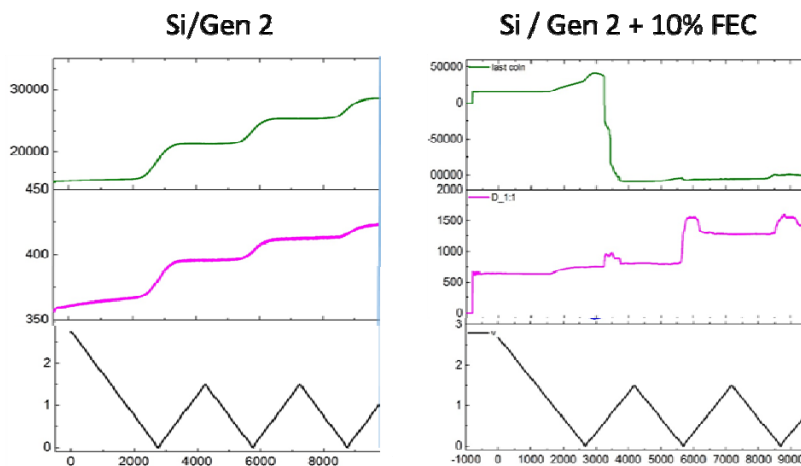


Figure 16. A comparison of the EQCM-D data for a silicon film cycled in (a) Gen2, and (b) Gen2 +10 wt.% FEC.

d. Inhomogeneous chemistry of the SEI layer

Despite such progress, a unified picture encompassing the morphology, phase, and chemical composition of SEI is still lacking, and most studies still refer to the schematic cartoon proposed by Peled for SEI on graphite anodes in 1991.^{21,22} In Fiscal Year 2018, we implemented tip-enhanced Raman spectroscopy (TERS) experiments on pristine and cycled amorphous silicon (a-Si) samples.²³ And we successfully demonstrated that the SEI has structural and chemical heterogeneity in nanoscale on the a-Si surface.

Figure 17 shows the topography (a, f, and k) and the intensity mapping of a few individual bands from the principal chemicals of SEI from each a-Si sample. The right-hand columns in Figure 17 show the dominant vibrational species as observed for each cycled a-Si sample. The topography and chemical imaging are on the same sample area, with the spatial resolution given by the scale bar in each map. The intensity of each vibrational signal is given by the color bar, which indicates the concentration of each chemical moiety. Those bands and their associated principal chemical components are summarized in Table 1.

To highlight the heterogeneous SEI chemical signatures at the nanoscale, we took nine spectra from nine spots (denoted by 1–9) for each a-Si sample, with each set of three spots 10 nm apart from each other. The spectra taken from those spots of each a-Si sample are shown in Figure 2. An immediate observation for 1X a-Si (cycled for once) TERS mapping (Figure 17) is that the distribution of the selected chemical moieties in each TERS mapping follows the AFM topography, in which the band intensity tends to distribute on top of the ridge-like a-Si, whereas this trend is not observed for 5X and 20X samples. This might be due to a thicker SEI grown on the latter two a-Si samples. For 1X a-Si, the band at 740 cm^{-1} is assigned to the $-\text{OCO}/\text{COC}$ deformation mode of LEDC (Figure 18a).²⁴ The convolution of $-\text{CH}_2$ rocking mode with this band cannot be ruled out at this frequency range.²⁴ The band centered at $1,281\text{ cm}^{-1}$ is the combination mode of CH_2 twisting and $-\text{CCO}$ asymmetric vibration, ascribed to PEO-like oligomer species in the SEI. It is clear that the distribution of the $1,281\text{ cm}^{-1}$ band on the 1X a-Si surface is different from that of the 740 cm^{-1} band, indicating different local distributions of the LEDC and PEO components in SEI in nanoscale.

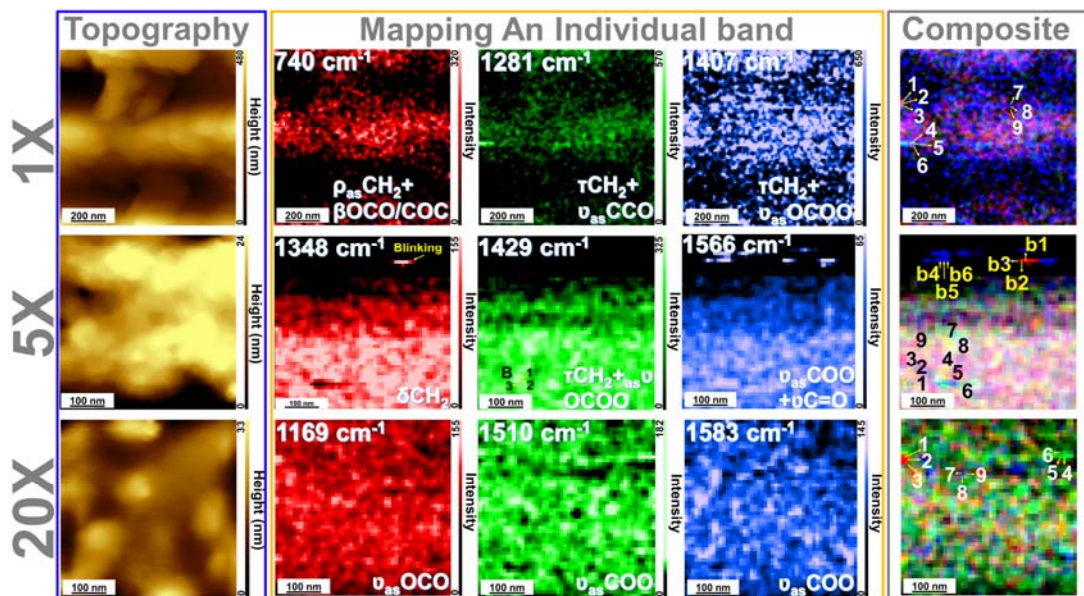


Figure 17. AFM topography (blue box), TERS mapping of an individual band (orange box) and composite TERS map (grey box) of 1X, 5X, and 20X cycled a-Si samples. The topography and chemical imaging are on the same sample area. The intensity roughly indicates the concentration of each chemical moiety. The individual band TERS mapping quantifies the intensity of a band, after spectral background correction, of each vibrational signal scaled by the false color bar. From left to right (orange box), TERS mapping indicates the overlap of $-\text{CH}_2$ rocking, $-\text{OCO}$ and $-\text{COC}$ deformation bands ($\sim 740\text{ cm}^{-1}$), $-\text{CH}_2$ twisting, asymmetric CCO stretching bands ($1,281\text{ cm}^{-1}$) and $-\text{CH}_2$ twisting, asymmetric OCOO stretching bands ($\sim 1,407\text{ cm}^{-1}$) collected from 1X a-Si, respectively. For 5X a-Si, TERS mapping respectively shows the combination of $-\text{CH}_2$ bending band ($1,348\text{ cm}^{-1}$), $-\text{CH}_2$ twisting, asymmetric OCOO stretching bands ($\sim 1,429\text{ cm}^{-1}$) and $-\text{CH}_2$ twisting, asymmetric COO stretching, and $\text{C}=\text{O}$ stretching bands ($1,566\text{ cm}^{-1}$). For 20X a-Si, TERS mapping exhibits the asymmetric $-\text{OCO}$ stretching band ($1,169\text{ cm}^{-1}$), bidentate asymmetric $-\text{COO}$ stretching band ($1,510\text{ cm}^{-1}$), and the monodentate asymmetric $-\text{COO}$ stretching bands ($1,583\text{ cm}^{-1}$). The right grey box shows the composite TERS maps for all samples. The number index of the composite map marks where the sample TERS spectrum was taken.

For 5X a-Si, we demonstrate that the more dominant species is LEDC in SEI, and the AFM topography does not correlate well to the TERS mapping like 1X a-Si. AFM topography and TERS mappings of three different vibrational modes of the 5X a-Si (Figure 17), namely $-\text{CH}_2$ bending ($1,348\text{ cm}^{-1}$), the hybrid of $-\text{CH}_2$ twisting and $-\text{OCOO}$ stretching ($1,429\text{ cm}^{-1}$), and the hybrid of asymmetric $-\text{COO}$ stretching and $\text{C}=\text{O}$ stretching ($1,566\text{ cm}^{-1}$), are shown in Figure 17 middle row (also see Figure 18b). The first band stems from PEO oligomer or LEDC, and the latter two are from LEDC monomer or dimer.²⁵ More detailed inspection of the spectra taken from the line pattern (spot b1 to b6 in the combined TERS mapping) indicates that the

corresponding bands are of much higher TERS intensity (up to 7-fold increase) than those taken from other places, attributed to the TERS “blinking” phenomenon in which extreme TERS intensity of probed species shows up intermittently.²⁶

For 20X a-Si, the most exciting findings include that the local dominant species evolves into carboxylate (RCO_2Li) compounds and fluorinated species ($\text{Li}_x\text{PO}_y\text{F}_z$). The nanoscale carboxylate molecular conformational change can be depicted by TERS, as confirmed by density functional theory (DFT) simulation (data provided by Prof. Kristin Persson’s group and not shown here). Figure 17 bottom row shows the 20X a-Si AFM topography and TERS mapping of $-\text{OCO}$ asymmetric stretching ($1,169\text{ cm}^{-1}$), bidentate $-\text{COO}$ asymmetric stretching ($1,510\text{ cm}^{-1}$), and monodentate $-\text{COO}$ asymmetric stretching ($1,583\text{ cm}^{-1}$) (Figure 18c). Several vibrational modes between $1,450\text{ cm}^{-1}$ and $1,650\text{ cm}^{-1}$ gain in intensity, which cannot be assigned to either PEO or LEDC, as observed in the case of 1X and 5X samples. Those bands are most likely ascribed to various carboxylate compounds (RCO_2Li),²⁵ which are formed either by thermal decomposition of the LEDC per prolonged galvanostatic cycling²⁶ or by ester radicals coordinating to Li^+ .²⁸

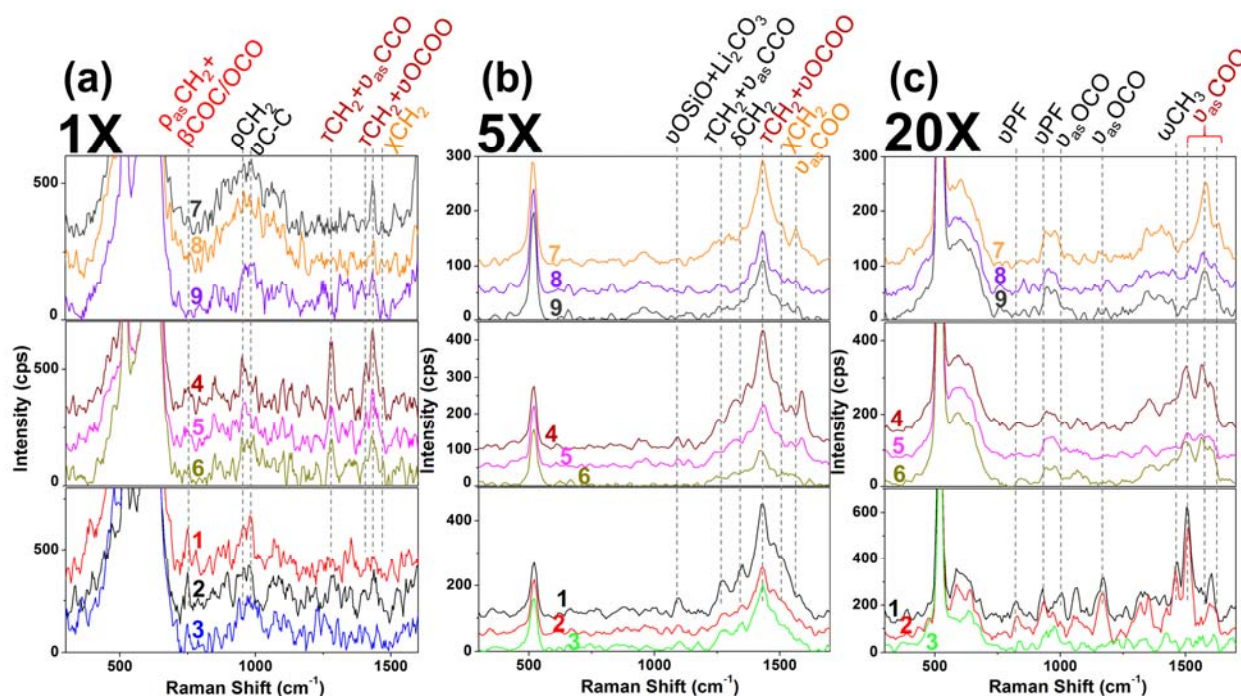


Figure 18. TERS spectra collected from various locations of (a) 1X sample, (b) 5X sample, and (c) 20X sample. The assignment for bands of interest are at the top of each plot. The Greek symbols denote corresponding vibrational modes: ν (stretching), δ (bending), χ (scissoring), τ (twisting), ρ (rocking), β (deformation), and ω (wagging).

Table 1. TERS spectral band assignment for cycled a-Si

Number of Cycles	Spectral Position (cm^{-1})	Principal Chemical/Vibrational Signature of SEI from TERS	Band Assignment
1X	740	LEDC	$\rho_{\text{as}}(\text{CH}_2) + \beta(\text{OCO}/\text{COC})$
	1,281	PEO	$\tau(\text{CH}_2) + \nu_{\text{as}}\text{CCO}$
	1,407	LEDC	$\tau(\text{CH}_2) + \nu_{\text{as}}\text{OCOO}$
	1,433	LEDC	$\tau(\text{CH}_2) + \nu_{\text{as}}\text{OCOO}$

5X	1,348	PEO/LEDC	$\delta(\text{CH}_2)$
	1,429	LEDC	$\tau(\text{CH}_2) + \nu\text{OCOO}$
	1,491	LEDC	$\chi(\text{CH}_2)$
	1,566	LEDC	$\nu_{\text{as}}(\text{COO}) + \nu(\text{C}=\text{O})$
	1,588	LEDC	$\nu_{\text{as}}(\text{OCO})$
	822	R_2POF	$\nu(\text{PF})$
	929	RPOF_2	$\nu(\text{PF})$
20X	1,169	LEDC	$\nu_{\text{as}}(\text{OCO})$
	1,460	monodentate carboxylate	$\omega(\text{CH}_3)$
	1,510	bidentate carboxylate	$\nu_{\text{as}}(\text{COO})$
	1,565	Bridging + monodentate carboxylate	$\nu_{\text{as}}(\text{COO})$
	1,583	monodentate carboxylate	$\nu_{\text{as}}(\text{COO})$
	1,632	monodentate carboxylate	$\nu_{\text{as}}(\text{COO})$

3. Morphology and physical properties of the SEI layer

Morphology of SEI layer formed on the two model Si wafer samples—including the Si wafer with a 15-nm SiO_2 thermally grown layer and Si wafer with a native oxide layer—have been obtained by using STEM, while the resistivity as a function of depth was monitored by using the SSRM technique. The Si wafer electrodes were lithiated at a constant current of $22 \mu\text{A cm}^{-2}$ for 5 hours. Figure 19 compares the resistivity obtained from these two Si electrodes. When using the Si sample with a 15-nm SiO_2 layer, higher resistivity was detected in the SEI layer, as compared to the SEI later on the Si sample with a native oxide. STEM high-angle annular dark-field images and energy-dispersive X-ray spectroscopy (EDS) images were captured from these two samples and are shown in Figure 20. EDS maps show a higher content of C and O and a lower content of F in the SEI layer formed on the Si electrode with a 15-nm SiO_2 layer, when compared to the SEI formed on a Si electrode with a native oxide layer. The high-content C and O in the Si electrode with a 15-nm SiO_2 layer indicate the formation of organic components in the SEI layer, resulting in more insulating behavior.

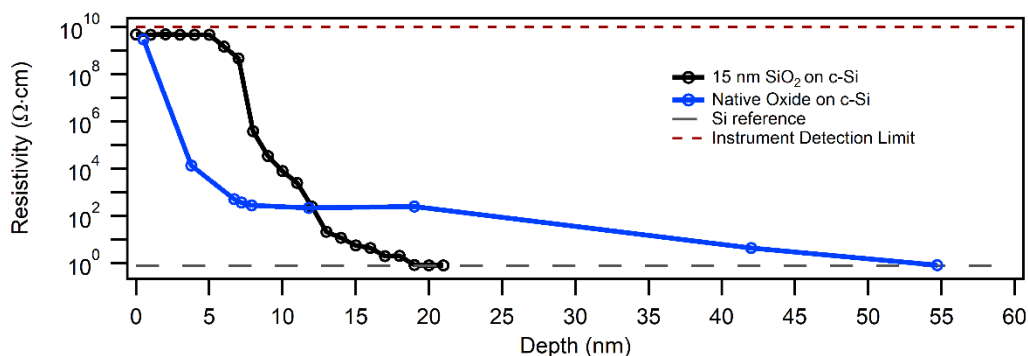


Figure 19. SSRM resistivity vs. depth profiles of SEI formed on 15-nm SiO_2 and native oxide on Si wafers after one cycle.

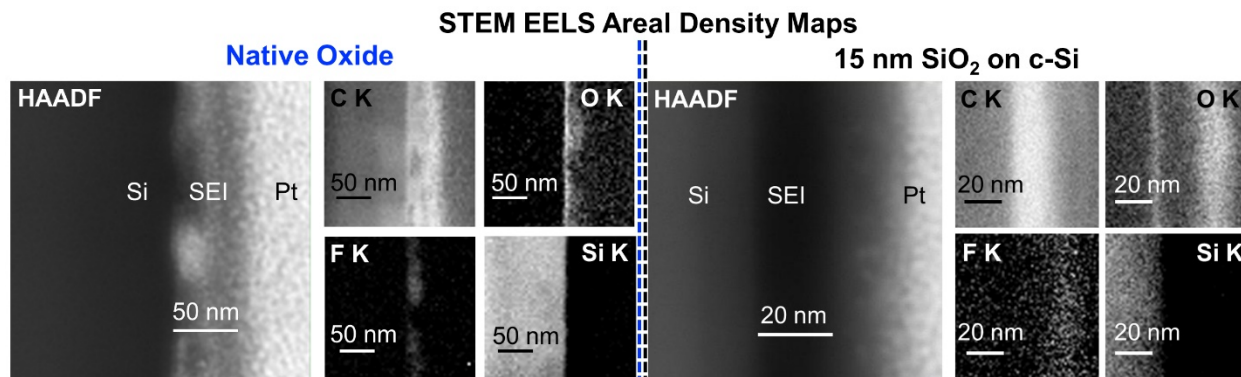


Figure 20. STEM EELS areal density maps on SEI formed on two model Si systems. SEI formed on native oxide is comparably thicker and less laterally homogenous when compared to that formed on SiO₂

Development of Characterization Techniques

1. Scanning Spreading Resistance Microscopy (SSRM) Technique Development: 3D Resistivity Mapping

To characterize the electronic resistivity of SEI, an experimental approach was developed using SSRM. The technique is described in Figure 21. We found that the electronic resistance is uniform in the lateral direction (plane view) within an order of magnitude. However, the resistance decreases steeply (up to 10 orders of magnitude) with depth, from the top surface toward the Si electrode (Figure 21e). The profile should qualitatively or semi-quantitatively reflect the resistivity change due to the different material compositions deposited by electrochemical reactions at different voltages in the lithiation/delithiation cycles. This resistivity profile also changes with SEI cycling conditions and electrolyte chemical composition, illustrating the material dependence of local 3-D resistivity.

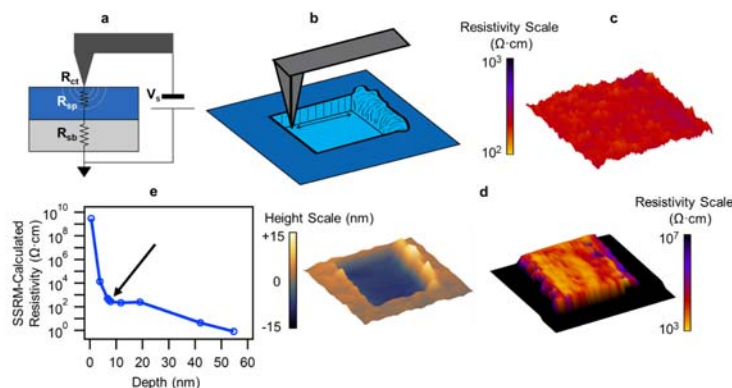


Figure 21. An example of 3-D resistance mapping of SEI. (a) SSRM schematic, where spreading resistance (R_{sp}) \gg sample and back-contact resistance (R_{sb}). By using appropriately large probe forces, the contribution of the contact resistance (R_{ct}) is reduced to a stable level. Curved arcs around the probe represent potential contour arcs, indicating the sampling volume, in a semi-infinite uniform material. (b) Conceptual diagram depicting measurement technique. A resistance map is captured at intermediate probe forces, resulting in uniform milling of the surface material to a defined depth. A larger scan is then taken over the measurement area to determine the depth of the resistance map. (c) $0.5 \times 0.5 \mu\text{m}$ resistance map captured with a probe forces of $15 \mu\text{N}$ on SEI on Si with SSRM, measuring resistance of SEI at a depth of 9 nm. (d) $1.0 \times 1.0 \mu\text{m}$ height channel image (left) captured at a low contact force ($< 1 \mu\text{N}$) over the location of the previously described resistance mapping raster scan, indicating the depth of the resistance map shown in (c). Resistance channel image (right)

captured in the same scan shows relative contrast in the electronic properties between the superficial and deeper structures of SEI. Slightly higher resistivities are measured at the milled area when compared to (c) due to the contribution of contact resistance when scanning with low contact forces. © Example resistivity vs. depth profile obtained from resistance and depth measurements shown in (c) and (d), respectively. The datapoint obtained from resistivity and height data presented in (c) and (d) is indicated on the profile with an arrow.

To validate the technique and determine its resolution, a reference sample was designed featuring an α -Si:H layer stack. Analysis of the sample with film resistivity measurement (to determine resistivities of individual layers), secondary-ion mass spectrometry (SIMS), and SSRM allowed validation of the SSRM 3-D resistivity mapping and determination of SSRM resolution with 10–50 nm in lateral and ~50 nm in vertical directions (Figure 22).

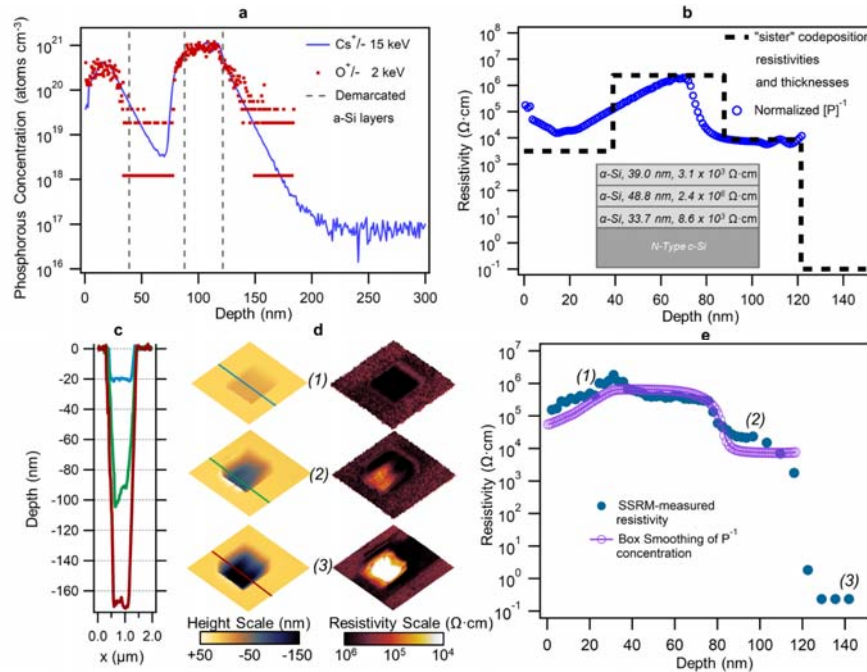


Figure 22. SIMS and SSRM data for doped α -Si:H on c-Si reference sample. (a) Dynamic SIMS P-concentrations measured with cesium and oxygen sputtering at 15 keV and 2 keV, respectively. (b) Inverse P-concentration, normalized to highest bulk resistivity, measured on “sister” co-deposition on glass. Sample schematic with thicknesses and bulk resistivities is shown in inset. (c) Line scans across overview height images captured during various stages of incremental SSRM profiling, showing three distinct depths within the structure. (d) $2 \times 2 \mu\text{m}$ height (left) and resistivity (right) overview images at three stages of incremental SSRM profiling, demonstrating contrast in electronic resistivities at different depths within the structure. (e) SSRM resistivity vs. depth profile for the sample. Box-smoothing of normalized inverse P-concentration data shows close agreement with SSRM data after smoothing to include 10 nm of previous points (to account for probe tip penetration and debris accumulation at the probe) and 40 nm of subsequent points (to account for the sampling volume of the spreading resistance).

2. Development of fluorescence probes

A variety of methods have been employed to characterize the properties of lithium ions because they are relevant to battery technology. But these techniques often either require highly specialized equipment (neutron scattering, neutron tomography), do not have the spatial resolution to probe micro- and nanostructured ion transport pathways (NMR), or do not probe the lithium ions themselves, but rather, assumed ion-transport tunnels (scanning probe microscopy, X-ray tomography). Very recently, fluorescence microscopy was proposed as a tool that could potentially satisfy all of these technical obstacles by providing information on high spatial and time resolution about the distribution of lithium ions using relatively accessible equipment.²⁹

However, many technical obstacles remain before such a technique could be employed *in operando* or even for *post-mortem* analysis to assess structural information in lithium-ion batteries.

In this work, we set out to develop fluorescent probes that would help determine how components of the silicon SEI layer evolve with cycling. The work specifically contributed to the SEISta project milestones by complimenting existing strategies to quantitatively measure soluble components of the SEI as well as measure the growth rate of the SEI components at fixed potentials and during cycling. In FT2018, work commenced with the synthesis of a model fluorescent probe recently described in the literature (Figure 23) that is highly sensitive and specific to lithium ions.³⁰ The organic molecule 2-(2-hydroxyphenyl)-naphthoxazole (HPNO) reportedly binds lithium in a 2:1 stoichiometry and maintains tetrahedral geometry, but the binding planarizes the organic molecule, which in turn red shifts its absorbance and fluorescence spectra. Following the synthesis and characterization of HPNO this quarter, we verified the response of its optical properties to increasing lithium ion concentration with simple solution absorbance measurements. As can be seen in Figure 23, absorbance red-shifts more than 40 nm in the presence of LiBr, and absorbance intensity scales with LiBr concentration.

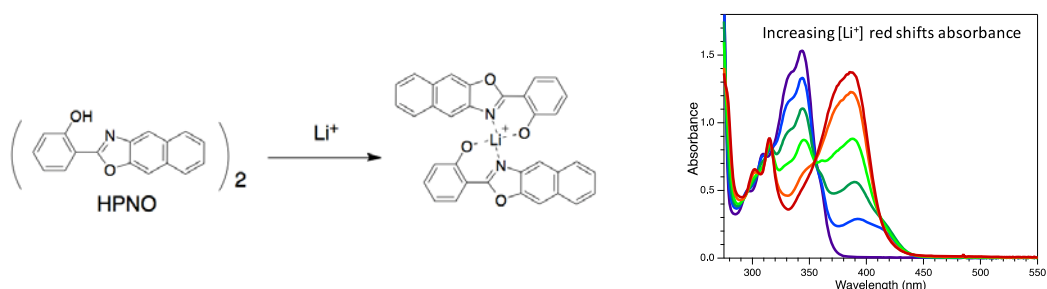
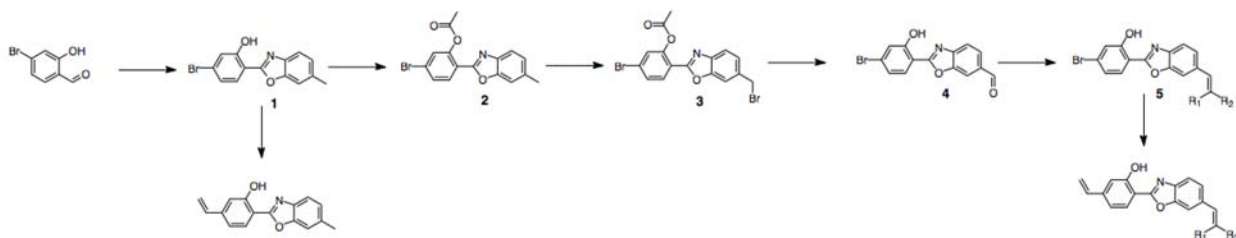


Figure 23. (Left) Scheme for lithium binding by HPNO fluorophore. (b) UV-vis spectra of 0.05 mM HPNO in propylene carbonate without lithium (purple) and increasing amounts of LiBr until the solution is saturated with LiBr (red).

We then designed and implemented experimental routes for the synthesis of two new Li ion fluorescent sensors based on a modified literature design for tuning chromophore fluorescence.³⁰ The strength of the different electron donating and withdrawing groups on these monomers (Scheme 1) would in principle allow the emission spectra of these compounds to be tuned so they do not significantly overlap with the background fluorescence of the SEI layer. As these compounds have not previously been reported in the literature, synthetic procedures were refined for each step.



Scheme 1. Synthesis of Li ion fluorescent sensors with tunable absorbance spectra. R groups represent strong electron withdrawing groups. n

A series of three monomeric fluorophores (M1–M3) were completed with a range of electron donating/withdrawing substituents, whose strength allowed the absorbance and emission spectra of these compounds to be tuned so they would not significantly overlap with the background fluorescence of the SEI layer. As can be seen in Figure 24 (top), where the absorbance spectra of each sensor was recorded in the presence of a large excess of Li salt, the “push-pull” effect of the strong electron-withdrawing cyano and ester group in the M3 sensor dramatically red-shifted the onset of absorbance by nearly 100 nm compared to the electron-donating effect of a methyl group (M1). The extended conjugation in M2 results in a very slight red-shift in absorbance relative to M1 by ~10–20 nm. The results indicate that excellent tunability of this sensor can be achieved over a range of 100 nm. The bottom half of Figure 24 illustrates that the sensitivity of each fluorophore to increasing concentrations of LiBr are all similar, although the new sensor M3 actually has a slightly increased sensitivity to lower concentrations of LiBr. For example, 0.05 mM of sensors M1 and M2 do not detect the presence of 10 eq. of LiBr (compare blue and purple traces), whereas M3 does begin to respond to this low concentration of Li salt.

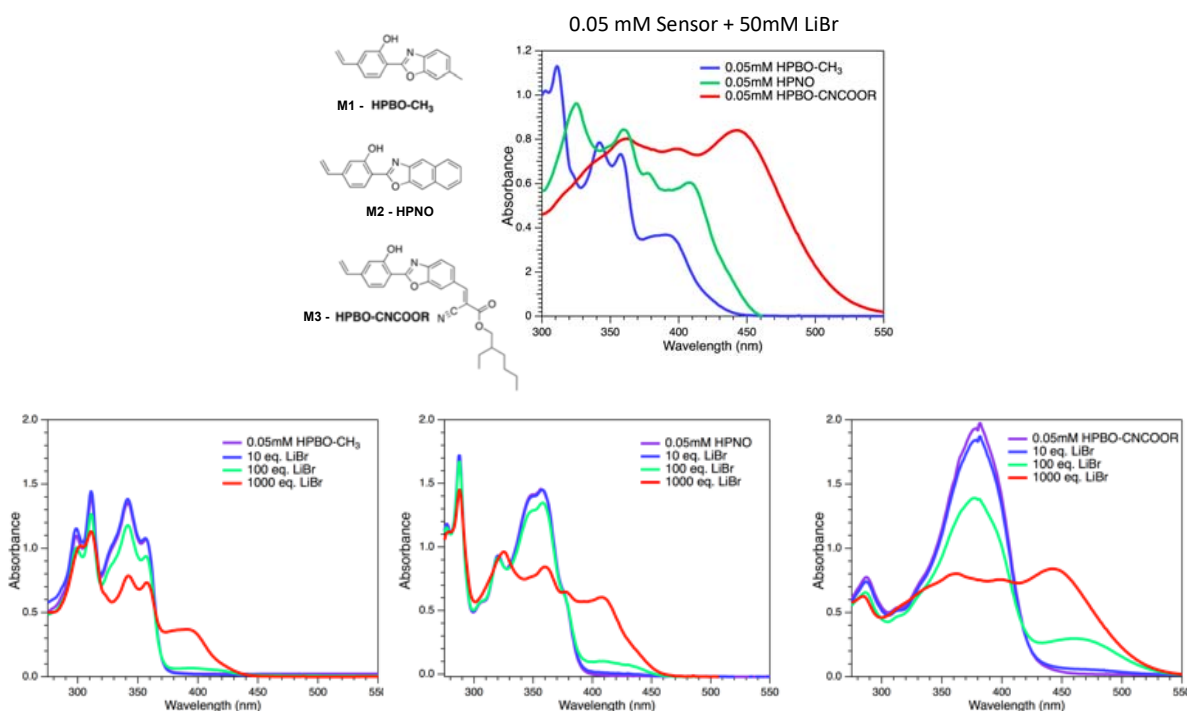


Figure 24. (top) Three new monomeric Li-ion fluorescent sensors developed in this program with “tunable” absorbance spectra over a range of ~100 nm. (Bottom) Sensitivity of the sensors to various LiBr concentrations.

Recently, the fluorophores have been incorporated into poly(methyl acrylate) and poly(acrylic acid) gels. The preliminary data from the absorbance/fluorescence spectra in the solid state indicate that the absorbance spectra are more responsive to small Li concentrations in the solid state than in solution (because the Li fluorophore is not “competing” for coordination with solvent molecules). Preliminary qualitative fluorescence data also indicate that too much Li salt can actually have a quenching effect on fluorescence, but smaller concentrations turn fluorescence “on.” We are currently studying the effects of different counteranions (LiBr vs. LiPF₆ vs. LiTFSI), both in PMA gels and PAA gels where the fluorophore represents 2 mol% of the binder. We have also begun some spectroelectrochemistry experiments with Mike Carrol, although the data are quite preliminary.

Conclusions

The study of the solvation structure of the carbonate electrolyte has identified the total solvation number of Li in bulk EC to be close to 6, whereas it reduces to 4 at the interface. Explicit interaction between the SiO₂ interface and electrolyte results in higher CIP ratio at the interface. Enhanced CIP at the SiO₂ interface hints at reaction pathways of SEI formation. By decoupling the early-stage SEI formation from the lithiation process, we have investigated the chemistry and electrochemical reduction of the early-stage SEI. Both the LiEDC and Li₂CO₃ are verified as the main components of early-stage SEI formed by the EC reductive reaction occurring at around 550 mV. At lower voltage of about 250 mV, Li_xSiO_y is observed due to the interaction between the surface silicon oxide and the electrolyte. Surprisingly, the EC reduction repeatedly occurs at the Si surface, although the reactivity dramatically reduces after the first cathodic process. Meanwhile, Li_xSiO_y continuously forms even after many cycles of cathodic process. During a long rest after the cathodic process, the carbonaceous-based components found in the early-stage SEI layer leave the surface of the Si electrode, resulting in a clean, smooth surface. We expect that some components of the early-stage SEI may decompose or dissolve in the electrolyte. The chemical instability of the early-stage SEI would contribute to low coulombic efficiency.

The chemistry of SEI—formed during the Si lithiation process, at a voltage below 50 mV—has also been studied. Among the components found in the SEI, lithium ethylene dicarbonate (LiEDC) has been identified as the only insoluble product of electrolyte reduction, observed only on the fully lithiated state (0.05 V), and it was concluded to be the primary component of the passive layer. In addition to LiEDC, P-F- and P-O-F-containing compounds were detected but were soluble and easily washed from the electrodes with EMC. LiF is not IR active and no conclusions related to it can be made here. We concluded that P-F and P-O-F compounds probably do not contribute to passivity, but reactions leading to these products would contribute to low coulombic efficiency. More importantly, the LiEDC features were lost upon delithiation to 1.5 V, and they reappeared upon subsequent lithiation back to 0.05 V. To date, the focus has been on correlating the properties of the silicon SEI film with the constituents of the electrolyte. We have noted that the interaction of the solvents (EC or FEC) are different with the charged silicon electrode surface. Correlating reported NMR data with the EQCM data indicates that the EC-derived film is much more porous and has steadier growth than the FEC-derived film, which appears denser.

The SEISta project has demonstrated the first TERS study of SEI, providing both topographical and chemical mapping of a-Si at nanoscale with extremely high sensitivity and surface selectivity, in contrast to ensemble-averaged information obtained from bulk spectroscopic techniques such as Raman and IR. TERS analysis of 1X, 5X, and 20X cycled a-Si shows that SEI composition gradually evolves with progressive cycling. The dominant SEI species at probed area are LiEDC and PEO-like oligomer for 1X a-Si, LiEDC for 5X a-Si, and carboxylate compounds for 20X a-Si. In addition to TERS, two characterization techniques—including SSRM and fluorescent probes—have been developed to help determine how components of the silicon SEI layer evolve with cycling. The work specifically contributed to the SEISta project milestones by complementing existing strategies to quantitatively measure soluble components of the SEI as well as measure the growth rate of the SEI components at fixed potentials and during cycling.

References

- ¹ Wood, K.N. and G. Teeter, *ACS Applied Energy Materials* 1(9), (2018): 4493–4504.
- ² Schroder, K.W., H. Celio, L.J. Webb, and K.J. Stevenson, *J. Phys. Chem. C* 116 (2012): 19737–19747.
- ³ Ferraresi, G., L. Czornomaz, C. Villevieille, P. Novák, and M. El Kazzi, *ACS Appl. Mater. Interfaces* 8 (2016): 29791–29798.
- ⁴ Aurbach, D., Y. Gofer, M. Ben-Zion, and P. Aped, *J. Electroanal. Chem.* 339 (1992): 451–471.

-
- ⁵ Aurbach, D., *J. Electrochem. Soc.* 141, L1–L3 (1994).
- ⁶ Zhuang, G.V., K. Xu, H. Yang, T.R. Jow, and P.N. Ross, *J. Phys. Chem. B* 109 (2005): 17567–17573.
- ⁷ Zhuang, G.V., H. Yang, B. Blizanac, and P.N. Ross, *Electrochem. Solid-State Lett.* 8 (2005): A441–A445.
- ⁸ Shi, F. P.N. Ross, G.A. Somorjai, and K. Komvopoulos, *J. Phys. Chem. C* 121 (2017): 14476–14483.
- ⁹ Ayache, M. S.F. Lux, and R. Kostecki, *J. Phys. Chem. Lett.* 6 (2015): 1126–1129.
- ¹⁰ Ayache, M. D. Jang, J. Syzdek, and R. Kostecki, *J. Electrochem. Soc.* 162 (2015): A7078–A7082.
- ¹¹ Yang, H., G.V. Zhuang, and P.N. Ross, *J. Power Sources* 161 (2006): 573–579.
- ¹² Veith, G.M., M. Doucet, R.L. Sacci, B. Vacaliuc, J.K. Baldwin, and J.F. Browning, *Sci. Rep.* 7 (2017): 6326–6341.
- ¹³ Solchenbach, S., M. Metzger, M. Egawa, H. Beyer, and H.A. Gasteiger, *J. Electrochem. Soc.* 165 (2018): A3022–A3028.
- ¹⁴ Kasrai, M., W.N. Lennard, R.W. Brunner, G.M. Bancroft, J.A. Bardwell, and K.H. Tan, *Applied Surface Science* 99 (1996): 303–312.
- ¹⁵ Saint, B.J., M. Morcrette, D. Larcher, L. Laffont, S. Beattie, J.P. Pérès, D. Talaga, M. Couzi, and J.M. Tarascon, *Adv. Funct. Mater.* 17 (2007): 1765–1774.
- ¹⁶ Schroder, K.W., A.G. Dylla, S.J. Harris, L.J. Webb, and K.J. Stevenson, *ACS Appl. Mater. Interfaces* 6 (2014): 21510–21524.
- ¹⁷ Philippe, B., R. Dedryève, J. Allouche, F. Lindgren, M. Gorgoi, H. Rensmo, D. Gonbeau, and K. Edström, *Chem. Mater.* 24 (2012): 1107–1115.
- ¹⁸ Jin, Y., N.-J.H. Kneusels, P.C.M.M. Magusin, G. Kim, E. Castillo-Martínez, L.E. Marbella, R.N. Kerber, D.J. Howe, S. Paul, T. Liu, and C.P. Grey, *J. Am. Chem. Soc.* 139 (2017): 14992–15004.
- ¹⁹ Yohannes, Y.B., S.D. Lin, and N.-L. Wu, *Journal of The Electrochemical Society* 164 (2017): A3641–A3648.
- ²⁰ Michan, A.L., M. Leskes, and C.P. Grey, *Chemistry of Materials* 28 (2016): 385–398.
- ²¹ An, S.J., J. Li, C. Daniel, D. Mohanty, S. Nagpure, and D.L. Wood III, The State of Understanding of the Lithium-Ion-Battery Graphite Solid Electrolyte Interphase (SEI) and Its Relationship to Formation Cycling. *Carbon* 105 (2016): 52–76.
- ²² Peled, E. and S. Menkin, SEI: Past, Present and Future. *J. Electrochem. Soc.* 164 (7), (2017): A1703–A1719.
- ²³ Jagjit Nanda, G.Y., D. Voylov, T. Hou, R.E. Ruther, M. Naguib, K. Persson, G.M. Veith, and A. Sokolov, Unraveling Nanoscale Chemical and Morphological Heterogeneity of Solid Electrolyte Interphase on Electrochemically Cycled Amorphous Silicon (*In preparation*) (2018).
- ²⁴ Zhuang, G.V., K. Xu, H. Yang, T.R. Jow, and P.N. Ross, Lithium Ethylene Dicarboxylate Identified as the Primary Product of Chemical and Electrochemical Reduction of EC in 1.2 M LiPF₆/EC: EMC Electrolyte. *J. Phys. Chem. B* 109 (37), (2005): 17567–17573.
- ²⁵ Socrates, G., *Infrared and Raman Characteristic Group Frequencies: Tables and Charts*. John Wiley & Sons: 2001.
- ²⁶ Agapov, R.L., A.V. Malkovskiy, A.P. Sokolov, and M.D. Foster, Prolonged Blinking with TERS Probes. *J. Phys. Chem. C* 115 (18), (2011): 8900–8905.
- ²⁷ Yoon, T., M.S. Milien, B.S. Parimalam, and B.L. Lucht, Thermal Decomposition of the Solid Electrolyte Interphase (SEI) on Silicon Electrodes for Lithium Ion Batteries. *Chem. Mater.* 29 (7), (2017): 3237–3245.
- ²⁸ Schroder, K.W., H. Celio, L.J. Webb, and K.J. Stevenson, Examining Solid Electrolyte Interphase Formation on Crystalline Silicon Electrodes: Influence of Electrochemical Preparation and Ambient Exposure Conditions. *J. Phys. Chem. C* 116 (37), (2012): 19737–19747.
- ²⁹ Padilla, N.A., M.T. Rea, M. Foy, S.P. Upadhyay, K.A. Desrochers, T. Derus, K.A. Knapper, N.H. Hunter, S. Wood, D.A. Hinton, A.C. Cavell, A.G. Masias, and R.H. Goldsmith, Tracking Lithium Ions via Widefield Fluorescence Microscopy for Battery Diagnostics. *ACS Sens.* 2 (2017): 903–908.

³⁰ Seo, J., S. Kim, and S. Young Park, Strong Solvatochromic Fluorescence from the Intramolecular Charge-Transfer State Created by Excited-State Intramolecular Proton Transfer. *JACS*, 126 (2004): 11154.